Instability mechanism and disaster prevention of the jointed rockmass

Edited by
Shuren Wang, Hongyuan Liu, Chengguo Zhang
and Xu Chang

Published in
Frontiers in Earth Science

About Frontiers

Frontiers is more than just an open access publisher of scholarly articles: it is a pioneering approach to the world of academia, radically improving the way scholarly research is managed. The grand vision of Frontiers is a world where all people have an equal opportunity to seek, share and generate knowledge. Frontiers provides immediate and permanent online open access to all its publications, but this alone is not enough to realize our grand goals.

Frontiers journal series

The Frontiers journal series is a multi-tier and interdisciplinary set of open-access, online journals, promising a paradigm shift from the current review, selection and dissemination processes in academic publishing. All Frontiers journals are driven by researchers for researchers; therefore, they constitute a service to the scholarly community. At the same time, the *Frontiers journal series* operates on a revolutionary invention, the tiered publishing system, initially addressing specific communities of scholars, and gradually climbing up to broader public understanding, thus serving the interests of the lay society, too.

Dedication to quality

Each Frontiers article is a landmark of the highest quality, thanks to genuinely collaborative interactions between authors and review editors, who include some of the world's best academicians. Research must be certified by peers before entering a stream of knowledge that may eventually reach the public – and shape society; therefore, Frontiers only applies the most rigorous and unbiased reviews. Frontiers revolutionizes research publishing by freely delivering the most outstanding research, evaluated with no bias from both the academic and social point of view. By applying the most advanced information technologies, Frontiers is catapulting scholarly publishing into a new generation.

What are Frontiers Research Topics?

Frontiers Research Topics are very popular trademarks of the *Frontiers journals series*: they are collections of at least ten articles, all centered on a particular subject. With their unique mix of varied contributions from Original Research to Review Articles, Frontiers Research Topics unify the most influential researchers, the latest key findings and historical advances in a hot research area.

Find out more on how to host your own Frontiers Research Topic or contribute to one as an author by contacting the Frontiers editorial office: frontiersin.org/about/contact

Instability mechanism and disaster prevention of the jointed rockmass

Topic editors

Shuren Wang – Henan Polytechnic University, China
Hongyuan Liu – University of Tasmania, Australia
Chengguo Zhang – University of New South Wales, Australia
Xu Chang – Huaqiao University, China

Citation

Wang, S., Liu, H., Zhang, C., Chang, X., eds. (2024). *Instability mechanism and disaster prevention of the jointed rockmass*. Lausanne: Frontiers Media SA.
doi: 10.3389/978-2-8325-5040-3

Table of contents

frontiers | Frontiers in Earth Science

Editorial: Instability mechanism and disaster prevention of the jointed rockmass

Shuren Wang[1]*, Hongyuan Liu[2], Xu Chang[3] and Chengguo Zhang[4]

[1]School of Civil Engineering, Henan Polytechnic University, Jiaozuo, China, [2]School of Engineering, University of Tasmania, Hobart, TAS, Australia, [3]School of Civil Engineering, Huaqiao University, Xiamen, China, [4]School of Minerals and Energy Resources Engineering, University of New South Wales, Sydney, NSW, Australia

Editorial on the Research Topic
Instability mechanism and disaster prevention of the jointed rockmass

Introduction

Discontinuities or joints such as cracks, fissures, faults, foliations and bedding planes resulting from different geological processes are commonly found in rock masses, which often play critical roles in the initiation, propagation, and coalescence of new cracks due to stress redistributions caused by engineering activities and/or natural disturbances. It is challenging to determine the instability mechanism of rock masses with the presence of these joints, i.e., the jointed rock mass, but vital for preventing or at least mitigating the instability disaster of engineering structures constructed in these jointed rock masses.

Correspondingly, the stability and control of the jointed rock mass have become a hot issue in the world. Moreover, the anisotropy of stratified rock mass and the discontinuity caused by structural planes can further induce the instability of the surrounding rock masses of underground engineering structures, such as roadway, tunnel and chamber. Therefore, combining laboratory test, numerical simulation and theoretical analysis, many scholars have studied the mechanical response characteristics of these rocks such as strain energy evolution and acoustic emission by uniaxial cyclic loading and triaxial compression test, the expansion and evolution characteristics of joints and cracks in the rock mass under external loads, and the propagation and energy attenuation characteristics of blasting vibration in tunnel surrounding rock. How to improve the breaking efficiency of these rock masses was also discussed. Therefore, it is necessary to exchange and summarize these achievements in this field.

Progress in the research topic

We then provide a forum for professionals and academics to communicate their impactful research on *Instability Mechanism and Disaster Prevention of the Jointed Rockmass*, which results in the 10 papers being published in this Research Topic that might be of

your interest. These papers mainly cover the following four aspects, such as uniaxial cyclic loading and triaxial compression test of rock and soil samples, experimental study on failure characteristics of stratified and fractured rock mass, blasting vibration propagation and energy attenuation characteristics in surrounding rock masses of tunnels, and evolution process of tunnel instability and prediction of breaking rock efficiency. Please visit the following website for more information: https://www.frontiersin.org/research-topics/52545/instability-mechanism-and-disaster-prevention-of-the-jointed-rockmass/magazine.

Uniaxial cyclic loading and triaxial compression test of rock and soil samples

Zhang et al. studied the mechanical properties and acoustic emission evolution of water-bearing sandstone under deep high stress mining environment under triaxial conditions. Since the rock mechanical properties and strain energy evolution under cyclic loads are obviously different from those under compression, Liu et al. carried out the mechanical properties and strain energy evolution in rocks (coal, white sandstone, red sandstone, and granite) under various types of uniaxial cyclic loading-unloading. Wang et al. conducted long-term cyclic tests for different frequencies on remolded soft clay with different sand contents, investigating how the frequency impacted the stress-strain, the dynamic shear modulus, and the damping ratio of the remolded samples.

Experimental study on failure characteristics of stratified and fractured rock mass

Combining physical model experiments with acoustic emission and moment tensor inversion techniques, Zhang et al. carried out the hydraulic fracturing experiments on the large-size cores under different stress differences to reveal the propagation law of hydraulic fracturing pathway in laminar marl continental shale. Yu et al. conducted the shear failure tests on layered rock masses under different bedding dip angles, different rock bridge width, different normal forces, and forward and reverse shear effects. Moreover, they analyzed the influence of fissure angles and bridge lengths on rock mechanical properties and failure by using the uniaxial compression test and the digital image correlation technique.

Blasting vibration propagation and energy attenuation characteristics in surrounding rock masses of tunnels

During the tunnel construction process using the drilling and blasting method, the induced blasting vibration always poses a great threat to the stability and safety of the supporting structure of adjacent tunnels. To improve the efficiency and safety of tunnel blasting construction, Qin et al. investigated the vibration propagation and peak particle velocity (PPV) distribution of the lining of an excavated tunnel during the blasting of an adjacent tunnel. They analyzed the evolution process and distribution characteristics of the PPV of the lining of adjacent tunnels. Lan et al. conducted on-site experiments and numerical simulations to reveal the influence of the number of free surfaces on the energy distribution and attenuation law of surrounding hole blasting vibration signals.

Evolution process of tunnel instability and prediction of breaking rock efficiency

These natural defects (cracks, faults and cavities) will have an impact on the stability of tunnels. Li et al. investigated different conditions of surrounding rock: intact surrounding rock, surrounding rock with open-flaw and surrounding rock with filled-flaw under the true triaxial test. They explored the effect of different surrounding rock conditions on the internal failure characteristics of tunnel under true triaxial conditions. A simple and accurate evaluation method of the rock-breaking efficiency of TBM disc cutters is an essential prerequisite to improve the rock-breaking performance of TBM. Zhou et al. summarized the classical force prediction equations of disc cutters and analyzed the applicability of each equation for the constant cross-section disc cutters.

We hope that these articles provide readers with valuable information on recent developments in science, technology, and related researches for achieving the goals of *Instability Mechanism and Disaster Prevention of the Jointed Rockmass*.

Conflict of interest

The authors declare that the research was conducted in the absence of any commercial or financial relationships that could be construed as a potential conflict of interest.

The author(s) declared that they were an editorial board member of Frontiers, at the time of submission. This had no impact on the peer review process and the final decision.

Publisher's note

All claims expressed in this article are solely those of the authors and do not necessarily represent those of their affiliated organizations, or those of the publisher, the editors and the reviewers. Any product that may be evaluated in this article, or claim that may be made by its manufacturer, is not guaranteed or endorsed by the publisher.

Check for updates

Study on rock-breaking efficiency evaluation of TBM disc cutters based on Rostami prediction equations

Guanghong Zhou[1], Xuchun Wang[1], Ding Wang[2,3]*, Minhe Luo[1], Zhanpeng Hao[1] and Wenrui Wu[1]

[1]School of Civil Engineering, Qingdao University of Technology, Qingdao, China, [2]State Key Laboratory for Geomechanics and Deep Underground Engineering, China University of Mining and Technology, Beijing, China, [3]School of Mechanical Electronic & Information Engineering, China University of Mining and Technology, Beijing, China

As the main cutting tool of Tunnel Boring Machine (TBM) for rock-breaking, the rock-breaking efficiency of TBM disc cutters directly affects the TBM's boring speed, which in turn affects the overall progress of the tunnelling project. Therefore, a simple and accurate evaluation method of the rock-breaking efficiency of TBM disc cutters is an essential prerequisite to improve the rock-breaking performance of TBM. In this paper, the classical force prediction equations of disc cutters were summarized and the applicability of each equation for the constant cross-section disc cutters was analyzed. The calculation equation of the specific energy per ring of TBM rock-breaking was derived based on the Rostami prediction equations and the specific energy theory for disc cutter rock-breaking. The specific energy per ring equation was verified through a practical engineering case. The results show that the maximum relative error of the effective thrust force and the effective torque of the cutter head based on the Rostami force prediction equations is 9.8%. The relative error of the specific energy per ring is 8.0%, which indicates that the prediction of the specific energy per ring equation can accurately reflect the rock-breaking efficiency of disc cutters. The derived equation of the specific energy per ring can not only simplify the rock-breaking efficiency evaluation of TBM disc cutters, but also serve as a valuable reference for practical engineering projects.

KEYWORDS

disc cutter, force prediction, rock-breaking specific energy, rock-breaking volume, specific energy per ring

1 Introduction

With the expansion of the scale of urban subway construction, the shield Tunnel Boring Machine (TBM) tunnelling method has become the primary construction method for urban underground railway tunnels, owing to its good adaptability, low environmental interference, high efficiency and safety (Lu et al., 2004; Yagiz, 2008). For TBM, the disc cutter is the main cutting tool for rock breaking. The working principle of the disc cutter involves the combined effect of the hydraulic propulsion and rotary system on the excavation surface to break the rock (Hu et al., 2022). Previous studies have shown that the load and impact are directly applied on the disc cutter and the tunneling efficiency and reliability of TBM is closely related to its rock-breaking condition (Zhang et al., 2021; Li et al., 2022).

Therefore, the mechanical condition of the disc cutter is the critical factor for the design and manufacture of TBM. However, due to the large impact and the harsh working environment that act on the disc cutter, abnormal failures such as partial grinding and breaking frequently appear and the cutting tools need to be constantly replaced during tunnel construction, leading to low overall boring efficiency and high construction costs for TBM tunnelling (Sun et al., 2019). Hence, it is of great significance to understand the rock-breaking mechanism of disc cutters, develop the accurate load prediction model, and make the rock-breaking efficiency evaluation of disc cutters simple and efficient.

Since the 1960s, as rapid development of TBM technology, a lot of research work has been carried out about the rock-breaking theory of disc cutters. At the present stage, the mainstream theories can be summarized into three categories: the shear rock-breaking theory, the tension rock-breaking theory, and the comprehensive rock-breaking theory (Zhang et al., 2022). The Colorado School of Mines (CSM) proposed the shear rock-breaking theory in 1977–1979 (Ozdemir and Wang, 1979). The CSM rock-breaking model was summarized based on the linear grooving test of the V-shaped disc cutter. In the 1980s, through theoretical analysis and experimental research on the rock-breaking model of disc cutters, the rock-breaking laboratory of the Northeast University of Technology put forward the tension rock-breaking theory (Jin, 1981; Jin et al., 1981). With new advances in research, some researchers have proposed that the rock-breaking process by disc cutters is a complex process with multiple forms of damage. Zhang et al. (Zhang et al., 1996; Zhang, 2008) carried out laboratory tests using disc cutters and proposed that the rock-breaking process of disc cutters is mainly subjected to shear load combined with extrusion and tension. Through observing the friction marks on the cross-section of the slag sample of rock-breaking test, Mao et al. (Mao and Liu, 1988) pointed out that the cracks caused by the rock-breaking process of disc cutter are the result of the combined effect of extrusion, tension, and shear load. At present, although many researchers have conducted in-depth studies on the rock-breaking mechanism and the force prediction model of disc cutters, the assumptions and applicability of the prediction models are quite different. Therefore, for the varying of actual engineering situations, it is still necessary to compare and analyze the applicability of these models.

In this paper, the existing classical force prediction models of disc cutters were summarized. The applicability of the Rostami force prediction equations for the constant cross-section disc cutters was then analyzed. Based on the Rostami force prediction equations, the calculation equation of the specific energy per ring of TBM rock-breaking was derived which quantifies the specific energy required for one ring excavation distance. The derived equation offers a simplified approach to evaluate the rock-breaking efficiency of TBM disc cutters. This approach eliminates the need to consider rock slag volume and the effect of surrounding cracks on rock-breaking energy. Instead, the rock-breaking volume per ring and the rock-breaking energy consumption per ring was used to calculate the rock-breaking specific energy of TBM, thus making the rock-breaking efficiency evaluation more simple and more efficient. Finally, the applicability and accuracy of the specific energy per ring equation were evaluated and verified based on the actual TBM tunneling parameters of a construction section of the Qingdao

metro, which can provide theoretical support and reference for related projects.

2 TBM disc cutters

The rolling cutter is the main cutting tool for TBM rock-breaking. According to the appearance forms of the rolling cutter, it can be classified into disc cutter and toothed cutter. According to the cutter ring structure, the disc cutter can be classified into conventional disc cutter and inserted tooth disc cutter. The toothed cutter is often used in soft rock, as shown in Figures 1B, D. According to the number of blades of the disc cutter, it can be classified into single-blade disc cutter, double-blade disc cutter, and multi-blade disc cutter, as shown in Figures 1A, B, D. Single-blade disc cutter and double-blade disc cutter are commonly used in tunnel construction in Qingdao.

According to the installation position, disc cutter can be classified into center cutter, face cutter, and gauge cutter, as shown in Figure 2. In general, the center cutter of TBM mostly adopts double-blade cutter, which has relatively small radius of rotation and complex force state. The face cutter mostly adopts the single-blade cutter, which is the main cutting tool for TBM tunneling. The gauge cutter adopts the single-blade cutter with increasing installation angle from the inside to the outside to produce rounding arc transition. The outermost edge cutters ensure the excavation diameter of the tunnel.

3 Force prediction theory for disc cutter rock-breaking

In the process of rock-breaking, the disc cutter ring intrudes into the rock, producing a normal destructive effect on the rock. The disc cutter rotates around the cutter shaft and revolves around the center of the cutter head, producing a tangential destructive effect on the rock. The destruction of the disc cutter to the rock is the interaction between the disc cutter ring and the rock mass of tunnel face. As the disc cutter is constantly loaded by the thrust cylinder as well as the main drive system, its resultant motion includes constant intrusion, revolution, and rotation motion. The rock mass of the tunnel face is constantly deformed and destroyed under the load of the disc cutter, which eventually leads to the failure and detachment of the rock mass from the tunnel face. As shown in Figure 3, the disc cutter is mainly subjected to a vertical force (F_V), a tangential force (F_R), and a lateral force (F_S) during the rock-breaking process.

3.1 Rock-breaking mechanism of disc cutters

The rock-breaking process of the disc cutter is influenced by many factors, such as the tunneling parameters of the TBM, the geometric parameters and arrangement of the cutter, as well as the macro-mechanical parameters and stress state of the rock mass at the tunnel face and the occurrence state of the joint fissure, etc. Due to the complexity of the rock-breaking process, there is no explicit and unified theory for rock-breaking process of the disc cutter.
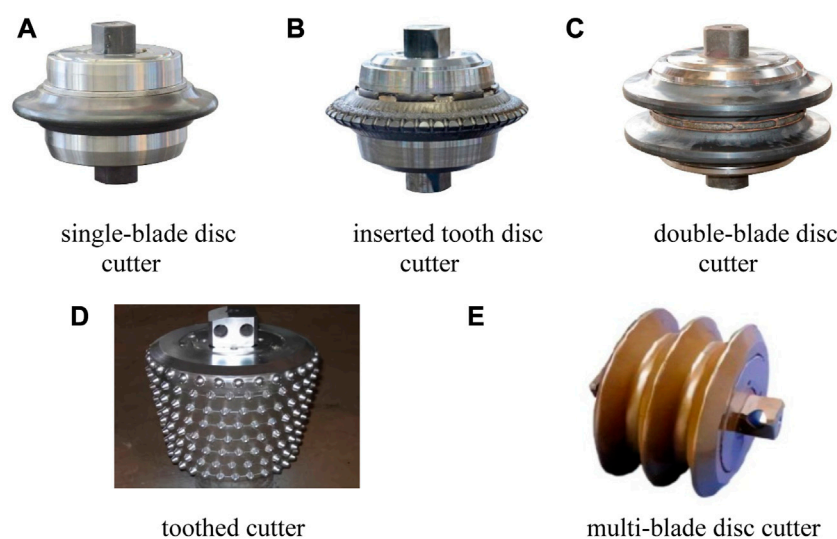
FIGURE 1
Common types of the TBM rolling cutter **(A)** single-blade disc cutter **(B)** inserted tooth disc cutter **(C)** double-blade disc cutter **(D)** toothed cutter **(E)** multi-blade disc cutter.
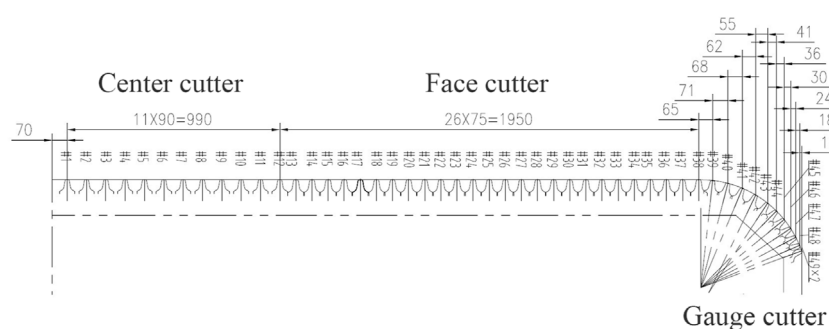
FIGURE 2
Schematic diagram of installation positions of disc cutters.

However, after years of exploration, three classical theories have been developed: shear rock-breaking theory, tension rock-breaking theory, and comprehensive rock-breaking theory.

The theory of shear rock-breaking assumes that the rock mass at the blade position of the disc cutter undergoes a stress concentration under the influence of vertical forces. Once the stress concentration reaches its limit, the rock mass is pulverized into fine particles, forming a compacted core subject to volumetric compression. This core, also called a dense core, plays a significant role in rock fragmentation during tunnel boring machine excavation.

According to the shear rock-breaking theory, a dense core is created when the rock mass at the blade of disc cutter is loaded by the vertical force. Owing to the inclined angle of the cutter edge, the rock mass on both sides of the dense core is broken as a result of shear failure under the cutter lateral force. The tension rock-breaking theory holds that the rock mass on both sides of the

dense core is broken due to tensile failure when the disc cutter intrudes into the rock. The comprehensive rock-breaking theory argues that the dense core is subjected to a combination of extrusion, tension, and shear force. The cracks developed around the dense core are mainly from tension failure and the rest are from shear failure. The rock slag is generated by the combined effect of these two failure modes.

3.2 Rock-breaking theories of disc cutters

As shown in Figures 4A, B, C, the cross-sectional form of the disc cutter ring mainly includes V-shaped section, wedge section, and constant cross-section. Compared to other cross-section disc cutters which tend to become dull and less efficient due to wear and tear, the constant cross-section disc cutters can maintain their dimensions
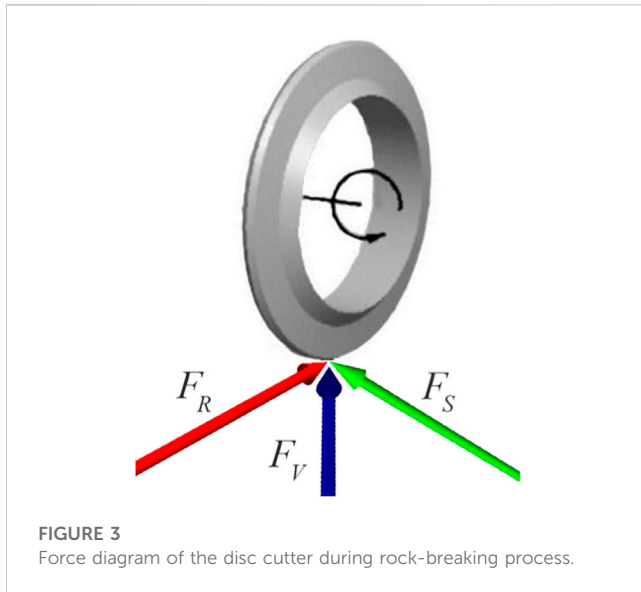
FIGURE 3
Force diagram of the disc cutter during rock-breaking process.

consistently despite wear and tear. Therefore, the constant cross-section disc cutters are generally preferred for rock-breaking and widely used in practical tunnel construction. The geometric parameters of the disc cutter are mainly the diameter (R) or radius (r), the half-angle of the cutter edge (α), the radius of the cutter nose (γ), etc. A series of force prediction equations of disc cutter have been proposed based on theoretical analysis, field tests, laboratory tests, etc. The classical force prediction equations of disc cutter for rock-breaking are summarized below.

Evans prediction equation: Through theoretical studies, Evans (Evans and Pomeroy, 1966) analyzed the vertical force loaded on the disc cutter in the rock-breaking process. Under a certain degree of penetration, it is considered that the vertical thrust of the disc cutter is proportional to the uniaxial compressive rock strength (σ_c) and the projected area (A_p) between the cutter ring and the rock surface. The projected area is the half of the area enclosed by two parabolas. However, it has been proved by experiments that the vertical thrust calculated by the Evans prediction equation is smaller than the actual vertical thrust of rock-breaking.

$$F_V = \sigma_c A_p = \frac{4}{3}\sigma_c p \sqrt{r^2 - (r-p)^2}\tan\alpha \qquad (1)$$

Where: r = Radius of cutter
p = Penetration per revolution
α = Half-angle of the cutting edge

(2) Tosaburo Akiyama prediction equations: Tosaburo Akiyama (Akiyama, 1970) developed the Evans prediction equation and proposed two equations for calculating the lateral force of the disc cutter:

① Based on the extrusion rock-breaking theory:

$$F_S = \frac{\sigma_c}{2}R^2\left(\phi - \sin\phi\cos\phi\right) \qquad (2)$$

② Based on the shear rock-breaking theory:

$$F_S = R\phi\delta S\sigma_c \qquad (3)$$

Where: S = Cutter space
δ = Rock-breaking coefficient (τ/σ_c)
τ = Unconfined shear strength of rock
ϕ = Relative Angle of Hob and Rock ($\sqrt{(3\sigma S/R)}$)

(3) Roxborough prediction equations: Roxborough and Phillips (1975) improved the calculation method of the projected area between the cutter ring and the rock surface in the Evans prediction equation. They regarded the contact surface between the cutter and the rock as a rectangle, and deduced the calculation equations of the vertical force, the tangential force and the lateral force of the V-shaped disc cutter:

$$F_V = 4\alpha_c p\tan\alpha\sqrt{2rp^3 - p^4} \qquad (4)$$

$$F_R = 4\sigma_c p^2\tan\alpha \qquad (5)$$

$$F_S = \frac{F_V}{2}\cot\alpha \qquad (6)$$

CSM prediction equations: Based on the shear rock-breaking theory and the tension rock-breaking theory, Ozdemir et al. [8] from Colorado School of Mines (CSM) conducted indentation experiments on different types of rocks by disc cutter. They regarded the contact surface between the disc cutter and the rock as a triangle, and derived the calculation equations of the vertical force and the tangential force of the V-shaped disc cutter:

$$F_V = \sqrt{2r}p^{1.5}\left[\frac{4}{3}\sigma_c + 2\tau\left(\frac{S}{p} - 2\tan\alpha\right)\right]\tan\alpha \qquad (7)$$
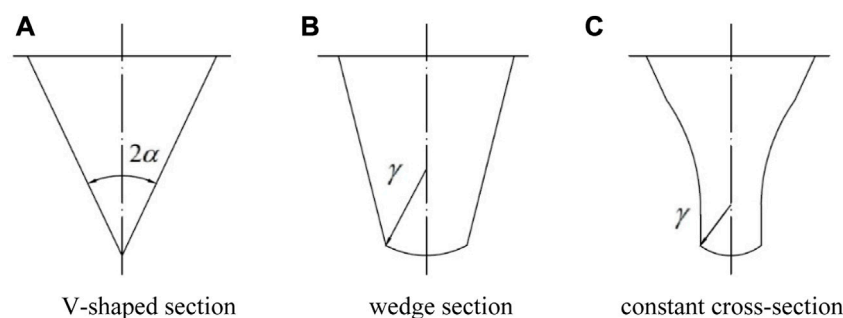
FIGURE 4
The cross-sectional forms of the disc cutter ring **(A)** V-shaped section **(B)** wedge section **(C)** constant cross-section.

$$F_R = \left[\sigma_c + p^2 + \frac{4\tau\phi(S - 2p\tan\alpha)}{r(\phi - \sin\phi \cdot \cos\phi)}\right]\tan\alpha \quad (8)$$

Where: ϕ = Contact angle between cutter and rock $(\arccos(r - p/r))$

τ = Shear strength of rock

Rostami prediction equations: Rostami and Ozdemir (1993) from Colorado School of Mines (CSM) developed the CSM model for the constant cross-section disc cutter, and deduced the calculation equation of the resultant force of the disc cutter in the rock-breaking process:

$$F = \frac{P\phi TR}{1 + \psi} \quad (9)$$

Where: P = Compressive stress in the breaking zone

ψ = Pressure distribution coefficient of the cutter edge

$$P = K\left(\frac{S\sigma_c^2\sigma_t}{\phi\sqrt{rT}}\right)^{(1/3)} \quad (10)$$

Where: K = A constant, approximately equal to 2.12

T = Edge width of the disc cutter

The calculation equations of the vertical force and the tangential force can be obtained by decomposing Eq.10:

$$F_V = K\frac{r\phi T}{1 + \psi}\left(\frac{S\sigma_c^2\sigma_t}{\phi\sqrt{rT}}\right)^{(1/3)}\cos\frac{\phi}{2} \quad (11)$$

$$F_R = K\frac{r\phi T}{1 + \psi}\left(\frac{S\sigma_c^2\sigma_t}{\phi\sqrt{rT}}\right)^{(1/3)}\sin\frac{\phi}{2} \quad (12)$$

(6) Prediction equations of the Northeast University of Technology: Based on the Evans prediction equation, Jin et al. [9] from the Northeast University of Technology proposed a powder nucleus-splitting model for calculating the rock-breaking force of disc cutters. They regarded that the vertical force of disc cutter rock-breaking is not constant, and there is a leap phenomenon:

$$F_v = \frac{4}{3}k_d\sigma_c + 2p\tan\alpha\sqrt{4rp - p^2} \quad (13)$$

$$F_R = \varepsilon k_d\sigma_c p^2\tan\alpha \quad (14)$$

Where: k_d = Rolling coefficient, normally 0.4–0.7

ε = Reduction coefficient, 2.0–2.5 for smooth rocks, 0.8 for rough rocks.

3.3 Evaluation of disc cutter force prediction theories

Since the above force prediction theories of disc cutter (summarized in Section 3.2) were based on different experimental and theoretical methods, a comparative evaluation of their predicted values is required. Cao et al. (2018), Wu et al. (2010), and Liu, (2015) analyzed the predicted force values of the constant cross-section disc cutter based on the actual TBM tunneling parameters. The relative errors between the calculated and the measured values are listed in Table 1.

As shown in Table 1, the relative errors of rock-breaking force calculated by the Rostami prediction equations are between 0.8%

and 13.7%, which are the minimal among all summarized equations. Therefore, in this study, we choose the Rostami prediction equations to calculate the force of the constant cross-section disc cutters.

4 Derivation of the rock-breaking specific energy per ring equation

In the process of TBM tunneling, breaking the largest volume of rock with the minimal energy consumption, i.e., improving the rock-breaking efficiency of TBM is an important goal of designing cutter head and cutting tool. In 1936, Teale, (1965) proposed the concept of rock-breaking specific energy (*SE*), which is defined as the energy consumed by disc cutters to break rock per unit volume and can be used to evaluate the rock-breaking efficiency of cutters. The smaller the rock-breaking specific energy of the disc cutter is, the higher the rock-breaking efficiency is. The equation of *SE* is:

$$SE = \frac{E}{V} = \frac{E_V + E_R}{V} = \frac{\sum F_V \cdot p + \sum F_R l}{V} \quad (15)$$

Where: E = Total energies of rock-breaking

V = Total volume of rock-breaking

E_V = Vertical rock-breaking energy

E_R = Tangential rock-breaking energy

p = Vertical cutting stroke of the disc cutter

l = Tangential cutting stroke of the disc cutter

How to calculate reasonably the volume of rock-breaking is a major difficulty in the application of the above rock-breaking specific energy equation. The main reason is that the rock slag generated in the rock-breaking process is irregular. It is worth noting that as the rock slag is generated during rock-breaking, there will be initiation of lateral cracks and vertical cracks in the rock which will also consume the rock-breaking energy. Therefore, considering only the volume of rock slag is not enough to reflect the effect of the rock-breaking energy on the rock. The cracks developed in the rock mass during rock-breaking are shown in Figure 5.

According to the actual TBM operation condition, the stiffness of the cutter is very large and its deformation is negligible. The normal displacement of each disc cutter after one rotation is equal, so there is no influence of the arc-shaped arrangement of the gauge cutters on the rock-breaking volume per ring of the TBM. In addition, since the abrasion loss of the gauge cutters is very small for one ring excavation distance, the excavation diameter of the TBM remains constant and the rock-breaking volume per ring can be assumed unchanged.

If the TBM tunneling parameters and the physical and mechanical properties of the rock remain constant, the crack distribution per ring of the tunnel face can be regarded as unchanged. Therefore, the energy consumed by the cracks is the same for each tunnelling ring. In this case, the rock-breaking volume per ring and the rock-breaking energy consumption per ring can be used to calculate the rock-breaking specific energy of TBM. Under these assumptions, the specific energy per ring can be derived which quantifies the specific energy required for one ring excavation distance. In addition, the specific energy per ring can be regarded as a critical indicator that reflects the overall energy consumption and the associated costs of the excavation process.

TABLE 1 The relative error of the disc cutter force prediction equations.

Literature	Literature 17		Literature 18	Literature 19
Force prediction equations	Vertical force error	Tangential force error	Vertical force error	Vertical force error
Evans	93.40%	/	74.50%	85%
Roxborough	80.30%	72.00%	23.60%	50%
CSM	72.00%	71.50%	15.90%	85%
Rostami	0.80%	7.10%	/	3%–13.70%
The Northeast University of Technology	85.40%	71.70%	84.70%	/

FIGURE 5
Schematic diagram of cracks developed in the rock mass during the rock-breaking process of disc cutter.

FIGURE 6
Geological profile of the Shanwu tunnel section of the Qingdao Metro.
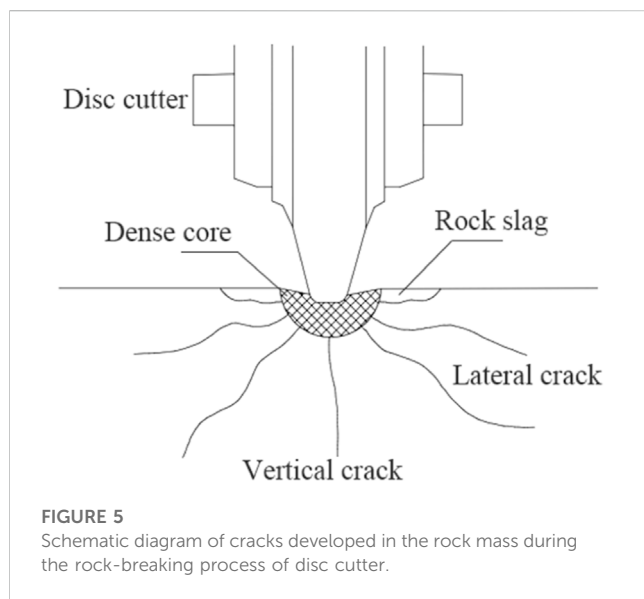
According to the rock-breaking specific energy equation of the disc cutter (Eq. 15), as long as the vertical force and tangential force of the disc cutter are known, the vertical energy consumption and tangential energy consumption of TBM rock-breaking can be obtained. Suppose the effective rock-breaking thrust is F, the total torque is M, the penetration is p, the length of each tunnel ring is L, and the rotation number of disc cutter per tunneling ring is L/h. The vertical energy consumption E_V and the tangential energy consumption E_V of the disc cutter per ring can be obtained:

$$E_V = \sum_{i=1}^{n} F_{Vi} L = FL \qquad (16)$$

$$E_R = \frac{L}{p} \sum_{i=1}^{n} 2\pi R_i F_{Ti} = 2\pi \frac{L}{p} \sum_{i=1}^{n} R_i F_{Ti} = \frac{2\pi LM}{p} \qquad (17)$$

It has been evaluated in Section 2.3 that the Rostami prediction equations have the minimal relative error to calculate the rock-breaking force of constant cross-section disc cutters. Therefore, combining the Rostami prediction equations with the rock-breaking specific energy equation, the rock-breaking specific energy per ring equation can be derived. Substituting the calculation results of the vertical force and tangential force of each disc cutter (F_{Vi}, F_{Ti}) from the Rostami prediction equations
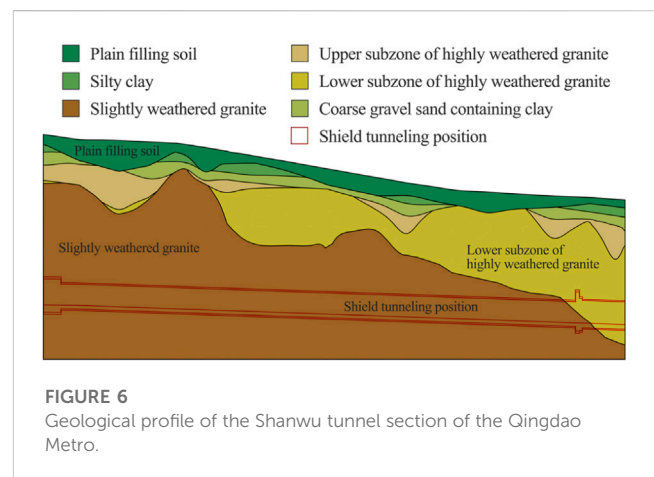
into Eq. 16 and Eq. 17, the prediction equation of the specific energy per ring can be obtained:

$$V = L\pi R_{max}^2 \qquad (18)$$

$$SE_{ring} = \frac{E_V + E_R}{V} = \frac{FL + 2\pi LMp^{-1}}{V} = \frac{F + 2\pi Mp^{-1}}{\pi R_{max}^2} \qquad (19)$$

According to the structure of Eq. 18 and Eq. 19, it can be seen that the rock-breaking specific energy prediction per ring equation can also be used to calculate the actual rock-breaking specific energy of TBM.

5 Validation of rock-breaking specific energy per ring equation

The Shanwu tunnel section of the Qingdao Metro is located in the Shinan District of Qingdao. The tunnel passes under Shandong Road which is a main road of Qingdao. Since there are many high-rise buildings and ultra-high buildings around the tunnel, the environmental risk of the tunnel is high. The tunnel body mainly passes through the slightly weathered granite stratum. The buried depth of the tunnel is 25–35 m, the inner diameter of the tunnel is 6 m, the outer diameter of the segment is 6.7 m, and the excavation diameter of TBM is 6.98 m. The length of each tunnel ring is 1.5 m. The groundwater type is mainly quaternary pore phreatic water and bedrock fissure water. The geological profile of the Shanwu tunnel section is shown in Figure 6.
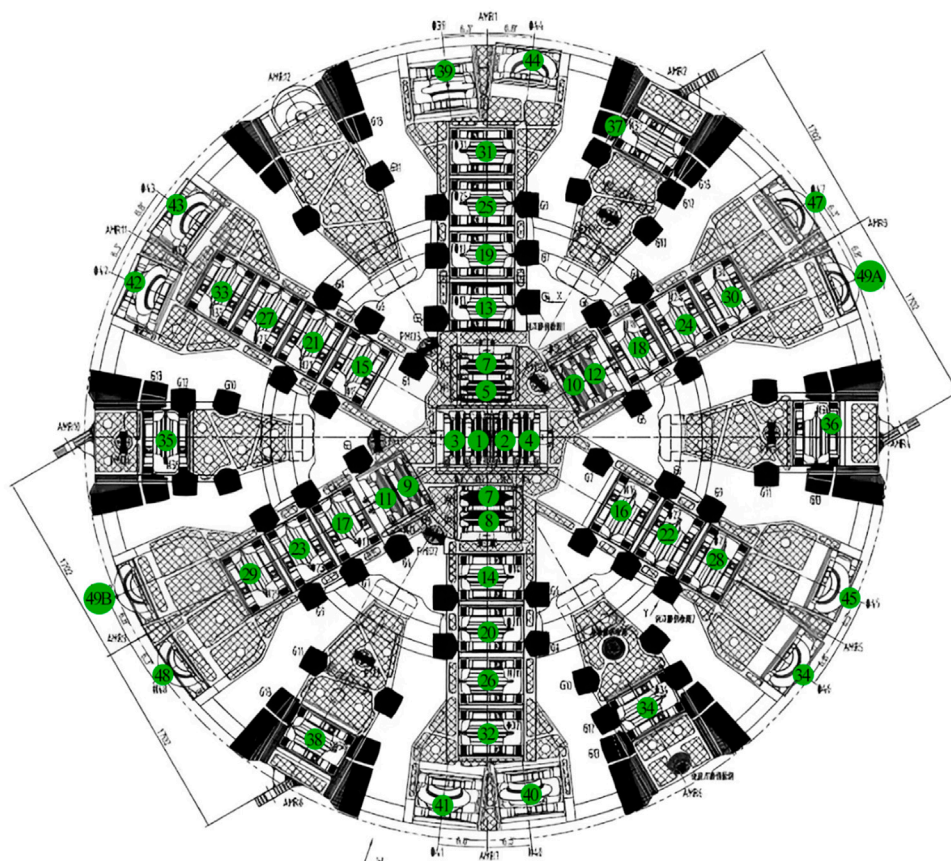
FIGURE 7
Schematic diagram of disc cutters arrangement.

FIGURE 8
Tunnel surface of the 205th ring in the Shanwu tunnel section.

Two dual-mode TBMs were used for tunnel excavation in this section. The dual-mode TMB was produced by the China Railway Engineering Equipment Group Co., Ltd. (CREG), which can be converted between shield mode and single shield TBM mode. The TBM utilizes a composite cutterhead and eighteen-inch disc cutters. The disc cutters mainly include six central cutters, twenty-six face cutters, twelve gauge cutters, and two edge cutters. And the central cutters adopt the double-blade cutter. The schematic diagram of disc cutters arrangement is shown in Figure 7.

The cutters of the TBM utilized in this study are all constant cross-section disc cutters. The cutter diameter is 457.22 mm, the edge width is 22 mm, the edge angle is 9.5°, the nose angle is 140°, and the rated load is 250 kN.

5.1 Acquisition of actual TBM tunneling parameters

In the Shanwu tunnel section, the right line tunnel face of the 205th ring is complete, and the joints are less exposed. The photograph of the tunnel face is shown in Figure 8.

TABLE 2 Rock mechanical parameters at the M8Z2-TAW-41 exploration hole.

Compressive strength (MPa)	Tensile strength (MPa)	Elastic modulus (GPa)	Poisson's ratio	Internal friction angle	Cohesion (MPa)
62.53	7.17	27.32	0.22	53.23°	8.24

FIGURE 9
The variations of the tunneling parameters from the 201st ring to the 207th ring. **(A)** gross thrust **(B)** penetration **(C)** cutter head torque.
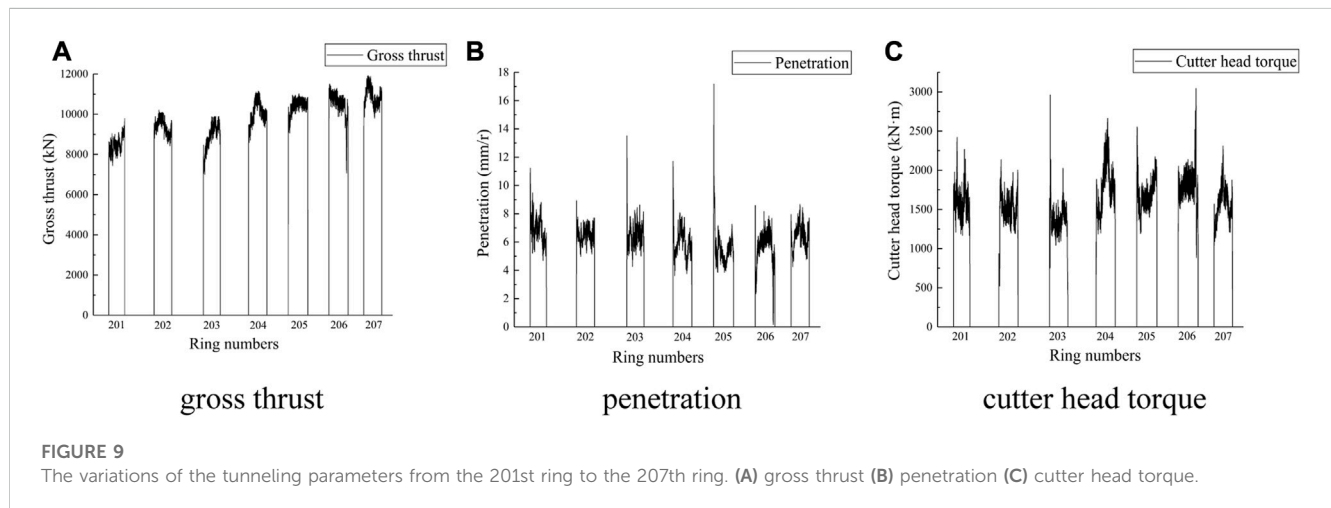
TABLE 3 Comparation between actual and predicted results.

Calculation items	Actual results	Predicted results	Relative error (%)
Effective thrust	7004.7 kN	7574.5 kN	8.6
Cutter head torque	1598 kN m	1726.0 kN m	9.8
Specific energy per ring	40.55 MJ/m3	43.80 MJ/m3	8.0

The M8Z2-TAW-41 exploration hole is located on the right side of the 205th ring. The rock mechanical parameters at the M8Z2-TAW-41 exploration hole were obtained by consulting the geological survey report of the rock mass (as shown in Table 2).

To verify the prediction equations of the cutter force and the specific energy per ring, the gross thrust, penetration, and cutter head torque of TBM from the 201st ring to the 207th ring were collected from the shield construction management information system of the Qingdao Metro. The variations of these three tunneling parameters are shown in Figure 9. It is obtained that the average gross thrust is 9564.7 kN, the average penetration is 6.5 mm/r, and the average cutter head torque is 1598 kNm from the 201st ring to the 207th ring.

The gross thrust of TBM is mainly composed of the effective rock-breaking thrust (F_1), the shield sliding friction (F_2), the traction resistance of rear supporting facilities (F_3), the component of TBM gravity caused by the tunnel slope (F_4), and the friction between the shield tail and the segment (F_5) (Guan et al., 2013).

$$F_{sum} = F_1 + F_2 + F_3 + F_4 + F_5 \qquad (20)$$

The gross thrust during the TBM exit process is not affected by the effective rock-breaking thrust, the slopes of the tunnel are

identical, and the gravitational component F_4 can be regarded as a constant. By querying the gross thrust data during the TBM exit process, it is obtained that $F_2 + F_3 + F_4 + F_5 = 2560$ kN, so the effective rock-breaking thrust (F_1) is calculated to be 7004.7 kN. Substituting the effective rock-breaking thrust and the average cutter head torque into the specific energy per ring equation, the actual specific energy per ring is obtained to be 40.55 MJ/m³.

5.2 Prediction of TBM tunneling parameters

The obtained TBM tunneling data were substituted into the Rostami prediction equations and the specific energy per ring equation. The installation angle of the gauge cutters was ignored in the calculation. To ensure the excavation diameter of the tunnel, two edge cutters with the same radius are set on the outermost side of the cutter head. In the calculation, the penetration value of the edge cutter is set to be half of the average penetration.

Obtained by the Rostami prediction equations, the effective thrust is 7574.5 kN and the cutter head torque is 1726.0 kNm. Substituting the calculated data into the specific energy per ring equation, the specific energy per ring is obtained to be 43.80 MJ/m³.

5.3 Comparation between actual and predicted results

The comparison between actual and predicted results based on the Rostami prediction equations is presented in Table 3. The table shows that the maximum relative error of the effective thrust and the cutter head torque is 9.8%. The relative error of the specific energy per ring is 8.0%. The predicted errors are all less than 10%, so the predicted results can provide a certain reference value for practical engineering projects.

6 Conclusion

1) In this study, the existing classical force prediction equations for disc cutters and their applicability to constant cross-section disc cutters were analyzed. The Rostami prediction equations were found to be the most suitable force prediction theory due to its minimal relative errors among all summarized equations. Furthermore, based on the Rostami prediction equations and the theory of rock-breaking specific energy, a specific energy per ring equation for TBM was proposed to calculate TBM's actual and predicted rock-breaking specific energy. This equation simplifies the calculation of rock-breaking volume, as it eliminates the need to consider rock slag volume and the effect of surrounding cracks on rock-breaking energy.

2) The applicability of the specific energy per ring equation was verified based on the actual TBM tunneling parameters in the Shanwu tunnel section of the Qingdao Metro. The verification results show that the maximum relative error of the effective thrust and the cutter head torque calculated by the Rostami prediction equations is 9.8%, and the relative error of the specific energy per ring equation is 8.0%. The predicted errors are all less than 10%, so the proposed specific energy per ring equation can provide a certain reference value for practical engineering projects.

Data availability statement

The raw data supporting the conclusions of this article will be made available by the authors, without undue reservation.

Conflict of interest

The authors declare that the research was conducted in the absence of any commercial or financial relationships that could be construed as a potential conflict of interest.

Publisher's note

All claims expressed in this article are solely those of the authors and do not necessarily represent those of their affiliated organizations, or those of the publisher, the editors and the reviewers. Any product that may be evaluated in this article, or claim that may be made by its manufacturer, is not guaranteed or endorsed by the publisher.

References

Akiyama, Tosaburo (1970). A theory of the rock-breaking function of the disc cutter. *Komatsu Technol.* 16 (3), 56–61. (In Japanese).

Cao, Jianfeng, Zhang, Na, and Liang, Guohui, (2018). Analysis of thrust and torque prediction method for TBM cutter head. *Constr. Mech.* 39 (05), 51–54. (In Chinese). doi:10.13311/j.cnki.conmec.2018.05.015

Evans, I., and Pomeroy, C. D. (1966). *Wedge penetration into coal.* Amsterdam, Netherlands: Science Direct. doi:10.1016/B978-1-4831-9633-6.50014-1

Guan, Huisheng, Yang, Yandong, and Guo, Lichang, (2013). Calculation on thrust force of dual-mode shield machine used in colliery inclined shaft. *Min. Process. Equip.* 41 (07), 123–127. (In Chinese). doi:10.16816/j.cnki.ksjx.2013.07.032

Hu, Mengmeng, Zhang, Bo, Li, Biao, Liu, B., Cao, W., and Xu, B. (2022). TBM-cutter rock-breaking effect and mechanism considering different cutting sequences. *Bull. Eng. Geol. Environ.* 81 (3), 102–121. doi:10.1007/s10064-022-02576-4

Jin, Guodong (1981). Analysis of rock breaking mechanism of disc cutter of full face rock tunnel boring machine (II). *Power Gener. Technol.* 102 (04), 21–27. CNKI: SUN: SLJX.0.1981-04-003 (In Chinese).

Jin, Guodong, Huang, Shifang, and Yu, Heji, (1981). Analysis of rock breaking mechanism of disc cutter of full face rock tunnel boring machine (I). *Power Gener. Technol.* 102 (03), 1–9. CNKI: SUN: SLJX.0.1981-03-000 (In Chinese).

Li, Xiaojing, Zhang, Huaken, Bai, Yifan, and Zhang, X. y. (2022). Factor analysis and numerical simulation of rock breaking efficiency of TBM deep rock mass based on orthogonal design. *J. Central South Univ.* 29 (4), 1345–1362. doi:10.1007/s11771-022-4994-9

Liu, Haijian (2015). *Numerical simulation study of rock fragmentation mechanism and effect by TBM disc cutter.* Beijing, China: China University of Geosciences. (In Chinese). doi:10.27493/d.cnki.gzdzy.2015.000006

Lu, Yang, Ma, Jiming, Xu, Qianjun, and Han, M. N. (2004). TBM in the future of China. *Mar. Georesources Geotechnol.* 22 (3), 185–193. doi:10.1080/10641190490467116

Mao, Chengjue, and Liu, Chunlin (1988). Indentation test analysis of disc rolling cutter in drifter. *Constr. Mach. Equip.* 04, 9–14+56. CNKI: SUN: GCJA.0.1988-04-002 (In Chinese).

Ozdemir, L., and Wang, F. D. (1979). Mechanical tunnel boring prediction and machine design. *Nasa Sti/Recon Tech. Rep. N.* 80, 16239. doi:10.1016/0148-9062(78)91060-4

Rostami, J., and Ozdemir, L. (1993). "New model for performance production of hard rock TBMs," in Proceedings of the Rapid Excavation and Tunneling Conference, Boston, MA, USA, January 1993, 793–809. doi:10.4236/jbbs.2013.32020

Roxborough, F. F., and Phillips, H. R. (1975). Rock excavation by disc cutter. *Int. J. Rock Mech. Min. Sci. Geomechanics Abstr.* 12 (12), 361–366. doi:10.1016/0148-9062(75)90547-1

Sun, Zhenchuan, Zhao, Hailei, Hong, Kairong, Chen, K., and Zhou, J., (2019). A practical TBM cutter wear prediction model for disc cutter life and rock wear ability. *Tunn. Undergr. space Technol.* 85, 92–99. doi:10.1016/j.tust.2018.12.010

Teale, R. (1965). The concept of specific energy in rock drilling. *Int. J. Rock Mech. Min. Sci. Geomechanics Abstr.* 2 (2), 57–73. doi:10.1016/0148-9062(65)90022-7

Wu, Qixing, Huang, Weiran, and Ma, Hongwei (2010). Research on methods of calculating normal rock breaking force by means of disc cutter of composite TBM. *Min. Process. Equip.* 38 (24), 58–63. (In Chinese). doi:10.16816/j.cnki.ksjx.2010.24.016

Yagiz, Saffet (2008). Utilizing rock mass properties for predicting TBM performance in hard rock condition. *Tunn. Undergr. Space Technol.* 23 (3), 326–339. doi:10.1016/j.tust.2007.04.011

Zhang, Qinglong, Zhu, Yanwen, Du, Canxun, Du, S., Shao, K., and Jin, Z. (2022). Dynamic rock-breaking process of TBM disc cutters and response mechanism of rock mass based on discrete element. *Adv. Civ. Eng.* 2022, 1–10. doi:10.1155/2022/1917836

Zhang, Xu, Wang, Juan, and Meng, Qingguo, (2021). Coal rock breaking simulation and cutting performance analysis of disc cutters. *Teh. Vjesn.* 28 (5), 1755–1761. doi:10.17559/TV-20210423115559

Zhang, Zhaohuang, Mao, Chengjue, and Liu, Chunlin (1996). Statistical analysis of disc cutter pressing mark results about full face rock tunnel boring machine. *Mod. Electr. Power* 23 (01), 63–68. (In Chinese). doi:10.19725/j.cnki.1007-2322.1996.01.011

Zhang, Zhaohuang (2008). *The research on theory and techniques of service life management of TBM disc cutters*. Beijing, China: North China Electric Power University. CNKI: CDMD: 1.2009.090407 (In Chinese).

Check for updates

Experimental studies of instability process and energy evolution of tunnels under true triaxial stresses: The role of pre-existed flaws

Binglei Li[1], Jianing Li[1], Hongyuan Hu[1], Jinrui Gong[1] and Tao Luo[2]*

[1]Zijin School of Geology and Mining, Fuzhou University, Fuzhou, China, [2]School of Resource Engineering, Longyan University, Longyan, China

In the natural geological environment, there are many joints, faults and cavities. These natural defects will have an impact on the stability of tunnels. This paper investigates different conditions of surrounding rock: intact surrounding rock, surrounding rock with open-flaw and surrounding rock with filled-flaw under the true triaxial test. The effect of different surrounding rock conditions on the internal failure characteristics of tunnel under true triaxial conditions is explored. According to the characteristics of energy evolution and chaos theory, the failure characteristics inside the tunnel is divided into stages. The results show that: 1) The failure characteristics in the tunnel are different for different surrounding rock conditions. The failure characteristics do not represent the stability of the surrounding rock of the tunnel; 2) The trend of energy dissipation is different under different surrounding rock conditions. The elastic stage of the surrounding rock is shortened and the dissipation energy shows an earlier upward trend as its integrity declines. 3) When analysing the tunnel, chaos theory can give early warnings about the instability of the surrounding rock, but it can not give early warning of particle spray and spalling inside the tunnel.

KEYWORDS

surrounding rock condition, energy evolution, tunnel, chaos theory, flaw

1 Introduction

At present, the geological environment around the tunnel excavation is becoming more and more complex, and there are many natural defects such as faults and cavities around the tunnel. These defects can have unpredictable consequences for the failure of surrounding rock.

Many scholars have explored the influence of these natural defects on surrounding rock, by carrying out laboratory tests (Wang H. et al., 2020; Li et al., 2021; Li et al., 2022; Yang et al., 2022; Zhang et al., 2022; Xue et al., 2023b). Prefabricated flaws usually include open flaws, filled flaws and a combination of prefabricated flaws and holes. For open cracks, (Zhang et al., 2020), studied the influence of prefabricated flaws on rock fracture toughness and provided a reference for the accurate measurement of limestone fracture toughness through experiment and numerical analysis. (Chen et al., 2022).studied the influence of prefabricated flaw size on mode I crack propagation of rock, and clarified the influence of prefabricated flaws on the directional crack propagation mechanism. (Liu X. X. et al., 2021). carried out

shear tests on rock samples with prefabricated flaws, taking into account the influence of the existence of cracks on crack propagation when rock shear failure occurs.

Natural rock joints are usually filled with materials such as sand, clay and broken rock fragments as weak bonds. For filled-flaw, (Zhang and Zhu, 2020), studied the influence of such filled flaws on the mechanical strength and failure characteristics of the rock mass and calibrated the parameters of various types of samples based on the uniaxial compression test (Zhou et al., 2021). monitored the degree of damage to rock by acoustic emission through defects with different filling materials. In addition, the qualitative analysis of crack behaviour was carried out by acoustic emission (AE) and photographic capturing technologies, which provide a theoretical memory for fracture behaviour and damage assessment of cracks (Sharafisafa et al., 2019). studied the influence of filling materials on the deformation and failure behaviour of 3D-printed rock-like Brazilian disk specimens with defects by static compression load and digital image correlation (DIC) technology. They found that the filling of the material can significantly increase the peak stress of the sample.

Natural geological conditions are usually not single fractures but are a combination of many fractures. Scholars have studied different fracture combinations. For combined fracture, (Wang et al., 2020d), studied the energy evolution and failure characteristics of combined cracks under fatigue load. The influence of stress amplitude on rock fatigue is investigated by 3D CT (Li and Cai, 2021). studied a specimen with open holes in the cross joint and explored the energy evolution process of the joint in the process of crack initiation (Mehranpour et al., 2018). extended the existing rock mass strength criteria. The 284 numerical simulation results of multi-axial, triaxial and biaxial compression tests of jointed rock blocks with one or two joint groups by PFC3D software were analysed, and two new three-dimensional rock mass strength criteria were established.

Scholars usually use AE (Worley et al., 2019; Zafar et al., 2020), DIC (Fakhimi et al., 2018; Afrazi et al., 2022; Xue et al., 2023a) and energy evolution (Chen et al., 2019; Wang et al., 2020c; Wang et al., 2022) to facilitate the study of crack propagation. The energy evolution analysis of rock is based on the assumption that there is no heat exchange in this process after the external work is done on the rock, and the deformation of the rock is converted into elastic energy and dissipated energy (Xie et al., 2005). The energy evolution analysis enables scholars to better understand the propagation of internal cracks in the compression stage of rock (Meng et al., 2019). studied the energy evolution law of lithology and loading rate on the whole process from deformation to failure. They then analysed the micro-mechanism of accumulation and dissipation of rock energy, and proposed a non-linear evolution model (Logistic equation) to provide theoretical support for an early warning system for engineering disasters (Wang C. L. et al., 2020). analysed the energy dissipation, energy conversion mode and stress-energy mechanism of rock failure induced by cyclic loading and unloading, and demonstrated the laws of stress release and energy dissipation during rock failure from the energy perspective (Liu G. L. et al., 2021). summarised the damage evolution model of rock, revealed the failure and instability mechanism of rock under load, analysed the relationship between crack development, damage evolution and energy evolution, and proposed a more specific understanding of the rock failure process.

At present, researchers paid more attention to the crack extension in rocks under different stress circumstances, and less attention is paid to the overall stability of the tunnel induced by the crack extension. There were few studies establishing the correlation of energy evolution with the failure at tunnel wall. In this paper, using a true triaxial experimental machine to simulate the underground stress environment, and use an embedded micro camera to capture the failure inside the tunnel, which can better obtain the crack propagation. Then the failure behavior inside the tunnel and energy evolution characteristic are correlated. Combining chaos theory with the energy evolution process clarifies the advantages and disadvantages of applying chaos theory to evaluate tunnel stability, and it provides further theoretical support for understanding the internal failure of tunnels from the perspective of energy evolution.

The innovation of this article is highlighted as follows: 1) Under true triaxial conditions, failure characteristics at the tunnel wall and energy evolution are correlated, and 2) Combined chaos theory with the energy evolution process, and use it to evaluate the damage degree inside the tunnel.

2 True triaxial tests on sandstone samples with tunnel

2.1 Specimens preparation

True triaxial tests of rock specimens with the tunnel were done by cutting out cubic specimens from the centre with a high-pressure water jet. The dimensions of the specimens were 100 mm × 100 mm × 100 mm, which was suggested by the ISRM (Muralha et al., 2014). The dimensions of the horseshoe-shaped tunnel and the surrounding rock conditions of the specimens are shown Figure 1. The uniaxial compressive strength (UCS) of sandstone is 73.52 MPa, elastic modulus is 5.6 GPa and Poisson's ratio is 0.12. The prefabricated flaw was made to penetrate the entire cubic specimen along the x-axial direction (Figure 1A). And the flaws were filled with gypsum, with a water to gypsum ratio of 1:5 and The UCS was 7.5 MPa. In terms of surrounding rock integrity, Group Intact displayed more integrity than Group Filled-flaw.

2.2 Stress path

The QKX-ZSZ-4000 rigid servo loading system was used in this research. In this system, the maximum vertical load can reach 4,000 kN and the maximum lateral load can reach 2,400 kN. The stress path in this test is shown in Figure 2. The stress path has two stages: an initial stage and a step stage. The initial stress for this test is the burial depth of 500 m and step loading is used to simulate the tunnel excavation process. Before arriving the initial pressure, the σ_x, σ_y, and σ_z loading rate was 0.5 kN/s. When the stress in all three directions reached 11.5 MPa, the directions of X and Y continued to be loaded at a rate of 0.5 kN/s, while σ_Z remained unchanged. When σ_X and σ_Y reached 17 MPa, the direction of X continued to be loaded at a rate of 0.5 kN/s, while σ_Y and σ_Z remained unchanged. When σ_X reached 29 MPa, σ_X was maintained for 30 s when the stress reached the initial pressure (σ_x=29 MPa; σ_y=17 MPa; σ_z=11.5 MPa), the loading method
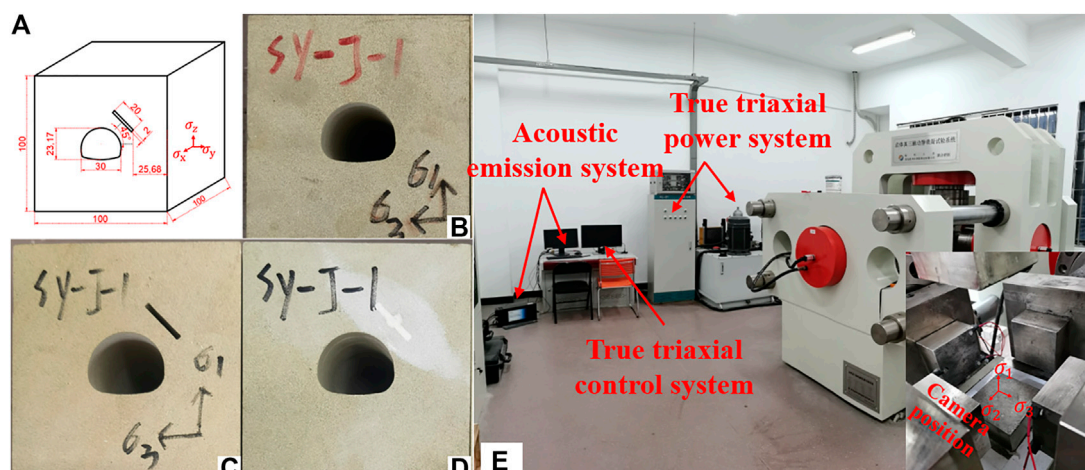
FIGURE 1
Test specimens: **(A)** distribution of tunnel and flaws; **(B)** intact specimens; **(C)** open-flaw specimens; **(D)** filled-flaw specimens; **(E)** QKX-ZSZ-4000 test equipment.
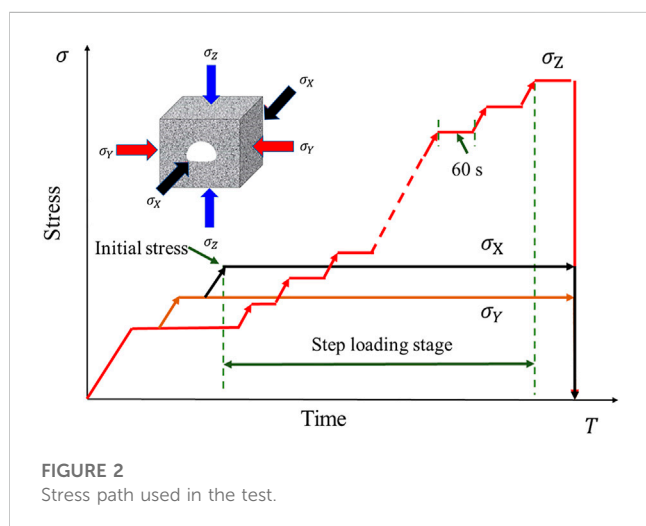
FIGURE 2
Stress path used in the test.

changed to 0.1 mm/min. In the step-loading stage, the σ_Z was maintained 60 s for every 10 MPa increase. For example, when σ_Z was 11.5 MPa at the beginning, it was loaded to 21.5 MPa at a loading rate of 0.1 mm/min, and maintained the resulting stress for 60 s. When σ_Z decreased to 90% of the peak stress, the experiment was terminated.

To ensure that the sample was not damaged during the unloading, it was done in stages unloading was employed. First, σ_x and σ_y stresses remained unchanged, while σ_z was decreased to 29 MPa. Then σ_y remained unchanged while reducing σ_x and σ_z stress to 17 MPa. Finally, the three stress were unloaded to 0 at the same time.

2.3 Test results

The triaxial test results of the three specimens are shown in Figure 3. The peak stress of specimens with intact surrounding rock

was 89.63 MPa, with open-flaw it was 81.05 MPa and with filled-flaw it was 85.59 MPa. Peak stress decreased continuously due to defects in the surrounding rocks.

Figure 4 shows the failed tunnel under true triaxial loading. Symmetrical V-shaped grooves appear on both sides of the intact specimens. In open-flaw specimens, the open-flaw appears at the upper right of the tunnel, and the V-shaped grooves on the right become a particle spray line. In the filled-flaw specimens, the V-shaped grooves on the right are bigger than on the left. This phenomenon means that the surrounding rock conditions affects the stability of tunnel.

3 Bifurcation and chaotic characteristics of rock energy evolution

3.1 Chaos theory and logistic system

Chaos theory implies that systems evolve from an ordered state to a disordered state and outlines the mechanism of the formation of random processes in a deterministic system. Logistic systems are simple chaotic systems (Zhang and Gao, 2012; Zhang, 2021). The Logistic equation is as follows:

$$\frac{dx}{dt} = f(x, \mu) = \mu x(1 - x) \tag{1}$$

The different form is obtained by continuous time discretisation.

$$x_{n+1} = f(x_n, \mu) = \mu x_n(1 - x_n), \ n = 1, 2, 3 \ldots \tag{2}$$

Where x_n is the state of x at time t_n, x_{n+1} is the state of x at time t_{n+1}; μ is a dimensionless parameter.

Figure 5 is a diagram of the Logistic equation. It shows that this equation divides the process into stability area, Bifurcation and chaos through μ. Table 1 shows the relationship between the state of x and the eigenvalue of μ (Zhang et al., 2000; Zhuang et al., 2017).
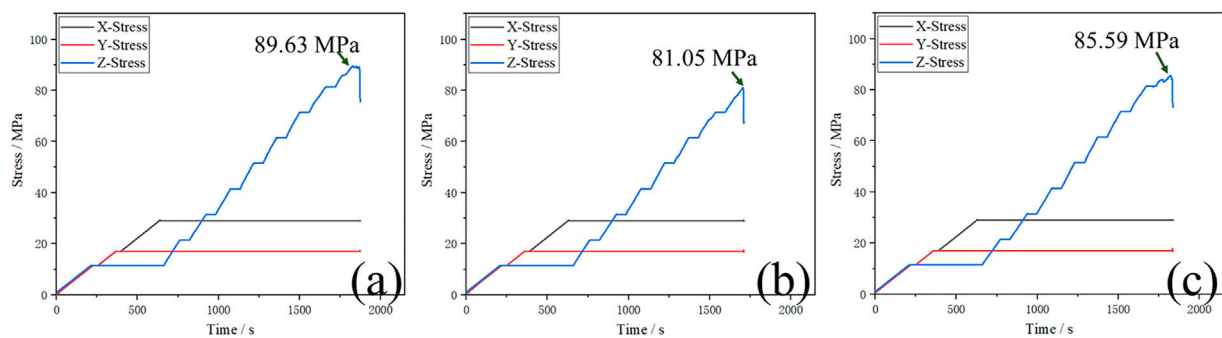
FIGURE 3
Test results: **(A)** intact specimens; **(B)** open-flaw specimens; **(C)** filled-flaw specimens.
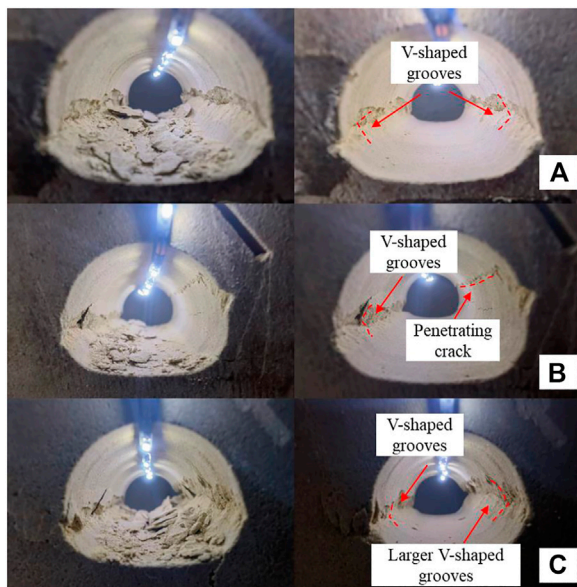
FIGURE 4
Internal images of the tunnel before and after debris cleaning: **(A)** intact specimens; **(B)** open-flaw specimens; **(C)** filled-flaw specimens.
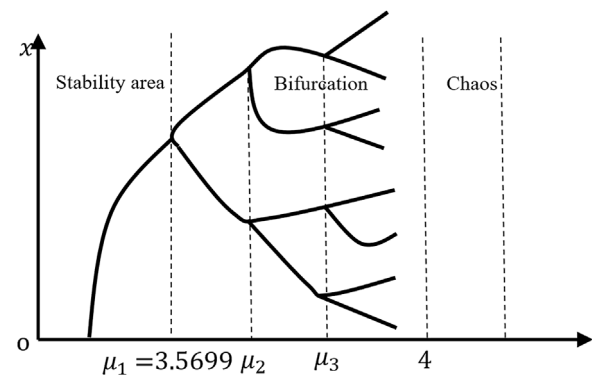
FIGURE 5
Solution graph of Logistic equation.

TABLE 1 Critical value of each area.

	μ
Stability	$\mu < 3.0000$
Bifurcation	$3.0000 \le \mu < 3.5699$
Chaos	$3.5699 \le \mu < 4.0000$

3.2 Chaos theory and stress

This research explores the relationship between maximum principal stress and energy density. We can write Eq. 1 in the following formula (Zhang, 2021):

$$U_{i+1}^e = \mu U_i^e \left(1 - \frac{U_i^e}{k}\right) \qquad (3)$$

Where U_i^e is the elastic energy corresponding to time t_i; U_{i+1}^e is the elastic energy corresponding to time t_{i+1}; μ is the iterative growth factor of energy, and k is the maximum value of energy accumulation in the rock. Based on this equation, the relationship between the increase of maximum principal stress and the internal energy accumulation of the rock was studied,

and the effect of different surrounding rock conditions was considered.

Figure 6 shows the relationship between the iterative growth factor μ and maximum principal stress. Under the three surrounding rock conditions, the value of μ increased exponentially with the increase of the maximum principal stress. This process can be divided into three stages: 1) Before μ approaches 3.0000, the surrounding rock is in the stability stage, and surrounding rock is continuously compressed. 2) When μ approached 3.0000 (Point A), the surrounding rock became unstable and the μ increased rapidly. 3) When μ reached 3.5699 (Point B), the bifurcation process ended, and the surrounding rock entered the chaos stage. When μ is at 3.0000 is usually considered to be the crack initiation stress. Beyond this point, the surrounding rock begins to fail.
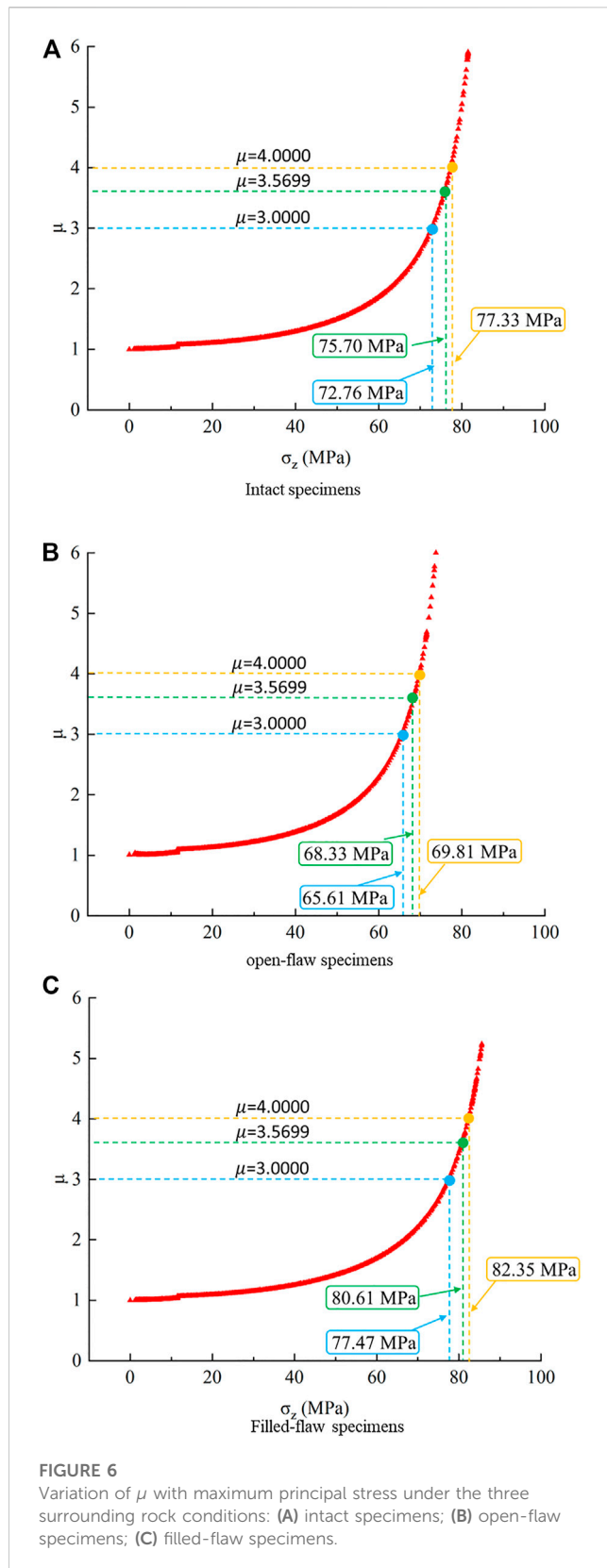
FIGURE 6
Variation of μ with maximum principal stress under the three surrounding rock conditions: **(A)** intact specimens; **(B)** open-flaw specimens; **(C)** filled-flaw specimens.

initiation stress of the surrounding rock. The crack initiation stress of intact specimens, open-flaw specimens and filled-flaw specimens are 72.76, 65.61, and 77.47 MPa respectively.

4 Energy evolution characteristics in the rock deformation process

4.1 Energy calculation principle

In the process of rock compression, the deformation of rock usually includes elastic deformation and plastic deformation. The process of energy transformation can also be divided into elastic strain energy and dissipated energy. Elastic strain energy is stored in the rock mass and energy is dissipated by damage to the rock mass. In the true triaxial test, the specimen is deformed due to compression. Assuming that there is no heat exchange in the process (Xie et al., 2009), the energy input by external work is the total energy U_0.

$$U_0 = U^e + U^d \tag{4}$$

Where U^e is the elastic energy, and U^d represents the dissipated energy.

But a true triaxial test would consider not only the maximum principal stress acting on the rock but also the confining pressure applying energy to the rock. So, the total energy U_0 can be understood as:

$$U_0 = U_z + U_x + U_y \tag{5}$$

Where U_0 is the total energy, U_z, U_x and U_y are the energy generated by the deformation in three directions, respectively. U_Z, U_X and U_Y can be expressed as:

$$U_z = \int \sigma_z d\varepsilon_z = \sum_{i=0}^{n} \frac{1}{2}(\varepsilon_{zi+1} - \varepsilon_{zi})(\sigma_{zi} + \sigma_{zi+1}) \tag{6}$$

$$U_x = \int \sigma_x d\varepsilon_x = \sum_{i=0}^{n} \frac{1}{2}(\varepsilon_{xi+1} - \varepsilon_{xi})(\sigma_{xi} + \sigma_{xi+1}) \tag{7}$$

$$U_y = \int \sigma_y d\varepsilon_y = \sum_{i=0}^{n} \frac{1}{2}(\varepsilon_{yi+1} - \varepsilon_{yi})(\sigma_{yi} + \sigma_{yi+1}) \tag{8}$$

Where σ_z and ε_z are maximum principal stress and maximum principal strain; σ_x and ε_x are intermediate principal stress and intermediate principal strain; σ_y and ε_y are minimum principal stress and minimum principal strain.

According to Eqs 6–8, the elastic strain energy is:

$$U^e = \frac{1}{2E_0}\left[\sigma_z{}^2 + \sigma_x{}^2 + \sigma_y{}^2 - 2\nu\left(2\sigma_z\sigma_x + \sigma_z\sigma_y + \sigma_x\sigma_y\right)\right] \tag{9}$$

Where E_0 and ν are the elastic modulus and Poisson's ratio, respectively.

4.2 Analysis of energy evolution characteristics

The loading plate was modified to observe the crack development in the tunnel. The loading plate in the axial direction of the tunnel is grooved, and a micro camera was

Comparing the intact specimens, the open-flaw specimens and the filled-flaw specimens showed that the decrease in the surrounding rock integrity does not directly affect the crack

FIGURE 7
Micro cameras and capture sample.

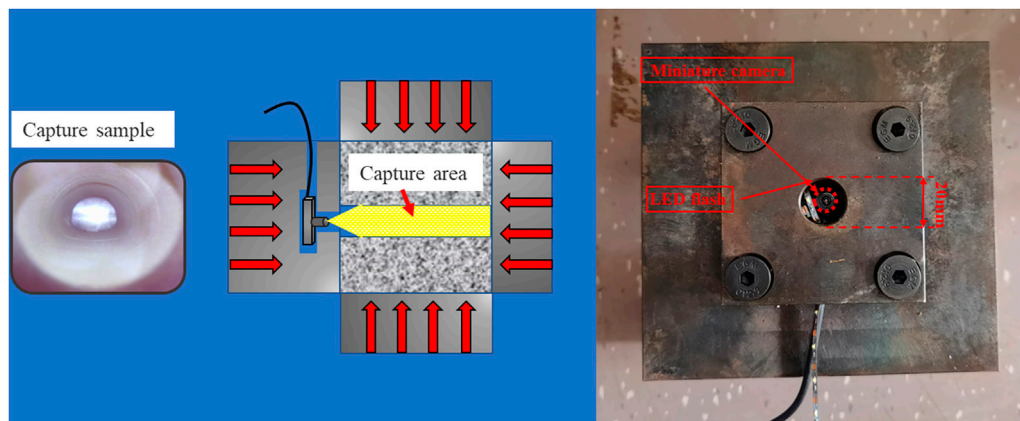placed in the loading plate to record the crack propagation in the tunnel (Figure 7). The resolution of the micro camera is 3,840 × 2,160 pixels, capture 30 photos per second. The diameter of the observation hole of the micro camera is 20 mm, which is smaller than the diameter of the opening in the sample. The effects of the observation hole of the micro camera on the stress calculation are not incorporated in the current study.

Figure 8 shows the relationship between energy evolution and stress, and the captured image shows the crack propagation state in the tunnel at different periods.

Energy evolution means the elastic energy stored in the rock is transformed into dissipated energy. The accumulation rate of energy in the surrounding rock is correlated with the loading rate. It is also obviously related to the structure of the surrounding rock (Figure 8). Furthermore, there are also many factors affecting the energy evolution in rocks.

In this research, the elastic energy under the three surrounding rock conditions has the same trend. Before the initial stage of loading, the surrounding rock is in the stage of pore compaction. The storage speed of elastic energy is slow. With the increase of stress, energy is continuously accumulated in the surrounding rock. At the same time, because the pores in the surrounding rock are compacted, a little elastic energy is transformed into dissipated energy. When the surrounding rock enters the elastic stage, the trend of energy accumulation is consistent with the trend of stress loading. It shows that elastic energy increases rapidly. However, with the rapid drop of stress, the elastic energy also decreases rapidly.

Dissipated energy shows some differences under different surrounding rock conditions. The dissipated energy increases slowly with the increase of stress at the initial stage. As the rock enters the elastic stage, the dissipated energy decreases slightly. The dissipated energy rises rapidly at the moment before the surrounding rock becomes unstable. There are some differences in the evolution characteristics of dissipative energy. When the rock enters the elastic stage, there is only a small decrease of dissipated energy in Group Open-flaw, which means that the open-flaw group continues to fail when the surrounding rock enters the elastic stage.

Internal images of some feature points are captured to better observe crack propagation in tunnels, which are divided into stages according to the level of dissipated energy. Point a represents the end of the first rise of dissipated energy, Point b represents the end of the linear segment after the dissipation energy first reaches the peak, and Point c represents the turning point where the dissipated energy rises again. At Point A (μ =3.0000) the surrounding rock is close to the limit of energy storage, representing the transition of the surrounding rock from a state of stability to bifurcation, and at Point B (μ =3.5699) the surrounding rock enters the chaotic stage.

Compare the images captured at each feature point and observe the image features at each stage. Point a and Point b are in the stable period (before Point A). In the characteristic point, no obvious damage is found in the surrounding rock but there is damage in the surrounding rock at Point A. This phenomenon is caused by the work that was done outside the surrounding rock, and energy is stored in the rock. The deformation of the surrounding rock concentrates the stress to a certain point in the tunnel. Point b shows the surrounding rock that is always between Point A and Point B. At Point c, the surrounding rock is damaged, and the damage at this stage is spalling. After Point B, the surrounding rock enters the chaos stage, and the damage becomes buckling failure.

So, the next step in the tunnel is particle injection. Before the surrounding rock enters the bifurcation process, the particle ejection phenomenon will occur inside the tunnel. When the surrounding rock enters the bifurcation process, there will be a spalling failure in the tunnel. V-shaped grooves on both sides of the tunnel are characteristic of spalling damage. Large buckling deformation of the tunnel occurs when the surrounding rock is in the chaos stage.

Compare captured images under different surrounding rock conditions. There is no crack generation at Point a or Point b in the stability stage. The surrounding rock is often damaged close to Point A, which represents the surrounding rock entering the bifurcation process. It is obvious that the damage of Group Intact and Group Filled-flaw in the bifurcation process seems to be
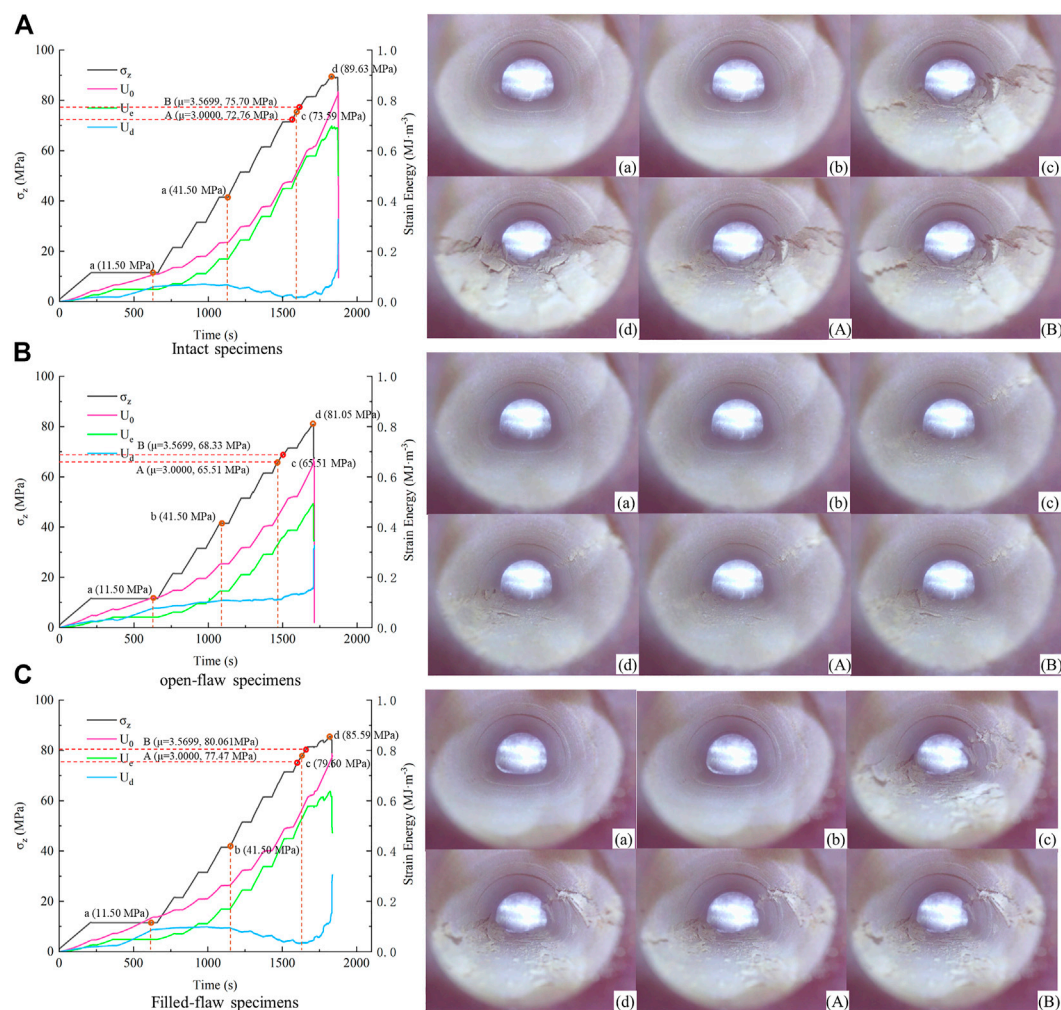
FIGURE 8
Energy evolution characteristics under the three surrounding rock conditions: **(A)** intact specimens; **(B)** open-flaw specimens; **(C)** filled-flaw specimens.

more serious but the dissipative energy of the two groups in the bifurcation process is in a lower value. The dissipative energy of Group Open-flaw rises continuously. This means that the surrounding rock of Group Intact and Group Filled-flaw in the bifurcation process is stable but the surrounding rock of Group Open-flaw may be unstable in the bifurcation process.

In addition, the dissipative energy at the bottom (Point c) is always between Point A and Point B. This phenomenon can prove that the bifurcation process is a continuation of the previous stage. It belongs to the process in which the surrounding rock is in the stage of stability and failure. This is the same as the stage after Point B. After Point B, the dissipative energy will increase rapidly.

In this work, the energy limit of Group Intact is 0.697 MJ/m³, Group Filled-flaw is 0.635 MJ/m³ and Group Open-flaw is 0.486 MJ/m³. As the integrity of the surrounding rock decreases, the energy stored in the surrounding rock also decreases significantly.

4.3 Dissipated energy ratio under the three surrounding rock conditions

Figure 9 shows the evolution of the dissipated energy ratio. The dissipated energy rate is the ratio of dissipated energy to total energy. This ratio can reflect the rate at which elastic energy is transformed into dissipated energy at each moment. When the dissipated energy ratio rises, more damage occurs to the surrounding rock.

Before the initial stress, the rock is in the stage of pore compaction, and a large number of pores are compacted with a high dissipated energy ratio (Figure 9) but a low dissipation energy value (Figure 6). In this step-loading process, loose pores in the surrounding rock have compacted. After the initial stress, with the increase in stress, the energy dissipation gradually decreases in a linear phase with different slopes under different surrounding rock conditions. It was found that the integrity of the surrounding rock decreased with the higher dissipation energy ratio in the whole loading process.
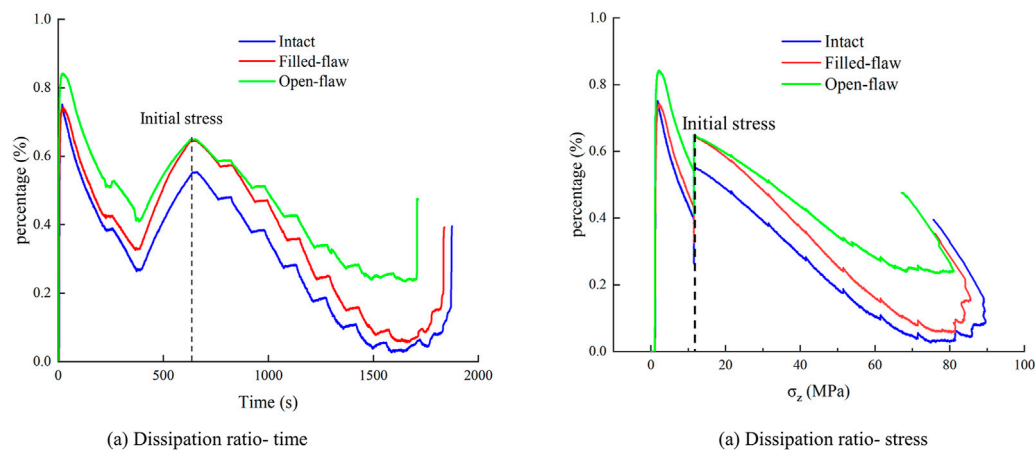
FIGURE 9
Dissipated energy ratio under the three surrounding rock conditions.
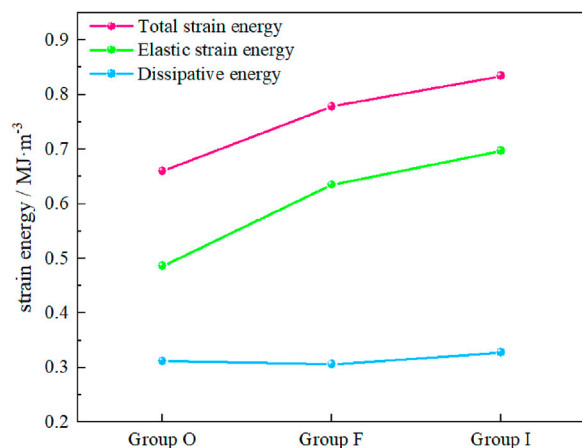
FIGURE 10
Comparative analysis of characteristic strain energy.

Another interesting phenomenon is that the dissipated energy ratio of Group Filled-flaw (0.645 MJ/m³) near the initial stress is close to that of Group Open-flaw (0.648 MJ/m³). However, the dissipated energy ratio of Group Filled-flaw (0.064 MJ/m³) is closer to Group Intact (0.034 MJ/m³) at the later stage of loading. This may reflect that the damage to Group Filled-flaw was similar to that of Group open-flaw in the early stage (Figure 8 open-flaw specimens (c) and Figure 8 filled-flaw specimens (c)) and similar damage to Group intact in the later stage (Figure 3). The same particle ejection phenomenon occurs in Group Open-flaw and Group Filled-flaw in the early stage because of the prefabricated flaws in the surrounding rock. The flaws of Group Filled-flaw are filled with gypsum but gypsum is not very strong and there will always be some spaces between the gypsum and the surrounding rock. These can cause cracks extending from the prefabricated flaw to the inside of the tunnel. When the stress is about to reach peak value, the gypsum filled in the prefabricated flaw inhibits the further collapse of the prefabricated flaw, and new damage is generated in

the tunnel. Filling the open flaw brings different forms of failure to the tunnel. This complex failure results in more fragments in the tunnel, but it also significantly increases the peak stress of the surrounding rock.

5 Discussion

The compression failure of rock is a complex process with a strong unpredictability (Hirata and Imoto, 1991; Zhang, 2021). Through chaos theory and energy evolution, the current stress state can be analysed, and the current state of the surrounding rock can be quickly and accurately predicted.

There are also different forms of failure inside the tunnel under different surrounding rock conditions. When open flaws appear around the tunnel, only particle spray failure occurs in the tunnel, but the surrounding rock may be close to instability damage. When open flaws are filled, spraying particles and spalling fragments in the tunnel will increase, but the peak stress will rise.

Figure 10 shows the characteristic strain energy under different surrounding rock conditions. The characteristic strain energy of different groups is significantly different. As the integrity of surrounding rock increases, the total elastic strain energy (0.660 MJ m⁻³, 0.778 MJ m⁻³, 0.834 MJ m⁻³) and elastic strain energy (0.486 MJ m⁻³, 0.635 MJ m⁻³, 0.697 MJ m⁻³) increase. However, there is no significant difference in the dissipative energy (0.312 MJ m⁻³, 0.306 MJ m⁻³, 0.328 MJ m⁻³) by surrounding rock during final failure.

These phenomena indicates that the fracture of tunnel surrounding rock mainly affects the elastic strain energy accumulated in the surrounding rock. The dissipative energy after the ultimate failure of the surrounding rock is not affected by these fractures. But the rate of energy dissipation is different during the elastic process. Group F and Group I showed a downward trend and Group O showed a slow upward trend during the elastic process (Figure 8). It indicates that the main function of fracture filled is to suppress the deformation of surrounding rock and improve the ability of surrounding rock to store energy. Then, it

explains the impact of fractures around tunnels on the stability of tunnel surrounding rocks from the energy perspective.

The application of chaos theory to rock is still being explored. In this study, chaos theory has been verified as able to determine whether the surrounding rock is stable or unstable, but it cannot accurately predict particle spray and spalling failure. In this research, we use chaos theory to analyse the damage inside the tunnel. The surrounding rock is in a stable stage, which does not mean that there is no failure in the tunnel. It only means that the surrounding rock will not lose stability, but the particle spray and spalling failure will still occur. However, we can use shotcrete support and other methods to prevent spray and spalling failure. When the surrounding rock is in the bifurcation process (μ =3.0000), spalling failure becomes more frequent. At this stage, the surrounding rock will not be unstable, and we should pay attention to this phenomenon and reinforce the tunnel. When the surrounding rock is in the chaos stage (μ =3.5699), the tunnel should be reinforced immediately because the surrounding rock can become unstable at any time.

It should be noted that the failure characteristics in the tunnel analysed in this paper are generated under conditions of increasing maximum principal stress, which may be different from practical engineering. However, analysing the current state of the tunnel and the surrounding rock by energy evolution and chaos theory is a reliable way to understand the failure characteristics of the surrounding rock.

6 Conclusion

In this paper, the true triaxial load is applied to a tunnel with a four-centre arch, and the internal failure characteristics of the tunnel are analysed from the perspective of energy evolution.

In this research, we changed the conditions of the rock surrounding the sample tunnel. Surrounding rock conditions include intact surrounding rock, open-flaw surrounding rock and filled-flaw surrounding rock. We found that the peak stress of the surrounding rock of the tunnel increased significantly after filling the open flaw, but it was slightly lower than that of the intact surrounding rock.

There are remarkable differences between the failure characteristics and mechanisms for the surrounding rock under different conditions. The different conditions of the surrounding rock also affected the process of energy evolution. As the integrity of surrounding rock increases, the dissipation energy of surrounding rock in the elastic stage becomes lower and led to the increases in the energy stored in the surrounding rock (0.486 MJ/m^3, 0.635 MJ/m^3 and 0.697 MJ/m^3).

The energy dissipation ratio can reflect the process of failure. The same failure behaviour has the same energy dissipation ratio. At the initial stage of step loading, the dissipated energy ratio of Group Filled-flaw (0.645 MJ/m^3) and Group Open-fl0.697aw (0.648 MJ/m^3) was similar and both had the same trends in failure. In addition, both Group Filled-flaw (0.064 MJ/m^3) and Group Open-flaw (0.034 MJ/m^3) have V-shaped grooves on both sides of the final failure characteristic.

Data availability statement

The original contributions presented in the study are included in the article/Supplementary Materials, further inquiries can be directed to the corresponding author.

Author contributions

BL: Funding acquisition, methodology, writing—review and editing. JL: Methodology, investigation, data curation, writinig—original draft. HH: Conceptualization, methodology, writing—review and editing. JG: Investigation, data curation. TL: Methodology, writing—review and editing.

Funding

Conflict of interest

The authors declare that the research was conducted in the absence of any commercial or financial relationships that could be construed as a potential conflict of interest.

Publisher's note

All claims expressed in this article are solely those of the authors and do not necessarily represent those of their affiliated organizations, or those of the publisher, the editors and the reviewers. Any product that may be evaluated in this article, or claim that may be made by its manufacturer, is not guaranteed or endorsed by the publisher.

References

Afrazi, M., Lin, Q., and Fakhimi, A. (2022). Physical and numerical evaluation of mode II fracture of quasi-brittle materials. *Int. J. Civ. Eng.* 20, 993–1007. doi:10.1007/s40999-022-00718-z

Chen, L., Guo, W., Zhang, D., and Zhao, T. (2022). Experimental study on the influence of prefabricated fissure size on the directional propagation law of rock type-I crack. *Int. J. Rock Mech. Min. Sci.* 160, 105274. doi:10.1016/j.ijrmms.2022.105274

Chen, Z. Q., He, C., Ma, G. Y., Xu, G. W., and Ma, C. C. (2019). Energy damage evolution mechanism of rock and its application to brittleness evaluation. *Rock Mech. Rock Eng.* 52, 1265–1274. doi:10.1007/s00603-018-1681-0

Fakhimi, A., Lin, Q., and Labuz, J. F. (2018). Insights on rock fracture from digital imaging and numerical modeling. *Int. J. Rock Mech. Min. Sci.* 107, 201–207. doi:10.1016/j.ijrmms.2018.05.002

Hirata, T., and Imoto, M. (1991). Multifractal analysis of spatial distribution of microearthquakes in the Kanto region. *Geophys. J. Int.* 107, 155–162. doi:10.1111/j.1365-246X.1991.tb01163.x

Li, P., and Cai, M. F. (2021). Energy evolution mechanism and failure criteria of jointed surrounding rock under uniaxial compression. *J. Cent. S. Univ.* 28, 1857–1874. doi:10.1007/s11771-021-4735-5

Li, Y., Liu, B., Wang, X., Shao, Y., Li, L., Wei, J., et al. (2021). The effect of a prefabricated crack on the crack growth in ceramics during quenching. *Ceram. Int.* 47, 3643–3648. doi:10.1016/j.ceramint.2020.09.215

Li, Z., Wang, L., and Li, W. (2022). Mechanical behavior and fracture characteristics of rock with prefabricated crack under different triaxial stress conditions. *Miner* 12, 673. doi:10.3390/min12060673

Liu, G. L., Chen, Y. L., Du, X., Xiao, P., Liao, S. M., and Azzam, R. (2021a). Investigation of microcrack propagation and energy evolution in brittle rocks based on the voronoi model. *Mater* 14, 2108. doi:10.3390/ma14092108

Liu, X. X., Wu, L. X., Zhang, Y. B., Wang, S. Z., Yao, X. L., and Wu, X. Z. (2021b). The characteristics of crack existence and development during rock shear fracturing evolution. *Bull. Eng. Geol. Environ.* 80, 1671–1682. doi:10.1007/s10064-020-01997-3

Mehranpour, M. H., Kulatilake, P., Ma, X. G., and He, M. C. (2018). Development of new three-dimensional rock mass strength criteria. *Rock Mech. Rock Eng.* 51, 3537–3561. doi:10.1007/s00603-018-1538-6

Meng, Q. B., Zhang, M. W., Zhang, Z. Z., Han, L. J., and Pu, H. (2019). Research on non-linear characteristics of rock energy evolution under uniaxial cyclic loading and unloading conditions. *Environ. Earth Sci.* 78, 650. doi:10.1007/s12665-019-8638-9

Muralha, J., Grasselli, G., Tatone, B., Blümel, M., Chryssanthakis, P., and Yujing, J. (2014). ISRM suggested method for laboratory determination of the shear strength of rock joints: Revised version. *Rock Mech. Rock Eng.* 47, 291–302. doi:10.1007/s00603-013-0519-z

Sharafisafa, M., Shen, L. M., Zheng, Y. G., and Xiao, J. Z. (2019). The effect of flaw filling material on the compressive behaviour of 3D printed rock-like discs. *Int. J. Rock Mech. Min. Sci.* 117, 105–117. doi:10.1016/j.ijrmms.2019.03.031

Wang, C. L., He, B. B., Hou, X. L., Li, J. Y., and Liu, L. (2020a). Stress-energy mechanism for rock failure evolution based on damage mechanics in hard rock. *Rock Mech. Rock Eng.* 53, 1021–1037. doi:10.1007/s00603-019-01953-y

Wang, C. L., Zhou, B. K., Li, C. F., Cao, C., Sui, Q. R., Zhao, G. M., et al. (2022). Experimental investigation on the spatio-temporal-energy evolution pattern of limestone fracture using acoustic emission monitoring. *J. Appl. Geophys.* 206, 104787. doi:10.1016/j.jappgeo.2022.104787

Wang, H., Li, Y., Cao, S., Pan, R., Yang, H., Zhang, K., et al. (2020b). Brazilian splitting test study on crack propagation process and macroscopic failure mode of pre-cracked black shale. *Chin. Rock Mech. Rock Eng.* 39, 912–926. doi:10.13722/j.cnki.jrme.2019.0839

Wang, Y., Feng, W. K., and Li, C. H. (2020c). On anisotropic fracture and energy evolution of marble subjected to triaxial fatigue cyclic-confining pressure unloading conditions. *Int. J. Fatigue* 134, 105524. doi:10.1016/j.ijfatigue.2020.105524

Wang, Y., Li, C. H., and Han, J. Q. (2020d). On the effect of stress amplitude on fracture and energy evolution of pre-flawed granite under uniaxial increasing-amplitude fatigue loads. *Eng. Fract. Mech.* 240, 107366. doi:10.1016/j.engfracmech.2020.107366

Worley, R., Dewoolkar, M. M., Xia, T., Farrell, R., Orfeo, D., Burns, D., et al. (2019). Acoustic emission sensing for crack monitoring in prefabricated and prestressed reinforced concrete bridge girders. *J. Bridge Eng.* 24. doi:10.1061/(ASCE)BE.1943-5592.0001377

Xie, H., Ju, Y., and Li, L. (2005). Criteria for strength and structural failure of rocks based on energy dissipation and energy release principles. *Chin. J. Rock Mech. Eng.* 24, 3003–3010.

Xie, H., Li, L., Peng, R., and Ju, Y. (2009). Energy analysis and criteria for structural failure of rocks. *J. Rock Mech. Geotech. Eng.* 1, 11–20. doi:10.3724/SP.J.1235.2009.00011

Xue, Y., Liu, S., Chai, J., Liu, J., Ranjith, P. G., Cai, C., et al. (2023a). Effect of water-cooling shock on fracture initiation and morphology of high-temperature granite: Application of hydraulic fracturing to enhanced geothermal systems. *Appl. Energy* 337, 120858. doi:10.1016/j.apenergy.2023.120858

Xue, Y., Ranjith, P. G., Gao, F., Zhang, Z., and Wang, S. (2023b). Experimental investigations on effects of gas pressure on mechanical behaviors and failure characteristic of coals. *J. Rock Mech. Geotech. Eng.* 15, 412–428. doi:10.1016/j.jrmge.2022.05.013

Yang, H., Lin, H., Chen, Y., Wang, Y., Zhao, Y., Yong, W., et al. (2022). Influence of wing crack propagation on the failure process and strength of fractured specimens. *Bull. Eng. Geol. Environ.* 81, 71. doi:10.1007/s10064-021-02550-6

Zafar, S., Hedayat, A., and Moradian, O. (2020). Evaluation of crack initiation and damage in intact barre granite rocks using acoustic emission. *Int. J. Geotech. Earthq. Eng.*, 399–408.

Zhang, Z., and Gao, F. (2012). Experimental research on energy evolution of red sandstone samples under uniaxial compression. *Chin. J. Rock Mech. Eng.* 31, 953–962. doi:10.3969/j.issn.1000-6915.2012.05.012

Zhang, L., Yu, Meng, Wang, Fanzhen, Zhang, Zaiquan, PengGao, Su, and Zhang, P. (2021). Energy evolution analysis and failure criteria for rock under different stress paths. *Acta Geotech.* 16, 569–580. doi:10.1007/s11440-020-01028-1

Zhang, L. Y., and Zhu, J. M. (2020). Analysis of mechanical strength and failure morphology of prefabricated closed cracked rock mass under uniaxial compression. *Geotech. Geol. Eng.* 38, 4905–4915. doi:10.1007/s10706-020-01335-0

Zhang, S., Wang, L., and Gao, M. (2020). Experimental and numerical study of the influence of prefabricated crack width on the fracture toughness of NSCB specimens. *Rock Mech. Rock Eng.* 53, 5133–5154. doi:10.1007/s00603-020-02211-2

Zhang, T., Liu, B., Wei, Z., Jiao, Z., Song, Z., and Zhang, H. (2022). Dynamic mechanical responses and crack evolution of burst-prone coal with a single prefabricated fissure. *Theor. Appl. Fract. Mech.* 121, 103494. doi:10.1016/j.tafmec.2022.103494

Zhang, Z. X., Kou, S. Q., Jiang, L. G., and Lindqvist, P. A. (2000). Effects of loading rate on rock fracture: Fracture characteristics and energy partitioning. *Int. J. Rock Mech. Min. Sci.* 37, 745–762. doi:10.1016/s1365-1609(00)00008-3

Zhou, X. P., Niu, Y., Cheng, H., and Berto, F. (2021). Cracking behaviors and chaotic characteristics of sandstone with unfilled and filled dentate flaw. *Theor. Appl. Fract. Mech.* 112, 102876. doi:10.1016/j.tafmec.2020.102876

Zhuang, D. Y., Tang, C. A., Liang, Z. Z., Ma, K., Wang, S. Y., and Liang, J. Z. (2017). Effects of excavation unloading on the energy-release patterns and stability of underground water-sealed oil storage caverns. *Tunn. Undergr. Space Technol.* 61, 122–133. doi:10.1016/j.tust.2016.09.011

Influence of coplanar double fissures on failure characteristics of sandstone and fracture mechanics analysis

Dechao Zhang, Haicheng She* and Taoli Xiao*

School of Urban Construction, Yangtze University, Jingzhou, Hubei, China

The influence of fissure angles and bridge lengths on rock mechanical properties and failure was analyzed using the uniaxial compression test and the Digital Image Correlation (DIC) technique. The research findings are as follows: 1) Peak stress and elastic modulus of the samples exhibited an obvious change trend with the change in fissure angle. The fissure angle has a more significant effect on a rock's mechanical properties than the length of the rock bridge. 2) With an increase in the fissure angle, the number of surface cracks, main failure cracks and surface spalling decreased, whereas the area of the falling blocks significantly increased. However, with an increase in bridge length, the characteristics of crack propagation and spalling are essentially the same. During crack propagation, the connection of the rock bridge is related to its fissure angle and length. 3) At a low fissure angle, the failure mode of rock samples is dominated by tensile-failure cracks; with an increase in fissure angle, the tension-damage to shear-damage crack transformation will form a mixed tensile-shear damage mode; at the same time, with an increase in bridge length, the rock bridge becomes more difficult to connect, and the local crack expansion failure changes from tensile-shear cracks to tensile cracks. 4) Stress on the coplanar double-fissured rock sample was simplified and analyzed to explain the behavior of fractures on the sample. These research results have an important guiding value for engineering optimal designs.

KEYWORDS

sandstone-like, coplanar double fissures, fissure angle, rock bridge length, DIC technique

Highlights

1. The influence of bridge length on mechanical properties was weaker than that of the fissure angles' influence.
2. With the increase of the fissure angle, the failure mode changes from tension to shear.
3. The increase of the length of the rock bridge affects its connection.
4. The bridge connection occurs only at a high fissure angle.
5. The failure behavior was affected by the normal stress double-clamped beam model and shear stress.

1 Introduction

The fissured rock mass is a common engineering medium in water conservancy and hydropower projects. Such fissure defects not only impact the mechanical properties of rock masses, but also increase the risk of engineering accidents, since more cracks may sprout and expand from internal cracks upon experiencing external disturbance (Lajtai et al., 1990; Hoek and Martin., 2014; He et al., 2022; Wong et al., 2022; Ren et al., 2023). It is therefore of great theoretical significance to investigate the influence of the geometric distribution of cracks on rock mass mechanical properties, crack propagation, and damage of rock masses. Lajtai (1969) believed that simulating real rock by using rock-like material to precast fissures, thus greatly simplifying sample preparation, was feasible; this is now widely accepted. Since then, Park and Bobet (2009) (Wong and Einstein., 2009; Yang and Jing., 2011) assigned a uniform name to the precast fissure. The terms "fissure" or "flaw" are used to describe a man-made pre-existing crack or fracture. In addition, the names of the cracks caused by the load in the rock samples are unified. Wing crack, anti-wing crack and secondary crack are unified Bobet (2000) determined the tensile and shear properties of the wing and secondary cracks. Previous studies mostly focused on Intact rock sample (Liang et al., 2022; Tang et al., 2022) and single-fracture rock samples (Wong and Einstein, 2009; Yang, 2011; Liang et al., 2012; Xiao et al., 2012; Xu et al., 2013; Jin et al., 2017), while current research on fissured rock masses has developed towards multiple fissure; many achievements have been made in double-fissured rock mass research. Zhang et al. (2006) conducted uniaxial compression tests on 45°, 55°, 65° coplanar double fissured sandstone specimens and observed that the secondary coplanar crack is easy to occur in the inner end of coplanar double fissure, forming coplanar shear through. Yang and Jing. (2011) studied coplanar double fissures with different dip angles and found that the degree of peak strength reduction in fissure samples was related to coplanar double fissures, ultimate failure modes are obviously dependent to coplanar fissure angle. Sun et al. (2018) conducted uniaxial compression tests on rock samples with different dip angles, fissure forms, and rock bridge spacings and discovered that peak strength showed a downward concave trend with increasing fissure dip angle; the smaller the rock bridge distance, the easier it is to connect and the smaller the peak strength. The length of coplanar double-fissure rock bridge becomes longer, and wing cracks and anti-wing cracks are easy to occur at the fissure tip. Wasantha et al. (2012) used cement mortar to make single-fissure cylindrical specimens with different angles and fissure lengths and studied the effects of fissure length and angle on the mechanical properties and fracture modes of the specimens under uniaxial compression. Specimens with longer partially-spanning joints, failure was seeded at the pre-existing fissure tip, whereas for specimens with shorter partially-spanning joints, failure was not associated with the pre-existing fissure. Xiao et al. (2015) conducted triaxial compression tests on two parallel fissured cylindrical rock samples and observed that when the fissures are arranged in coplane, the failure mode is X-type shear failure formed by coplane propagation crack and anti-wing crack. In the non-superimposed arrangement, the failure modes range from tensile shear failure at medium and low confining pressures to anti-wing crack penetration failure at high confining pressures. Yang et al. (2022) used a conventional triaxial compression test to study granite samples

with two non-coplanar open fissures, and defined five modes of crack penetration. The results from Yang et al. (2022)'s investigation show that, under uniaxial and low confining pressure conditions, the rock bridge angle has a significant influence on the crack evolution behavior. However, under high confining pressure, with the propagation of the anti-wing crack, a shear will lead to final failure. Yin et al. (2014) studied the bonding mechanism between surface cracks of two parallel fissures in granite samples under uniaxial compression and found that the anti-wing crack initiation process is tensile, and the penetration of the precast fissure occurs on both the surface and internally. Wang et al. (2018) conducted a biaxial test on prefabricated double-fissure rock samples and divided the rock bridge connection into three categories: the influence of lateral stress caused by the original fissure angle, rock bridge angle, and crack propagation in the coalescence mode. Cao et al. (2015) produced rock samples with two and three fissures and analyzed the effect of prefabricated fissures on the crack formation process. Wang et al. (2018) studied rock samples with parallel-fissure clusters and obtained four damage modes for jointed rock samples under compression-shear loading; dip angle had a significant effect on the damage mode. With increasing fissure angle, the coalescence mode changes from the propagation of two wing cracks that coalesces to form a single wing crack coalescence mode. Research on cracks has become more increasingly complicated, including fissure groups (Prudencio and Van., 2007; Wang et al., 2018; Zhang et al., 2020), fissures in the form of pores (Zhang et al., 2006; Pu et al., 2010; Zhao et al., 2013; Chen et al., 2017; Yang et al., 2017; Gong et al., 2020), and non-parallel irregular cracks (Park and Bobet, 2010; Janeiro and Einstein, 2010; Yang et al., 2013; Cao et al., 2015). Although the fissure tendency is complicated, the core of the research is always the influence of defects on the specimen and the form and propagation of the cracks generated by loading.

Many studies on double fissures have primarily focused on parallel fissures, and mainly on the fissure and rock bridge dip angles on rock damage mode, crack extension, and rock bridge penetration. Conversely, fewer studies address coplanar double fissures and the length of the rock bridge between two fissures. At the same time, study of rock sample failure tends to focus on the final failure mode, lacking the summary of the law of rock sample failure characteristics and failure mechanism in the whole loading process. Therefore, this study considers sandstone specimens of the special coplanar double fissures in parallel cracks as the research objective to explore the influence of different coplanar double fissures angle and bridge length on the mechanical properties and failure characteristics of sandstone. In addition, this paper summarizes the fracture mechanics model, explains the fracture behavior of each rock sample and reveals the failure mechanism of rock sample.

2 Test apparatus and test program design

The main instrument consisted of a loading system and a DIC system, as shown in Figure 1. Figure 2 shows the physical picture of the instrument; the loading system included WAW-1000B Microcomputer Servo-controlled Universal Testing Machine and data acquisition system, and the DIC system included both a
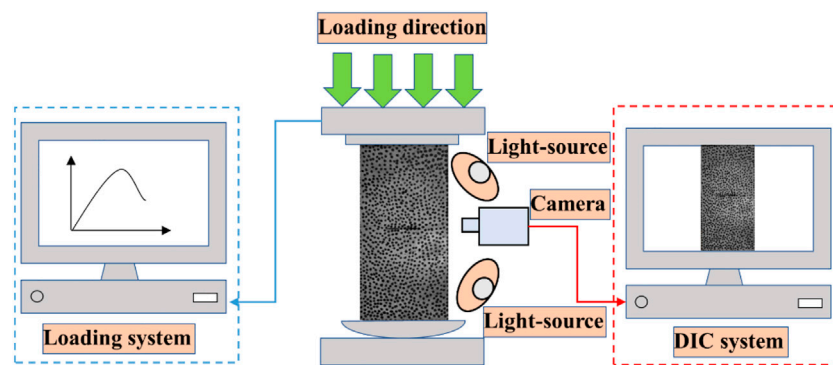
FIGURE 1
Schematic diagram of the test system.

FIGURE 2
Test instrument physical picture.

FIGURE 3
Mold diagram.

shooting system and a digital image calculation system with a maximum load of 1,000 kN. The loading system not only controlled the force or displacement of the sample, but also conducted uniaxial compression, tensile and cyclic loading, and creep tests. The loading system adopted a displacement control, and the displacement loading rate was 0.2 mm/min. The DIC system was comprised of non-contact, optical, and three-dimensional measurement equipment for material displacement, strain measurement, and analysis. The system was primarily composed of a computer control system (DIC software, control box), a support system (tripod, platform, beam), and a measurement system (camera and light source). Double cameras at both ends of the beam were used for monitoring. The resolution, frame rate, lens focal length, light-source focal length, and pixel size were 4096 px × 3000 px, 30 fps, 12 mm, 10 mm, and 3.45 μm, respectively.

Owing to the difficulty of sampling in the field to obtain coplanar double-fissured sandstone specimens of similar size, the required samples needed to be made manually. In recent years, laboratory simulation tests with similar materials have been applied to jointed fissured and layered rock masses. Many scholars have developed rock-like materials and have achieved substantial results.

The mass ratio of the rock sample was 32.5R ordinary silicate cement: quartz sand: pure water: polycarboxylate acid early strength water reducing agent: defoamer = 1:1:0.28:0.002:0.003. A cuboid mold with dimensions of 70 mm × 70 mm × 143 mm was adopted, as shown in Figure 3, and the steel sheet was pre-inserted into the mold before pouring. After the initial setting, the steel sheet was removed, creating a perforating crack without filling.

The schematic diagram of the fissure distribution of the rock sample is shown in Figure 4 below. In Figure 4B, a is the fissure length, mm; $2b$ is the rock bridge length, mm; α is the fissure dip angle, (°); β is the rock bridge dip angle, (°); and $\alpha = \beta$. In the uniaxial compression test, the WAW-1000B was used for loading at a rate of 0.2 mm/min. The whole process of rock surface crack evolution was monitored by the DIC system; the camera frame rate was 1 frame/s.

To investigate the effects of the fissure angle and rock bridge length on the mechanical strength properties and damage mode of
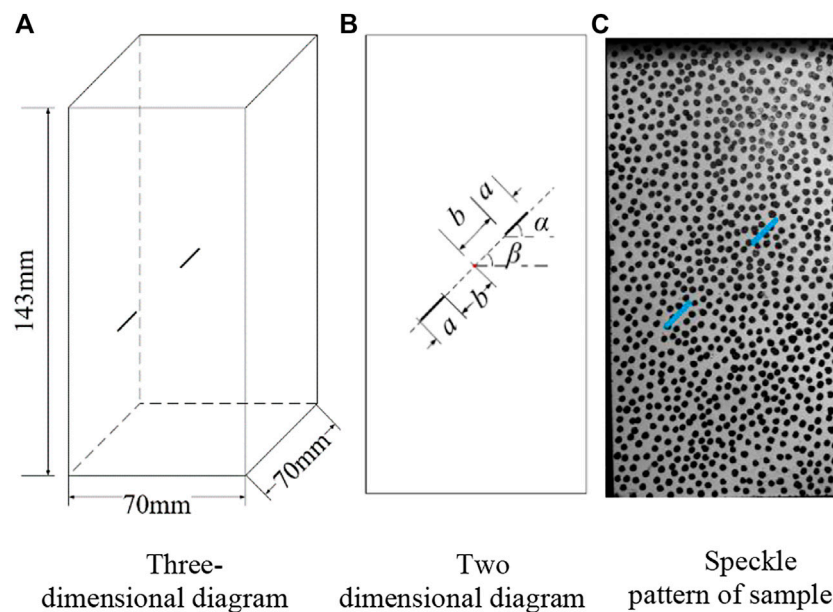
FIGURE 4
Distribution diagram of coplanar double fissures. **(A)** Three-dimensional diagram; **(B)** Two dimensional diagram; **(C)** Speckle pattern of sample.

TABLE 1 Test plan and specimens' number.

α/(°) 2b/mm	0	30	45	60	90
7	0–7	30–7	45–7	60–7	90–7
14	0–14	30–14	45–14	60–14	90–14
21	0–21	30–21	45–21	60–21	90–21
28	0–28	30–28	45–28	60–28	90–28

coplanar double-fissured sandstone, the two fissure lengths (a) prefabricated in the rock samples were 10 mm, and the fissure thickness was 0.5 mm. The fissure dip angles (a) were taken as 0°, 30°, 45°, 60°, and 90°, and the rock bridge lengths (2b) were taken as 7 mm, 14 mm, 21 mm, and 28 mm. The rock sample numbers were named in α-2b format, and the test protocol and specimen numbers are listed in Table 1.

3 Test results and analysis

3.1 Effects of fissure dip angle and rock bridge length on the mechanical properties of rock samples

Uniaxial compression tests were performed on each rock sample according to the test scheme presented in Table 1, and the stress-strain curves of the rock samples were obtained, as seen in Figure 5.

As shown in Figure 5, the stress-strain curve obtained from the test contains three stages: compression-density, elastic, and yield. There is no obvious plastic deformation before the peak stress of the stress-strain curve, where a long elastic stage is seen, indicating that the rock sample

has a strong brittle characteristic. There is a slight stress drop appearing in the stage before reaching peak stress, that is, a sudden change in slope, which indicates that new cracks sprouted in-between prefabricated fissures within the rock sample. Statistical analysis of the test data shows that the peak stress and elastic modulus of each rock sample vary with the fissure angle and length of the rock bridge, as shown in Figures 6, 7.

From Figure 6A, it can be seen that the peak stress tends to increase significantly with the increase of fissure angle at the same rock bridge length. When $\alpha = 0°$, the peak stress of the rock sample is between 51.5 and 53.1 MPa, which is a serious weakening of the rock sample's mechanical strength when compared with 74.0 MPa of the intact rock sample, with a weakening degree of 30.4%–28.2%. When $\alpha = 90°$, the peak stress of the rock sample is between 68.7 and 73.0 MPa, with a weakening degree of 7.3%–1.3%, which is very close to the strength of the intact rock sample. From Figure 6B, it is observed that under the same fissure angle, peak stress increases with the length of the rock bridge, and its value is more similar in magnitude. Demonstrating the law of increasing first and then decreasing or decreasing in a small way. Overall variation range of peak stress is small, and the difference between the maximum and minimum value of peak stress of rock samples with different bridge lengths is between 1.5 and 5.7 MPa under five fissure angles. Bridge length has little influence on the peak strength of rock samples. As can be seen from Figure 7, the elastic modulus of the rock sample displays an increasing trend with the increase in the fissure angle, but the growth rate varies widely, with a maximum growth rate of 30.4% and a minimum growth rate of 3.4%. The elastic modulus of the rock sample shows a concave trend of decreasing and then increasing, with an increase in bridge length, and an elastic modulus change rate of between −8.8% and 10.5%. In summary, coplanar double-fissure specimen mechanical properties increase with an increase in fissure angle, and the influence of rock bridge length on the mechanical properties of rock samples is small, and the degree of influence on the mechanical properties of rock samples is weaker than fissure angle.
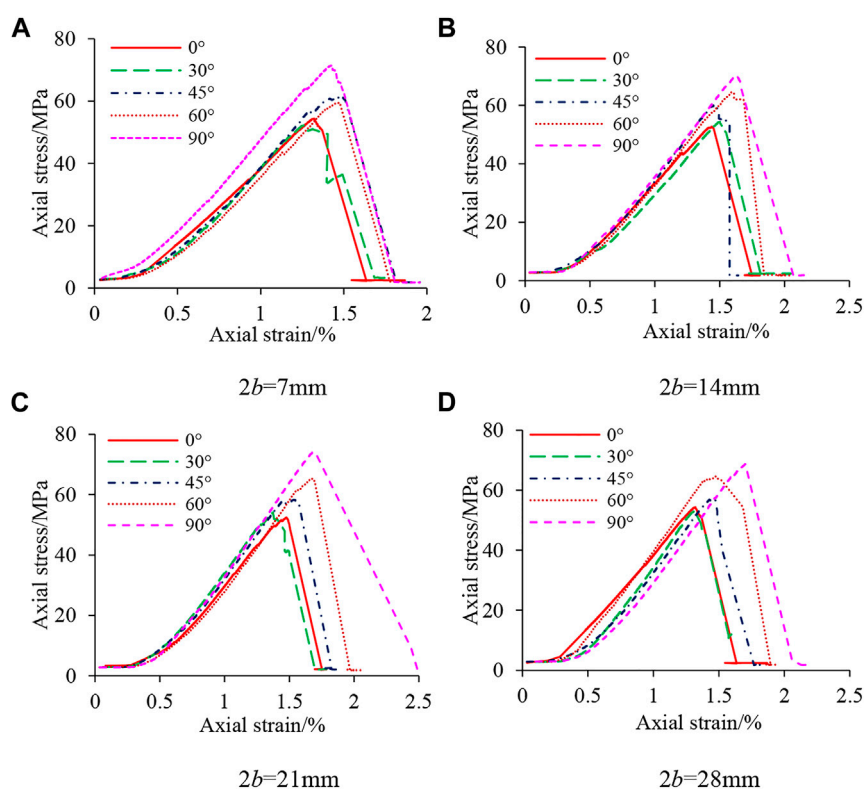
FIGURE 5
Axial stress-strain curve of rock specimens with different fissured angles. **(A)** 2*b* = 7 mm; **(B)** 2*b* = 14 mm; **(C)** 2*b* = 21 mm; **(D)** 2*b* = 28 mm.
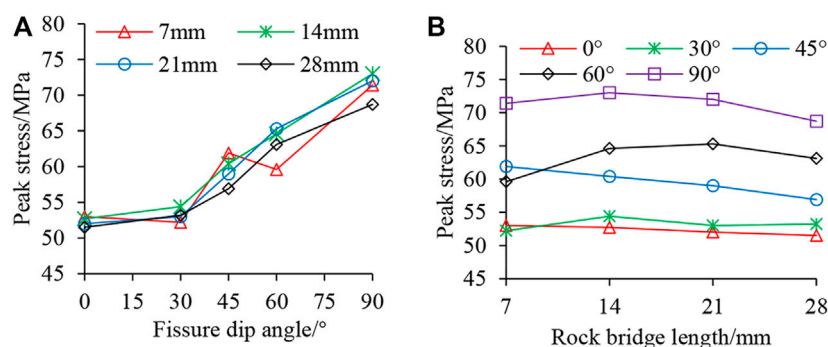
FIGURE 6
The variation of peak stress with fissured angles and rock bridge lengths. **(A)** Fissure dip angle VS. Peak stress; **(B)** Rock bridge length VS. Peak stress.

3.2 Influence of fissure dip angle and bridge length on the damage characteristics of rock samples

In the uniaxial compression test, the strain cloud map generated by the DIC system was used to assist in the analysis of the crack expansion process on the surface of the rock samples. The sequence of crack generation at different stress levels in rock samples was captured by the camera, as displayed by specimens 0–14 in Figure 8. Crack generation speed is

extremely high. The moment when a large number of cracks suddenly occur is defined as a batch of crack generation. Numbers ①, ②, ③, and ④ in the figures represent successive batches of cracks generated at different stress levels. The main rupture crack at the time of damage is indicated by a solid black thick line. Surface spalling is indicated by the gray variegated color in the interior of the rock sample; simultaneous spalling blocks are indicated in black.

The surface crack propagation law of the rock sample is as follows: at low-stress levels, as seen in Figure 8A, ① appeared near
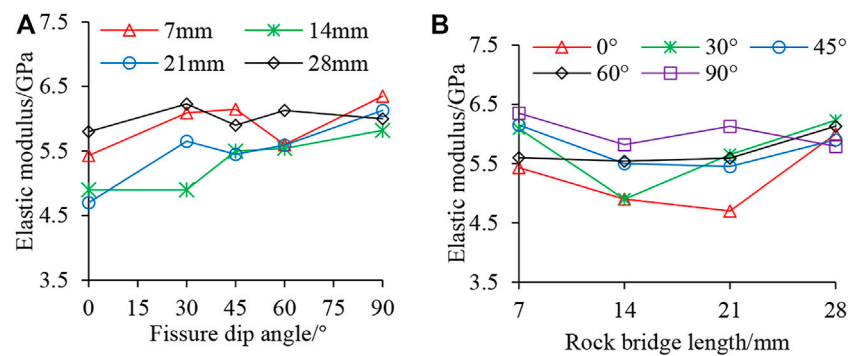
FIGURE 7
The variation of elasticity modulus with fissured angles and rock bridge lengths. **(A)** Fissure dip angle VS. Elastic modulus; **(B)** Rock bridge length VS. Elastic modulus.
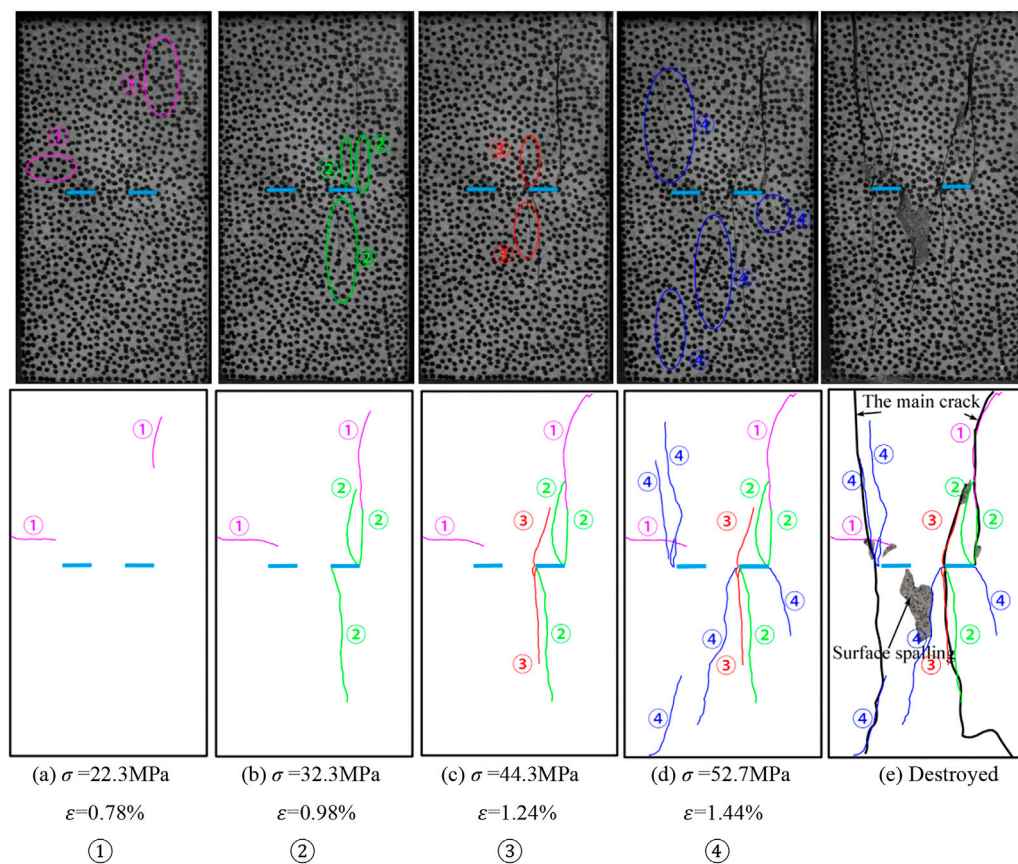
FIGURE 8
Crack propagation and failure of rock samples with α = 0° and $2b$ = 14 mm.

the upper face and left edge of the rock sample, and belonged to far-field cracks, which are caused by uneven upper and lower end faces of the rock sample, or uneven force on the end faces. At medium stress levels, cracks appeared at the tips of the precast fissures and expanded towards the ends of the rock sample. In Figures 8B, C, ② is a wing crack and ③ possesses both a wing crack and an anti-wing

crack. In both Figures, ② and ③ are fused with the ① far-field cracks. They are mainly concentrated at both ends of the right prefabricated fissure, which indicates that the force on the end face is not uniform. At high-stress levels, cracks occurred at the two prefabricated fissure tips, rapidly propagated to the end of the rock sample, and integrated with other batches of cracks,

FIGURE 9
Crack closure.
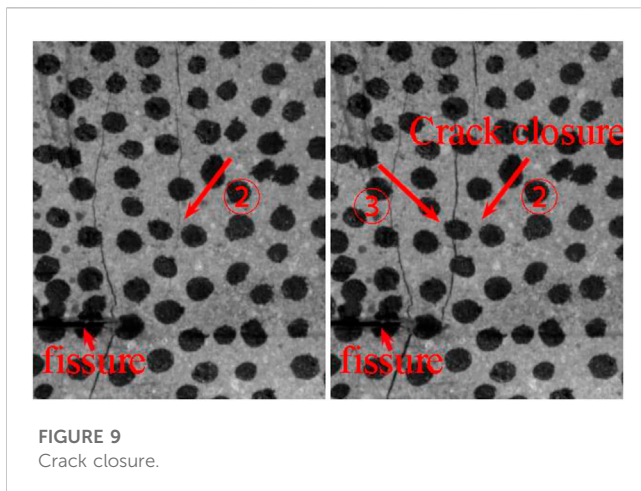
forming an obvious main failure crack composed of wing cracks and anti-wing cracks, as well as spalling off the falling block. As shown in Figures 8D, E failure diagram, ④ were still mainly wing cracks and anti-wing cracks. At this point, the stress dropped abruptly, damaging the rock sample.

By combining the cracks of each batch marked in the rock sample failure diagram with the stress-strain curve of the rock sample failure process, owing to small stress that does not reach the crack initiation levels in the compression-density stage. The cracks in batches ① and ② appear in the elastic stage as the stress increases. When the yield damage stage, the stage where most cracks are produced, is reached, the cracks expand rapidly to form ③, ④, ultimately reaching peak strength and destroying the rock sample. From the damage diagram of each rock sample, the ① and ② batches of cracks are identified as the far-field cracks near the end, as well as the wing cracks at the tip of the crack. The ③ and ④ batches are easily identified as: the new cracks expanding onto the path of ① and ②, the far-field cracks that further break the rock sample, the wing cracks at the tip of the fissure, and the tensile cracks in the middle of the fissure. However, batches ③ and ④ were not all formed by the deepening of the crack growth caused by batches ① and ②. With the increase in stress level, cracks generated by batches ① and ② continued to expand, and new cracks were simultaneously generated. The new crack expansion caused the crack closure phenomenon in the original ① and ② batches. As shown in Figure 9, the crack closure of batch ② was caused by the crack expansion of batch ③ in rock samples 0–7, but the closure of the crack did not affect the development of the main crack at the failure stage of the rock samples. The closed crack in the failure diagram of rock samples 0–7 eventually forms the main fracture crack. Meanwhile, the formation and development of the main cracks were not determined by the batch of cracks.

Besides illustrating the law of crack propagation with stress increase, the failure diagram can also reveal the failure characteristics of rock samples. Therefore, the failure diagram is used below to explore the failure characteristics of rock samples with the angle of fissure and the length of the rock bridge, as shown in Figure 10.

As can be seen from Figure 10, 1) with the influence of fissure angle on the damage characteristics of rock samples, and under

the same rock bridge length combined with an increase in fissure angle, i) the number of cracks trended towards being significantly reduced, and the number of main damage cracks changed from two to one, thus indicating that the damage mode of the specimen has changed from tension damage to shear damage; ii) surface spalling usually occurs where the crack manifests, which is a sign of large deformation and a large number of cracks. With an increase in the fissure angle, the number of surface spalling dropped blocks decreased, and the area of the falling blocks increased significantly. This is because under a high fissure angle, the number of cracks on the sample surface is small, and the block area formed between cracks or surrounded by the sample edge is large; thus, the area of the falling blocks is large. Figure 6 also shows that the number of cracks decreased and the failure mode changed from tensile failure to shear failure. Some rock samples exhibited severe failure, with rock blocks collapsing and spalling along the cracks. This phenomenon occurred mostly on both sides of the rock samples, which is a manifestation of the severe energy dissipation of the rock samples. iii) Whether the rock bridge is connected is shown as follows. First, three rock bridge connecting modes are defined, as shown in Table 2. When the fissure angle was low ($\alpha = 0°$ and $\alpha = 30°$), rock bridge penetration did not occur. When the fissure angle was high ($\alpha = 45°$, $60°$, and $90°$), rock bridge penetration occurred. 2) The influence of bridge length on the damage characteristics of rock samples: Under the same fissure angle, with the increase in rock bridge length, i) damage characteristics, such as a crack extension or spalling block on the surface of rock samples, are the same. ii) the longer the bridge, the more difficult it is to connect at the fissure dip angle. 3) From the point of view of the fine damage mechanism, i) at a low fissure angle ($\alpha = 0°$ or $30°$), the cracks produced on the surface of the rock sample are mainly tension cracks; there are few shear cracks. At a low fissure dip angle, a large shear stress cannot be formed locally, and the stress concentration at the fissure tip instead forms a local tension stress, which causes tension cracks and expands in the direction of maximum principal stress, extending from the tip to the end of the sample, and forming a "butterfly shape" failure of two main cracks on its surface; the failure mode is similar with the change of rock bridge length. ii) When $\alpha = 45°$ and $\alpha = 60°$, and the length of the rock bridge is relatively small, the rock bridge is connected, forming an elongated shear zone, increasing the proportion of shear damage of the specimen. The cracks generated on the surface are mixed shear and tension cracks, which manifest as a mixed tension-shear failure, causing the surface of the specimen to form a main rupture crack of "single-wing butterfly"-like damage. When $\alpha = 60°$, the shear stress was larger because this angle was closer to the fracture surface $45°+ \varphi/2$ (φ is the internal friction angle) of the sample. When $\alpha = 45°$, and $2b = 14$ mm, the rock bridge can be connected, which is consistent with the analysis results of the Mohr-Coulomb criterion. As rock bridge length increases, the bridge does not connect, and the proportion of tension cracks increases, ultimately creating a "butterfly" failure with two main cracks formed on the surface of the rock sample. iii) When $\alpha = 90°$, the cracks generated on the rock surface were mixed shear and tension cracks, and the specific gravity of the two was similar. Similarly, with an
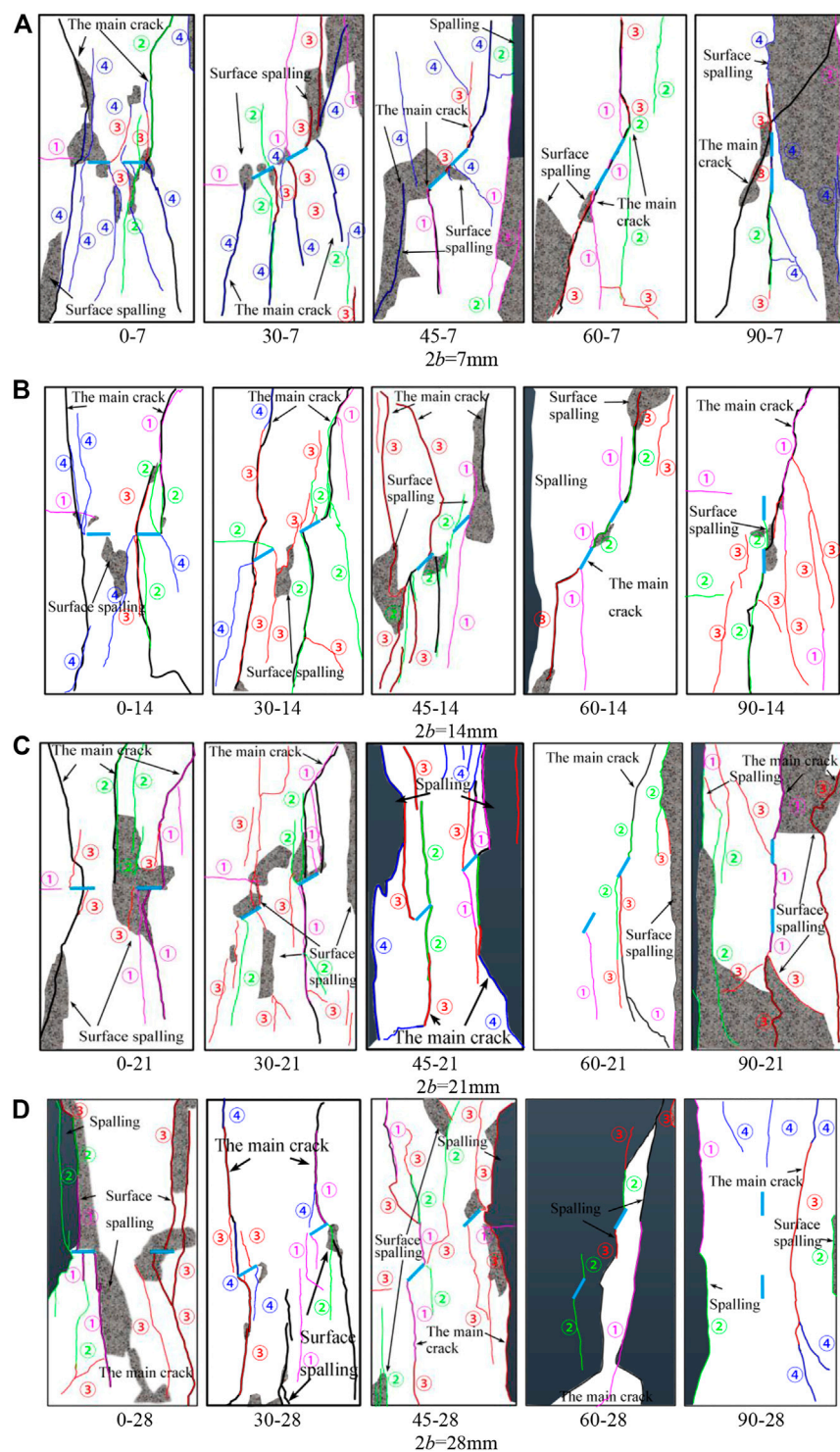
FIGURE 10
Crack propagation and failure diagram of various rock samples. **(A)** 2b = 7 mm; **(B)** 2b = 14 mm; **(C)** 2b = 21 mm; **(D)** 2b = 28 mm.

increase in the length of the rock bridge, the rock bridge does not connect, which shows a mixed failure of tension-shear, increased tensile failure and decreased shear failure. The failure characteristics and mechanism of each rock sample were analyzed and summarized in Table 3.

As can be seen from Table 3, the fissure angle and length of the rock bridge jointly affect the rock bridge connection and failure mode of the rock samples. The bridge connection occurred only at a high fissure angle. With an increase in the fissure angle, when the rock sample failed, the rock bridge between the two prefabricated

TABLE 2 Three kinds of rock bridges through modes of coplanar double-fissured sandstones.
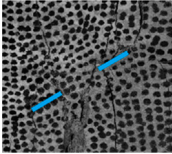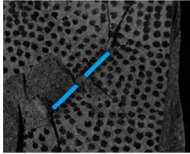
Mode	I	II	III
Description	No coalescence	Indirect coalescence	Direct coalescence
Pattern			
Image of coalescence			
Crack characterization	There are no cracks between the fissures to connect the rock bridge	The rock bridge is connected by a wing crack and an anti-wing crack	Shear cracks connect directly through the rock bridge

TABLE 3 Failure characteristics and mechanism of rock samples.

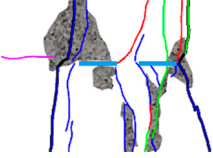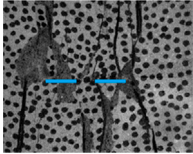| $\alpha/(°)$ / $2b$/mm	0	30	45	60	90
7	Rock bridge is not connected, mainly tensile failure	Rock bridge is not connected, mainly tensile failure	Rock bridge directly through	Rock bridge directly through	Rock bridge directly through
			Pull-shear mixed failure	Pull-shear mixed failure	Pull-shear mixed failure
14	Rock bridge is not connected, mainly tensile failure	Rock bridge is indirectly connected, with more tensile failure and less shear failure	The rock bridge is indirectly connected	Rock bridge directly through	Rock bridge directly through
			Pull-shear mixed failure	Pull-shear mixed failure	Pull-shear mixed failure
21	Rock bridge is not connected, mainly tensile failure	Rock bridge is indirectly connected, with more tensile failure and less shear failure	The rock bridge is not connected	The rock bridge is not connected	Rock bridge directly through
			More tension failure, less shear failure	Pull-shear mixed failure	Pull-shear mixed failure
28	Rock bridge is not connected, mainly tensile failure	Rock bridge is indirectly connected, with more tensile failure and less shear failure	The rock bridge is not connected	The rock bridge is not connected	The rock bridge is not connected
			More tension failure, less shear failure	Pull-shear mixed failure	More tension failure, less shear failure

fissures changed from disconnected to indirectly connected, and then directly connected, further indicating that the failure mechanism of the rock sample has changed from tension crack to tension-shear crack. The length of the rock bridge is directly proportional to the difficulty of connecting the rock bridge. As the length increases, the rock bridge between two prefabricated fissures becomes increasingly difficult to connect, especially when α = 45°, 60°, and 90°, and the rock bridge changes from directly connected to indirectly connected or completely disconnected. This change also indicates that the failure mechanism of the rock sample changes from tension-shear mixed cracks to tensile cracks. This observation is consistent with the mechanical properties of the rock samples.

The effect of the fissure angle on the mechanical properties of rock samples with double fissures is similar to that of single fissures, but there are differences in the crack growth and failure modes. When fissure lengths are the same, the two fissures indicate that the proportion of defects is larger. Furthermore, whether the rock bridge is connected or not changes the failure mode of the sample between tensile or shear. Conversely, this relationship between rock bridge connectivity and changing failure mode is not present for single-fissured rock samples.

3.3 Simplified analysis of force on coplanar double-fissured sandstone

A series of tests were carried out on coplanar double-fissured rock samples, and the data was collated and analyzed to obtain the

FIGURE 11
Double-clamped beam model.

FIGURE 12
Shear stress wear zone.
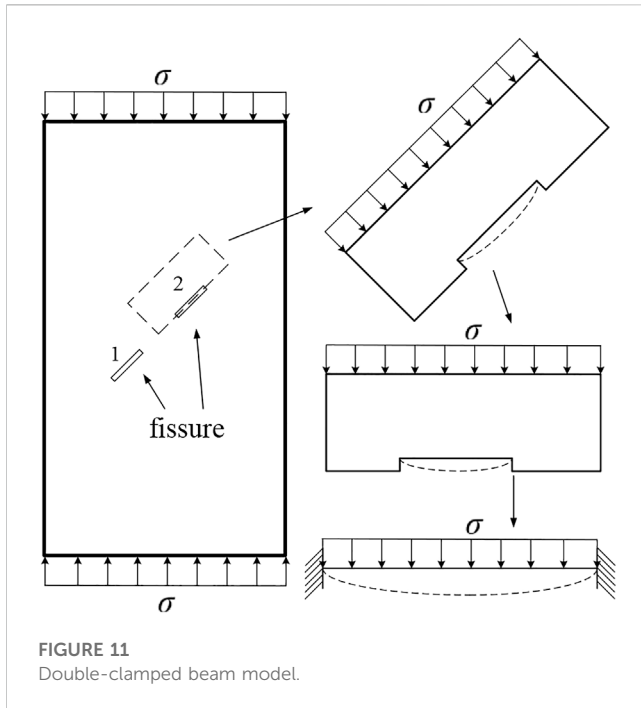
mechanical properties and failure laws of the coplanar double-fissured sandstone samples. The fracture behavior of the coplanar double-fissured rock sample was analyzed after the force was simplified (Xiao et al., 2022). As shown in Figure 11, the external force analysis diagram of the fissure sample indicates that the upper and lower ends of the rock sample are subject to a uniformly distributed load σ. In the rock sample, the fissure length is a and the angle is α; therefore, the fissure surface can be decomposed into normal stress σ_n and shear stress τ.

Thus, the normal stress σ_n shear stress τ on fissure surface 2 is:

$$\sigma_n = \sigma\cos^2\alpha + f_{12}\sigma\cos^2\alpha \tag{1}$$

$$\tau = \sigma\sin\alpha\cos\alpha\sigma_n + f_{12}\sigma\sin\alpha\cos\alpha\sigma_n \tag{2}$$

f_{12} is the fissure interaction coefficient (Chen, 1984; Xi et al., 2015), which is inversely proportional to rock bridge distance. The smaller the distance of the rock bridge, the larger the interaction coefficient.

When the fissure is pressed to closure, the effective shear force acting on the crack surface is (Horii and NematNasser., 1986; Li et al., 2007; Sun et al., 2018)

$$\tau_e = a(\tau - \mu\sigma_n) \tag{3}$$

Where μ is the friction coefficient of the fissured surface.

Substituting Eqs 1, 2 into Eq. 3 to obtain the effective shear force equation, see Eq. 4.

$$\tau_e = a\sigma(1 + f_{12})\left[(\sin\alpha\cos\alpha - \mu\cos^2\alpha)\right] \tag{4}$$

The normal stress on the fissured surface can be simplified into a double-clamped beam model (Zhang et al., 2018; Zeng et al., 2020; Sun et al., 2022), as shown in the figure for the analysis.

According to structural mechanics, the torque of the fixed end is:

$$M_1 = -\sigma a^2/12 \tag{5}$$

The torque at the center is:

$$M_2 = \sigma a^2/24 \tag{6}$$

The maximum deflection in the middle is:

$$\delta_{max} = \sigma a^4/384EI \tag{7}$$

The tensile stress at the middle of the section under the action of the bending moment is

$$\sigma_1 = \sigma a^2/4bh^2 \tag{8}$$

The tensile stress at both ends of the section under the action of the bending moment is

$$\sigma_2 = \sigma a^2/2bh^2 \tag{9}$$

Considering the influence of crack 1 on crack 2, the tensile stresses at both ends are:

$$\sigma_2 = (1 + f_{12})\sigma a^2/2bh^2 \tag{10}$$

When $\alpha = 0°$, there is no shear stress at the crack tip, and the fracture behavior can be explained by the double-clamped beam. For the four groups of rock samples with $\alpha = 0°$, as shown in Figure 6, cracks can easily appear at either the tip or middle of the fissure. When the double-clamped beam is subjected to a uniform vertical load, the mid-span experiences the greatest bending moment and deflection, causing cracks to form in the middle of the fissure. However, cracks in the $\alpha = 0°$ rock are mostly generated at the fissure tip, on the one hand, the tensile stress of the fissure tip is larger. In addition, the upper and lower crack surfaces first contact and produce closure when the crack is deformed, hindering the generation of tensile cracks in the middle of the crack. This is related to the crack opening

FIGURE 13
Force analysis diagram of fissure sample.

FIGURE 14
The relation between τ_e and α under different friction coefficients μ.

that provides the external conditions for rock bridge connection. The theoretical fracture angle of the pure type II crack model under uniaxial compression calculated in fracture mechanics is 70°32′, which is consistent with the experimental results. The first crack in the fissure tip of the rock sample was the wing crack, and the crack that continued to expand was tensile, resulting in local volume expansion. However, shear failure occurred during the late loading stage, caused by a large shear plane that formed when the fissure tip had a sufficiently large shear force and the middle material of the two cracks was small enough to be connected by the shear force. The tensile and shear failures of the rock samples were ultimately determined by the different shear forces of the fissure tips. When the crack angle increased from $\alpha = 0°$, incidences of failure caused by normal stress decreased, changed into shear failure caused by shear force.

When $\alpha = 90°$, it can be seen from the above model that when the effective shear force is $\tau_e = 0$, the fissure tip does not produce shear, shear slide does not occur, and the model cannot be simplified into the double-clamped beam force model. The deformation and failure of the mechanical parameters of the rock sample were similar to those of the intact rock sample; $\alpha = 90°$ had the least influence on rock samples.

4 Conclusion

(1) The peak stress and elastic modulus increased when the fissure angle increased. With an increase in the rock bridge length, the change in the peak stress of the rock sample is smaller, the elastic modulus shows a trend of decreasing and then increasing, with a small variation range. The influence of bridge length on rock samples was weaker than that of the fissure angles' influence.

(2) Rock sample damage characteristics are as follows: under the same bridge length, the number of cracks tends to decrease significantly with an increase in the fissure angle, and the main damage crack changes from two to one; the number of surface spalling blocks decreases and the area of spalling blocks

degree. In this test, the thickness of the cracks is 0.5 mm thick. If the thickness of the cracks is increased, the deflection deformation of the fissure surface will induce cracks in the middle of the crack to increase (Zeng et al., 2020).

When $\alpha = 30°$, 45°, and 60°, shear stress exists between the cracks. The shear slide along the shear plane of the generated shear crack occurs during the loading process, as shown in Figure 12. The white wear zone caused by the shear slide is also shown.

According to the force analysis diagram in Figure 13, after the fissure is pressed to close, the shear force generated is composed of the shear stress and the friction formed by the normal stress on the fissure surface. When the crack is not pressed to closure, there is only shear stress and no friction, which can be regarded as $\mu = 0$. During the experiment, the internal friction coefficient of the rock sample was $\mu = 0.42$, and the friction coefficient fluctuated slightly owing to the different degrees of fracture. However, the friction coefficient cannot affect the relationship between fissure angle α and effective shear force τ_e, as shown in Figure 14. In this case, $f_{12} = 0.3$ is taken. The figure clearly shows that the effective shear force τ_e is the maximum when $\alpha = 45°$ and 60°, which occurs when there is no friction force in the early loading stage and when there is a friction force after the fissure is closed since

increases; the bridge connection occurs only at a high fissure dip angle; Under the same fissure angle, with the increase of the length of rock bridge, the surface crack propagation and spalling block failure characteristics are basically the same. The difficulty of the rock bridge to connect at the fissure angle increases as the length of the bridge itself increases. (3) The damage mechanism primarily manifests as follows: at a low fissure angle, tensile damage cracks are dominant, and shear damage cracks are rare. With an increase in the fissure angle, the damage mode changes from tensile damage cracks to shear damage cracks to form a mixed tensile-shear damage mode. With an increase in the rock bridge length, the bridge changes from a direct connection to either an indirect connection or no connection. Simultaneously, the damage mechanism of the rock sample changes from mixed tensile-shear cracks to increased tensile cracks.

(4) Based on a simplified analysis of the force on the coplanar double-fissured rock sample, the failure behavior of the rock sample was affected by the normal stress double-clamped beam model and shear stress. The rock sample was dominated by tensile failure, and the proportion of shear failure increased as the fissure angle also increased.

Data availability statement

The datasets presented in this study can be found in online repositories. The names of the repository/repositories and accession number(s) can be found in the article/Supplementary Material.

Author contributions

Conceptualization: DZ and TX; methodology: DZ and TX; software: DZ and TX; formal analysis: DZ and HS; data curation: DZ, TX, and HS; writing—original draft preparation: DZ and TX; writing—review and editing: DZ and TX; supervision: TX; project administration: TX and HS; funding acquisition: TX. All authors have read and agreed to the published version of the manuscript.

Funding

Conflict of interest

The authors declare that the research was conducted in the absence of any commercial or financial relationships that could be construed as a potential conflict of interest.

Publisher's note

All claims expressed in this article are solely those of the authors and do not necessarily represent those of their affiliated organizations, or those of the publisher, the editors and the reviewers. Any product that may be evaluated in this article, or claim that may be made by its manufacturer, is not guaranteed or endorsed by the publisher.

References

Bobet, A. (2000). The initiation of secondary cracks in compression. *Eng. Fract. Mech.* 66 (2), 187–219. doi:10.1016/s0013-7944(00)00009-6

Cao, P., Liu, T., Pu, C., and Lin, H. (2015). Crack propagation and coalescence of brittle rock-like specimens with pre-existing cracks in compression. *Eng. Geol.* 187, 113–121. doi:10.1016/j.enggeo.2014.12.010

Cao, P., Liu, T., Pu, C., and Lin, H. (2015). Crack propagation and coalescence of brittle rock-like specimens with pre-existing cracks in compression. *Eng. Geol.* 187, 113–121. doi:10.1016/j.enggeo.2014.12.010

Chen, M., Jing, H., Ma, X., and Zhu, T. (2017). Fracture evolution characteristics of sandstone containing double fissures and a single circular hole under uniaxial compression. *Int. J. Min. Sci. Technol.* 27 (3), 499–505. doi:10.1016/j.ijmst.2017.03.027

Chen, Y. (1984). *Multiple crack problems in an infinite plate.* Journal of Northwestern Polytechnical University, (04) 367–379.

Gong, C-G., Wang, W., Shao, J-F., Wang, R-B., and Feng, X-W. (2020). *Effect of water chemical corrosion on mechanical properties and failure modes of pre-fissured sandstone under uniaxial compression.* New York, NY: Acta Geotechnic. doi:10.1007/s11440-020-01071-y

He, M., Sui, Q., Li, M., Wang, Z., and Tao, Z. (2022). Compensation excavation method control for large deformation disaster of mountain soft rock tunnel. *Int. J. Min. Sci. Technol.* 32 (5), 951–963. doi:10.1016/J.IJMST.2022.08.004

Hoek, E., and Martin, C. D. (2014). Fracture initiation and propagation in intact rock–a review. *J. Rock Mech. Geotechnical Eng.* 6 (4), 287–300. doi:10.1016/j.jrmge.2014.06.001

Horii, H., and NematNasser, S. (1986). *Brittle failure in compression: Splitting, faulting and brittle-ductile transition.* London, United Kingdom: Philosophical Transactions of the Royal Society of London. Series A, Mathematical and Physical Sciences. doi:10.1098/rsta.1986.0101

Janeiro, R. P., and Einstein, H. H. (2010). Experimental study of the cracking behavior of specimens containing inclusions (under uniaxial compression). *Int. J. Fract.* 164, 83, 102. doi:10.1007/s10704-010-9457-x

Jin, J., Cao, P., Chen, Y., Pu, C., Mao, D., and Fan, X. (2017). Influence of single flaw on the failure process and energy mechanics of rock-like material. *Comput. Geotechnics* 86, 150–162. doi:10.1016/j.compgeo.2017.01.011

Lajtai, E. Z., Carter, B. J., and Ayari, M. L. (1990). Criteria for brittle fracture in compression. *Eng. Fract. Mech.* 37 (1), 59–74.

Lajtai, E. Z. (1969).Shear strength of weakness planes in rock. In *Int. J. Rock Mech. Min. Sci. Geomechanics Abstr.* 6. Pergamon, 499–515.

Li, Y., Wu, Y., and Yang, C. (2007). Comparison of sliding crack models for rock-like materials. *Chin. J. Rock Mech. Eng.* (02), 278–284. CNKI:SUN:YSLX.0.2007-02-007.

Liang, Xin, Tang, Shibin, Tang, Chun'an, Hu, Lihua, and Chen, Feng (2022). Influence of water on the mechanical properties and failure behaviors of sandstone under triaxial compression. *Rock Mech. Rock Eng.* 56 (2), 1131–1162. doi:10.1007/S00603-022-03121-1

Liang, Z. Z., Xing, H., Wang, S. Y., Williams, D. J., and Tang, C. A. (2012). A three-dimensional numerical investigation of the fracture of rock specimens containing a pre-existing surface flaw. *Comput. Geotechnics* 45, 19–33. doi:10.1016/j.compgeo.2012.04.011

Park, C. H., and Bobet, A. (2009). Crack coalescence in specimens with open and closed flaws: A comparison. *Int. J. Rock Mech. Min. Sci.* 5, 819–829. doi:10.1016/j.ijrmms.2009.02.006

Park, C. H., and Bobet, A. (2010). Crack initiation, propagation and coalescence from frictional flaws in uniaxial compression. *Eng. Fract. Mech.* 77 (14), 2727–2748. doi:10.1016/j.engfracmech.2010.06.027

Prudencio, M., and Van Sint Jan, M. (2007). Strength and failure modes of rock mass models with non-persistent joints. *Int. J. Rock Mech. Min. Sci.* 44 (6), 890–902. doi:10.1016/j.ijrmms.2007.01.005

Pu, C. Z., Cao, P., Zhao Y., L., Zhang, X. Y., Yi Y., L., and Liu Y., K. (2010). Numerical analysis and strength experiment of rock-like materials with multi-fissures under uniaxial compression. *Rock Soil Mech.* (11), 3661–3666. doi:10.16285/j.rsm.2010.11.038

Ren, F. Q., Zhu, C., He, M. C., Shang, J. L., Feng, G. L., and Bai, J. W. (2023). Characteristics and precursor of static and dynamic triggered rockburst: Insight from multifractal. *Rock Mech. Rock Eng.* 56, 1945–1967. doi:10.1007/s00603-022-03173-3

Sun, B., Zou, C., Zeng, S., Fang, Y., and Wang, F. (2018). Failure characteristics of rock-like mass with different fracture types under uniaxial compression. *J. Disaster Prev. Mitig. Eng.* (06), 959–966. doi:10.13409/j.cnki.jdpme.2018.06.009

Sun, B., Zou, C. H., Zhen, S., Fang, Y. C., and Wang, F. L. (2018). Failure characteristics of rock-like mass with different fracture types under uniaxial compression . *J. Disaster Prev. Mitig. Eng.* 38(6), 959–966. doi:10.13409/j.cnki.jdpme.2018.06.009

Sun, H., Chen, S., Jin, A., and Zhu, D. (2022). Uniaxial compressive strength characteristics and crack evolution laws of rock-like samples with flaws. *J. Northeast. Univ. Sci.* (03), 404–413. CNKI:SUN:DBDX.0.2022-03-014.

Tang, Shibin, Li, Jiaming., Ding, Shun, and Zhang, Leitao (2022). The influence of water-stress loading sequences on the creep behavior of granite. *Bull. Eng. Geol. Environ.* 81, 482. doi:10.1007/s10064-022-02987-3

Wang, F., Cao, P., Cao, R. H., Gao, Q. P., Xiong, X. G., and Wang, Z. (2018)Influence of parallel joint interaction on mechanical behavior of jointed rock mass . *J. Central South Univ. Technol.* 49(10):2498–2507.

Wang, Min, Wen, Wan, and Zhao, Yanlin (2020). Experimental study on crack propagation and the coalescence of rock-like materials with two preexisting fissures under biaxial compression. *Bull. Eng. Geol. Environ.* 79, 3121–3144. doi:10.1007/s10064-020-01759-1

Wang, Q., Xu, S., Xin, Z., He, M., Huayong, W., and Jiang, B. (2022). Mechanical properties and field application of constant resistance energy-absorbing anchor cable. *Tunn. Undergr. Space Technol. incorporating Trenchless Technol. Res.* doi:10.1016/J.TUST.2022.104526

Wang, Y., Tang, J., Dai, Z., and Yi, T. (2018). Experimental study on mechanical properties and failure modes of low-strength rock samples containing different fissures under uniaxial compression. *Eng. Fract. Mech.* 197, 1–20. doi:10.1016/j.engfracmech.2018.04.044

Wasantha, P. L. P., Ranjith, P. G., Viete, D. R., and Luo, L. (2012). Influence of the geometry of partially-spanning joints on the uniaxial compressive strength of rock. *Int. J. Rock Mech. Min. Sci.* 50, 140–146. doi:10.1016/j.ijrmms.2012.01.006

Wong, L. N. Y., and Einstein, H. H. (2008). Systematic evaluation of cracking behavior in specimens containing single flaws under uniaxial compression. *Int. J. Rock Mech. Min. Sci.* 46 (2), 239–249. doi:10.1016/j.ijrmms.2008.03.006

Wong, L. N. Y., and Einstein, H. H. (2009). Systematic evaluation of cracking behavior in specimens containing single flaws under uniaxial compression. *Int. J. Rock Mech. Min. Sci.* 46 (2), 239–249. doi:10.1016/j.ijrmms.2008.03.006

XI, J., Zhong-hui, C., Zhu, D., and Chen, Q. (2015). Stress intensity factors and initiation of unequal collinear cracks in rock. *Chin. J. Geotechnical Eng.* (04), 727–733.

Xiao, T. L., Li, X. P., and Guo, Y. H. (2012). Experimental study of failure characteristic of single jointed rock mass under triaxial compression tests. *Rock Soil Mech.* 33 (11), 3251–3256. doi:10.16285/j.rsm.2012.11.008

Xiao, T. L., Li, X. P., and Jia, S. P. (2015). Failure characteristics of rock with two pre-existing transfixion cracks under triaxial compression. *Chin. J. Rock Mech. Eng.* (12), 2455–2462. doi:10.13722/j.cnki.jrme.2014.1443

Xiao, Y., Qiao, Y., He, M., Li, H., Cheng, T., and Tang, J. (2022). A unified strain-hardening and strain-softening elastoplastic constitutive model for intact rocks. *Comput. Geotechnics* 148, 104772. doi:10.1016/J.COMPGEO.2022.104772

Xu, T., Ranjith, P. G., Wasantha, P. L. P., Zhao, J., Tang, C., and Zhu, W. C. (2013). Influence of the geometry of partially-spanning joints on mechanical properties of rock in uniaxial compression. *Eng. Geol.* 167, 134–147. doi:10.1016/j.enggeo.2013.10.011

Yang, S-Q., Huang, Y-H., Tian, W-L., and Zhu, J-B. (2017). An experimental investigation on strength, deformation and crack evolution behavior of sandstone containing two oval flaws under uniaxial compression. *Eng. Geol.* 217, 35–48. doi:10.1016/j.enggeo.2016.12.004

Yang, S. Q. (2011). Crack coalescence behavior of brittle sandstone samples containing two coplanar fissures in the process of deformation failure. *Eng. Fract. Mech.* 78 (17), 3059–3081. doi:10.1016/j.engfracmech.2011.09.002

Yang, S. Q., Dong, J. P., Yang, J., Yang, Z., and Huang, Y. H. (2022). An experimental investigation of failure mechanical behavior in cylindrical granite specimens containing two non-coplanar open fissures under different confining pressures. *J. Central South Univ.* 29 (5), 1578–1596. doi:10.1007/s11771-022-5035-4

Yang, S. Q., and Jing, H. W. (2011). Strength failure and crack coalescence behavior of brittle sandstone samples containing a single fissure under uniaxial compression. *Int. J. Fract.* 168 (2), 227–250. doi:10.1007/s10704-010-9576-4

Yang, S. Q., and Jing, H. W. (2011). Strength failure and crack coalescence behavior of brittle sandstone samples containing a single fissure under uniaxial compression. *Int. J. Fract.* 168 (2), 227–250. doi:10.1007/s10704-010-9576-4

Yang, S. Q., Liu, X. R., and Jing, H. W. (2013). Experimental investigation on fracture coalescence behavior of red sandstone containing two unparallel fissures under uniaxial compression. *Int. J. Rock Mech. Min. Sci.* 63, 82–92. doi:10.1016/j.ijrmms.2013.06.008

Yin, P., Wong, R. H. C., and Chau, K. T. (2014). Coalescence of two parallel pre-existing surface cracks in granite. *Int. J. Rock Mech. Min. Sci.* 68, 66–84. doi:10.1016/j.ijrmms.2014.02.011

Zeng, J-j., Zhang, Z-j., Zhang, X-x., and Pu, C-z. (2020). Fracture test and analysis of horizontal fissure rock-like specimens influenced by apertures. *Chin. J. Geotechnical Eng.* (03), 523–532. doi:10.11779/CJGE202003014

Zhang, K., Liu, X., Kun, L. I., and Wu, W. (2018). Investigation on the correlation between mechanical characteristics and fracturing fractal dimension of rocks containing a hole and multi-flaws. *Chin. J. Rock Mech. Eng.* (12), 2785–2794. doi:10.13722/j.cnki.jrme.2018.0894

Zhang, P., Li, N., and He, R. L. (2006). Mechanism of fracture coalescence between two pre-existing flaws under dynamic loading. *Chin. J. Rock Mech. Eng.* 25(6): 1210–1217.

Zhang, P., Li, N., He, R. L., and Xu, J, G. (2006). Mechanical properties of fractured media containing intermittent fractures at different strain rates. *Chin. J. Geotechnical Eng.* 06, 750–755. CNKI:SUN:YTGC.0.2006-06-014.

Zhang, Y., Jiang, Y., Asahina, D., and Wang, C. (2020). *Experimental and numerical investigation on shear failure behavior of rock-like samples containing multiple non-persistent joints*. Wien, Austria: Rock Mechanics and Rock Engineering. doi:10.1007/s00603-020-02186-0

Zhao, Y, L., Wan, W., Wang, W. J., Wang, M., and Peng, Q, Y. (2013). Fracture experiments on ordered multi-crack body in rock-like materials under uniaxial compression and numerical simulation of wing cracks. *Chin. J. Geotechnical Eng.* 11, 2097–2109. CNKI:SUN:YTGC.0.2013-11-024.

Experimental study on the shear failure of layered rock bridges

Jianxin Yu[1,2]*, Zhibin Zhou[1], Huanchun Liu[2]*, Lianhao Zhou[1], Zhenzhen Li[1] and Long Cheng[1,3]

[1]International Joint Research Laboratory of Henan Province for Underground Space Development and Disaster Prevention, Henan Polytechnic University, Jiaozuo, Henan, China, [2]College of Safety Science and Engineering, Henan Polytechnic University, Jiaozuo, Henan, China, [3]School of Civil Engineering, Luoyang Institute of Science and Technology, Luoyang, Henan, China

The structural face of rock plays a decisive role in the stability of geotechnical engineering, and the mechanism of failure destabilization of layered rock masses is still unclear. By preparing rock-like materials, shear failure tests on layered rock masses were carried out under different bedding dip angles, different rock bridge width, different normal forces, and forward and reverse shear effects. With the increase in the rock bridge width, the influence of the joint inclination angle on the shear failure process of the rock sample decreases; the peak shear strength of the specimen is the largest when the joint inclination angle is 60°, followed by 90°, 30° and 0° from large to small; the failure mode in forward shear is mainly tensile failure, and the failure mode in reversed shear is mainly shear failure; the peak number of acoustic emission events is proportional to the joint inclination angle and the rock bridge width of the specimen, and the number of acoustic emission events is proportional to the joint inclination angle and the rock bridge width of the specimen. The number of acoustic emission peak events is proportional to the bedding angle of the sample and the width of the rock bridge. The peak number of acoustic emission events in the reverse shear of the layered rock mass is greater than that in the forward shear. The angle of the lamina and the width of the rock bridge are both important factors affecting the strength of the rock. The results of this study provide a basis for identifying the shear failure mechanism of rock bridge in layered rock masses.

KEYWORDS

geotechnical engineering, layered rock, shear failure, rock bridge width, failure mechanism

1 Introduction

The angle of laminations and the extension of fractures in rock masses have always been a hot spot and focus of research in geotechnical stability analysis, and rock bridge penetration often becomes a key factor in rock slides (Sun et al., 2020). The failure of layered rock masses is determined by the physical and mechanical properties of the structural body and the structural face, and research focuses mainly on the strength of the structural face and the destabilization of the failure regularity (Zhu and Zeng, 2005). The strength of a jointed rock mass is between the strength of the rock material itself and the strength of the joint surface, and its failure mechanism and failure mode are very complicated (Liu et al., 2019).

Many scholars have analyzed the stability of slopes by studying empirical expressions for the shear strength and joint inclination of layered rock masses under different normal force conditions and relating them to the geometrical mechanics of the layered rock masses themselves to invert the effect of the joint inclination of layered rock masses on some

mechanical parameters, such as the shear and compressive strength of the rock masses (Zhang and Liu., 2001; Liu and Zhang, 2002; Ran et al., 2016). Researchers at home and abroad have studied the effect of bedding direction on the strength and failure mode of layered rock masses through Brazilian splitting tests (Debecker and Vervoort, 2009; Tavallali and Vervoort, 2010a; Cho et al., 2012; Vervoort et al., 2014; Tan et al., 2015). Xia et al. (2020) concluded from extensive simulations that the shear strength of the rock mass is lowest when the laminae dip at 0° and highest at 30°. Tavallali and Vervoort (2010b) concluded from their study that the tensile strength of laminated sandstone increases with increasing quartz grains. Song et al. (2020) combined indoor tests and numerical simulations to conclude that variations in the dip angle of the rock joints lead to different forms of failure in through-jointed rock masses. Heng et al. (2019) obtained from direct shear tests that when laminated shale laminae were sheared at 30° and 60° angles, a wild goose column of fractures along the laminae was formed. Wang et al. (2017) analyzed the fracture pattern around the shear surface of jarosite with different laminae orientations and observed different degrees of laminae cracking and wild goose column fractures, which showed obvious laminae orientation effects. Li et al. (2019) found that the sample can be divided into four failure modes: tensile failure, shear failure, mixed failure, and shear failure. Liang et al. (2023) obtained through experiments that the increase of confining pressure will promote the development of shear cracks. Bao et al. (2023) obtained by numerical simulation that the sliding failure of layered rock mass is layered. Wang et al. (2022) found that CREAC showed advantages in impact deformation and energy absorption.

Rock bridges also play a very important role in the stability of the rock mass. Zhang et al. (2015) concluded that as the rock bridge becomes narrower and wider, the failure mode of the rock mass transforms from shear failure to extensive shear failure. Zhang et al. (2018) and Qin et al. (2019) showed that the direct shear failure of rock bridges exhibited three failure modes: tension failure, tension-shear failure and shear failure. Lajtai (1969) classified the failure of rock bridges into tension, shear and extrusion failure according to the magnitude of normal stress. It was concluded from the tests that the shear resistance of the shear failure surface composed of the structural surface and the rock bridge showed a good linear growth relationship, the breakage of the rock bridge originated from the tip of the joints, and the failure process was characterized by obvious stages (Savilabti et al., 1990; Shen et al., 1999; Zhao et al., 2014). Zhu et al. (2020) verified the formation of stress concentration and tensile stress zones at the joint ends from the perspective of flow fields. Gehle and Kutter (2003) carried out large deformation direct shear tests and concluded that the mechanisms that govern the different shear phases could be identified as 1) tensile rupturing. 2) rolling and sliding friction of dilatant joint zones and 3) sliding within the joint filling composed of brecciated material. Zhang et al. (2005) found that the propagation of wing cracks depends on the joint separation and the joint azimuth angle, and the connection of wing cracks dominates the eventual failure pattern and determines the peak shear load of the rock specimens. Yuan (2020) used numerical simulation to derive that there are three types of rock bridge failure in the locked section: tension through failure, tension shear through failure, and no through failure. Qi et al. (2021) concluded that when the shear displacement of the rock bridge reached 2.0–3.9 mm, the specimen started to generate a large number of acoustic emission events with the rapid growth of shear stress. Chen et al. (2017) concluded from indoor direct shear tests that, with the variation of normal stress and

connectivity, the failured surface of the rock body showed "—", "X", "sawtooth", "Z" and composite type "Z" and composite failure forms.

In summary, domestic and foreign researchers have conducted a lot of research on the shear failure mechanism of layered rock mass and rock bridge, and have achieved guiding research results. However, there are few studies on the shear failure of rock under the condition of multiple factors. In this paper, by making layered rock mass samples and conducting direct shear tests, the effects of different bedding angles, different normal forces, different rock bridge widths and forward and reverse shear factors on the shear effect are systematically studied. At the same time, the energy release process in the shear process of the sample is reflected by the acoustic emission device during the experiment, which provides a theoretical basis for further understanding the propagation and evolution mechanism of rock shear failure cracks under the condition of multiple factors.

2 Test scheme

2.1 Specimen preparation

The test rock was prepared as similarly as possible to the natural rock, using a high-strength cement mortar with cement: fine sand: water = 1:1:0.35. The uniaxial compressive strength and uniaxial tensile strength of the sample are 64.31 MPa and 3.62 MPa, respectively, and the elastic modulus is 6.00 GPa. The mold used for the test was a modified mold with a special angled steel plate in the middle of the ordinary mold to create different lamellar angles when pouring, with a mold size of 100 mm × 100 mm × 100 mm, as shown in Figure 1.

The cement and sand were weighed in proportion, put into a mixer, and mixed well. Then, water was slowly added to make it well mixed, and the mixed mortar was poured into the mold. The test is poured in layers, half of which is poured first, vibrated, and compacted. Then, after two and a half hours, the other half is poured, after which the steel plate is withdrawn, vibrated, and compacted, and the surface is smoothed. The cast specimens were placed in the maintenance room and demolded after 24 h. The demolded specimens were maintained for 28 days, and finally, the maintained specimens were taken to the fabrication plant for seam cutting.

2.2 Test program

The test equipment used is the KYZW-100 Rock Weak Face Straight Shear Instrument manufactured by Jinan Mining and Rock Testing Instruments Co. The DS-2 acoustic emission instrument was used to monitor the crack expansion within the specimen and to reflect the stability of the material deformation or rupture. To observe the crack extension of the specimen more visually, a camera was used to take pictures of the whole process of specimen failure during the test, and the test equipment is shown in Figure 2.

2.3 Test program

Considering the four conditions of bedding inclination, normal force, rock bridge width and positive and negative shear, 23 specimens were made, and the bedding inclination was

FIGURE 1
Mold of the sample.
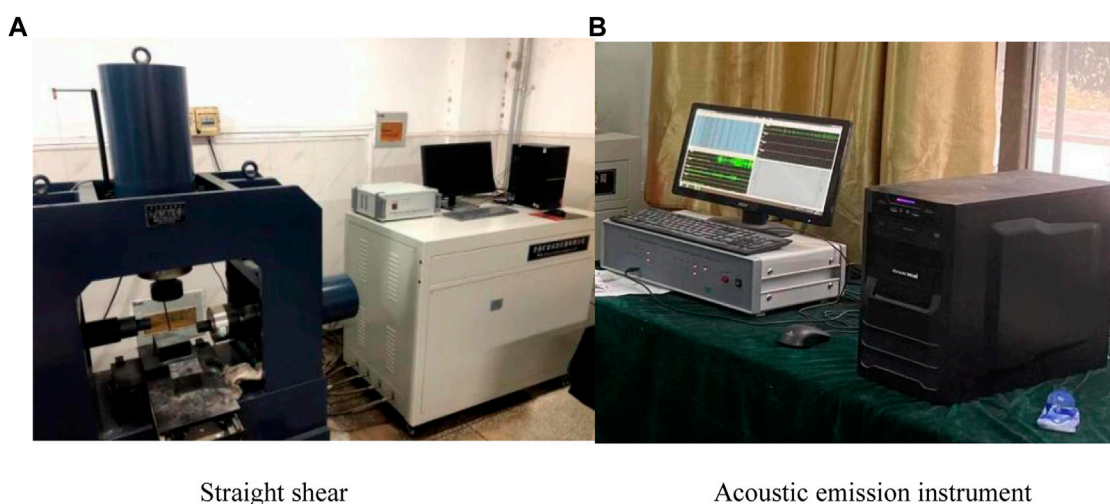
FIGURE 2
Test equipments. **(A)** Straight shear. **(B)** Acoustic emission instrument.

divided into four groups: 0°, 30°, 60° and 90°, where the width of the rock bridge at 0°, 30° and 90° was 80 mm, the positive and negative shear tests were carried out at 30°, and the width of the rock bridge at 60° was 60 mm, 70 mm, 80 mm and 90 mm. Four normal forces of 10 kN, 20 kN, 30 kN and 40 kN were applied for the shear tests, and the specific test protocols are listed in Table 1.

2.4 Test procedure

1) Before the specimen is tested in shear, the acoustic emission probe is arranged on the surface of the specimen to prevent the acoustic emission probe from falling off during the test, and the probe and the specimen are taped together with adhesive tape. To achieve better test results, two acoustic emission probes were used during the test, one on each side of the shear surface, numbered 1 and 2, and the acoustic emission probes were arranged as shown in Figure 3.

2) Place the specimen arranged for acoustic emission on the shear apparatus, first load the normal force at a rate of 2 kN/s to the design value and stabilize it, then apply the shear force at a rate of 0.004 mm/s, turn on the acoustic emission apparatus at the same time and collect data from both apparatuses simultaneously until the specimen is damaged and the data are stabilized to end the test.

Normal stress during shear failure of a specimen and shear stress can be expressed as

$$\sigma = \frac{P}{A}, \tau = \frac{T}{A} \tag{1}$$

Where P denotes the normal phase pressure to which the specimen is subjected during the straight shear test. T denotes the shear force to which the specimen is subjected during the straight shear test. A denotes the effective shear area of the specimen.

TABLE 1 Test scheme.

Number of samples	Bedding angle/°	Positive pressure/kN	Crack length/mm
0–10	0	10	20
0–20		20	
0–30		30	
0–40		40	
30–10	30	10	20
30–20		20	
30–30		30	
30–40		40	
30–10-r		10	
30–20-r		20	
30–30-r		30	
30–40-r		40	
60–10	60	10	20
60–20		20	
60–30		30	
60–40		40	
60–20-d1		20	10
60–20-d3			30
60–20-d4			40
90–10	90	10	20
90–20		20	
90–30		30	
90–40		40	

Note: No. 0–10 represents bedding inclination of 0°, positive pressure 10 kN forward shear; 30–10-r represents bedding angle 30, positive pressure 10 kN reverse shear; 60–20-d1 represents bedding angle 60, positive pressure 20 kN, fracture length 10 mm forward shear.

3 Test results
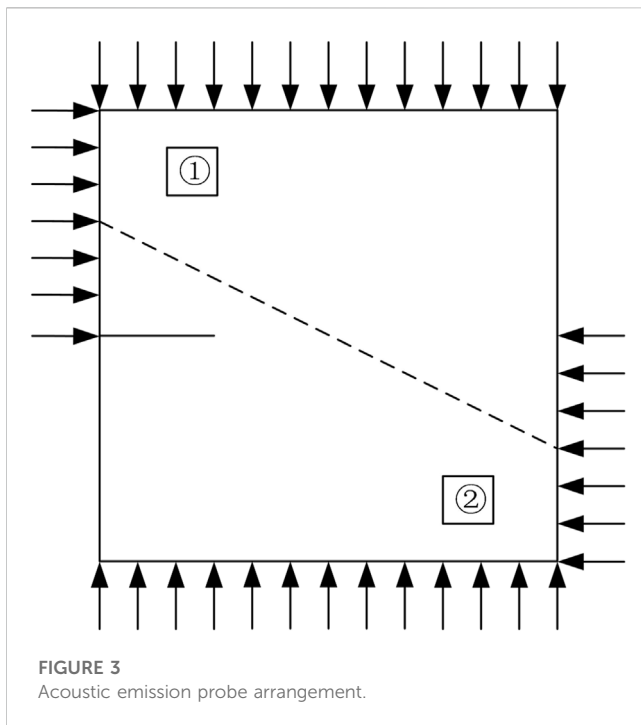
3.1 Shear displacement-shear stress analysis under different normal force conditions

To investigate the effect of normal force on the shear failure of layered rock bridges, the shear failure process of four bedding dip specimens with the same rock bridge width (80 mm) and different normal forces was analyzed, and the variation in shear stress and shear displacement is shown in Figure 4, where the failure pattern of 30° bedding dip specimens is shown in Figure 5.

From Figure 4, it can be seen that the specimen shear failure has obvious brittle characteristics, and the trends of the shear stress and shear displacement curve characteristics under different normal force conditions are basically the same. In the initial stage of loading, the shear displacement increases relatively quickly, and the shear stress increases relatively slowly. With increasing shear force, the shear stress increases rapidly, and the shear displacement increases slowly. When the shear stress increases to the maximum value, the specimen is sheared off, and the curve will appear to fall off a cliff and finally tend to stabilize. The peak shear strength of the specimen increases with the increase in normal force.

It can be seen from Figure 5 that when the normal force is 10 kN, tiny tensile cracks are produced in the specimen initially, the main crack is produced by the tip of the joint, and the crack extends and penetrates along the rock bridge (Figure 4A). When the normal force increases to 20 kN, the specimen is subjected to tensile stresses during shear, and tensile cracks appear in the specimen. With the increase in shear displacement, the tensile cracks expand, and eventually, the specimen is failured (Figure 4B). When the normal force exceeds 20 kN, before shear is applied, the specimen has already produced compression tensile cracks because of the normal force. The tensile cracks mainly appear at the weak corner at the bottom of the specimen, accompanied by the application of shear. The shear cracks are also produced by the tip of the joint and shear the rock bridge off (Figures 4C,D). As the normal force increases, the shear failure of the layered rock bridge goes through three stages: shear failure, shear-tension failure, and

FIGURE 3
Acoustic emission probe arrangement.

compression-shear failure. This is different from the literature (Lajtai, 1969), because the existence of the bedding plane has an effect on the shear failure of the sample, which is different from the shear failure of the ordinary rock bridge.

3.2 Shear displacement-shear stress analysis under different bedding dip angles

To study the effect of the joint inclination angle on the shear failure of layered rock bridges, the same rock bridge width (80 mm) was used to analyze the shear failure process under four normal forces and different joint inclination angles. The variation law of shear stress and shear displacement is shown in Figure 6, and the shear failure pattern of the specimen with a normal force of 20 kN is shown in Figure 7.

As shown in Figure 6, the overall characteristics of the shear stress and shear displacement curves under different bedding dip angles are basically the same as those under different normal force conditions. The maximum shear strength of the rock sample is the shear strength of the lamina surface when the joint inclination angle is 0°, and the lamina surface has the least effect on the shear failure of the specimen when the joint inclination angle is 90°, so the maximum shear strength is the shear strength of the specimen material itself. The peak shear strength of the specimen at 60° of bedding inclination is the greatest and is greater than the maximum shear strength of the rock sample, which is consistent with the conclusions obtained in the literature (Heng et al., 2014) using laminated shale shear. With the exception of the 60° case, the peak shear strengths were, in descending order, 90°, 30°, and 0°.

As shown in Figure 7, at a normal force of 20 kN, the shear cracks for specimens with different bedding dip angles all arise and

extend from the tip of the joints, and the shear failure surface for specimens with a bedding dip angle of 0° arises along the bedding face, forming a through shear failure surface. For specimens with a bedding dip angle of 30°, the shear failure cracks arise from the joints and extend along the rock bridge, and when the cracks extend to the bedding face, they then form shear failure along the bedding face. In specimens with a joint inclination of 60°, the main shear failure crack forms a through crack along the shear face bridge and forms a tiny crack in the lamina face. This mode of failure is one of the reasons for the maximum shear strength of this lamina face. In specimens with a joint inclination of 90°, the main shear failure crack forms a through crack along the shear face bridge perpendicular to the lamina face.

3.3 Analysis of forward shear *versus* reverse shear

The specimens were subjected to forward and reverse shear tests at a specimen rock bridge width of 80 mm and a joint inclination angle of 30°. The variation pattern of shear stress and shear displacement is shown in Figure 8.

Figure 8 shows that the peak shear strength of forward shear is greater than the peak shear strength of reverse shear for specimens with the same joint inclination angle under different normal force conditions, and the peak shear strength increases with increasing normal force, both of which are proportional to the law of variation of shear strength with normal force in rock shear tests.

In the comparison analysis of Figure 5B and Figure 7B, the normal force is 20 kN, the bedding dip angle is 30°, and the specimen is damaged for forward shear and reverse shear. In the case of forward shear, the failure mode of the specimen is mainly tension failure, and in the case of reverse shear, the main failure mode of the specimen is shear failure. The shear strength in forward shear is greater than the peak shear strength in reverse shear.

3.4 Shear displacement-shear stress analysis for different rock bridge widths

To study the effect of different rock bridge widths on the shear failure of layered rock, shear failure tests were carried out at the same bedding dip angle (60°) and constant positive pressure (20 kN), varying the widths of the rock bridges of the specimens to 90 mm, 80 mm, 70 mm and 60 mm, and the various patterns of shear stress and shear displacement are shown in Figure 9, and the failure patterns are shown in Figure 10.

Analysis of Figure 9 shows that the shear failure results for different rock bridge widths under the same conditions of the same normal force and bedding dip angle reveal that the specimens have basically the same characteristics of shear stress and shear displacement curves during shear failure, with the peak shear strength of the specimens increasing with the increase in rock bridge width and the shear displacement of the specimens increasing with the increase in rock bridge width.

As shown in Figure 10, as the width of the rock bridge increases, the influence of the joint inclination angle on the shear failure of the rock sample decreases. At 60 mm and 70 mm rock bridge widths, the
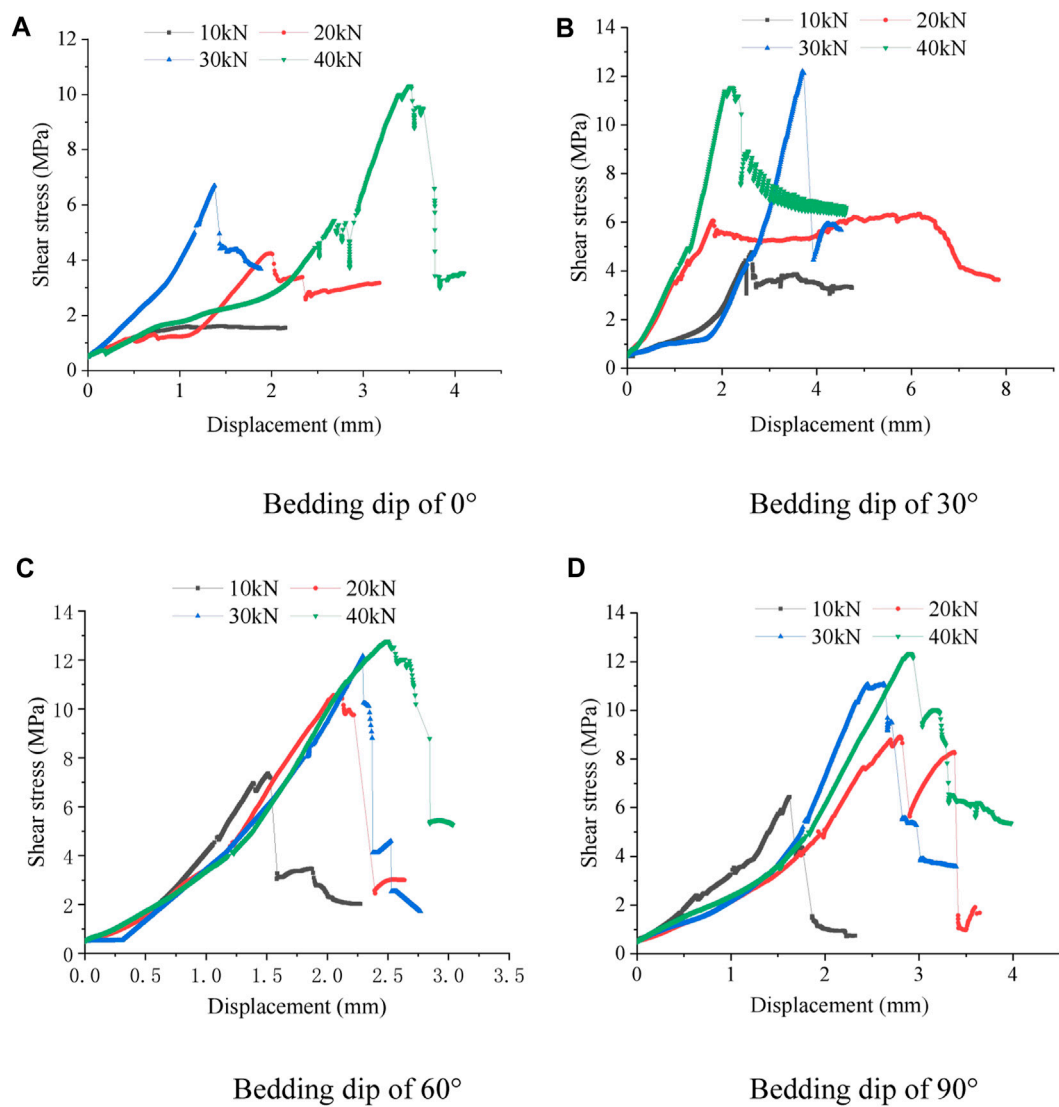
FIGURE 4
Shear stress and shear displacement curves under different normal forces. **(A)** Bedding dip of 0°. **(B)** Bedding dip of 30°. **(C)** Bedding dip of 60°. **(D)** Bedding dip of 90°.
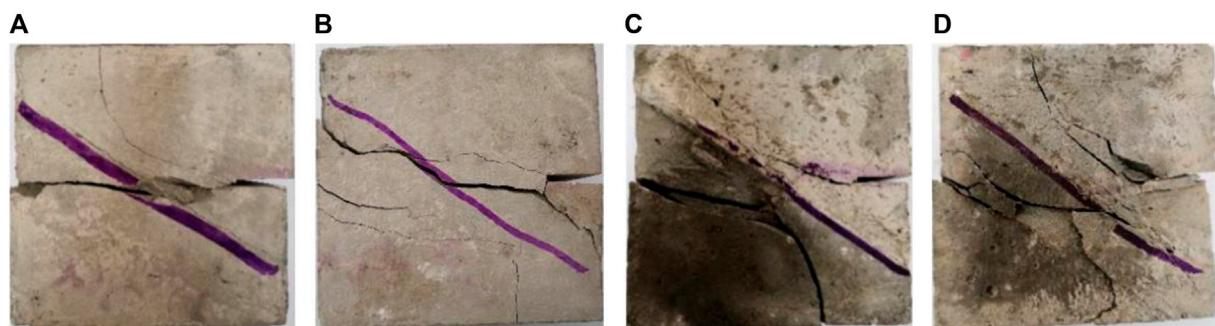
FIGURE 5
Shear failure pattern of specimens with different normal forces at a bedding dip angle of 30°. **(A)** 10 kN. **(B)** 20 kN. **(C)** 30 kN. **(D)** 40 kN.
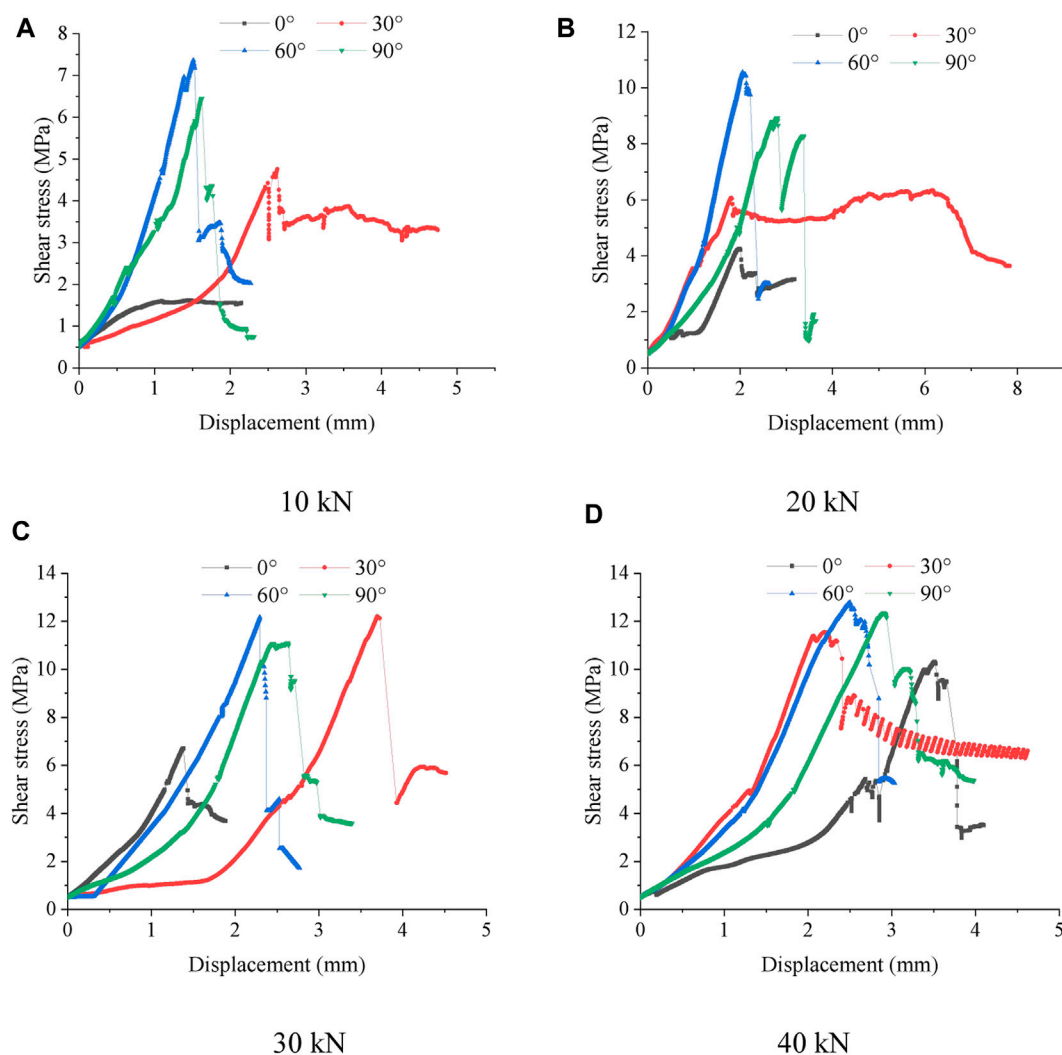
FIGURE 6
Shear stress vs. shear displacement curves for different bedding inclination angles. **(A)** 10 kN. **(B)** 20 kN. **(C)** 30 kN. **(D)** 40 kN.
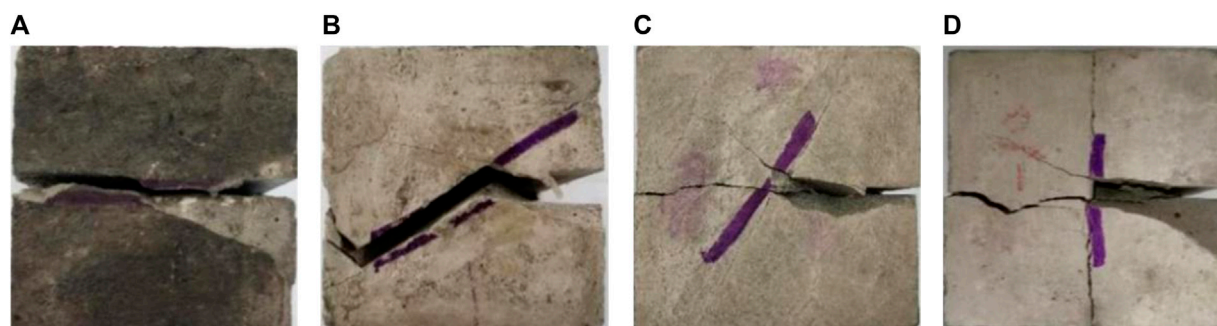
FIGURE 7
Shear failure pattern of specimens with different bedding dip angles for a normal force of 20 kN. **(A)** 0°. **(B)** 30°. **(C)** 60°. **(D)** 90°.

main fracture from shear failure of the specimen extends and breaks along the laminae. In contrast, for rock bridge widths of 80 mm and 90 mm, the main fracture runs through the bridge of the specimen, and the laminae face is less affected by the failure. This indicates that the rock bridge width is one of the important factors affecting the strength of the rock.
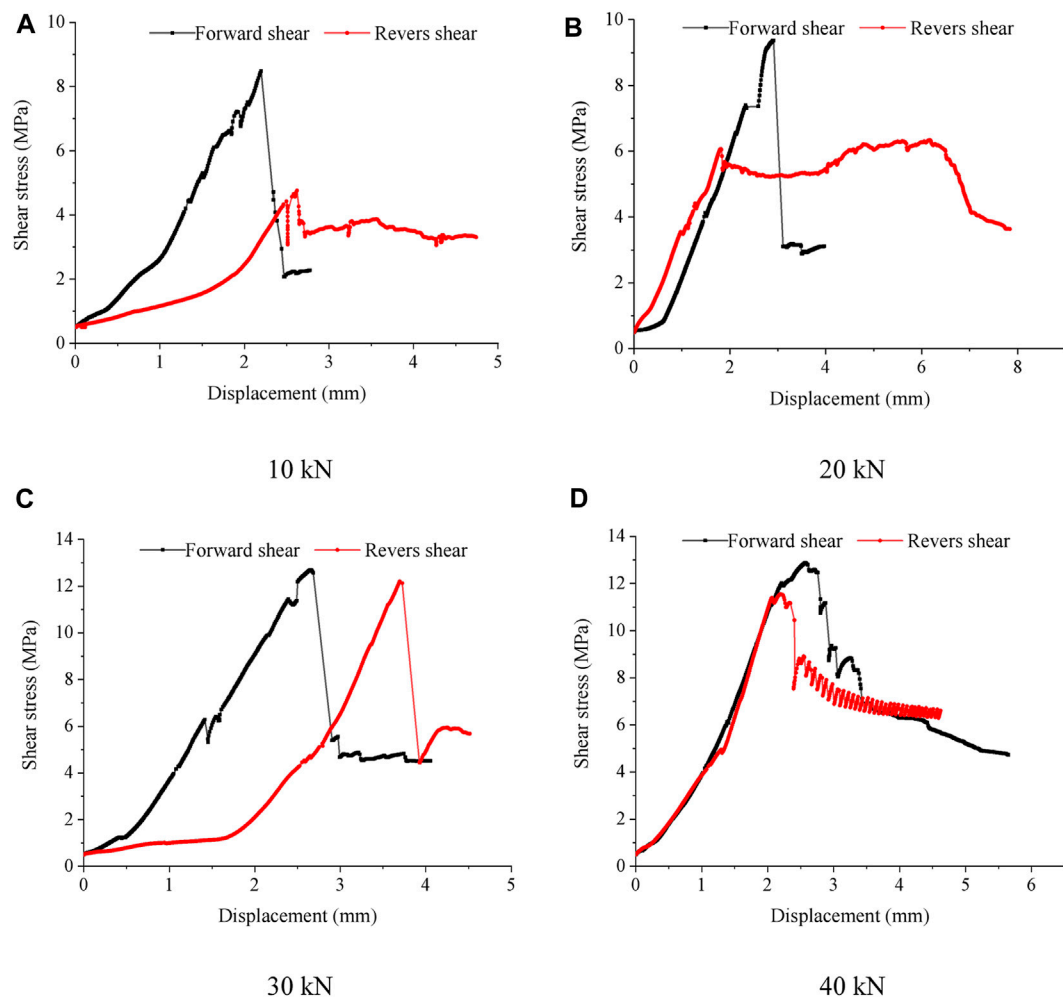
FIGURE 8
Plots of positive and negative shear stress and shear displacement of specimens under different normal forces. **(A)** 10 kN. **(B)** 20 kN. **(C)** 30 kN. **(D)** 40 kN.
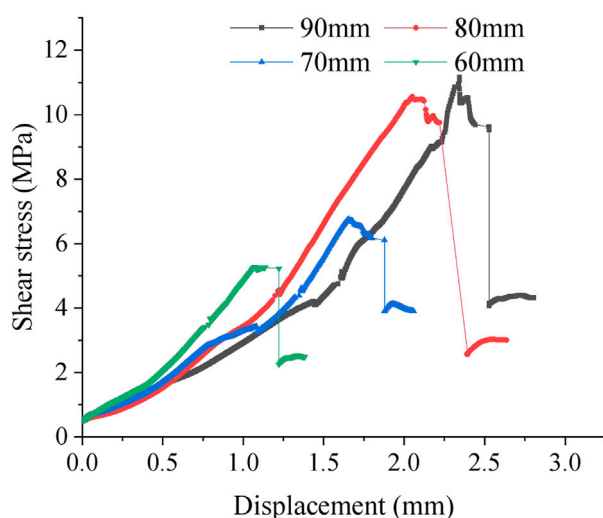
FIGURE 9
Shear stress *versus* shear displacement curves for specimens with different rock bridge widths.

4 Nomenclature analysis of acoustic emission monitoring results

In the early stage of shear force application, the specimen is in the elastic deformation stage, and the number of acoustic emission events is low. With increasing shear force, the crack continues to expand, and after the shear force reaches its peak, the specimen is suddenly damaged, and the shear stress will show a cliff-type drop. At this time, the number of acoustic emission events will increase considerably. The number of acoustic emission events under different test conditions are shown in Figure 11, Figure 12 and Figure 13.

As shown in Figure 11, when the normal force is 20 kN and the bedding angle is 60°, the acoustic emission characteristics of different rock bridge widths are analyzed. When the rock bridge width is 90 mm, 80 mm and 70 mm, the number of instantaneous acoustic emission events of shear failure of the sample is basically the same, which is about 3,250 times. However, when the rock bridge width is 60 mm, the number of instantaneous acoustic emission events of shear failure of the sample is large, which is about 4,200 times. This is because when the rock bridge width is 60 mm, the sample will be destroyed instantaneously along the bedding plane during the shear
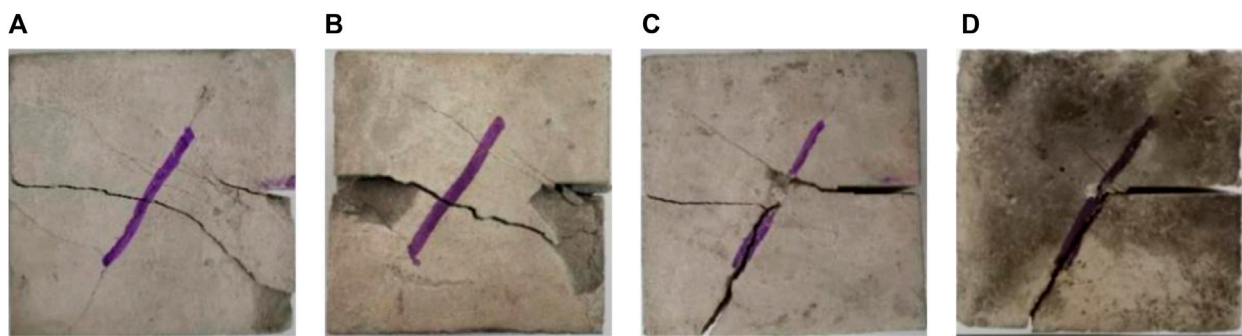
FIGURE 10
Shear failure pattern under different rock bridge width conditions. **(A)** 90 mm. **(B)** 80 mm. **(C)** 70 mm. **(D)** 60 mm.
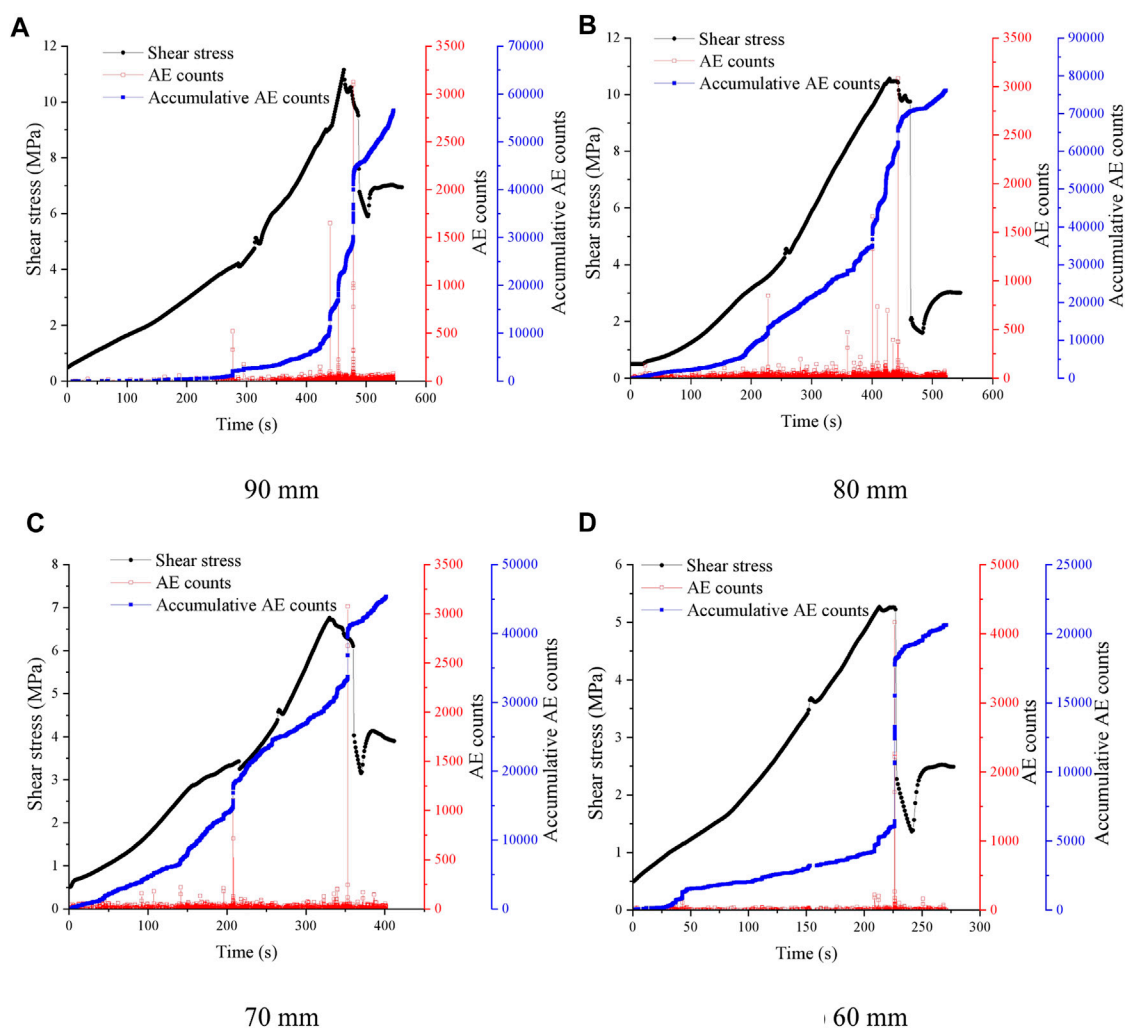
FIGURE 11
Acoustic emission counts over time during shear at different rock bridge widths. **(A)** 90 mm. **(B)** 80 mm. **(C)** 70 mm. **(D)** 60 mm.

FIGURE 12
Acoustic emission counts with time for shear processes at different bedding dip angles. **(A)** 0°. **(B)** 30°. **(C)** 60°. **(D)** 90°.

process. With the increase of the width of the rock bridge, the peak value of the cumulative number of acoustic emission events in the whole process of shear shows an increasing trend. This is because the width of the rock bridge is larger, the energy accumulated inside the sample during shear failure is larger, and the energy released at the moment of failure is relatively larger.
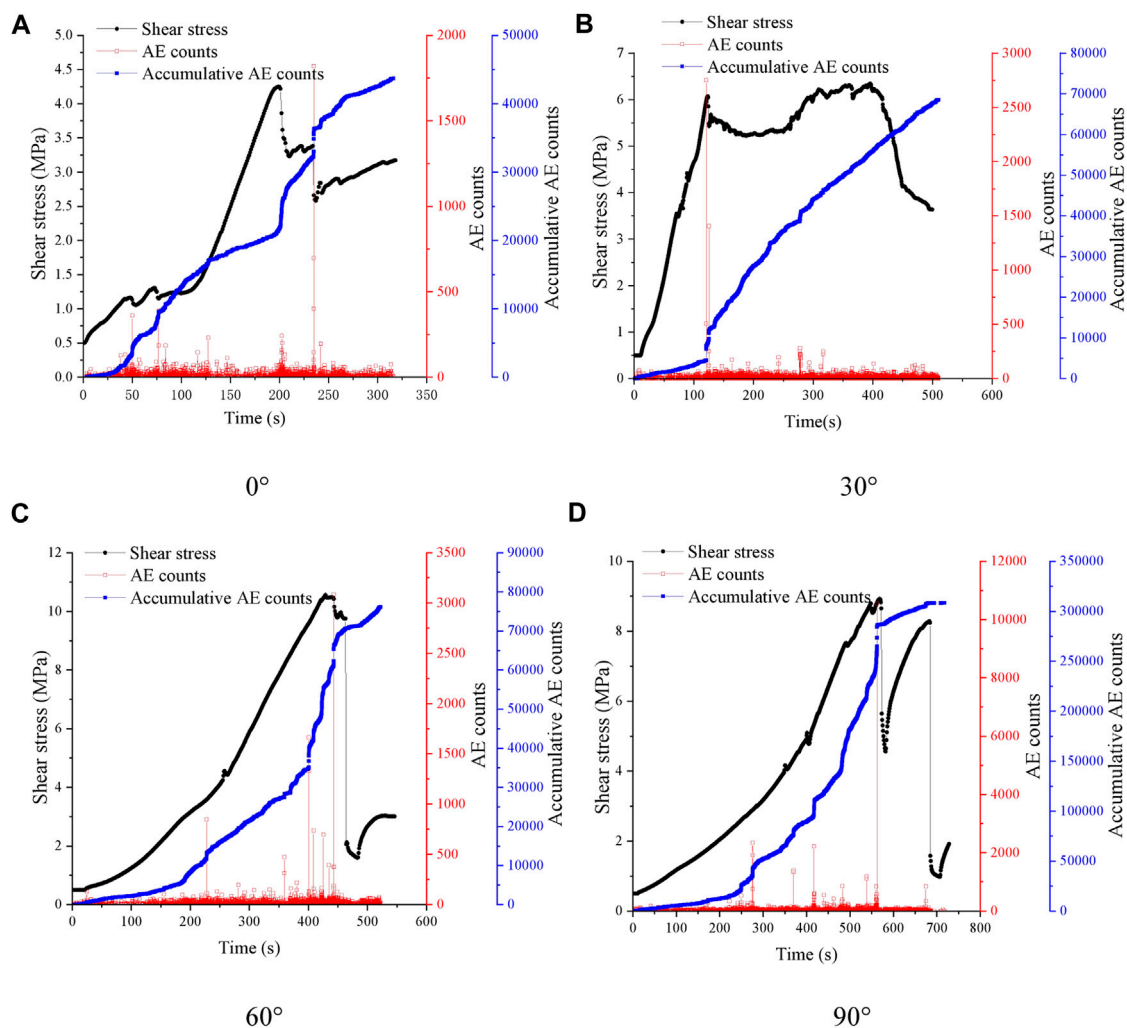
As shown in Figure 12, when the normal force is 20 kN and the width of the rock bridge is 80 mm, the acoustic emission characteristics under different bedding dip angles are analyzed. With the increase of the bedding dip angle, the number of instantaneous acoustic emission events and the cumulative number of acoustic emission events in the whole process of sample shearing are increasing. Although the peak shear strength is the largest when the bedding angle is 60°, the number of acoustic emission time is not the largest. The maximum is 90° and the minimum is 0°. Because when the bedding angle is 0°, in the process of shear failure of the sample, the cracks are generated and developed along the weak plane of the bedding, the shear failure ability of the sample is low, the energy accumulated inside the

sample is the smallest, and the peak value of the acoustic emission event is the smallest. When the bedding angle is 90°, the cracks are perpendicular to the weak plane of the bedding, and the energy accumulated inside the sample is the largest, so the peak value of the acoustic emission event is the largest.

From the comparative analysis of 3.3 forward shear and reverse shear, it can be seen that the failure mechanisms of forward shear and reverse shear of layered rock are different, and the number of acoustic emission events generated by the two shear methods also differs significantly. Figure 13 and Figure 12B show the characteristic curves of the acoustic emission events of the specimens in forward and reverse shear at 30°, respectively. In the process of forward shear, the specimens are mainly damaged by tension, there is less energy accumulated inside the specimens, and the number of peak acoustic emission events is small when they are damaged. Conversely, when the specimen is in reverse shear, it is mainly shear failure, the energy accumulated inside the specimen is large, and the number of peak acoustic emission events at the time of failure is relatively large.

FIGURE 13
Acoustic emission counts over time during forward shear.
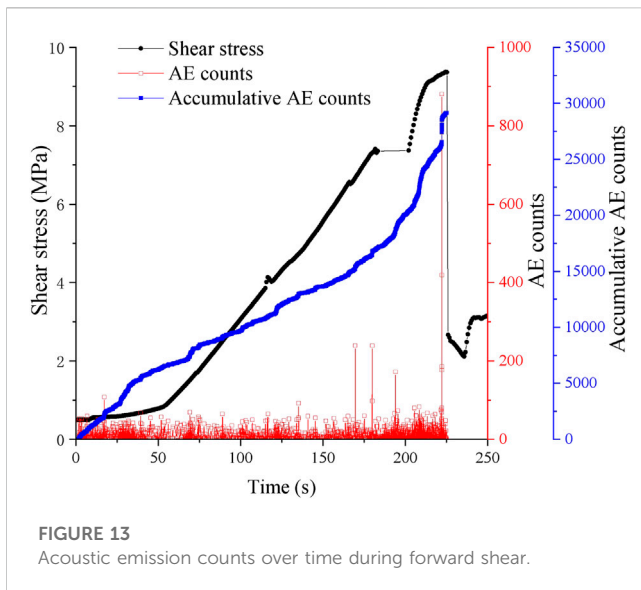
5 Discussion

During shear failure of rocks, the angle of laminae and joints can have a dramatic effect on the extension of cracks. When the angle of shear to the laminae was greater than 90°, similar phenomena were observed when it was less than 90° (Ikari et al., 2015). For specimens with different laminae inclination angles, cracks generated at the tips of the joints caused local failure to the specimens under shear, and as the shear force continued to increase, the cracks continued to expand, eventually forming a through shear failure zone, which was consistent with the literature (Savilabti et al., 1990; Shen et al., 1999; Zhao et al., 2014). During the shear failure process, the pre-cracking of the specimen will tend to close due to the action of the normal force at the joint tip. Coupled with the increasing shear force, the specimen will produce tension cracks, and the joint tip will appear to be broken, slagged and spalled. The width of the rock bridge has a great influence on the crack extension of the laminated specimen. When the width of the rock bridge is relatively large, the shear force of the specimen is mainly provided by the rock bridge, and the specimen has tension cracks in the shear failure process. The failure surface presents a certain angle and eventually forms through failure. The failure process of the weak side of the lamina has less influence on the failure. When the width of the rock bridge of the specimen is small, before the application of shear force, because of the action of the normal force. When the specimen rock bridge width is small, before the shear force is applied, because of the normal force, the specimen produces a compression pull crack at the tip of the joint. With the shear force applied, the specimen produces a shear crack. When extended to the laminated weak surface, the specimen eventually breaks along the laminated surface. In this process, the laminated surface plays a major role in the destruction of the specimen.

For specimens with bedding inclinations of 0° and 90°, the presence of the joints has relatively little effect on crack extension during shear failure. For 0° specimens, shear failure is

mainly in the form of slip along the bedding surface; for 90° specimens, it is mainly shear fracture perpendicular to the bedding surface. For the 30° and 60° specimens, there is a clear difference between the crack extension in forward and reverse shear. In forward shear, the specimen is sheared by a tensile crack perpendicular to the bedding surface from the tip of the joints, and the tensile crack expands during the shear process and eventually penetrates; in reverse shear, a tensile crack first appears at the tip of the joints, and with increasing shear force, the crack expands and eventually penetrates along the bedding surface. The specimen undergoes shear failure.

Shear strength weakening with sliding is an important property of intact and fractured rocks, a mechanism for landslides or collapse tipping of rocky slopes containing fractures, and an important model for analyzing earthquake mechanisms and precursor phenomena in seismology (Heng et al., 2019). The angle of the lamina and the width of the rock bridge are both important factors affecting the strength of the rock. Through the indoor direct shear test, the shear failure of the rock under different working conditions is simulated, the crack generation and expansion pattern of the specimen during the shear failure is observed, and the mechanical properties of the specimen before and after the failure are analyzed, which is of great significance for the study of the collapse of layered rocky slopes containing joints and the slip movement of faults in the event of earthquakes.

6 Conclusion

To analyze the shear failure characteristics of layered rock bridges, an indoor shear test was carried out by preparing similar rock materials. Combined with acoustic emission monitoring, shear tests under different bedding dip angles, different normal forces, different rock bridge widths and positive and negative shear were analyzed. The main conclusions are as follows.

(1) Under different normal force conditions, the specimen shear damage has obvious brittle characteristics, the peak shear strength is proportional to the normal force, the peak shear strength of layered rock is influenced by the width of the rock bridge, and the greater the width of the rock bridge is, the greater the peak shear strength.

(2) Under different joint inclination angle conditions, the maximum shear strength of the rock sample is the shear strength of the lamina face when the joint inclination angle is 0°; when the joint inclination angle is 90°, the lamina face has the least effect on the shear failure of the specimen, and the maximum shear strength is the shear strength of the specimen material itself; the peak shear strength is 60°, 90°, 30° and 0° in descending order.

(3) When the joint inclination angle is the same, the shear stress and shear displacement curves of the specimens under forward and reverse shear conditions are basically the same, and the peak shear strength is proportional to the normal force. The failure mode of the specimens in forward shear is mainly tension failure, while the failure mode of the specimens in reverse shear is mainly shear failure.

(4) Acoustic emission has an obvious phase, the peak number of acoustic emission events is proportional to the width of the rock bridge and the dip angle of the lamina, and its peak time and the

peak time of shear stress are basically the same; the peak number of acoustic emission events of reverse shear is greater than that of forward shear.

(5) Bedding angle, normal force and rock bridge width are important factors affecting rock strength.

Data availability statement

The original contributions presented in the study are included in the article/Supplementary Material, further inquiries can be directed to the corresponding authors.

Author contributions

JY conceived of and designed the experiments. JY, ZZ, and ZL performed the experiments. ZZ, LC, and HL analyzed the data. ZZ and LZ wrote the paper. All authors contributed to the article and approved the submitted version.

Funding

Acknowledgments

Conflict of interest

The authors declare that the research was conducted in the absence of any commercial or financial relationships that could be construed as a potential conflict of interest.

Publisher's note

All claims expressed in this article are solely those of the authors and do not necessarily represent those of their affiliated organizations, or those of the publisher, the editors and the reviewers. Any product that may be evaluated in this article, or claim that may be made by its manufacturer, is not guaranteed or endorsed by the publisher.

References

Bao, Y. D., Chen, J. P., Su, L. J., Zhang, W., and Zhan, J. W. (2023). A novel numerical approach for rock slide blocking river based on the CEFDEM model: A case study from the samaoding paleolandslide blocking river event. *Eng. Geol.* 312, 106949. doi:10.1016/j.enggeo.2022.106949

Chen, G. Q., Wang, J. C., Wang, W., Luo, F. Y., and Li, Z. B. (2017). Direct shear failure characteristics of discontinuous jointed rock mass with different connectivity. *J. Eng. Geol.* 25, 322–329. doi:10.13544/j.cnki.jeg.2017.02.008

Cho, W. J., Kim, H., Jeon, S., and Min, K. B. (2012). Deformation and strength anisotropy of Asan gneiss, Boryeong shale, and Yeoncheon schist. *Int. J. Rock Mech. Min. Sci.* 50, 158–169. doi:10.1016/j.ijrmms.2011.12.004

Debecker, B., and Vervoort, A. (2009). Experimental observation of fracture patterns in layered slate. *Int. J. Fract.* 159, 51–62. doi:10.1007/s10704-009-9382-z

Gehle, C., and Kutter, H. K. (2003). Breakage and shear behaviour of intermittent rock joints. *Int. J. Rock Mech. Min. Sci.* 40, 687–700. doi:10.1016/S1365-1609(03)00060-1

Heng, S., Yang, C. H., Zeng, Y. J., Zhang, B. Q., Guo, Y. T., Wang, L., et al. (2014). Anisotropy of shear strength of shale based on direct shear test. *Chin. J. Rock Mech. Eng.* 33, 874–883. doi:10.13722/j.cnki.jrme.2014.05.002

Heng, S., Li, X. Z., Liu, X., and Zhang, X. D. (2019). Study on the propagation mechanism of shale fractures under direct shear conditions. *J. Rock Mech. Eng.* 38, 2438–2450. doi:10.13722/j.cnki.jrme.2019.0557

Ikari, M. J., Niemeijer, A. R., and Marone, C. (2015). Experimental investigation of incipient shear failure in foliated rock. *J. Struct. Geol.* 77, 82–91. doi:10.1016/j.jsg.2015.05.012

Lajtai, E. Z. (1969). Shear strength of weakness planes in rock. *Int. J. Rock Mech. Min. Sci. Geomech. Abstr.* 6, 499–515. doi:10.1016/0148-9062(69)90016-3

Li, B., Huang, D., Jiang, Q. H., and Cheng, G. Q. (2019). Fracture pattern and toughness of layered sandstone influenced by layer orientation. *J. Geotech. Eng.* 41, 1854–1862. doi:10.11779/CJGE201910009

Liang, X., Tang, S. B., Tang, C. A., Hu, L. H., and Chen, F. (2023). Influence of water on the mechanical properties and failure behaviors of sandstone under triaxial compression. *Rock Mech. Rock Eng.* 56 (2), 1131–1162. doi:10.1007/s00603-022-03121-1

Liu, K. D., and Zhang, Y. J. (2002). Influence factors on shear failure orientation of layered rocks. *J. Rock Mech. Eng.*, 335–339.

Liu, W., Zeng, Y. W., Xia, L., and Chen, X. (2019). Dendrobium sonia polysaccharide regulates immunity and restores the dysbiosis of the gut microbiota of the cyclophosphamide-induced immunosuppressed mice. *Eng. J. Wuhan Univ.* 52, 600–607. doi:10.1016/S1875-5364(19)30062-7

Qi, Y. Y., Wei, W., Chen, Z. Q., and Gao, X. (2021). Acoustic emission characteristics of shear failure of rock bridges. *Bull. Sci. Technol.* 37, 72–76. doi:10.13774/j.cnki.kjtb.2021.03.013

Qin, C. A., Chen, G. Q., Zheng, H. J., and Tang, P. (2019). Failure of rock bridge at the end fracture condition under direct shear tests. *Geotechnics* 40, 642–652. doi:10.16285/j.rsm.2017.1424

Ran, Y., Chen, G. Q., Huang, B. R., Zhang, X. D., and Chen, C. S. (2016). Experimental study on failure characteristics of rock bridge different widths under direct shear. *J. Changjiang Acad. Sci.* 33, 131–134+144. doi:10.11988/ckyyb.20150684

Savilabti, T., Nordlund, E., and Stephansson, O. (1990). "Shear-boxtesting and modeling of joint bridge," in Proceedings of International Symposium for Rock Joints. Editors N. R. Barton and O. Stephansson (Norway), 295–300. doi:10.1016/0148-9062(91)92236-r

Shen, T., Feng, D. X., Ren, W. Z., and Bai, S. W. (1999). Research on strength property of shear including discontinuity and rock bridge. *Geotechnics*, 34–39. doi:10.16285/j.rsm.1999.01.006

Song, Y., Zang, F. Y., Li, Y. Q., Du, Y. Q., and Wang, & W. Y. (2020). Analysis of shear failure characteristics of anchored jointed rock mass. *Chin. J. Geol. Hazard Control* 31, 133–140. doi:10.16031/j.cnki.issn.1003-8035.2020.05.18

Sun, X., Chen, G. Q., Zhang, G. Z., Wang, D., and Qin, C. A. (2020). Study on meso-failure characteristics and dilatancy effect of rock bridge direct shear. *J. Eng. Geol.* 28, 246–254. doi:10.13544/j.cnki.jeg.2019-039

Tan, X., Konietzky, H., Frühwirt, T., and Dan, Q. D. (2015). Brazilian tests on transversely isotropic rocks: Laboratory testing and numerical simulations. *Rock Mech. Rock Eng.* 48, 1341–1351. doi:10.1007/s00603-014-0629-2

Tavallali, A., and Vervoort, A. (2010a). Effect of layer orientation on the failure of layered sandstone under Brazilian test conditions. *Int. J. Rock Mech. Min. Sci.* 47 (02), 313–322. doi:10.1016/j.ijrmms.2010.01.001

Tavallali, A., and Vervoort, A. (2010b). Failure of layered sandstone under Brazilian test conditions: Effect of micro-scale parameters on macro-scale behaviour. *Rock Mech. Rock Eng.* 43, 641–653. doi:10.1007/s00603-010-0084-7

Vervoort, A., Min, K. B., Konietzky, H., Cho, J. W., Debecker, B., Dinh, Q. D., et al. (2014). Failure of transversely isotropic rock under Brazilian test conditions. *Int. J. Rock Mech. Min. Sci.* 70, 343–352. doi:10.1016/j.ijrmms.2014.04.006

Wang, P. T., Ren, F. H., Miao, S. J., Cai, M. F., and Yu, Q. L. (2017). Evaluation of the anisotropy and directionality of a jointed rock mass under numerical direct shear tests. *Eng. Geol.* 225, 29–41. doi:10.1016/j.enggeo.2017.03.004

Wang, Q., Xu, S., Xin, Z. G., He, M. C., and We, I. H. Y. (2022). Mechanical properties and field application of constant resistance energy-absorbing anchor cable. *Tunn. Undergr. Space Technol.* 125, 104526. doi:10.1016/j.tust.2022.104526

Xia, L., Yao, J. S., and Jiang, L. (2020). Effect of bedding characteristics on shear mechanical properties of layered rock mass. *J. Water Resour. Archit. Eng.* 18, 37–43+69. doi:10.3969/j.issn.1672-1144.2020.01.007

Yuan, X. H. (2020). Study on deformation failure mode and evolution mechanism of middle locked rock bridge under uniaxial compression. *J. Saf. Sci. Technol.* 16, 116–121. doi:10.11731/j.issn.1673-193x.2020.09.018

Zhang, Y. J., and Liu, Y. P. (2001). Anisotropy of shear strength of layered rock and determination of shear failure plane. *Geotech. Mech.* (03), 254–257. doi:10.16285/j.rsm.2001.03.004

Zhang, H. Q., Zhao, Z. Y., Tang, C. A., and Song, L. (2005). Numerical study of shear behavior of intermittent rock joints with different geometrical parameters. *Int. J. Rock Mech. Min. Sci.* 43 (5). doi:10.1016/j.ijrmms.2005.12.006

Zhang, G. F., Chen, G. Q., Ao, C. Q., Zhang, Y., and Zhao, Y. J. (2015). Experimental study on direct shear of rock bridge with different width. *Railw. Eng.* (11), 89–91+120. doi:10.3969/j.issn.1003-1995.2015.11.26

Zhang, L. M., Chen, G. Q., Li, Z. B., Luo, F. Y., and Zhou, Y. X. (2018). Failure process of coplanar discontinuous rock bridge in direct shear test. *J. Chang jiang Acad. Sci.* 35, 120–125+142. doi:10.11988/ckyyb.20170371

Zhao, Y. L., Peng, Q. Y., Wan, W., Wang, W. J., and Zhao, F. J. (2014). Experimental and numerical analysis on rupture of rock bridge with Non-Coplanar intermittent joints under direct shear. *Civ. Constr. Environ. Eng.* 36, 59–67. doi:10.11835/j.issn.1674-4764.2014.01.009

Zhu, Z. Q., and Zeng, Y. W. (2005). Study on uniaxial compressive strength and shear failure surface of layered rock mass. *Geotech. Eng. World* 8, 27–29. doi:10.3969/j.issn.1674-7801.2005.04

Zhu, L., Huang, R. Q., Chen, G. Q., and He, S. M. (2020). Equivalent calculation of the fracture paths of jointed rock masses based on flow theory. *J. Rock Mech. Eng.* 39, 22–33. doi:10.13722/j.cnki.jrme.2019.0650

frontiers | Frontiers in Earth Science

The influence of the number of free surfaces on the energy distribution and attenuation law of blasting vibration signals from peripheral holes: field experiment and simulation

Riyan Lan[1], Zhen Wang[2], Jianyou Lu[2]*, Zilong Zhou[2], Lu Chen[3] and Shan Gao[1]

[1]Guangxi Xinfazhan Communication Group Co. Ltd., Nanning, Guangxi, China, [2]School of Resources and Safety Engineering, Central South University, Changsha, Hunan, China, [3]College of Civil Engineering, Changsha University of Science and Technology, Changsha, China

Tunnels are commonly excavated using drilling and blasting methods, and the surrounding rock is greatly affected by the vibration of surrounding hole blasting. To study the influence of the number of free surfaces on the energy distribution and attenuation law of surrounding hole blasting vibration signals, on-site experiments and numerical simulation experiments were conducted. The research results indicate that the higher the number of free surfaces, the smaller the peak vibration velocity. The longitudinal Fourier main frequency decreases with the distance from the monitoring point. The more free surface, the greater the centroid frequency and zero crossing frequency. In addition, numerical simulation shows that the degree of rock fragmentation after blasting increases with the increase of the number of free surface of rock.

KEYWORDS

tunnel excavation, controlled blasting method, peripheral holes, vibration, free surface

1 Introduction

As an efficient and economical construction technology, a blasting process is widely applied to mining, basic engineering construction and hydropower engineering (Xia et al., 2018). Nonetheless, only 20%–30% of the energy generated by an explosion can contribute to rock fragmentation, while the rest is dissipated as vibrations, noise, and flying rocks (Trivedi et al., 2014). There is a direct correlation between blasting-induced vibrations and damage to the surrounding structure in these manifestations (Ma et al., 2000; Xia et al., 2013). The researchers mainly describe the blasting-induced vibration through three parameters to establish the relationship it and structural damage, namely, particle peak vibration velocity (PPV), frequency and energy. A convenient measurement, intuitive and easy-to-operate characteristic of PPV makes it a popular criterion for blasting-induced vibration control in practical engineering (Noret et al., 2012). In recent years, researchers have found that it is unreliable to simply use PPV as the criterion of blasting-induced vibration, and the different frequency spectrum structures induced by blasting vibration are also an important cause of structural damage (Aldas, 2010). When the vibration frequency of a structure reaches a

certain relationship with its natural frequency, it will cause the amplitude of the structure to amplify, increasing the probability of damage. In general, a structure's natural frequency is below 10 Hz, so vibration at lower frequencies will cause more structural damage than vibration at higher frequencies (Singh and Roy, 2010). As people's requirements for blasting vibration control become more and more stringent, two-factor blasting vibration safety criterion based on vibration velocity-frequency has gradually become the mainstream. A detailed understanding of the propagation law of blasting-induced frequency and vibration velocity is a prerequisite for safety evaluation. A blasting vibration's frequency and velocity depend on many factors (Yilmaz and Unlu, 2013; Qiu et al., 2018; Yang et al., 2019; Peng et al., 2021), including the millisecond time, propagation medium, type of explosive, etc.

Tunnel blasting requires drilling a circle of blast holes along the excavation section, with the spacing of the blast holes matching the minimum load and the depth being the same as the pre advance depth. These holes are called peripheral holes. The significant distinction between smooth blasting and presplit blasting is the order in which the peripheral hole and the main blasting area are detonated. Smooth blasting refers to the blasting that occurs before the peripheral hole is detonated relative to the main blasting area. Otherwise, it is called presplit blasting. According to previous literature, researchers have conducted extensive research on smooth blasting and presplit blasting. Li et al. (2017) reported the smooth blasting technology under the condition of decoupling charge by numerical simulation, the results indicated by using smooth blasting technology, damage to reserved rock can be reduced effectively. An optimized model for smooth blasting parameters has been proposed by Liu and Liu (2017). There has been a comparison between these two blasting techniques from different perspectives by some scholars. From the perspective of contour formation, Lu et al. (2012) compared presplit blasting with smooth blasting. Their research illustrated when the in-site stress is greater than 10~12 MPa, presplit blasting cannot form contour cracks well. Hu et al. (2014) compared the two blasting techniques from the point of view of over-excavation and under-excavation, and the results demonstrated that Pre splitting blasting is inferior to smooth blasting in terms of effectiveness in excavation profile effect. Zhou et al. (2019) compared the two blasting techniques from the characteristics of blasting-induced vibration. Results showed that smooth blasting produces a vibration signal with a higher PPV and dominant frequencies than presplit blasting. To meet the blasting safety standards, tunnel excavation often uses millisecond delay blasting to reduce the amount of single explosive. It is worth noting that when different detonator sections do are detonated, the blasting of the former section do will usually provide a new free surface for the latter section do to reduce the restriction of the blast hole. In the two different controlled blasting methods of presplit blasting and smooth blasting, the constraint degree of the peripheral holes are different when they are detonated. The rock fragmentation and vibration intensity induced by explosion are significantly affected by the number, location and range of free surfaces. Some researchers have investigated the impact of the number of free surfaces to blasting-induced vibration. In terms of numerical simulation and on-site experiments, Lu et al. (2018) investigated the influence of free surface on blasting-induced PPV. Results stated that the PPV induced by blasting decreases nonlinearly as the number of free

FIGURE 1
The field experiment site.

surfaces increases. However, through a field test, Uysal et al. (2007) discovered that burden significantly affects blasting-induced vibration and that the velocity of the vibration reduces as burden increases. Blair and Armstrong (2001) conducted a detailed statistical analysis of blast vibration data from a series of stone harvesting fields monitored and the statistical results found that whether the blasthole is constrained or not has no significant effect on the vibration intensity induced by blasting. Through the field test and related numerical simulation analysis, Yang et al. (2016) revealed that when the distance of the measuring point is fixed, the mean frequency induced by blasting decreases with the increase of burden. However, at present, field experimental studies on the impact of the number of free surfaces on the vibration signals and energy distribution rules induced by peripheral hole blasting are insufficient, and the failure mechanism needs further research.

Up to now, blasting vibration's influence on free surfaces is not well understood.

Compared with the research results of blasting-induced PPV, research on the frequency of blasting-induced vibrations is insufficient. The vibration induced by the peripheral holes have a obvious influence on the rock mass in millisecond delay blasting technique. In this research, the vibration blasting-induced by the peripheral holes in presplit blasting method and smooth blasting method is taken as the research background, and the relationship between the vibration characteristics induced of peripheral holes under different blasting conditions and PPV, frequency and energy is analyzed, and then the potential influence mechanism is further revealed. This study plays a substantial guiding role in blasting parameter optimization and vibration control.

2 Field experiments for the excavation of tunnel

In this section, taking the excavation of a mountain highway tunnel by drilling and blasting as an example, the tunnel excavation
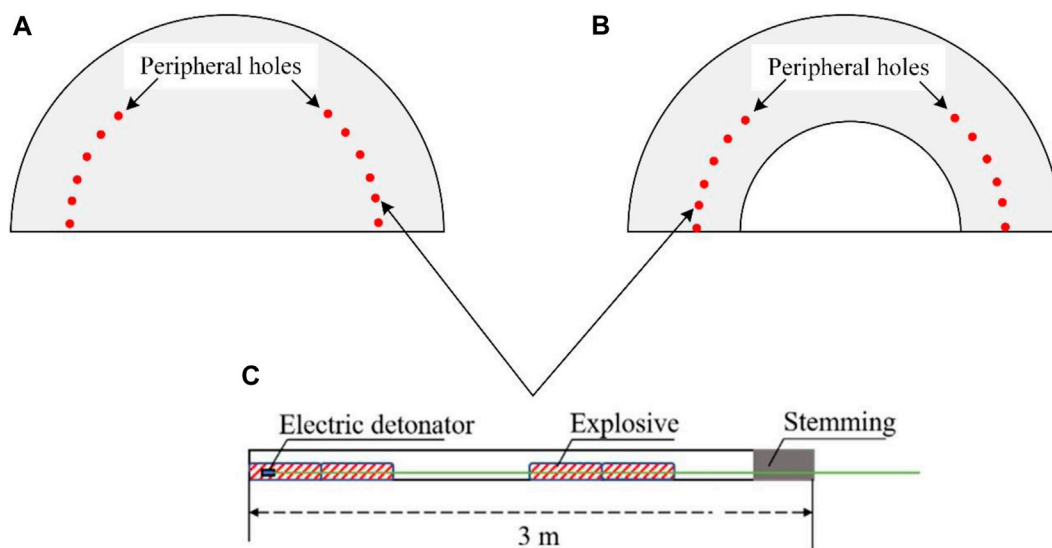
FIGURE 2
Schematic diagram of blast hole arrangement for peripheral hole blasting with different number of free surfaces: **(A)** number of free surfaces 1, **(B)** number of free surfaces 2, **(C)** charge structure of peripheral holes.

is carried out by smooth blasting and presplit blasting, respectively. Moreover, the vibration velocity, frequency and energy distribution induced by peripheral holes blasting are monitored and analyzed, its propagation law is analyzed and summarized.

2.1 Project background

As shown in Figure 1, the site of the field test is selected as a mountain highway tunnel under construction in Guangxi Zhuang Autonomous region. In the double-hole, cross-ridge tunnel, the buried depth is 358.724 m and the design length is 2,791 m. The tunnel's left and right lines are both long, and the study was conducted on the right line during all on-site tests. The strata in the tunnel area are mainly composed of lower Permian bedrock, mainly composed of moderately weathered limestone, gray-white, cryptocrystalline structure and hard rock.

2.2 Implementation of the field experiments

The step method is used for the tunnel drilling and blasting excavation, and the upper section is tested by the smooth blasting method. To conduct comparative experiments and reduce workload, the peripheral holes at the two waists are set as a separate section. The blasting parameters are arranged as shown in Figures 2A, B, there are 14 blastholes in total, 42 mm is the diameter of the blasthole, the hole spacing of peripheral holes are 0.6 m, all blastholes are filled with 2# rock emulsion explosive, cartridge diameter 32 mm. Decked charge structures are used in axial direction of peripheral holes, and eccentric decoupling charge structure is adopted in the radial direction, the charge structure of the hole is shown in Figure 2C, to ensure accuracy of the test, the

industrial digital electronic detonator is used to detonate each hole, and the advance per round is 3 m.

To better compare the differences in vibration signals caused by peripheral hole blasting with different number of free surfaces, the layout, geometric shape, charging structure, and initiation method of blast holes with different number of free surfaces are consistent. The portable data acquisition instrument and three-dimensional velocity sensor shown in Figure 3A are used to monitor blasting vibration signals. Figures 3B, C show the on-site physical map of the monitoring location and the layout diagram of the monitoring location, respectively. A total of four monitoring locations have been set, with monitoring locations set at distances of 18, 24, 27, and 30 m from the excavation face. Monitor the blasting vibration velocity in the longitudinal, lateral, and vertical directions.

3 Field experiment results

3.1 PPV analysis

As a general rule, a PPV predictor derived from the United States Bureau of Mines (USBM) can be used to estimate blasting probabilities (Duvall and Fogelson, 1962):

$$PPV = K(SD)^{-\beta} \left(\text{with } SD = R/Q^{1/2} \right) \qquad (1)$$

where, β is the attenuation coefficient, K is the field geology coefficient and blast design, R represents the distance between the monitoring point and the blasting source, SD represents the scaled distance, and Q represents the explosive amount per delay.

According to above theoretical analysis, the main factors affecting PPV are the explosive amount per delay, the arrangement of blasting parameters, the distance between the monitoring point and the blasting source, and engineering
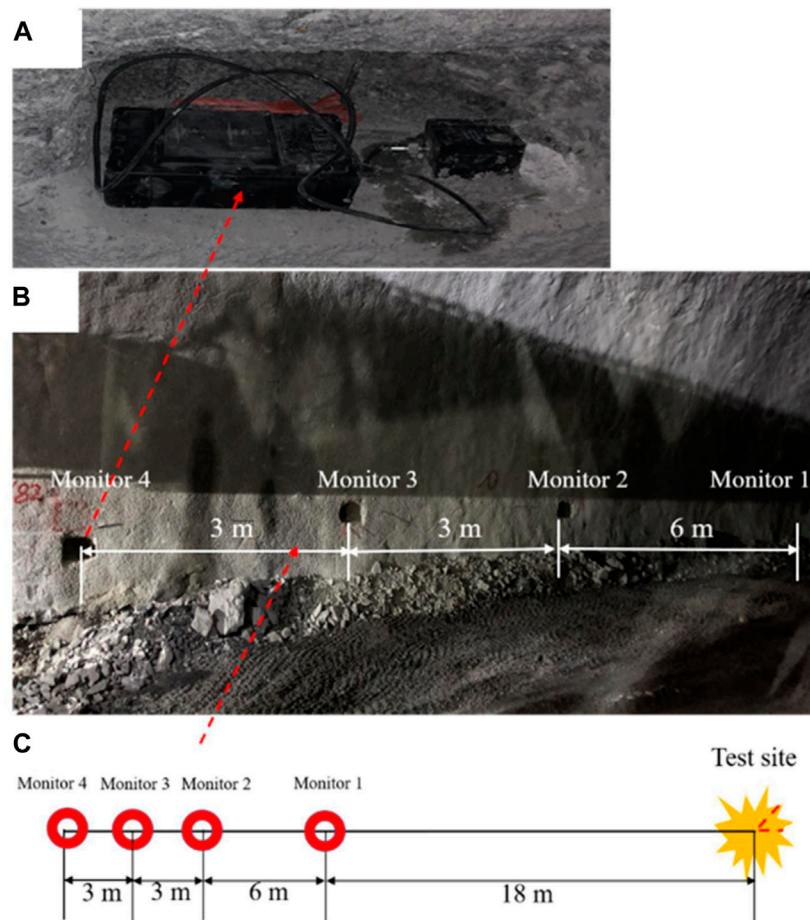
FIGURE 3
Monitoring points implementation scheme: **(A)** Blasting vibration measurement instrument, **(B)** Blasting vibration monitoring point, **(C)** schematic diagram of measuring points.

geological conditions. Considering that although the two groups of the tests are conducted in the same tunnel, the geological conditions may not be exactly the same, so allow differences in test results between the two groups. Because the two groups of tests are carried out in two adjacent tunnel excavations, and there is little difference in geological conditions, therefore the influence of geological conditions is ignored. Figure 4 shows the evolution rule of blasting vibration velocity with time monitored at different monitoring positions under different number of free surfaces. According to the signals at different monitoring points, the PPV curves induced by blasting under different number of free surfaces are plotted, as shown in Figure 5. It can be found that regardless of the free surfaces number being 1 or 2, the PPV induced by peripheral hole blasting decreases as the propagation distance increases. It is worth noting that at the same distance from the source of the explosion, the larger the number of free surfaces, the smaller the PPV caused by peripheral hole blasting. This is different from the theoretical analysis results of the PPV prediction formula. The longitudinal PPV caused by peripheral hole blasting with 2 free surfaces is defined as PPV_1. The longitudinal PPV generated by peripheral hole blasting with a number of free surfaces of 1 is defined as PPV_2. In order to quantitatively analyze the characteristics of

longitudinal PPV caused by peripheral hole blasting with different number of free surfaces, the mathematical expression for the amplitude attenuation coefficient P is defined as:

$$P = \left(\frac{PPV_1 - PPV_2}{PPV_1} \right) \times 100\% \qquad (2)$$

The results show that the longitudinal PPV induced by peripheral hole blasting with 2 free surfaces is significantly lower than that with 1 free surface, with an average amplitude attenuation of 22%.

3.2 Frequency analysis

Another way to evaluate vibration signals besides blasting velocity is to determine the frequency (Yang et al., 2016b). Favreau (1969) proposed a theoretical solution for the phenomenon of elastic waves excited by spherical cavities in elastic media. On this basis, Lu et al. (2013) introduced the expression of vibration velocity spectrum in viscous rock mass during blasting by adding medium damping term:
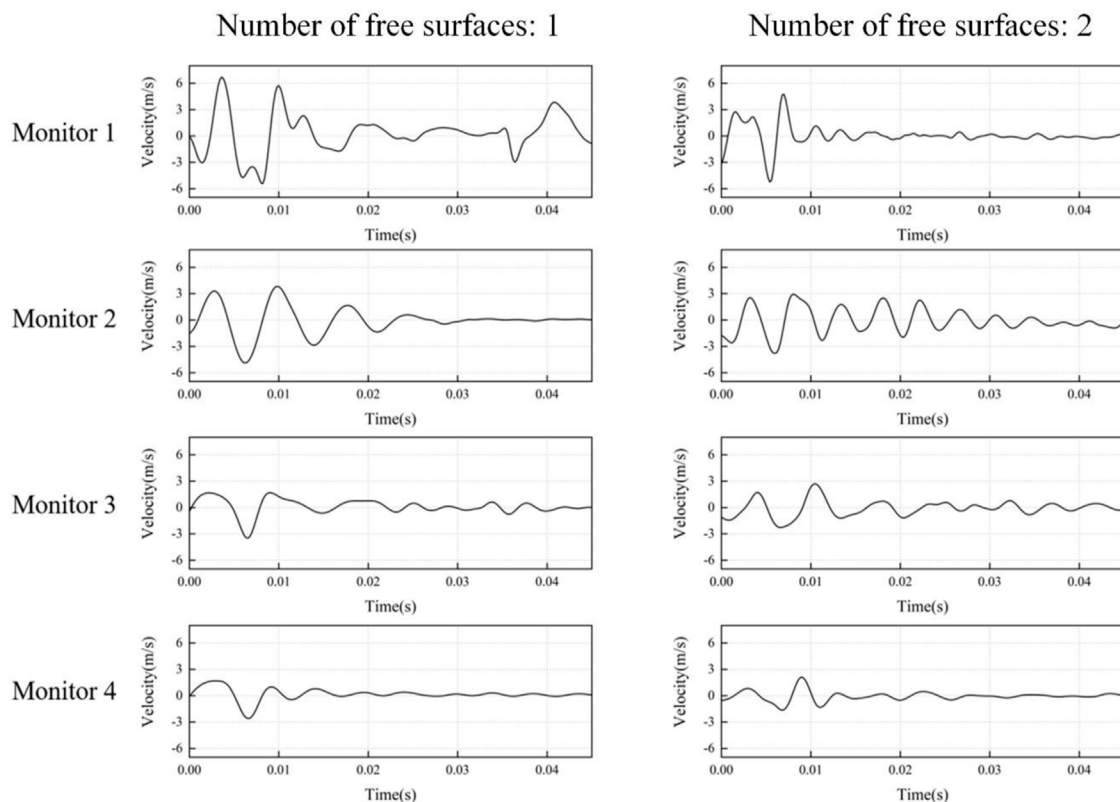
FIGURE 4
A longitudinal velocity-time history of the two sets of blasting tests.
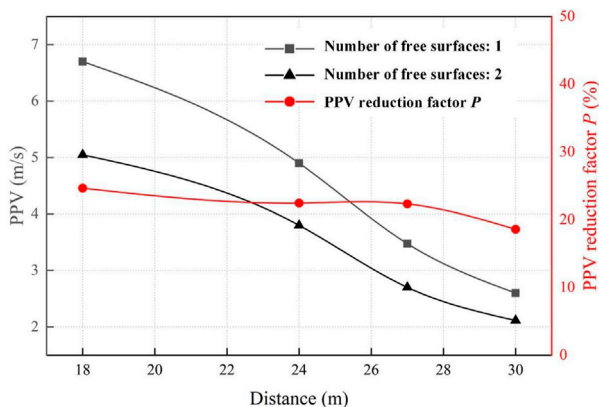

FIGURE 5
Comparison of the PPV-distance curves in the two sets blasting test.

$$F_n(\omega) = \frac{\exp\left(-\frac{\omega r}{2Q_r C_p}\right)|S_\sigma(j\omega)|r_e C_P \omega \sqrt{C_P^2 + r^2\omega^2}}{4\mu r^2 \sqrt{\left(C_P/r_e\right)^4 + \left[1 - (\lambda + 2\mu)/(2\mu)\right]\left(C_P/r_r\right)^2 \omega^2 + \left[(\lambda + 2\mu)/(4\mu)\right]^2 \omega^4}}$$

(3)

where λ, μ is the Lame coefficient, r_e is radius of elastic cavity, C_p is the longitudinal wave velocity, $S_\sigma(j\omega)$ represents the load spectrum

in the elastic cavity, Q_r is the geological quality factor of rock, ω is the angular velocity, r is the distance between the monitoring point and the blasting point.

Among them, it is assumed that the triangular blasting load is acting in the elastic cavity, and the blasting load spectrum is as follows:

$$|S_\sigma(j\omega)| = \{1 + a_e^2 + b_e^2 + 2a_e b_e \cos(\omega\tau) - 2[a_e \cos(b_e\omega\tau) \\ + b_e \cos(a_e\omega\tau)]\}^{1/2} \frac{\sigma_{\max}}{a_e b_e \tau \omega^2}$$

(4)

where τ and $\sigma_{\max}$ are the duration load and the peak load, respectively. $a_e = \tau_1/\tau$, $b_e = \tau_2/\tau$, τ_1 and τ_2 are load rising time and the time when the load decreases from peak to zero, respectively.

From the expression of blasting vibration velocity spectrum $F_n(\omega)$, it can be found that the main influencing factors of blasting vibration velocity spectrum $F_n(\omega)$ are the distance between the measuring point r and the explosion source, physical and mechanical parameters of rock λ, μ, C_p and Q_r, and radius of elastic cavity r_e, load rising time τ_1 and the time when the load decreases from peak to zero τ_2, the peak load $\sigma_{\max}$. Under the condition that the factors affecting $F_n(\omega)$ are all the same, the vibration velocity spectrum induced by blasting should be the same in theory.

According to the spectrum analysis of blasting vibration, in general, some characteristic frequencies will be used to describe the

FIGURE 6
Schematic diagram of characteristic frequency definition.

FIGURE 7
Comparing the amplitude-frequency spectra of vibration signals
collected at different monitoring sites.

FIGURE 8
Comparisons of the Centroid frequency and the Zero-crossing
frequency of vibration signals at different monitoring points.
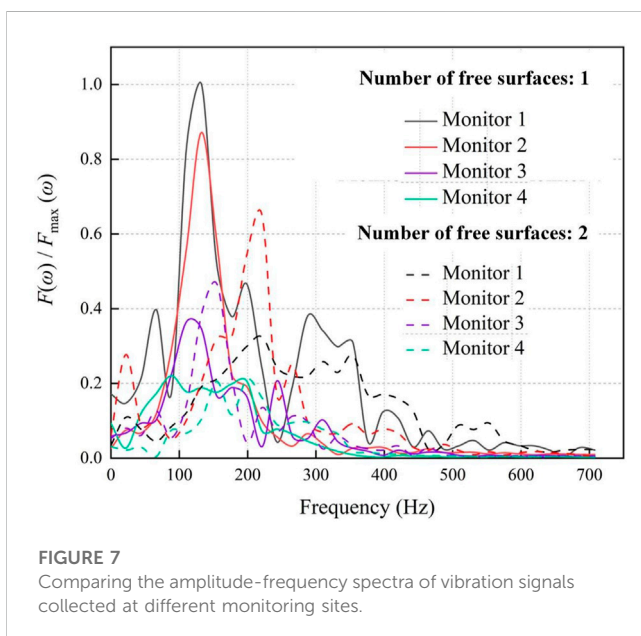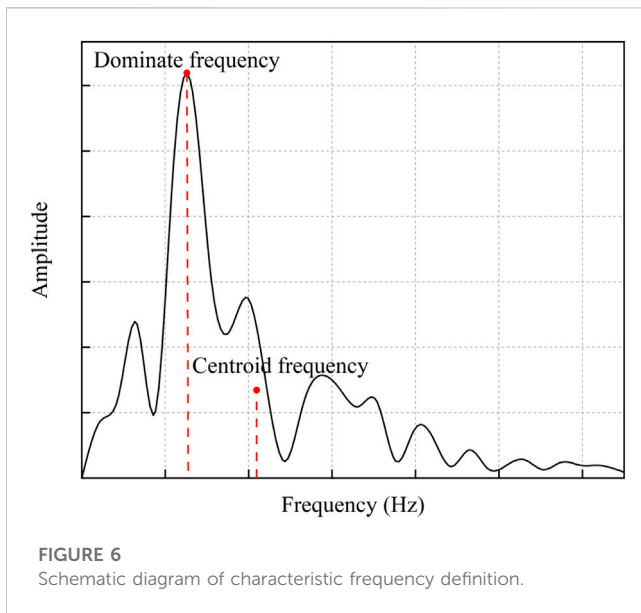
main characteristics of the frequency spectrum. This paper mainly
describes the spectrum characteristics in three aspects as shown in
Figure 6. Dominate frequency, Centroid frequency and Zero-
crossing frequency. The blasting vibration signal undergoes
Fourier transform to obtain the amplitude spectrum of the
vibration velocity, where the frequency corresponding to the
maximum amplitude of the vibration velocity amplitude
spectrum is the Fourier dominant frequency, and the
mathematical expression of the Fourier transform is as follows:

$$F(\omega) = \int_{-\infty}^{+\infty} v(t)e^{-j\omega t}dt \qquad (5)$$

where $F(\omega)$ is the Fourier amplitude spectrum. $v(t)$ and ω are the
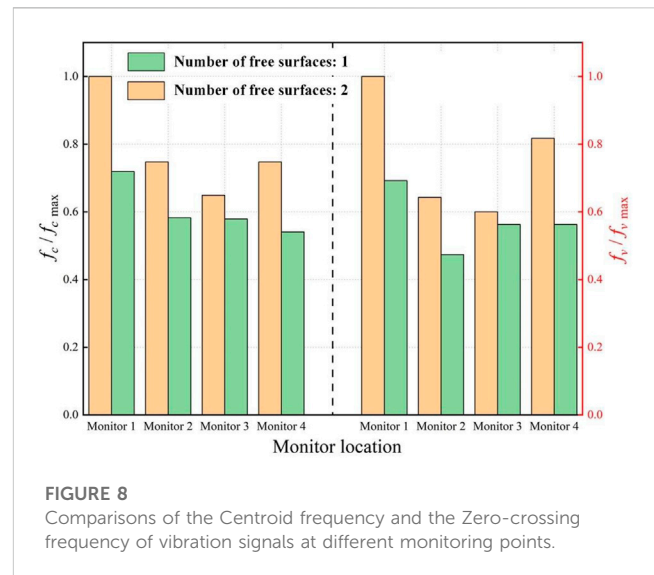vibration velocity of blasting and is the angular velocity, respectively.

Figure 7 shows the spectrum characteristics generated by
peripheral hole blasting with different free surface number. In
order to better compare the results of the tests, a ratio of the
current amplitude to the maximum amplitude is represented on
the Y-axis. But a change in Fourier dominant frequency occurs with
an increase in propagation distance, and there is no good linear
relationship with the propagation distance, which could not well
show the attenuation law of the frequency.

Except to the Fourier dominant frequency, the spectral
characteristics can also be described by the Fourier centroid
frequency proposed by Trivino et al. (2012). Blasting vibration
signals have a centroid frequency that corresponds to the
centroid of their velocity amplitude spectrum curves, and the
mathematical expression of the centroid frequency is as follows:

$$f_c = \sum_{i=1}^{n} A_i f_i \bigg/ \sum_{i=1}^{n} A_i \qquad (6)$$

where A_i is the amplitude corresponding to f_i in the amplitude
spectrum, f_i is any frequency in the amplitude spectrum and f_c is
the Fourier centroid frequency. The left half of Figure 8 shows
the centroid frequencies of vibrations generated by peripheral hole
blasting with different number of free surfaces.

Both the Fourier centroid frequency and the Fourier dominant
frequency need to be calculated to obtain the spectral characteristics,
while the value of the Zero-crossing frequency can be directly
obtained according to the abscissa of vibration velocity-time
curve monitored during blasting. The Zero-crossing frequency is
calculated by selecting the time corresponding to velocity-time curve
of blasting vibration peak velocity as half a cycle, the Zero-crossing
frequency is convenient to calculate and easy to obtain, which is a
method for preliminary estimation of blasting vibration frequency.
The right half of Figure 8 shows the Zero-crossing frequency of
vibration generated by peripheral hole blasting with different
number of free surfaces. The mathematical expression is:

$$f_v = \frac{1}{2\Delta t} \qquad (7)$$

where Δt is the time corresponding to the peak velocity and f_v is the Zero-crossing frequency.

According to the above test results, the longitudinal Fourier dominant frequency induced by peripheral hole blasting in different numbers of free surfaces decreases with increasing distance from monitoring point, and its centroid frequency and zero-crossing frequency also exhibit a attenuation rule. The smaller the number of free surfaces, the smaller the centroid frequency and zero crossing frequency at the same distance from the explosion source.

3.3 Energy analysis

By analyzing the blasting signal's PPV and frequency, we can have a clear understanding of the instantaneous change of the blasting signal. The analysis of blasting signal energy can comprehensively evaluate the velocity and duration of blasting signal. In this paper, wavelet transforms are used to analyze the energy of each frequency band of blasting signals. Using wavelet transform, the blasting signal is first decomposed into two components: High-frequency and low-frequency, and then the low frequency part is further decomposed into two parts, and so on. If the blasting signal has frequency 0~X, it can be decomposed into two parts: 0~X/2 and X/2~X high-frequency and low-frequency, and then the low-frequency part 0~X/2 is continue decomposed into 0~X/4 and X/4~X/2 until it is decomposed to a suitable frequency.

After the blasting signal is decomposed in n layers by wavelet transform, calculating the energy coefficient of each reconstructed signal is as follows:

$$E_{N,j}(t) = \sum_{t=1}^{m} \left| f_{N,j}(t) \right|^2 \qquad (8)$$

where $f_{N,j}(t)$ represents the reconstruction energy of the j frequency band in the N layer and $E_{N,j}(t)$ represents the energy coefficient of reconstructed signal.

Following are the characteristics of energy distribution in different frequency bands under blasting vibration:

$$W_{N,j} = E_{N,j}(t) \Big/ \sum_{j=0}^{2^{N}-1} E_{N,j}(t) \qquad (9)$$

where the energy percentage of different frequency bands under blasting vibration is given by $W_{N,j}$.

Wavelet transform is used to calculate the energy distribution of blasting signals in different frequency bands, to obtain the best decomposition effect, the appropriate number of decomposition layers and wavelet basis must be determined (Ling and Xi-Bing, 2004). Decomposition layers is determined according to the specific blasting signal and blasting vibration measurement instrument's minimum working frequency, in this experiment, the signal sampling frequency of the blasting vibration measurement instrument is 4,800 Hz. Nyquist's sampling theorem states, the highest frequency that can be recorded by this blasting vibration measurement instrument is 2,400 Hz. According to the minimum working frequency of the blasting vibration measurement instrument in this test and avoiding the distortion in the process of decomposition, the decomposition layers number is determined to
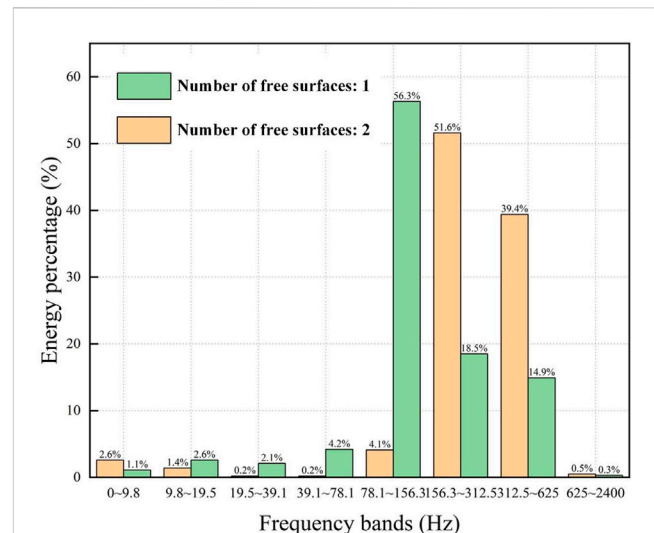

FIGURE 9
The monitoring point 1 percentage of energy distribution in different frequency bands.

be 8 layers and the minimum frequency band is 0~9.77 Hz. Due to the diversity of wavelet basis types, the selection of wavelet basis determines the quality of signal decomposition, the Daubechies' wavelets have the characteristics of biorthogonality, tight support, approximate symmetry and fast calculation, which makes it effective in blasting signal processing, therefore, according to the characteristics of blasting signal and the requirements of wavelet basis determination, 8th-order Daubechies is used in the previous research.

Taking monitoring point 1 as an example, Figure 9 shows the energy distribution in different longitudinal frequency bands induced by peripheral hole blasting under different free surface number. In the case of 1 free surface, the frequency band of blasting vibration induced by peripheral hole blasting is mainly concentrated in 78.1 Hz–156.3 Hz, accounting for 56.3% of the total energy, and the energy in the 156.3 Hz–312.5 Hz frequency band accounts for 18.5% of the total energy. In the case of 2 free surfaces, the frequency band of blasting vibration induced by peripheral hole blasting is also mainly concentrated in 78.1 Hz–156.3 Hz, accounting for 51.6% of the total energy. The energy in the 78.1 Hz–156.3 Hz frequency band accounts for 4.1% of the total energy, and the energy in the 312.5 Hz–625 Hz frequency band accounts for 39.4% of the total energy. According to the results, the ratio of high-frequency energy induced by peripheral hole blasting with 2 free surfaces is greater than with 1 free surface.

Through comparative analysis of test results from the field, this can be found that under the condition that the blasting parameters and geological conditions are approximately the same, the higher the number of free surfaces, the lower the vibration velocity induced by peripheral hole blasting, the higher the vibration frequency, and the higher the proportion of high-frequency vibration energy in the total energy.

When the number of free surfaces is 2, the crushing resistance and movement resistance of the rock mass in the blasting layer are relatively small, which makes it easier for the explosive gas to escape from the cracks and stay in the blast hole for a shorter time, resulting in a decrease in the rise time and duration of pressure on the rock mass. As the working time decreases, the spectrum of blasting load
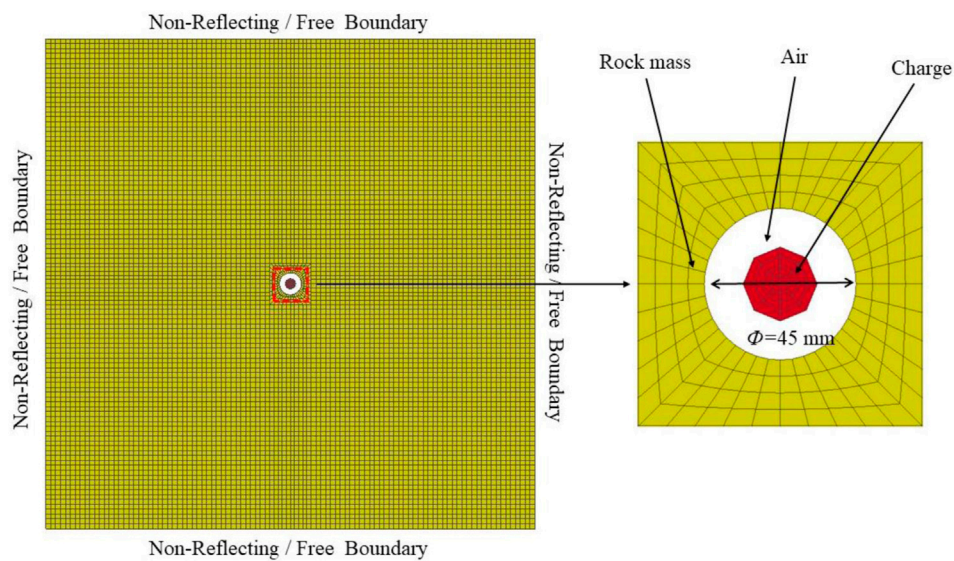
FIGURE 10
Numerical model.
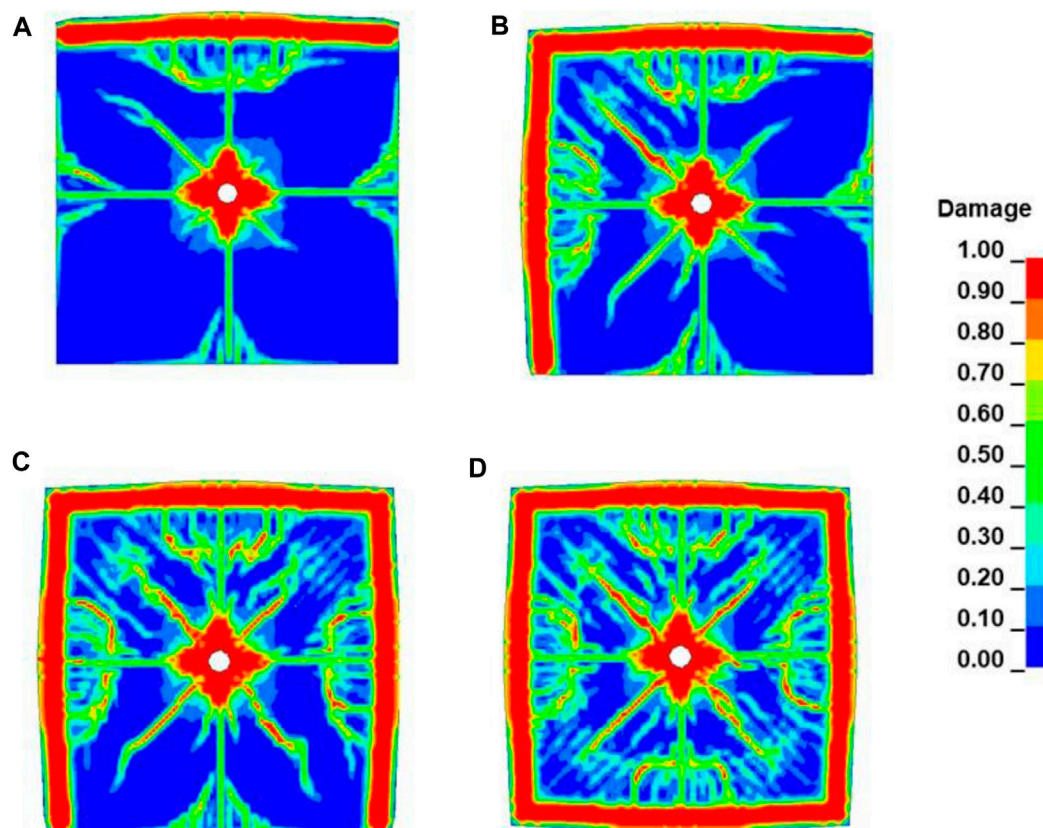
FIGURE 11
The failure characteristics of rock after blasting with different number of free surfaces: **(A–D)** indicate that the number of free surfaces is 1, 2, 3, and 4 respectively.

will move towards high frequencies, which naturally leads to high frequency vibration. During the propagation process of blasting induced stress waves, when the stress waves propagate to the free surface, they are reflected as sparse waves that propagate in a reverse direction. The superposition of the reflected waves and the initial stress waves results in a decrease in the intensity of the stress waves, a decrease in the blasting load pressure, and a decrease in the blasting load pressure resulting in a decrease in the induced vibration intensity. Therefore, when the number of free surfaces is 2, the vibration speed is lower than when the number of free surfaces is 1. On the other hand, due to the greater resistance to rock mass breakage and movement when the number of free surfaces is 1, explosive gas is not easy to escape from the cracks. A large amount of explosive gas exists in the blast hole for a long time, and more energy is converted into vibration energy, which can induce higher vibration velocities. The results show that the vibration induced by peripheral hole blasting with a number of free surfaces of 1 is higher than that with a number of free surfaces of 2. In addition, at a certain frequency, the greater the velocity of blasting induced vibration, the greater the damage to the structure. At a certain speed, due to the lower natural frequency of buildings, low-frequency vibration is more likely to cause structural damage. When the number of free surfaces is 2, from the perspective of vibration caused by peripheral hole blasting, it can reduce the vibration speed caused by blasting, move the spectrum structure towards high frequency, and effectively reduce the damage to the structure caused by blasting vibration.

4 Numerical simulation results

As shown in Figure 10, a single hole numerical model was established to analyze the fragmentation effect of rock mass after blasting. Because the blast hole's length is much larger than its diameter, in order to improve the computational efficiency, a simplified two-dimensional model of plane strain was established, using an uncoupled charge structure with a blast hole diameter of 45 mm and an explosive diameter of 22 mm. The interaction of air, explosives, and rock mass was simulated by combining the Fluid-Structure Interaction algorithm with the Arbitrary Lagrangian-Eulerian method. The number of free surfaces is controlled by setting the boundaries of the rock as free boundary conditions and non reflective boundary conditions. Riedel Hiermaier-Thoma (RHT) model is used as a material model for rock masses in this paper due to its excellent ability to simulate rock fragmentation and fracture using cumulative damage indicators (Wang et al., 2021). For more detailed information on RHT model parameters in this article, refer to references (Xie et al., 2016; Liu et al., 2018; Li et al., 2021).

Figure 11 shows the failure characteristics of rock mass after blasting with different number of free surfaces. Figures 11A–D display the failure characteristics when the number of free surfaces is 1, 2, 3, and 4, respectively. The darker the red color, the more obvious the damage characteristics are. From the research results in Figure 11, it can be found that the rock mass with a free surface has more obvious damage near the free surface after blasting,
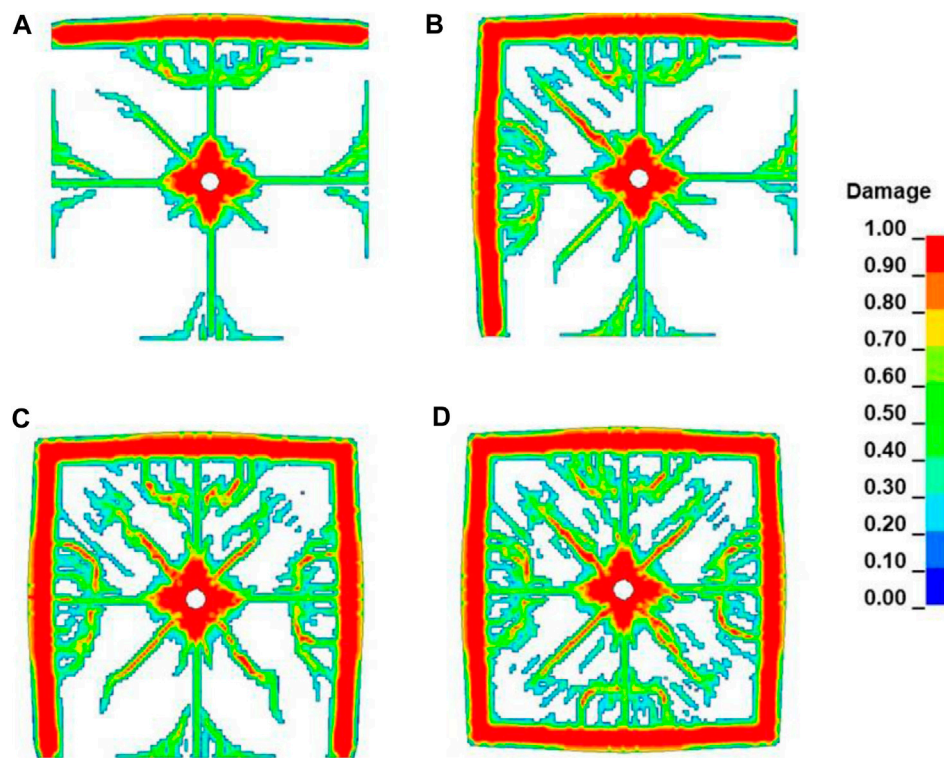
FIGURE 12
The number of blasting induced cracks under different number of free surfaces: (A–D) indicate that the number of free surfaces is 1, 2, 3, and 4, respectively.

possibly due to the formation of tensile stress waves after the stress waves generated after blasting are reflected on the free surface, and the tensile strength of the rock is often much smaller than the compressive strength, so the rock is more prone to damage under the action of tensile stress waves. From the research results, it can also be found that with the increase in the number of free surfaces of rock, the degree of fragmentation of rock after blasting increases significantly. Figure 12 shows the number of cracks in rock masses with different number of free surfaces after blasting. It can also be found that the more free surfaces, the more cracks in the rock mass after blasting.

5 Conclusion

The damage of structures under blasting is directly related to the vibration caused by blasting. A detailed understanding of the propagation law of blasting vibration can better evaluate the harm of blasting vibration. This article studies the propagation law of vibration induced by blasting in the surrounding holes of tunnels with the number of free surfaces through on-site experiments and numerical simulation experiments, and draws the following main conclusions:

(1) The number of free surface has a significant impact on PPV caused by peripheral hole blasting. Under the same blasting parameters and propagation medium, the fewer the number of free surfaces, the higher the PPV caused by peripheral hole blasting.
(2) The number of free surface has a significant influence on the frequency of vibration signals caused by peripheral hole blasting. The smaller the number of free surface, the smaller the centroid frequency and zero crossing frequency.
(3) The number of free surface has a significant impact on the frequency band energy caused by the peripheral hole blasting. The higher the number of free surfaces, the greater the high-frequency energy ratio of peripheral hole blasting.
(4) The number of free surface has a great influence on the degree of rock fragmentation after blasting. With the increase of the number of free surface of rock, the degree of rock fragmentation becomes more obvious after blasting.

Data availability statement

The original contributions presented in the study are included in the article/supplementary material, further inquiries can be directed to the corresponding author.

References

Aldas, G. G. U. (2010). Explosive charge mass and peak particle velocity (PPV)-frequency relation in mining blast. *J. Geophys. Eng.* 7, 223–231. doi:10.1088/1742-2132/7/3/001

Blair, D. P., and Armstrong, L. W. (2001). The influence of burden on blast vibration. *Fragblast* 5, 108–129. doi:10.1076/frag.5.1.108.3315

Duvall, W. I., and Fogelson, D. E. (1962). Review of criteria for estimating damage to residences from blasting vibration. https://xueshu.baidu.com/usercenter/paper/show?paperid=2af0ef4bf56d48e7057ab5874a8f6936&site=xueshu_se.

Favreau, R. F. (1969). Generation of strain waves in rock by an explosion in a spherical cavity. *J. Geophys. Res.* 74, 4267–4280. doi:10.1029/JB074i017p04267

Conflict of interest

Authors RL and SG were employed by Guangxi Xinfazhan Communication Group Co. Ltd.

The remaining authors declare that the research was conducted in the absence of any commercial or financial relationships that could be construed as a potential conflict of interest.

Publisher's note

All claims expressed in this article are solely those of the authors and do not necessarily represent those of their affiliated organizations, or those of the publisher, the editors and the reviewers. Any product that may be evaluated in this article, or claim that may be made by its manufacturer, is not guaranteed or endorsed by the publisher.

Hu, Y., Lu, W., Chen, M., Yan, P., and Yang, J. (2014). Comparison of blast-induced damage between presplit and smooth blasting of high rock slope. *Rock Mech. Rock Eng.* 47, 1307–1320. doi:10.1007/s00603-013-0475-7

Li, X. P., Huang, J. H., Luo, Y., and Chen, P. P. (2017). A study of smooth wall blasting fracture mechanisms using the Timing Sequence Control Method. *Int. J. Rock Mech. Min. Sci.* 92, 1–8. doi:10.1016/j.ijrmms.2016.12.001

Li, X., Zhu, Z., Wang, M., Wan, D., Zhou, L., and Liu, R. (2021). Numerical study on the behavior of blasting in deep rock masses. *Tunn. Undergr. Space Technol.* 113, 103968. doi:10.1016/j.tust.2021.103968

Ling, T. H., and Xi-Bing, L. I. (2004). Laws of energy distribution in different frequency bands for blast vibration signals. *J. Central South Univ. Technol. Sci.*, 310–315.

Liu, K., Li, Q., Wu, C., Li, X., and Li, J. (2018). A study of cut blasting for one-step raise excavation based on numerical simulation and field blast tests. *Int. J. Rock Mech. Min. Sci.* 109, 91–104. doi:10.1016/j.ijrmms.2018.06.019

Liu, K., and Liu, B. (2017). Optimization of smooth blasting parameters for mountain tunnel construction with specified control indices based on a GA and ISVR coupling algorithm. *Tunn. Undergr. Space Technol.* 70, 363–374. doi:10.1016/j.tust.2017.09.007

Lu, W., Chen, M., Geng, X., Shu, D., and Zhou, C. (2012). A study of excavation sequence and contour blasting method for underground powerhouses of hydropower stations. *Tunn. Undergr. Space Technol.* 29, 31–39. doi:10.1016/j.tust.2011.12.008

Lu, W., Leng, Z., Hu, H., Chen, M., and Wang, G. (2018). Experimental and numerical investigation of the effect of blast-generated free surfaces on blasting vibration. *Eur. J. Environ. Civ. Eng.* 22, 1374–1398. doi:10.1080/19648189.2016.1262285

Lu, W., Zhang, L., Zhou, J., Jin, X., Chen, M., and Yan, P. (2013). Theoretical analysis on decay mechanism and law of blasting vibration frequency. *Blasting* 30, 1–6+11. doi:10.3963/j.issn.1001-487X.2013.02.001

Ma, G. W., Hao, H., and Zhou, Y. X. (2000). Assessment of structure damage to blasting induced ground motions. *Eng. Struct.* 22, 1378–1389. doi:10.1016/S0141-0296(99)00072-3

Noret, E., Prod'homme, G., Yalamas, T., Reimeringer, M., Hanus, J.-L., and Duong, D.-H. (2012). Safety of atmospheric storage tanks during accidental explosions. *Eur. J. Environ. Civ. Eng.* 16, 998–1022. doi:10.1080/19648189.2012.699740

Peng, Y., Liu, G., Wu, L., Zuo, Q., Liu, Y., and Zhang, C. (2021). Comparative study on tunnel blast-induced vibration for the underground cavern group. *Environ. Earth Sci.* 80, 68. doi:10.1007/s12665-020-09362-z

Qiu, X., Shi, X., Gou, Y., Zhou, J., Chen, H., and Huo, X. (2018). Short-delay blasting with single free surface: Results of experimental tests. *Tunn. Undergr. Space Technol.* 74, 119–130. doi:10.1016/j.tust.2018.01.014

Singh, P. K., and Roy, M. P. (2010). Damage to surface structures due to blast vibration. *Int. J. Rock Mech. Min. Sci.* 47, 949–961. doi:10.1016/j.ijrmms.2010.06.010

Trivedi, R., Singh, T. N., and Raina, A. K. (2014). Prediction of blast-induced flyrock in Indian limestone mines using neural networks. *J. Rock Mech. Geotechnical Eng.* 6, 447–454. doi:10.1016/j.jrmge.2014.07.003

Trivino, L. F., Mohanty, B., and Milkereit, B. (2012). Seismic waveforms from explosive sources located in boreholes and initiated in different directions. *J. Appl. Geophys.* 87, 81–93. doi:10.1016/j.jappgeo.2012.09.004

Uysal, O., Arpaz, E., and Berber, M. (2007). Studies on the effect of burden width on blast-induced vibration in open-pit mines. *Environ. Geol.* 53, 643–650. doi:10.1007/s00254-007-0679-9

Wang, H., Wang, Z., Wang, J., Wang, S., Wang, H., Yin, Y., et al. (2021). Effect of confining pressure on damage accumulation of rock under repeated blast loading. *Int. J. Impact Eng.* 156, 103961. doi:10.1016/j.ijimpeng.2021.103961

Xia, X., Li, H. B., Li, J. C., Liu, B., and Yu, C. (2013). A case study on rock damage prediction and control method for underground tunnels subjected to adjacent excavation blasting. *Tunn. Undergr. Space Technol.* 35, 1–7. doi:10.1016/j.tust.2012.11.010

Xia, X., Li, H., Liu, Y., and Yu, C. (2018). A case study on the cavity effect of a water tunnel on the ground vibrations induced by excavating blasts. *Tunn. Undergr. Space Technol.* 71, 292–297. doi:10.1016/j.tust.2017.08.026

Xie, L. X., Lu, W. B., Zhang, Q. B., Jiang, Q. H., Wang, G. H., and Zhao, J. (2016). Damage evolution mechanisms of rock in deep tunnels induced by cut blasting. *Tunn. Undergr. Space Technol.* 58, 257–270. doi:10.1016/j.tust.2016.06.004

Yang, J., Cai, J., Yao, C., Li, P., Jiang, Q., and Zhou, C. (2019). Comparative study of tunnel blast-induced vibration on tunnel surfaces and inside surrounding rock. *Rock Mech. Rock Eng.* 52, 4747–4761. doi:10.1007/s00603-019-01875-9

Yang, J. H., Lu, W. B., Jiang, Q. H., Yao, C., and Zhou, C. B. (2016a). Frequency comparison of blast-induced vibration per delay for the full-face millisecond delay blasting in underground opening excavation. *Tunn. Undergr. Space Technol.* 51, 189–201. doi:10.1016/j.tust.2015.10.036

Yang, J., Lu, W., Jiang, Q., Yao, C., Jiang, S., and Tian, L. (2016b). A study on the vibration frequency of blasting excavation in highly stressed rock masses. *Rock Mech. Rock Eng.* 49, 2825–2843. doi:10.1007/s00603-016-0964-6

Yilmaz, O., and Unlu, T. (2013). Three dimensional numerical rock damage analysis under blasting load. *Tunn. Undergr. Space Technol.* 38, 266–278. doi:10.1016/j.tust.2013.07.007

Zhou, Z., Cheng, R., Cai, X., Jia, J., and Wang, W. (2019). Comparison of presplit and smooth blasting methods for excavation of rock wells. *Shock Vib.* 2019, 1–12. doi:10.1155/2019/3743028

Experimental study on the hydraulic fracture propagation of laminar argillaceous limestone continental shale

Zilin Zhang[1,2], Anhai Zhong[2], Feng Yang[2], Liaoyuan Zhang[2], Mingjing Lu[2], Lu Chai[1] and Lianchong Li[1]*

[1]School of Resources and Civil Engineering, Northeastern University, Shenyang, China, [2]Research Institute of Petroleum Engineering Technology, Shengli Oilfield Branch Company SINOPEC, Dongying, China

Laminar argillaceous limestone continental shale is an important oil reservoir in Jiyang Depression, Bohai Bay Basin of China. Affected by the laminar structure, the spatial propagation morphology of hydraulic fracturing is not clear. To reveal the propagation law of hydraulic fracturing pathway in laminar marl continental shale, the mineral content and basic rock mechanics test are firstly carried out on the cores from the wells in Jiyang Depression. Secondly the similar material cores with standard-size and large-size are manufactured and processed. Finally, combined with physical model experiments, acoustic emission and moment tensor inversion techniques, the hydraulic fracturing experiments on the large-size cores under different stress differences are conducted. The experimental results show that the *in situ* stress (confining stresses), laminar structure, and lithological distribution jointly affect the propagation mode of fractures. As the horizontal stress difference increases, the stimulated reservoir volume gradually decreases, and the number of shear fractures decreases accordingly. Macroscopically, the pump pressure curve shows obvious fluctuation in the case with lower horizontal stress difference, which is the external performance of hydraulic fracture initiation−obstruction−turning−penetrating−obstruction−turning. The content of brittle and plastic minerals has a significant impact on the fracture complexity, particularly the layers with high argillaceous content have a significant inhibitory effect on fracture propagation. The weakly cemented lamination or bedding plane is easy to capture the fracture and make it propagate along the bedding plane, thereby increasing the complexity of fracture network. The research results are expected to provide a theoretical reference for design and optimization of hydraulic fracturing parameter in continental shale oil exploration and development.

KEYWORDS

continental shale, hydraulic fracturing, fracture propagation, acoustic emission monitoring, true triaxial experiment

1 Introduction

The favorable lithofacies of the continental shale in Jiyang depression mostly consists of laminated argillaceous limestone. The reservoir is mainly located in Es2, Es3, and Es4 sections with carbonate content as the primary brittle mineral. The brittle mineral generally incorporates brittle mineral more than 60% in content. The test development of

FIGURE 1
Laminar argillaceous limestone cores.
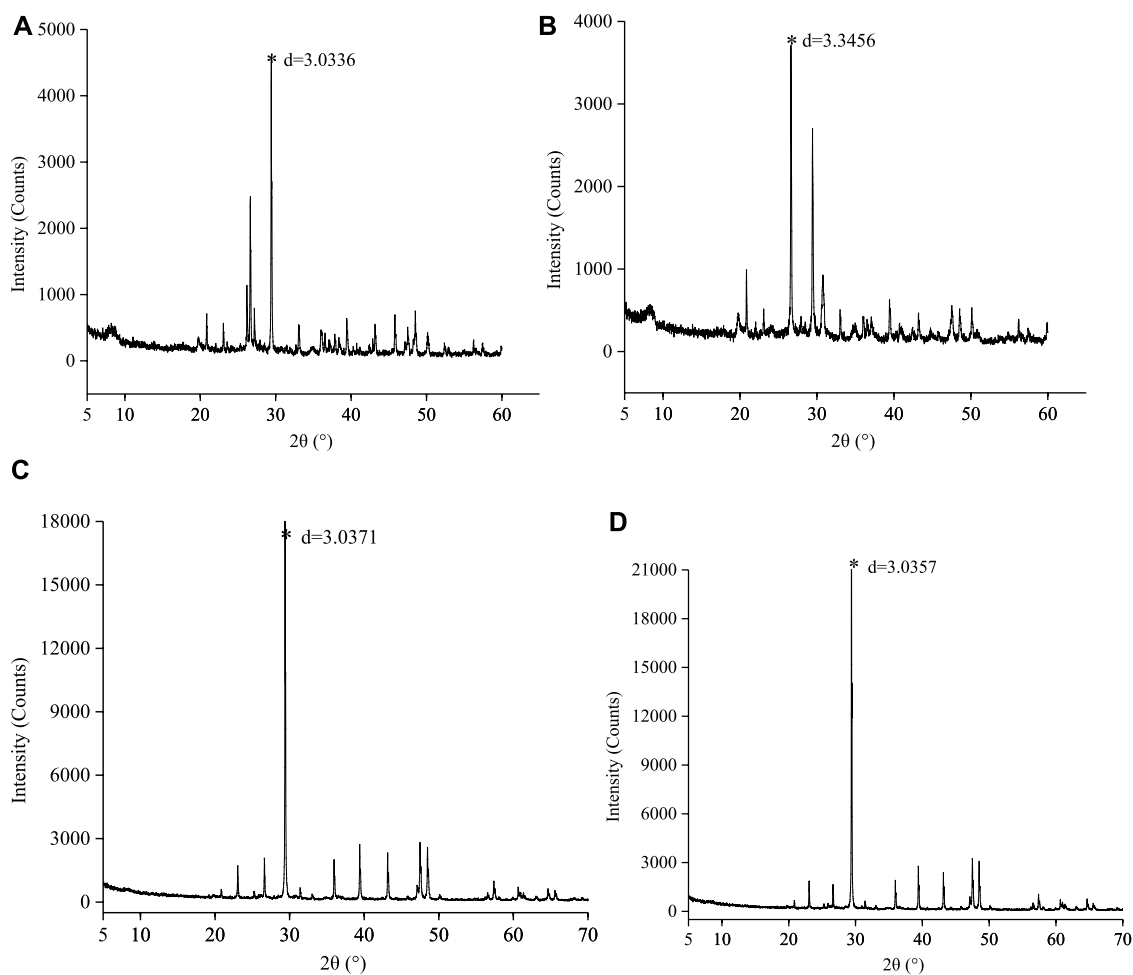
FIGURE 2
XRD mineral content characteristic value d of cores **(A)** Core form well X1, **(B)** Core form well X2, **(C)** Core form well X3, and **(D)** Core form well X4.

TABLE 1 Mineral content analysis of the cores.

Well	Depth (m)	Content (%)									
		Quartz	Potassium feldspar	Plagioclase	Calcite	Dolomite	Iron dolomite	Pyrite	Anhydrite	Total clay	Siderite
X1	4221.0	9.1	0.0	0.7	0.0	68.2	0.0	1.5	0.3	1.2	19.1
X2	3653.1	23.5	0.1	1.5	30.7	0.0	0.0	4.0	1.1	17.6	21.4
X3	3678.0	7.2	0.0	0.2	86.0	0.0	0.9	1.6	0.0	3.9	0.3
X4	3054.2	7.3	0.0	0.3	85.8	1.6	0.0	2.7	0.0	2.3	0.0

FIGURE 3
Limestone cores (low clay content) and argillaceous cores (high clay content) **(A)** The cores for uniaxial compression experimental test, and **(B)** Stress-strain curves.
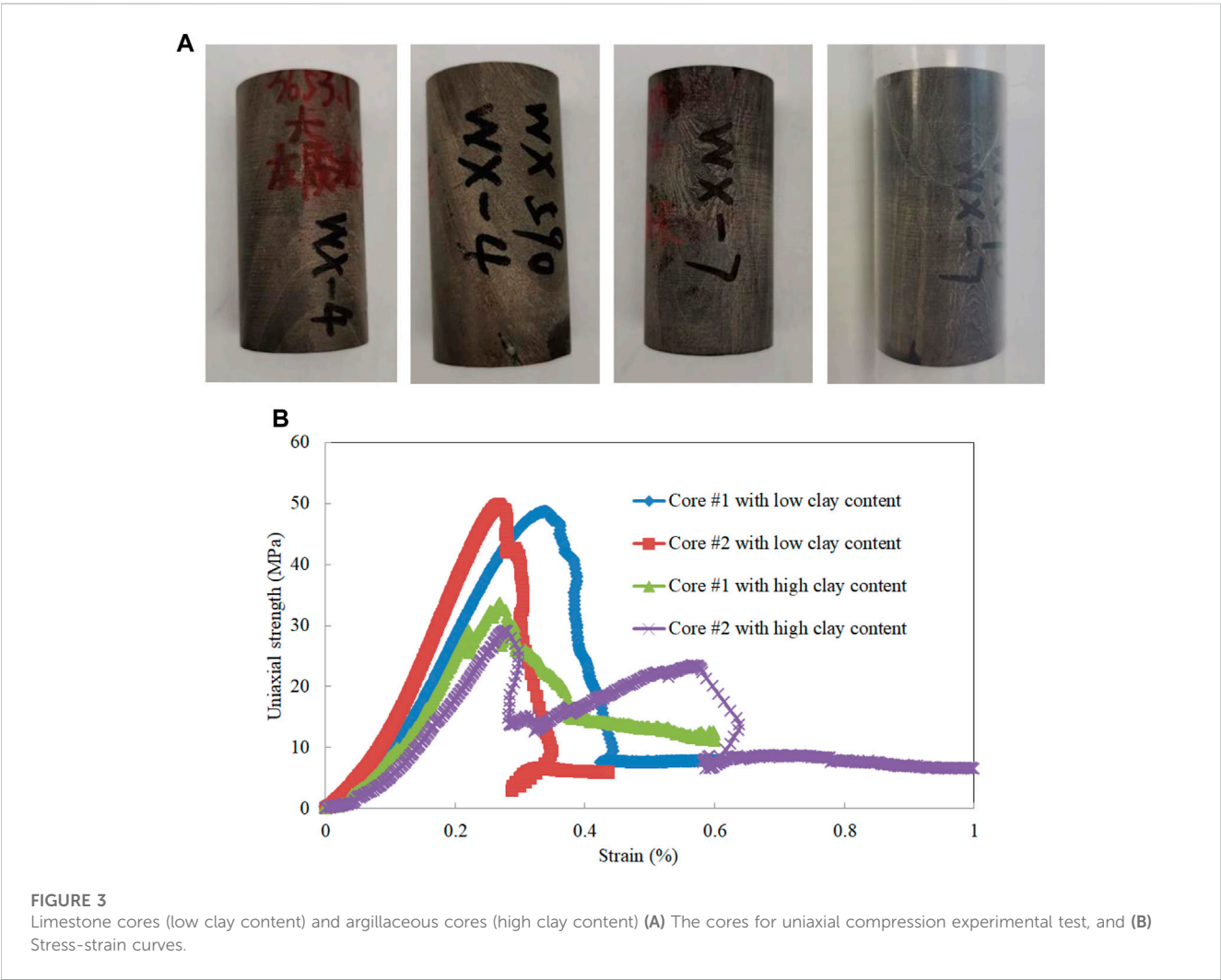
continental shale reservoir in the early stage in Shengli Oilfield showed that the pump pressure in field fluctuated significantly, and there is also a significant difference in the amount of sand added to each fracturing section. The reason for these phenomena has not yet been fully clarified.

As a complex lithofacies, shale shows significant anisotropy, with a complex failure pattern greatly impacted by stress difference (Vasin et al., 2013; Wu et al., 2016; Weijermars et al., 2020). Stanchits et al. (2015); Li et al. (2018); Jiang et al. (2020) adopted acoustic emission (AE) and tracer to conduct the

hydraulic fracturing test on the thick interlayer, and analyzed the pump pressure curve and AE signal from the perspective of energy. Based on the analysis of the mineral content in shale, (Zhang et al., 2016; Hattori et al., 2017) found that the high brittleness were more likely to lead to more multi-branch and turning fractures under the external load. Zhao et al. (2014); Dan et al. (2015) investigated the sensitivity of each influencing factor due to the pattern of hydraulic fracture propagation when the process pipeline and shale lamination formed different angles. Taghichian et al. (2014); Garcia-Teijeiro et al. (2016); Ju et al.

FIGURE 4
Shale cores before and after Brazil splitting.
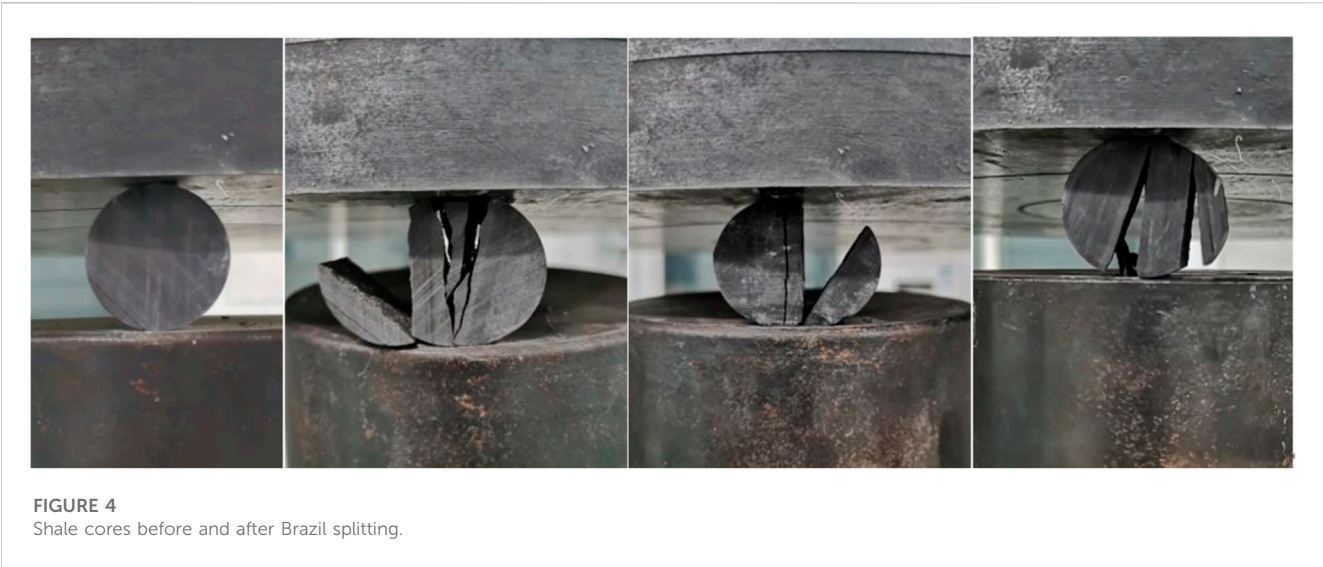
TABLE 2 Brazilian splitting test results of shale core.

Number	Well	Depth (m)	Peak load (kN)	Tensile strength (MPa)	Average strength (MPa)
1	X2	3653.1	0.78	1.59	1.76
2	X2	3653.1	0.94	1.92	
3	X2	3653.1	0.86	1.76	

FIGURE 5
Standard size artificial cores **(A)** before demoulding **(B)** after demoulding.

FIGURE 6
Artificial rock cores after experiment **(A)** Uniaxial compression **(B)** Brazilian splitting.

TABLE 3 Comparison of mechanical parameters between natural core and artificial core.

		UCS (MPa)	Tensile strength (MPa)	Elastic modulus (GPa)
Natural cores	argillaceous rock	33.4	1.59	17.4
	Limestone	50.2	1.92	23.5
Artificial cores	argillaceous rock	23.2	1.41	13.5
	Limestone	35.5	1.85	18.2

(2020) studied the cracking behaviors such as the approaching, shearing, penetrating, and steering of the hydraulic fractures caused by the induced stress in the crack tip. It has been pointed out that the mechanical parameters and brittleness difference resulting from the physical anisotropy of shale reservoir had a significant impact on the selection of fracturing block and optimization of hydraulic fracturing parameter (Rogers et al., 2010; Thomsen, 2013; Almutairi, 2014; Ghahfarokhi, 2017). Weijers et al. (2000); McClure and Horne (2013); Lu et al. (2015); Ju et al. (2019) optimized the fracturing parameter using numerical simulation and found that the stimulated reservoir volume (SRV) and oil–gas production after fracturing are closely positively correlated. With the improvement of experimental technology, some scholars have carried out many new experiments on hydraulic fracturing in recent years, including experiments with new similar materials (Abe et al., 2021; Wang et al., 2021; Zhai et al., 2021; Yang et al., 2022; Zheng et al., 2022).

To further reveal the influence of the laminar structure on spatial morphology of fracture propagation, in this study, the mineral content and basic rock mechanics test are firstly carried out on the cores from the wells in Jiyang Depression. Secondly the similar material cores with standard-size and large-size are manufactured and processed. Finally, combined with physical model experiments, acoustic emission and moment tensor inversion techniques, the hydraulic fracturing experiments on the large-size cores under different stress differences are conducted.

2 Mechanical parameters analysis of rock core

The continental shale cores in this study were taken from well X1 4221 m in depth, well X2 3653.1 m in depth, well X3 3678 m in depth and well X4 3054.2 m in depth in Shengli Oilfield. The marl content of each core was calculated by XRD technique. Uniaxial
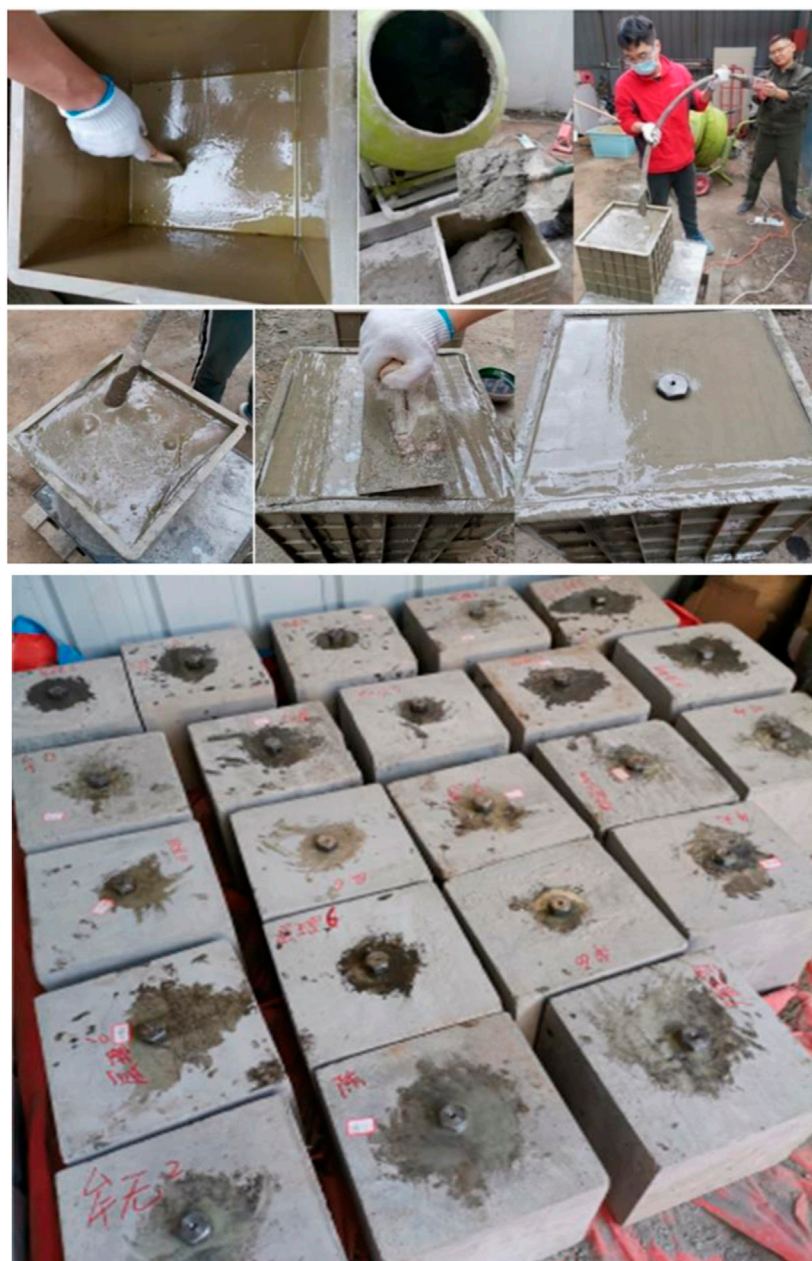
FIGURE 7
Pouring process of similar material cores for hydraulic fracturing test.

compression strength and tensile strength of cores were tested by Rockman rock mechanics experimental machine.

2.1 Mineral content of cores

X-ray diffraction (XRD) technology was used to test the mineral content of typical cores as shown in Figure 1. According to the 2θ-d conversion table, as shown in Figure 2, the corresponding minerals of d value at each peak point were found in order to determine the mineral composition content, and the whole-rock mineral analysis results were obtained. The content of each argillo–calcareous core

are shown in Table 1. Although the mineral composition of rock core is not a mechanical parameter, the experiment in this section provides a basic reference for the subsequent preparation of artificial rock cores, as the content of brittle and plastic minerals in the argillaceous limestone continental shale has a significant impact on the complexity of fracturing fractures. When preparing artificial rock cores in subsequent Section 3, it is necessary to refer to the proportion of clay and limestone mineral content.

Calcareous minerals were mainly dolomite and calcite, with few other carbonate materials, while argillaceous minerals were mainly clay, with a small amount of quartz, potassium feldspar, and plagioclase. A higher content of calcareous minerals leads to
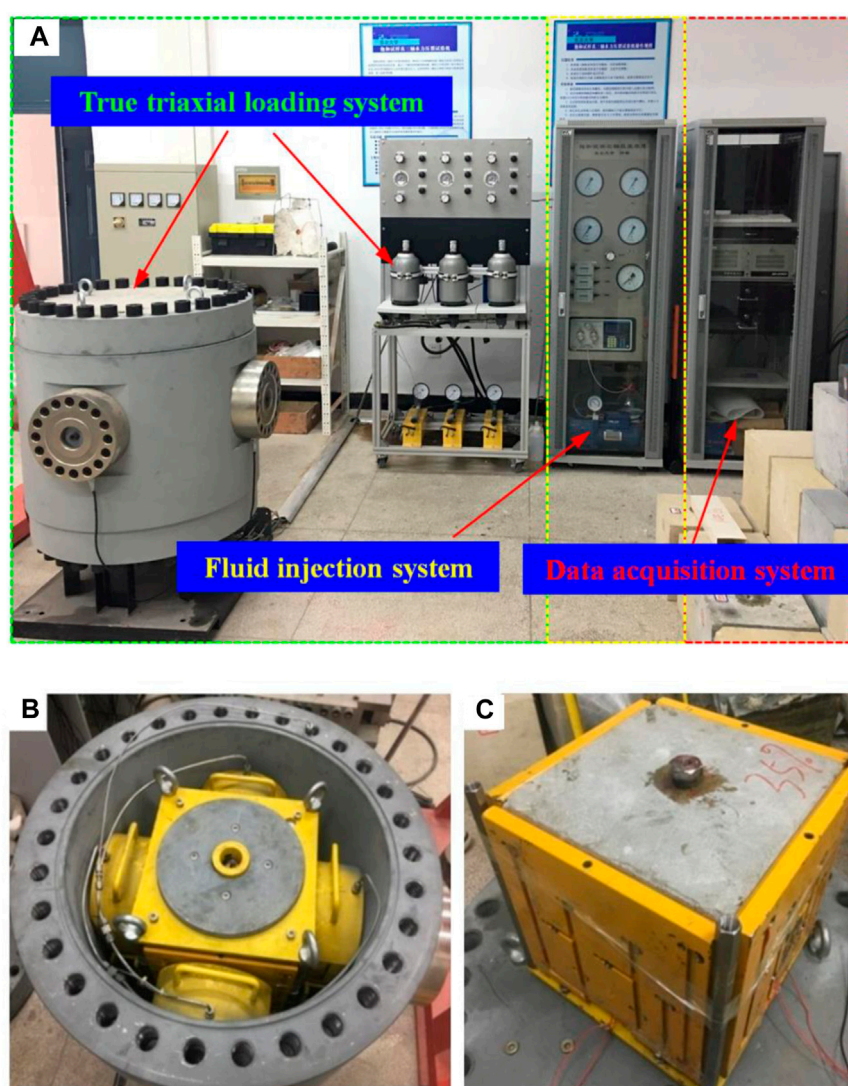
FIGURE 8
True triaxial hydraulic fracturing test system **(A)** the general machine configuration, **(B)** attaching AE probes, and **(C)** placing the specimen into triaxial servo loading system.

stronger brittleness, making it more likely to be fracture initiation and thus form complex fracture network; a higher content of argillaceous minerals leads to stronger plasticity, making it less likely to be fracture initiation and thus form simple flat fracture. As observed, the calcareous content could be as large as 50%–80% and each core had great difference in its mineral content. Thus, relying on merely the mineral content would be helpful to fully classify and assess the brittleness and compressibility core or reservoir.

2.2 Uniaxial compression strength and tensile strength

The above shale cores were processed into cylindrical cores with 50 mm in diameter and 25 mm in height in the laboratory. Four

cores were selected to conduct uniaxial compression test. Figure 3 is the cores and the corresponding stress-strain curves. The experimental results show there is a good consistency between the strength characteristics of rock cores and mineral content. The strength of limestone is significantly higher than that of clay rock, and its brittleness is also significantly better than that of argillaceous rock, which indicates that the complexity of hydraulic fractures in limestone may be higher. The purpose of the mechanical parameters analysis of rock core is to provide a basic reference for subsequent artificial core parameters, to ensure that the mechanical parameters of artificial cores do not deviate significantly.

The core was also processed into a standard cylinder with 25 mm in diameter and 12.5 mm in height. Corresponding to the uniaxial compression test above, three cores from Well X2 in 3653.1 m depth were selected to conduct Brazilian splitting test. The test results are shown in Figure 4 and Table 2. As shown in

FIGURE 9
The acoustic emission monitoring system **(A)** AE workstation and **(B)** amplifier.

FIGURE 10
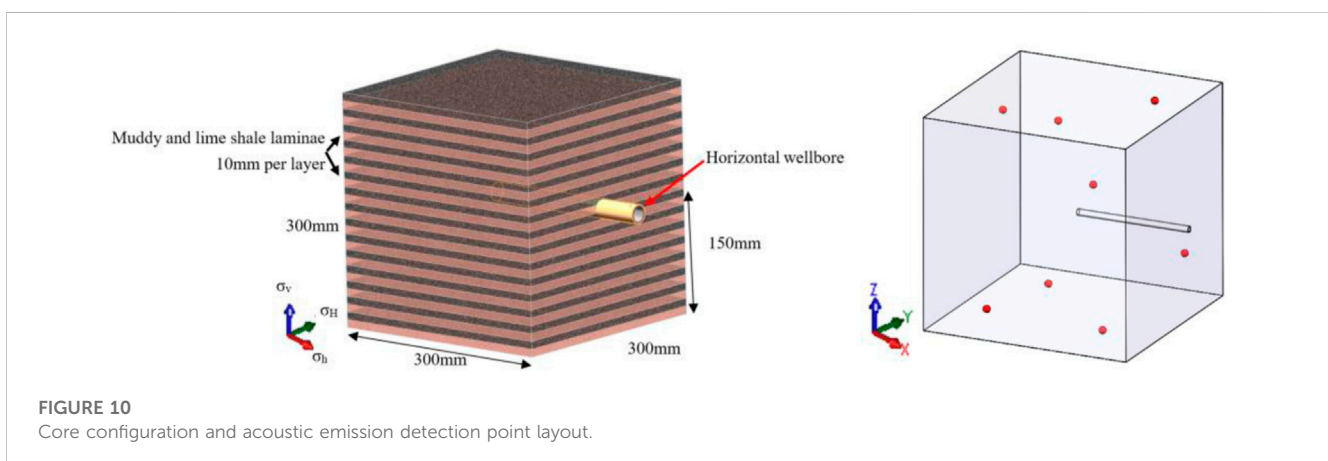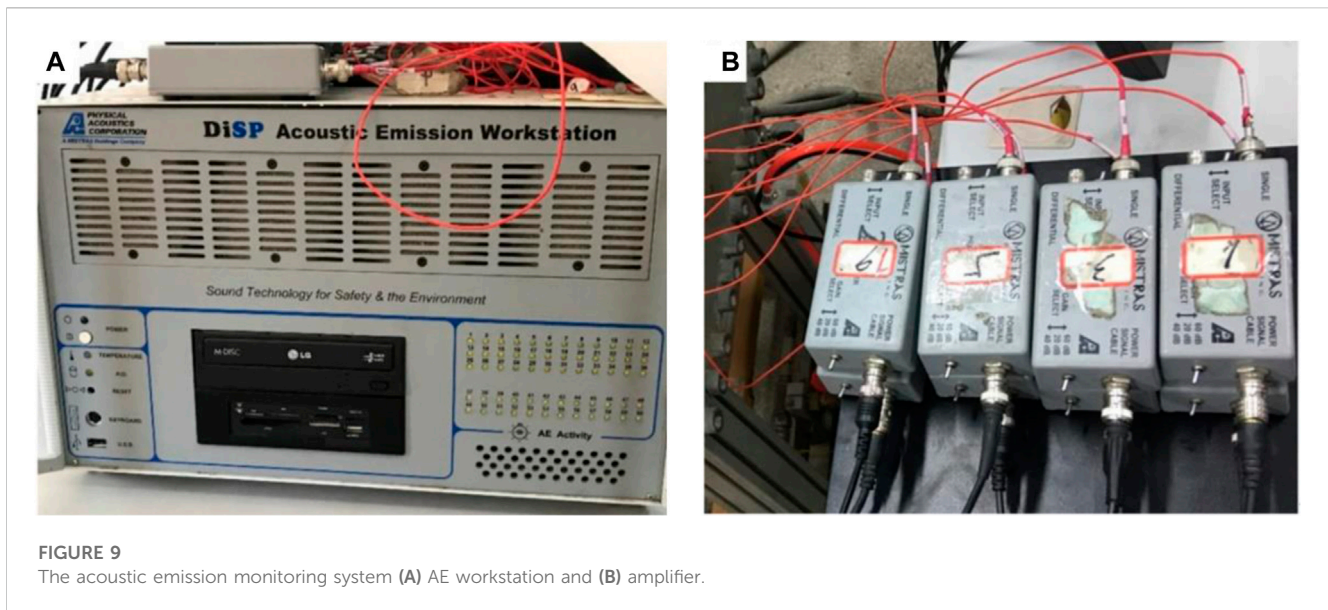Core configuration and acoustic emission detection point layout.

Figure 4, the core tensile failure occurred along the bedding plane. Shale cores all showed multiple fracture surfaces, implying that most lamina or bedding plane has low cementation strength. During hydraulic fracturing, weakly cemented stratification tended to "capture" fractures and cause them to spread along the stratification interface, thus increasing fracture bandwidth and constraining fracture propagation in the direction of fracture height. If the hydraulic fracture was needed to effectively connect the reservoir area longitudinally, it was suggested to adopt construction measures with large pump rate and high viscosity to promote the propagation of the fracture height.

3 Experimental test of hydraulic fracture in similar material cores

Due to the difficulty in collecting large-size deep cores *in situ* (Sharifigaliuk et al., 2021), this study utilized similar materials to setup rock cores and perform hydraulic fracturing test.

3.1 Artificial cores production

Before pouring large-sized rock cores, standard cylindrical rock cores were also poured to determine the mechanical parameters of similar materials. In general, 32.5 Portland cement, 20–40 mesh quartz sand, 325 mesh Kaolin (China Clay), and water were used for artificial core production. Figure 5 shows the standard cylindrical rock cores of similar materials poured. Correspondingly, their rock mechanics parameters are tested on the Rockman rock mechanics machine. Cores of similar materials after testing are shown in Figure 6. The summarized mechanical parameters of similar material cores and *in situ* continental shale cores are listed in Table 3. The modulus and strength parameters of the two types of rock cores basically meet the similarity criteria. After several times of matching, the ratio of cement, sand, and Kaolin in the similar materials for limestone is 2:2:1, and the ratio of cement, sand, and Kaolin in the similar materials for argillaceous rock is 1:1:3. In addition, the antifoaming agent accounted for about 1%.
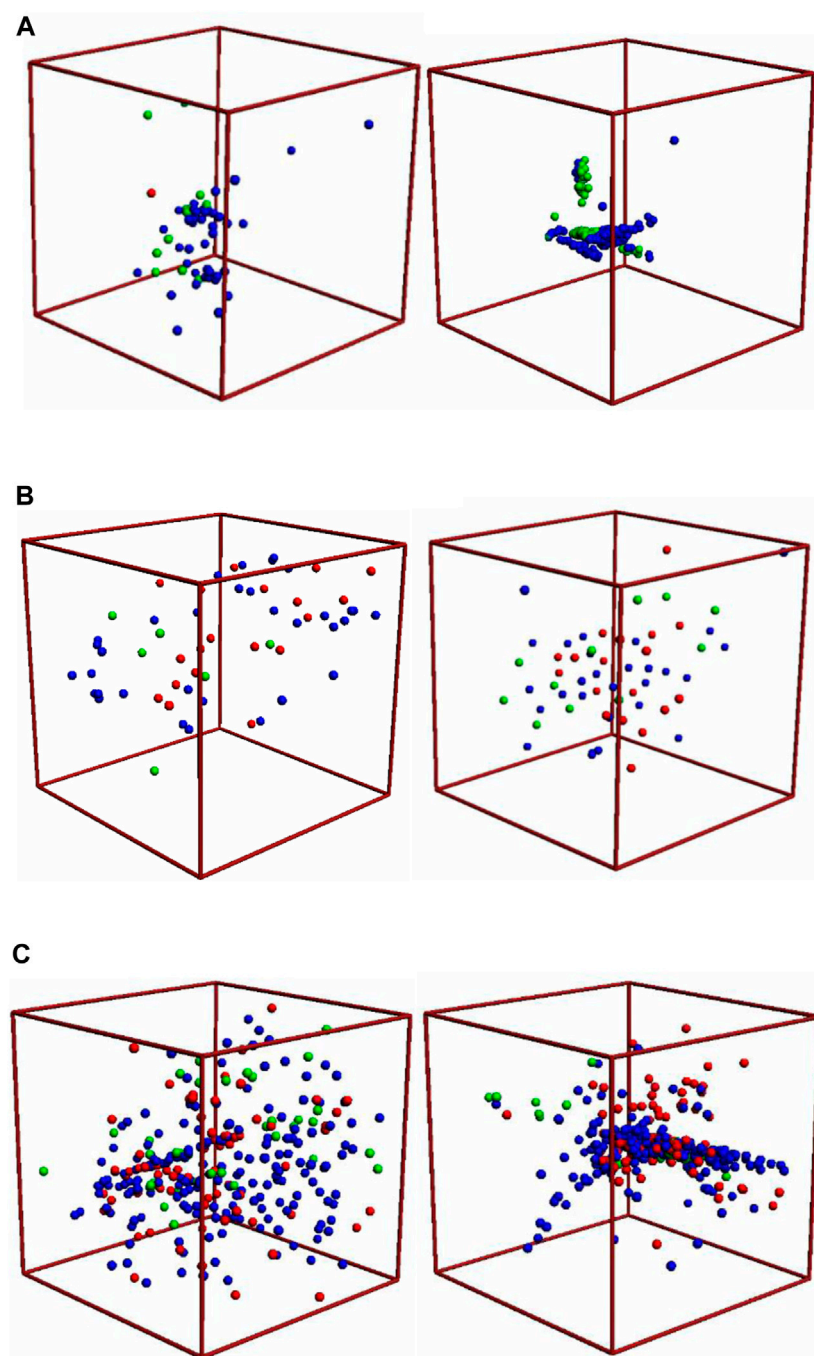
FIGURE 11
Inversion of acoustic emission moment tensor of the cases under different stress differences **(A)** Group A with confining pressure 10,8,2 MPa, **(B)** Group B with confining pressure 10, 6, 2 MPa, and **(C)** Group C with confining pressure 10, 4, 2 MPa.

After determining the ratio of similar materials, large-sized rock cores are poured. The cubic laminated core with the size of $300 \times 300 \times 300 \text{ mm}^3$ was poured. The bottom of the material required a shaking table while the upper part of the vibrator to remove foam. The casting process and parameters of the core are presented in Figure 7. The experimental process includes the following steps, i.e., oiling the mold surfaces, filling the mold, vibrating inside, vibrating outside, smoothing the surfaces, and presetting the wellbore. In the actual pouring process, the limestone layer and argillaceous layer are alternately laid, which means a certain thickness of ash layer is laid first, followed by a 1 cm thickness of argillaceous layer, and then a limestone layer is laid, repeating the above process. In the whole process, controlling the overall volume content of mudstone (about 30%) is needed.

FIGURE 12
The relationship among stress difference, SRV and shear fracture ratio.
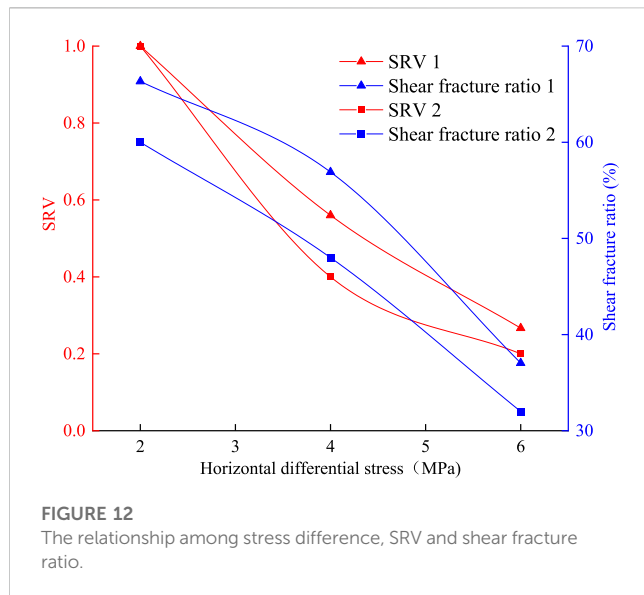
Moreover, the laying time interval between layers should not exceed 10 min, which not only prevents complete hardening and layering between the layers, but also allows for slight intrusion of adjacent layers, making them to be a complete entity. A total of 6 cores were poured.

3.2 Experimental equipment and procedures

The hydraulic fracturing simulation test was conducted on a self-developed true triaxial hydraulic fracturing test system, as illustrated in Figure 8. The system consists of three main parts, i.e., 1) a true triaxial servo loading system, 2) a fluid injection servo control system, and 3) a automatic data acquisition and processing system, as shown in Figure 8A. A cubic specimen with maximum allowable dimensions of 300 mm is placed in the test frame surrounded by pressurizing pistons. The confining stresses were loaded independently using the true triaxial assembly. The confining stresses could be loaded up to 10 MPa. The fluid injection servo control system was used to accurately determine the injection rate and injection pressure. The maximum injection rate and injection pressure are 10 mL/min and 40 MPa, respectively. Figures 8B,C shows how to attach AE probes and placing the specimen into triaxial servo loading system. The acoustic emission (AE) monitoring system, manufactured by an American acoustic company, was applied to analyze the focal mechanism of hydraulic fracture, as presented in Figure 9.

Triaxial confining pressures were set as vertical stress σ_v, maximum horizontal principal stress σ_H, and minimum horizontal principal stress σ_h, respectively. In this study, the confining pressures were 10-8-2 MPa in group A, 10-6-2 MPa in group B, and 10-4-2 MPa in group C, respectively. Each group contains two cores. There are a total of six cores in this experiment. To simulate fluid injection, a single cluster perforating fracture pipe was embedded with an inner diameter of 20 mm. The fracturing fluid was water and the pump inject rate is 10 mL/min until the pump was stopped without a significant change in

pressure. In the whole process, 8 AE probes were used in the AE monitoring system to obtain the AE signals associated with the initiation and extension of the HFs. In this study, AE monitoring was conducted for each core in the fracturing test. AE probes were laid out, as shown in Figure 10. The lower left corner was the coordinate origin (0, 0, 0), and the coordinate points were (200, 200, 300), (100, 100, 300), (200, 0, 200), (100, 0, 100), (200, 100, 0), (100, 200, 0), (200, 100, 300), (100, 200, 300). The coordinate unit is mm.

3.3 Experimental results

With the application of the AE test system to collect the information and comparing probe information triggered at the same time, it helps to better understand damage, fracture initiation, and propagation in the core. Through the effective AE event loci and waveform analysis, the initial amplitude is calculated. Then moment tensor Inversion is used to analyze specific tensile and shear failure patterns. Considering the similarity with seismology, the moment tensor theory is introduced into acoustic emission test to judge the fracture failure mode in the rock core. The force at the rupture source is decomposed into an isotropic source, a dual couple source, and a compensated linear dipole. Based on moment tensor inversion, the various components of the source mechanism are obtained. Consequently shear and tensile failure are judged based on the corresponding components and their proportions (Shi et al., 2018). AE monitoring results after hydraulic fracturing were inverted by moment tensor, as shown in Figure 11. In these figures, blue dots represent shear failure, red dots represent tensile failure, and green dots represent mixed failure. As the horizontal stress difference decreased, AE events increased, and the fracture modes became more complex. Besides, the fracture types (shear, tensile and mixed failure) also reflect a trend, i.e., with the increase in the horizontal stress difference, the shear fracture ratio significantly decreased. The volume enveloped by AE event points in the fracturing process was regarded as the reconstructed volume SRV, and the relationship between stress difference-SRV-shear fracture ratio is shown in Figure 12. SRV is a statistical value, specifically, SRV is the three-dimensional envelope space of each discrete acoustic emission event. Due to the fact that the SRV is significantly small in physical model experiments, normalization was performed on the SRV. The curves show that, although the experimental data has slight discreteness, the trend of changes in SRV is consistent. As the horizontal stress difference increases, the SRV gradually decreases, and the number of shear fractures decreases accordingly.

The corresponding hydraulic fracturing pump pressure curves are given in Figure 13. As observed, with the decrease in the horizontal stress difference, the pressure shows multiple peaks, the fracture becomes more complex, and the pressure curve shows obvious fluctuation. The intrinsic reason could be that the fracture keeps repeating the propagation process of "initiation–obstruction–turning–penetrating–obstruction–turning". Once the initiating fracture encounters argillaceous rock layer, the fracture is obstructed and has to propagate along the interface. After propagating a certain distance along the argillo–calcareous laminate interface, the hydraulic fracture could turn again and continue to propagate along the direction of maximum horizontal principal
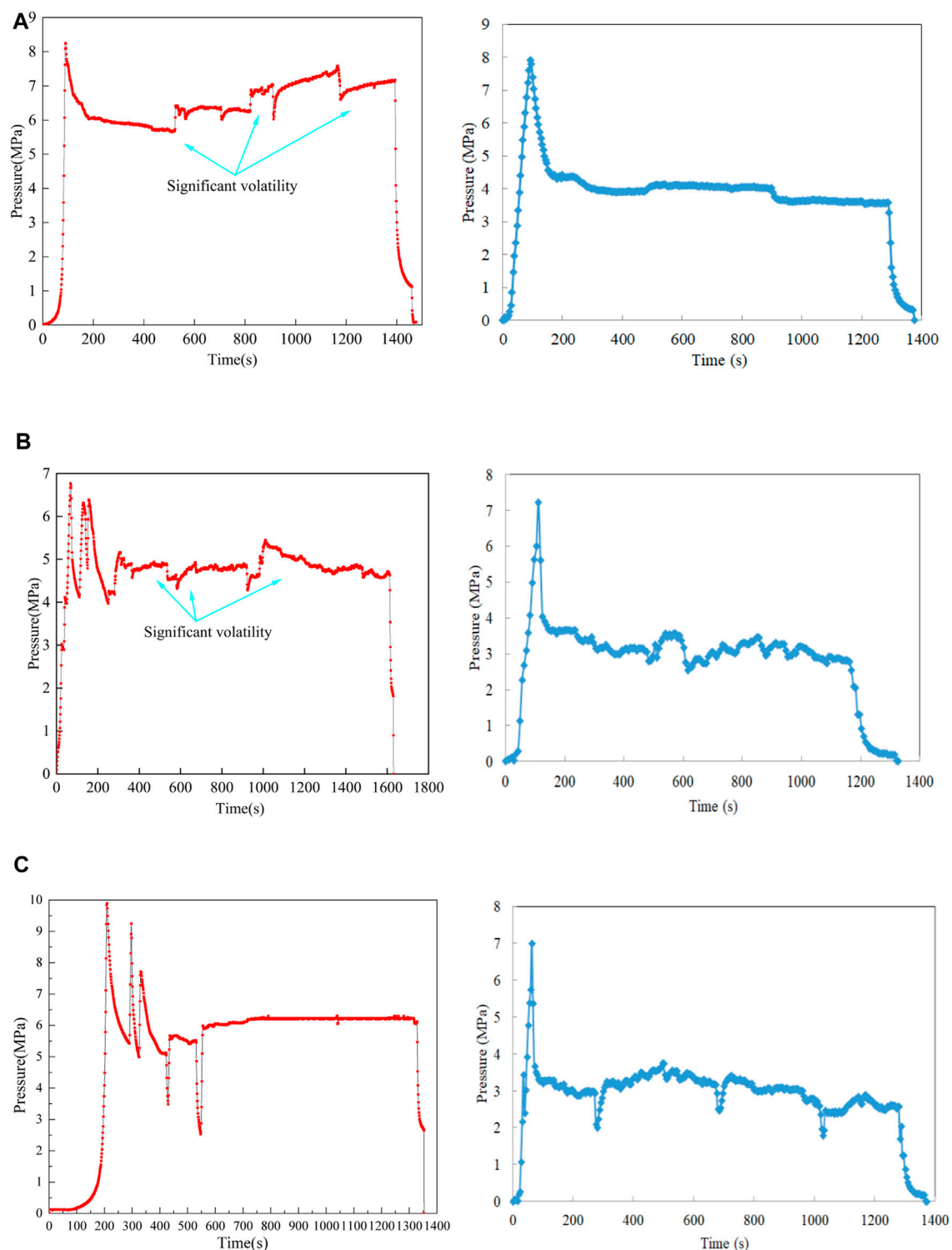
FIGURE 13
Hydraulic fracturing pump pressure curves under different stress differences **(A)** Group A with confining pressure 10,8,2 MPa **(B)** Group B with confining pressure 10, 6, 2 MPa and **(C)** Group C with confining pressure 10, 4, 2 MPa.

stress. Small fluctuations in pump pressure curve were caused by fracturing fluid passing through the lamina. In the calcareous or limestone layer, the permeability was relatively high. As the fracturing fluid was injected, the pressure gradually increased and

reached the pressure required for crossing the layer again, which would propagate again. If there is more fracture turning, there will be more shear fractures, which is consistent with the acoustic emission response in Figure 11.
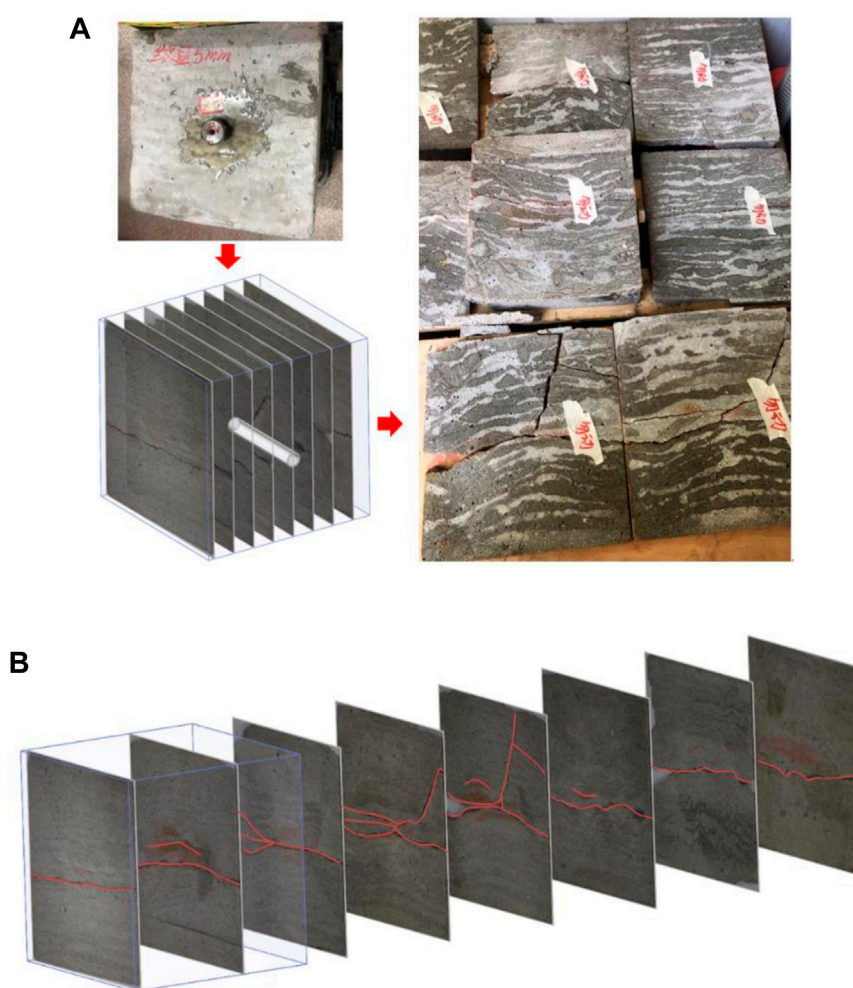
FIGURE 14
Hydraulic fracture reconstruction **(A)** manually cut slices, and **(B)** fracture reconstruction.

To confirm the above conjecture, one core from Group B was manually cut into slices. Figure 14 shows that the tracer magenta has obvious diffusion in the fracture development zone. After fracture reconstruction, the fracture morphology exhibits multiple groups of parallel fractures, and deflection occurs at the heterogeneous point at the interface of argillo–calcareous material, particularly the rock layers with high argillaceous content have a significant inhibitory effect on fracture propagation. Therefore, the height of fracture is relatively small. These observed fracture propagation modes in laboratory tests were the internal cause of obvious pressure fluctuation in different marl sections.

3.4 Discussions

In situ stress (confining stresses in the experimental test) definitely has an important impact on fracture propagation, but it is not the only factor affecting fracture formation. In addition to the injection rate and viscosity of the fracturing fluid, from the data of this experiment alone, it can be reflected that the following factors also have a significant impact on fracturing mode.

(1) Based on the fluctuation characteristics of fracture types and pressure curves, it can be recognized that the content of argillaceous rock and limestone may have a significant impact on the fracture path, especially in the case of high limestone content, which may be more conducive to the complexity of fractures. Argillaceous layer are generally believed to have strong plasticity and are not conducive to fracture propagation.

(2) The lamination or bedding plane has a significant impact on fracture propagation. Although it is not possible to achieve high-density bedding when making the similar materials rock cores, the influence of bedding on fractures has been fully demonstrated, especially with a significant inhibitory effect on fracture height, as shown in Figure 14. In subsequent research, it can be attempted to use full-size natural cores to conduct experiment on the influence of high-density interlayers on fracture propagation paths.

(3) Multiple perforation clusters may slightly alter the overall pattern of fracture network. Although the stress shadow effect has become less important in the current popular design of close cut fracturing, the injection energy and its

distribution of fracturing fluid in the case of multiple cluster perforations can change the ability of fractures to propagate along the bedding plane and pass through the argillaceous layer.

4 Conclusion

Based on hydraulic fracturing experiments with artificial rock cores, the following conclusions can be drawn.

In situ stress (confining stresses in the experimental test) definitely has an important impact on fracture propagation. As the horizontal stress difference increases, the SRV gradually decreases, and the number of shear fractures decreases accordingly. In the case with higher horizontal stress difference, the fractures are not easy to slide and turn. If there is more fracture turning, there will be more shear fractures, which is consistent with the acoustic emission response.

Although the mineral composition of rock core is not a mechanical parameter, the content of brittle and plastic minerals in the argillaceous limestone continental shale has a significant impact on the fracture complexity, particularly the rock layers with high argillaceous content have a significant inhibitory effect on fracture propagation. In addition, with the characteristics of high permeability and low cementation strength, the lamination or bedding plane also combines with lithology to jointly affect the propagation mode of fractures, especially the evolution of fracture height.

Data availability statement

The raw data supporting the conclusion of this article will be made available by the authors, without undue reservation.

Author contributions

ZZ, writing original draft. AZ, data curation. FY, formal analysis. LZ, investigation ML, methodology LC, formal analysis LL,writing—review and editing. All authors contributed to the article and approved the submitted version.

Conflict of interest

Authors ZZ, AZ, FY, LZ, and ML were employed by the company Shengli Oilfield Branch Company SINOPEC.

The remaining authors declare that the research was conducted in the absence of any commercial or financial relationships that could be construed as a potential conflict of interest. The authors declare that this study received funding from China Petroleum & Chemical Corporation Technology Development Project, grant number 30200019-22-ZC0699-0019. The funder had the following involvement in the study: the funder provided the original rock cores of continental shale.

Publisher's note

All claims expressed in this article are solely those of the authors and do not necessarily represent those of their affiliated organizations, or those of the publisher, the editors and the reviewers. Any product that may be evaluated in this article, or claim that may be made by its manufacturer, is not guaranteed or endorsed by the publisher.

References

Abe, A., Kim, T. W., and Roland, N. (2021). Laboratory hydraulic stimulation experiments to investigate the interaction between newly formed and preexisting fractures. *Int. J. Rock Mech. Min. Sci.* 141, 104665. doi:10.1016/j.ijrmms.2021.104665

Almutairi, A. (2014). *In evaluation of the impact of scale on the well test behaviour of fissured reservoirs (Single-Phase), international discrete fracture newwork engineering conference*. Canada: Vncouver. Vncouver, Canada.

Dan, X., Ruilin, H., Wei, G., and Jiaguo, X. (2015). Effects of laminated structure on hydraulic fracture propagation in shale. *Petroleum Explor. Dev.* 42 (4), 573–579. doi:10.1016/s1876-3804(15)30052-5

Garcia-Teijeiro, X., Rodriguez-Herrera, A., and Fischer, K. (2016). The interplay between natural fractures and stress as controls to hydraulic fracture geometry in depleted reservoirs. *J. Nat. Gas Sci. Eng.* 34, 318–330. doi:10.1016/j.jngse.2016.06.049

Ghahfarokhi, P. K. (2017). The structured gridding implications for upscaling model discrete fracture networks (DFN) using corrected Oda's method. *J. Petroleum Sci. Eng.* 153, 70–80. doi:10.1016/j.petrol.2017.03.027

Hattori, G., Trevelyan, J., Augarde, C. E., Coombs, W. M., and Aplin, A. C. (2017). Numerical simulation of fracking in shale rocks: Current state and future approaches. *Archives Comput. Methods Eng.* 24 (2), 281–317. doi:10.1007/s11831-016-9169-0

Jiang, Z., Li, Q., Hu, Q., Liang, Y., Xu, Y., Liu, L., et al. (2020). Acoustic emission characteristics in hydraulic fracturing of stratified rocks: A laboratory study. *Powder Technol.* 371, 267–276. doi:10.1016/j.powtec.2020.05.050

Ju, Y., Li, Y., Wang, Y., and Yang, Y. (2020). Stress shadow effects and microseismic events during hydrofracturing of multiple vertical wells in tight reservoirs: A three-dimensional numerical model. *J. Nat. Gas Sci. Eng.* 84, 103684. doi:10.1016/j.jngse.2020.103684

Ju, Y., Wang, Y., Xu, B., Chen, J., and Yang, Y. (2019). Numerical analysis of the effects of bedded interfaces on hydraulic fracture propagation in tight multilayered reservoirs considering hydro-mechanical coupling. *J. Petroleum Sci. Eng.* 178, 356–375. doi:10.1016/j.petrol.2019.03.049

Li, N., Zhang, S., Zou, Y., Ma, X., Zhang, Z., Li, S., et al. (2018). Acoustic emission response of laboratory hydraulic fracturing in layered shale. *Rock Mech. Rock Eng.* 51 (11), 3395–3406. doi:10.1007/s00603-018-1547-5

Lu, Q., Guo, J., Zhu, H., and Zhao, X. (2015). "Cluster spacing optimization based on a multi-fracture simultaneous propagation model," in *SPE/IATMI asia pacific oil & gas conference and exhibition* (United States: OnePetro).

McClure, M. W., and Horne, R. N. (2013). *Discrete fracture network modeling of hydraulic stimulation_ coupling flow and geomechanics*. Germany: Springer.

Rogers, S., Elmo, D., Dunphy, R., and Bearinger, D. (2010). *In Understanding hydraulic fracture geometry and interactions in the Horn River Basin through DFN and numerical modeling*. OnePetro: Canadian Unconventional Resources and International Petroleum Conference.

Sharifigaliuk, H., Mahmood, S. M., Ahmad, M., and Rezaee, R. (2021). Use of Outcrop as substitute for subsurface shale: Current understanding of similarities, discrepancies, and associated challenges. *Energy & Fuels* 35 (11), 9151–9164. doi:10.1021/acs.energyfuels.1c00598

Shi, P., Angus, D., Nowacki, A., Yuan, S., and Wang, Y. (2018). Microseismic full waveform modeling in anisotropic media with moment tensor implementation. *Surv. Geophys.* 39 (4), 567–611. doi:10.1007/s10712-018-9466-2

Stanchits, S., Burghardt, J., and Surdi, A. (2015). Hydraulic fracturing of heterogeneous rock monitored by acoustic emission. *Rock Mech. Rock Eng.* 48 (06), 2513–2527. doi:10.1007/s00603-015-0848-1

Taghichian, A., Zaman, M., and Devegowda, D. (2014). Stress shadow size and aperture of hydraulic fractures in unconventional shales. *J. Petroleum Sci. Eng.* 124, 209–221. doi:10.1016/j.petrol.2014.09.034

Thomsen, L. (2013). In on the use of isotropic parameters to understand anisotropic shale behavior: 83rd annual international meeting, SEG, expanded abstracts. *Abstract* 2013, 320–324.

Vasin, R. N., Wenk, H.-R., Kanitpanyacharoen, W., Matthies, S., and Wirth, R. (2013). Elastic anisotropy modeling of Kimmeridge shale. *J. Geophys. Research-Solid Earth* 118 (8), 3931–3956. doi:10.1002/jgrb.50259

Wang, J., Xie, H., and Li, C. (2021). Anisotropic failure behaviour and breakdown pressure interpretation of hydraulic fracturing experiments on shale. *Int. J. Rock Mech. Min. Sci.* 142, 104748. doi:10.1016/j.ijrmms.2021.104748

Weijermars, R., Wang, J., and Nelson, R. (2020). Stress concentrations and failure modes in horizontal wells accounting for elastic anisotropy of shale formations. *Earth-Science Rev.* 200, 102957. doi:10.1016/j.earscirev.2019. 102957

Weijers, L., Wright, C., Sugiyama, H., Sato, K., and Zhigang, L. (2000). "Simultaneous propagation of multiple hydraulic fractures-evidence, impact and modeling implications," in *International oil and gas conference and exhibition in China* (United States: OnePetro).

Wu, Z., Zuo, Y., Wang, S., Yi, T., Chen, S., Yu, Q., et al. (2016). Numerical simulation and fractal analysis of mesoscopic scale failure in shale using digital images. *J. Petroleum Sci. Eng.* 145, 592–599. doi:10.1016/j.petrol.2016.06.036

Yang, W., Huang, C., Zhang, Y., Lv, X., Yu, R., and Yao, J. (2022). Study on the influence of stress differences on hydraulic fracturing based on true triaxial experiments and discrete element numerical simulations. *Geomech. Geophys. Geo-energ. Geo-resour.* 8, 139. doi:10.1007/s40948-022-00449-4

Zhai, H., Chang, X., Zhu, W., Lei, X., and Xue, Z. (2021). Study on anisotropy of Longmaxi shale using hydraulic fracturing experiment. *Sci. China Earth Sci.* 64 (2), 260–277. doi:10.1007/s11430-020-9691-2

Zhang, D., Ranjith, P. G., and Perera, M. S. A. (2016). The brittleness indices used in rock mechanics and their application in shale hydraulic fracturing: A review. *J. Petroleum Sci. Eng.* 143, 158–170. doi:10.1016/j.petrol.2016.02.011

Zhao, L., Liu, F., Wang, P., Liu, P., Luo, Z., and Li, N. (2014). A review of creation and propagation of complex hydraulic fracture network. *Oil gas Geol.* 35 (4), 562–569. doi:10.11743/ogg201417

Zheng, S., Lin, M., Jiang, W., Qiu, X., and Chen, Z. (2022). New method of *in situ* high-resolution experiments and analysis of fracture networks formed by hydraulic fracturing. *J. Petroleum Sci. Eng.* 217, 110849. doi:10.1016/j.petrol. 2022.110849

Evolution of residual strain and strain energy in rocks under various types of uniaxial cyclic loading-unloading

Zhixi Liu and Xiaodie Liu*

School of Architectural Engineering, Tongling University, Tongling, Anhui, China

In the process of roadway excavation, the rock mass around the roadway is often subjected to cyclic loads, and the rock mechanical properties and strain energy evolution under cyclic loads are obviously different from those under compression, so it is urgent to carry out research on rock mechanical properties and strain energy evolution under cyclic loads. This study aims to investigate the evolution of residual strain and strain energy in rocks under uniaxial cyclic loading-unloading experiments (UCLUE). Four types of rocks, namely coal, white sandstone, red sandstone, and granite, were subjected to uniaxial compression experiments (UCE) and various uniaxial cyclic loading-unloading experiments (UEACLUE). The findings are as follows: analysis of UEACLUE revealed a gradual decrease in residual strain with an increasing number of cycles, leading to its eventual disappearance. However, if the cyclic loading-unloading (CLU) was continued beyond this point, the rocks displayed a reappearance of residual strain. The number of cycles required to eliminate residual strain was found to be inversely proportional to the peak strength of the rocks, while directly proportional to the upper limit value of UCLUE. Among the different stages of the uniaxial cyclic loading and unloading test, the plastic stage of white sandstone exhibited the largest disparity in dissipated strain energy, followed by the plastic stage of red sandstone, with coal displaying the smallest difference. Analysis of dissipated strain energy in the four types of uniaxial cyclic loading and unloading tests revealed differences of $0.00348\,\mathrm{mJ{\cdot}mm^{-3}}$, $0.03488\,\mathrm{mJ{\cdot}mm^{-3}}$, $0.02763\,\mathrm{mJ{\cdot}mm^{-3}}$, and $0.01619\,\mathrm{mJ{\cdot}mm^{-3}}$ in the plastic stage for the respective rock types. Furthermore, examination of the input strain energy density (ISED) and dissipated strain energy density (DSED) during the CLU process showed a linear relationship between these variables. Additionally, the investigation of ISED and DSED in other types of UCLUE demonstrated adherence to the cyclic-linear dissipation law (CLDL). The study of mechanical properties and strain energy evolution under CLU is of positive significance for the development of rock fatigue damage and rock damage mechanics.

1 Introduction

The mechanical properties and evolution of strain energy in rock masses subjected to CLU present distinct characteristics in comparison to those under UCE (Yang et al., 2018; Arora et al., 2019; Stavropoulou et al., 2021). To achieve a comprehensive understanding of the failure mechanism and ensure the long-term stability of rock masses, it is crucial to investigate the mechanical properties and strain energy evolution specifically under CLU conditions. Extensive research conducted by various scholars has yielded substantial achievements in the study of mechanical properties under UCLUE. Liu et al. (2022) studied the mechanical properties of rock under triaxial multistage CLU, and the results showed that the elastic modulus, damping ratio, and damping coefficient of the sample generally reduced with the increase of the cycle. Liu et al. (2018) used random sinusoidal waves simplified from Wenchuan seismic waves to study the mechanical properties of rock mass with discontinuous joints. Ding et al. (2022) conducted UCLUE experiments on coal mass and found that the mechanical behavior of coal mass showed cyclic hysteresis under cyclic load, and the failure mode was more serious. Meng et al. (2021) conducted rock experiments under CLU, and the research results showed that the stress-strain curve of rock under CLU showed a hysteretic effect, and discussed the evolution law of strength, deformation characteristics, and expansion characteristics with the change of confining pressure. He et al. (2015) and He et al. (2017) used CLU experiments to analyze rock deformation and strain energy characteristics and studied rock damping ratio and damping coefficient under different conditions. In the research of rock damping under CLU, Liu et al. (2008) and Liu et al. (2010) studied the damping and damping coefficient of triaxial CLU experiment and proposed that these increase linearly with the increasing of cyclic load cycles. Zhang et al. (2011) found that the hysteresis ring was not a closed ring by analyzing the hysteresis ring in the conventional triaxial experiment of rocks, and redefined the calculation method of the hysteresis ring. Chang et al. (2019) conducted a study on the mechanical properties of rock-concrete subjected to cyclic loads. The results revealed the occurrence of three typical failure modes, namely, shear cracking, tensile cracking, and combined shear and wing cracking, in all specimens subjected to cyclic and static loads. Guo et al. (2022) performed impact dynamics tests on rock-concrete materials, providing a detailed analysis of failure modes, mechanical properties, and energy dissipation characteristics, thereby contributing to the existing research on the dynamics of rock-concrete materials. Ali et al. (2016) investigated the shear mechanism of rock joints under pre-peak cyclic load and identified two categories of influences: shrinkage and degeneration. Momeni et al. (2015) examined the effect of cyclic loads on the mechanical properties of granite and observed that fatigue damage analysis under different load levels indicated crack nucleation during a significant portion of the fatigue life span, with crack growth occurring under higher stress levels. Manoj and Petroš (2009) found that the microstructure of rock specimens has an impact on the fatigue characteristics of rock under dynamic cyclic loads. Yoshinaka et al. (1997) investigated the change in pore pressure and related failure modes through triaxial cyclic load tests on soft rock. Some scholars have studied the mechanical properties of rocks under unilateral unloading under true triaxial

compression and analyzed their failure forms (Liu et al., 2020a; Liu et al., 2023).

The study of strain energy evolution in rocks is a prominent topic in rock mechanics, garnering significant attention from scholars both domestically and internationally, resulting in extensive research and fruitful outcomes (Xie et al., 2005; Xie et al., 2008). Investigations into the strain energy evolution of rocks primarily focus on understanding the laws governing strain energy under UCE, conventional triaxial loading, impact loads, and the distribution of strain energy throughout the loading process (Justo et al., 2018; Rashidi Moghaddam et al., 2018). ZHANG and GAO (2012a), ZHANG and GAO (2012b), and ZHANG and GAO (2015) analyzed the strain energy of red sandstone by examining the elastic strain energy at each unloading point. They further explored nonlinear theories of rock behavior. Meng et al. (2015) utilized strain energy calculation formulas to study the dissipation and accumulation of strain energy in rocks, considering factors such as size effect and loading rate. They obtained strain energy data from rock UCE experiments conducted with various sizes and loading rates. Building upon the study of strain energy evolution under UCE, Gong et al. (2018), Gong et al. (2019a), and Gong et al. (2019b) conducted uniaxial loading-unloading experiments to investigate strain energy accumulation and dissipation throughout the entire loading process. They proposed linear rules governing strain energy storage and dissipation, contributing to the theoretical understanding of rock strain energy evolution. Additionally, they improved the calculation formula for the peak strain energy impact index and established a rockburst tendency criterion based on the residual elastic strain energy index (the difference between pre-peak elastic strain energy density and post-peak failure strain energy density). Through an examination of the elastic properties of rocks in UCLUE, Liu et al. (2020b) observed that the elastic strain energy of rocks remained constant. Furthermore, Liu et al. (2021) postulated that the load at each unloading point in uniaxial fractional loading-unloading experiments was equal to that in UCE. They then proposed a method for analyzing the strain energy law in UCE.

The existing studies primarily focus on the damping characteristics and strain energy evolution of rocks under UCLUE. However, there is a relative dearth of research on the residual strain of rock mass and its internal relationship with different forms of energy. Investigating the internal relationship between residual strain and strain energy during UCLUE is crucial for effectively preventing and predicting rock fatigue damage and dynamic disasters. Therefore, it is imperative to conduct investigations to explore the correlation between the residual strain of rock masses and strain energy under UCLUE.

2 UCLUE method and curve analysis

2.1 UCE curve analysis

The experimental study involved four materials: coal, white sandstone, red sandstone, and granite. Both UCLUE and UCE were conducted using the RMT-150B rock mechanics test system.
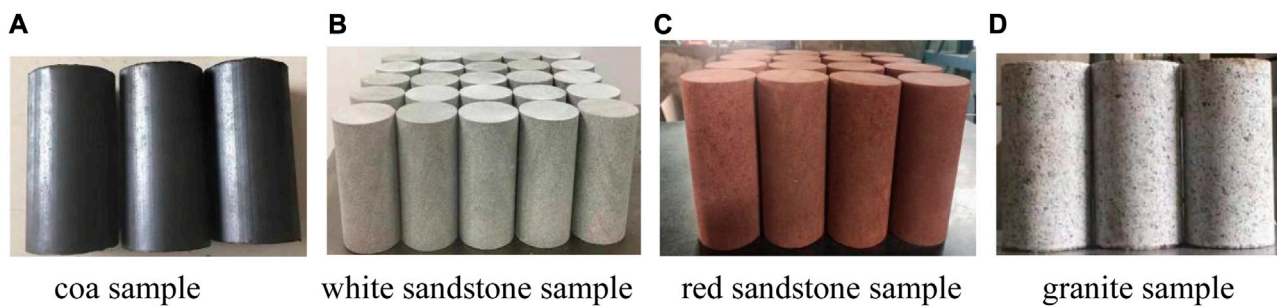
FIGURE 1
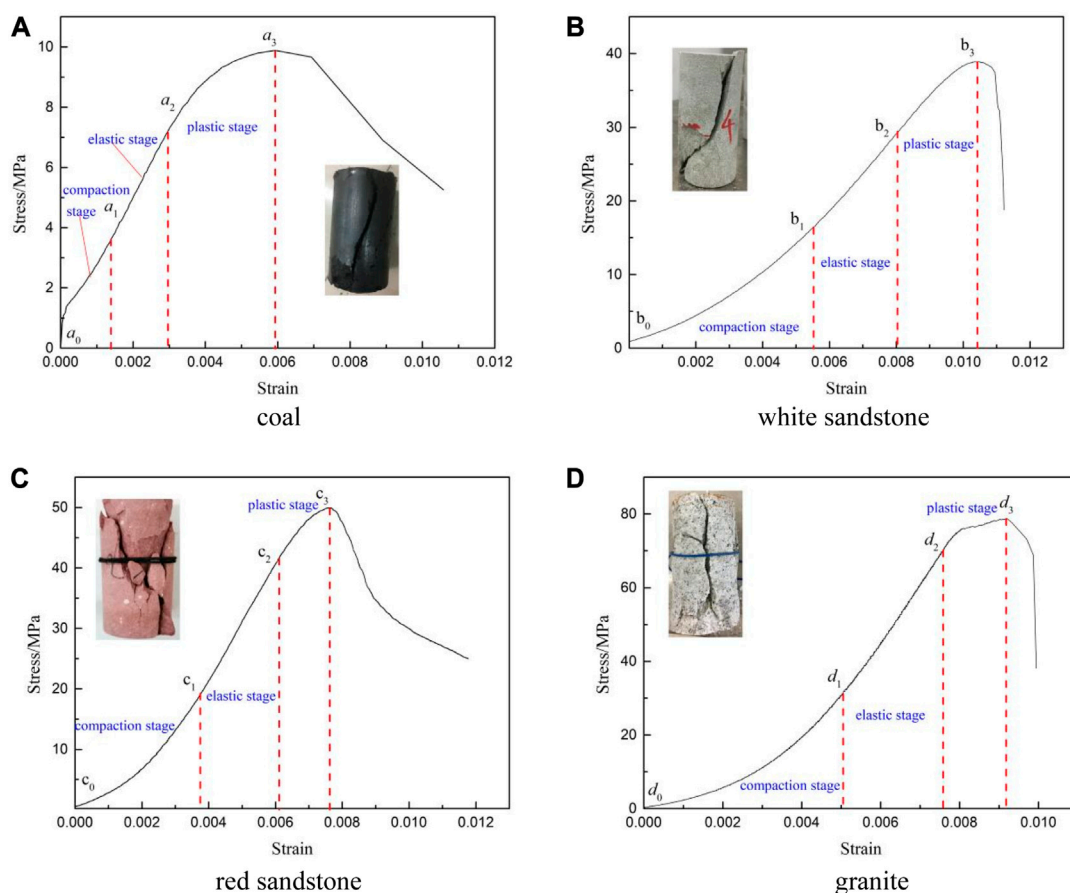Four rock samples. **(A)** Coal sample. **(B)** White sandstone sample. **(C)** Red sandstone sample. **(D)** Granite sample.

FIGURE 2
Uniaxial compression curve of rock. **(A)** Coal. **(B)** White sandstone. **(C)** Red sandstone. **(D)** Granite.

In accordance with internationally recognized standards in rock mechanics, standard rock specimens were prepared using cutting and polishing techniques. These procedures were performed to meet the specified dimensional requirements for precise and dependable testing. Figure 1 provides a visual representation of the specimens. The uniaxial compressive strength values for coal, white sandstone, red sandstone, and granite are 10.24, 39.40, 60.94, and 80.71 MPa,

respectively. Additionally, the elastic moduli for the four rocks are 5.01, 9.72, 10.22, and 19.21 GPa, respectively. The corresponding peak strains for each rock are 0.05930, 0.01038, 0.00773, and 0.00915, respectively. Figure 2 illustrates the stress-strain curves of the investigated rocks, showcasing the correlation between applied stress and resulting strain for each rock type. These curves enable the visualization of the different stages experienced
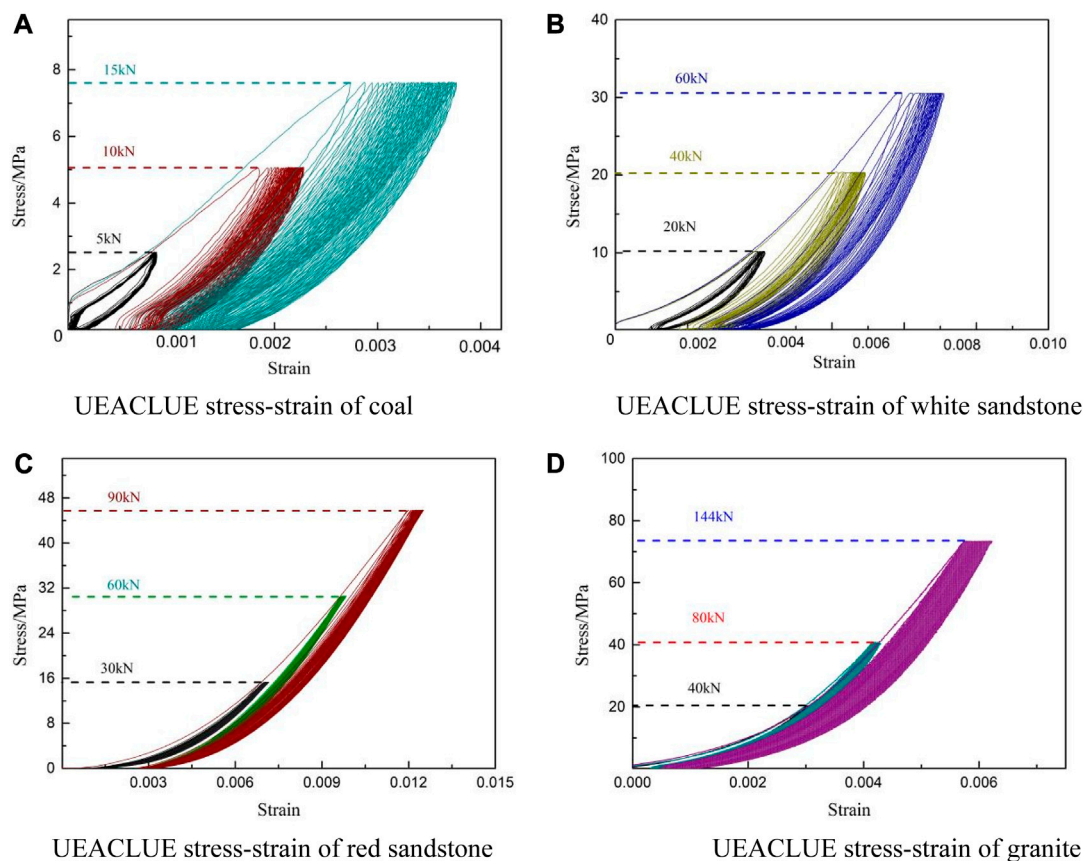
FIGURE 3
UEACLUE stress-strain of four rock. **(A)** UEACLUE stress-strain of coal. **(B)** UEACLUE stress-strain of white sandstone. **(C)** UEACLUE stress-strain of red sandstone. **(D)** UEACLUE stress-strain of granite.

during the loading process. Specifically, the stress-strain curve can be divided into three distinct stages based on the rate of stress-strain growth: compaction, elastic, and plastic stages. During the compaction stage, the strain growth rate increases in relation to the applied stress. The elastic stage is characterized by a linear stress-strain relationship. Finally, in the plastic stage, the strain growth rate gradually diminishes as the stress increases.

2.2 Analysis of UEACLUE curve

In order to facilitate the analysis of residual strain in the UEACLUE experiments for different rock specimens, it is assumed that the upper stress limits for each type of rock are within the load range corresponding to the compaction stage, elastic stage, and plastic stage. The lower stress limits are set to 0. The upper limits for coal in the uniaxial cyclic loading and unloading tests are 5, 10, and 15 kN, respectively. For sandstone, the upper limits are 20, 40, and 60 kN, respectively. Red sandstone has upper limits of 30, 60, and 90 kN in the single-axis cyclic loading and unloading tests. As for granite, the upper limits are 40, 80, and 144 kN, respectively. The loading rate for the experiments is set at 0.5 kN/s, and a total of 20 cycles are conducted. Following the

completion of the cyclic loading and unloading process, the specimens are not subjected to any further experiment.

From the visual representation presented in Figure 3, it is evident that the loading stress-strain path of sandstone under cyclic load is different from the unloading stress-strain. In particular, the nonlinearity of the unloading curve indicates that the rock has the hysteretic effect, and the initial loading-unloading will produce large residual strain. The residual strains has produced by the first loading-unloading of coal are 7×10^{-5}, 4.89×10^{-4}, and 6.36×10^{-4}, respectively. The residual strains produced by the first loading-unloading of white sandstone are 9.3×10^{-4}, 1.77×10^{-3}, and 2.3×10^{-3}, respectively. The residual strains produced by the first loading-unloading of red sandstone are 1.1×10^{-3}, 2.02×10^{-3}, and 2.63×10^{-3}, respectively. The residual strains produced by the first loading-unloading of granite are 3.1×10^{-4}, 4.11×10^{-4}, and 4.8×10^{-4}, respectively. The residual strain of the four rock types exhibits a positive correlation with the upper limit of the applied uniaxial cyclic loading and unloading stress. This correlation demonstrates that cracks can develop in the rock during the elastic stage, while the subsequent propagation of cracks remains stable. Notably, high-strength rocks exhibit relatively lower levels of residual strain during the initial loading and unloading processes.
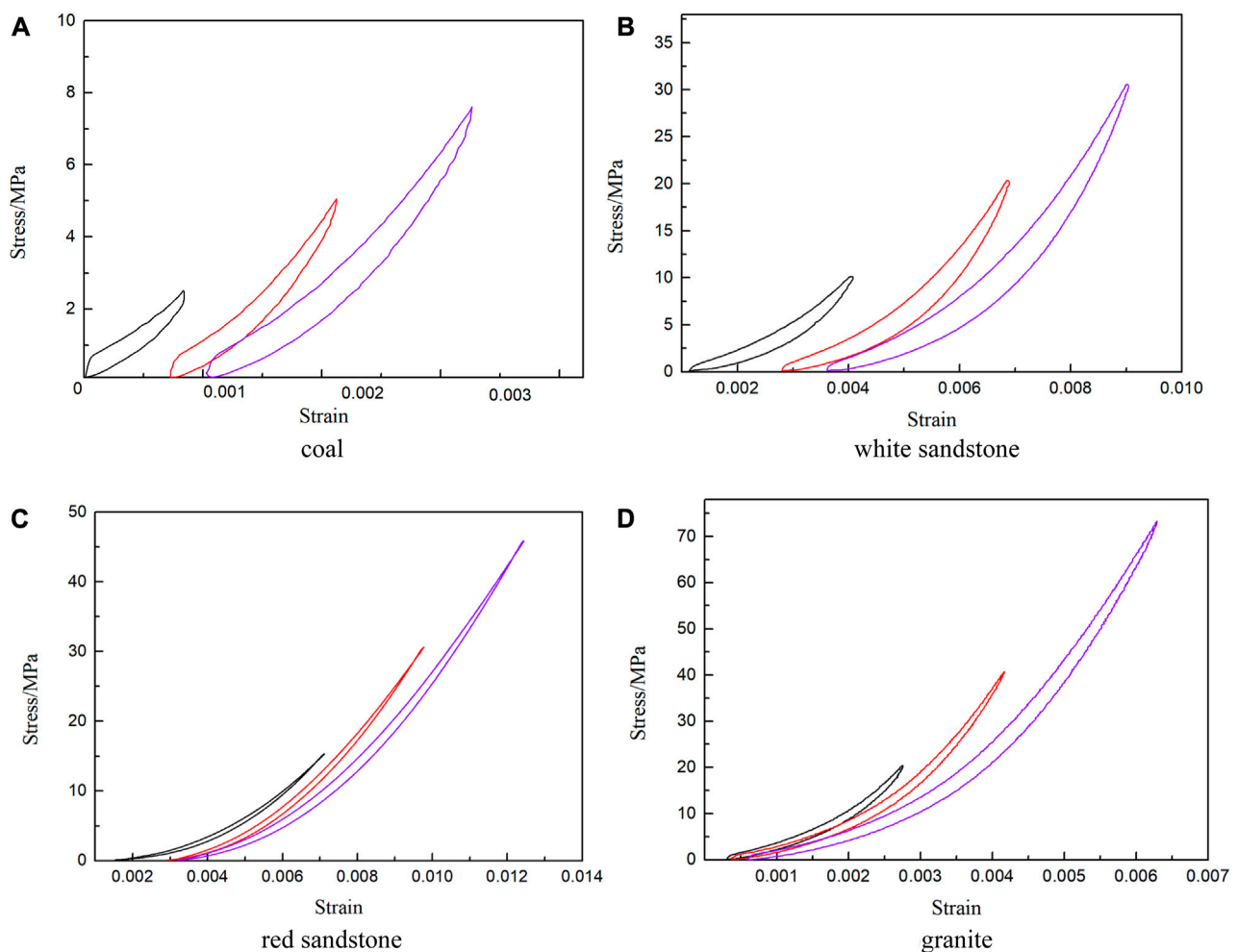
FIGURE 4
Non-residual strain of the four rocks. **(A)** Coal. **(B)** White sandstone. **(C)** Red sandstone. **(D)** Granite.

3 The evolution law of rock residual strain

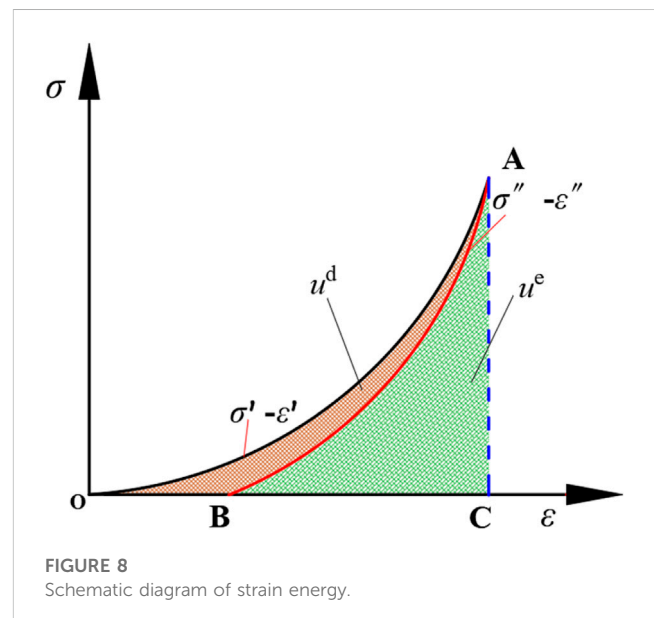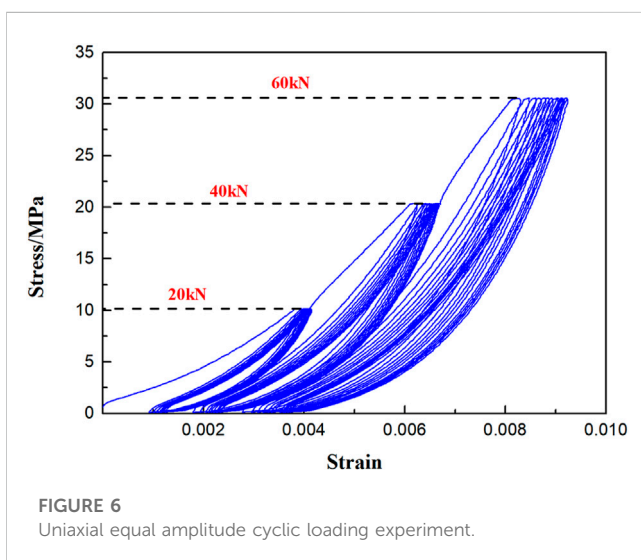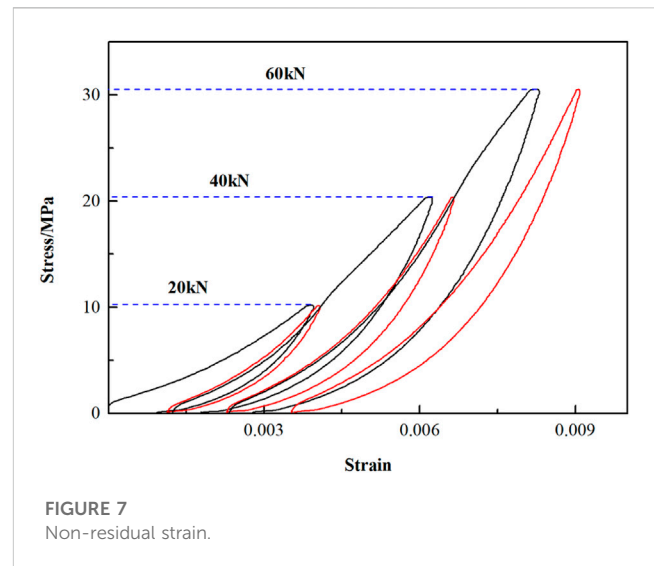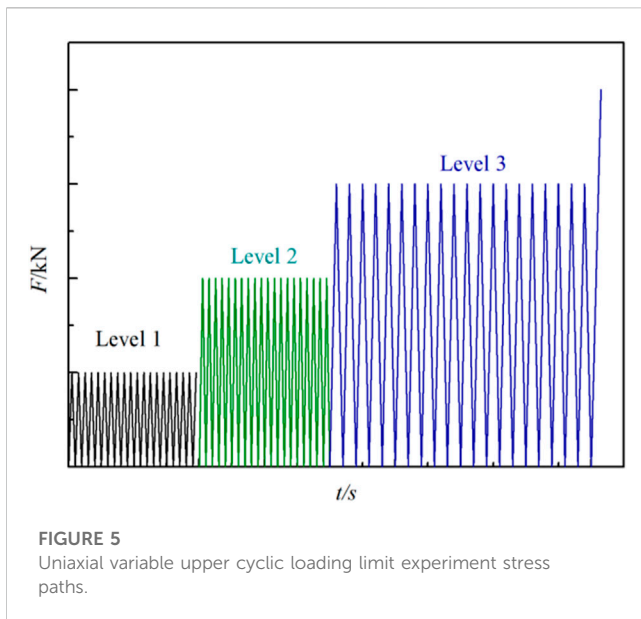## 3.1 Uniaxial cyclic loading-unloading experiment

Figure 4 illustrates the gradual reduction in residual strain observed for the four rock types as the cycle number increases during the experiment. Eventually, a point is reached where a non-residual strain phenomenon is observed.

The UEACLUE yielded distinct stress limits at which non-residual strain phenomena all will occurred for different rock types. Specifically, the coal sample exhibited non-residual strain at the 8th, 14th, and 15th cycles in the compaction, elastic, and plastic stages, respectively. Likewise, white sandstone demonstrated non-residual strain at the 7th, 12th, and 14th cycles in the compaction, elastic, and plastic stages, respectively. Similarly, for red sandstone, the stress limit was observed at the 6th, 10th, and 10th cycles in the compaction, elastic, and plastic stages, respectively. Finally, granite displayed non-residual strain at the 5th, 7th, and 8th cycles in the compaction, elastic, and plastic stages, respectively.

During the experimental procedure, the residual strain of the rocks exhibited a gradual decrease until reaching a state of non-residual strain. However, if the loading-unloading process was continued beyond this point, the residual strain reappeared. The occurrence of the non-residual strain phenomenon was found to be directly related to the applied stress, showing a proportional relationship. Among the four types of rocks investigated in this study, it was observed that higher-strength rocks experienced fewer occurrences of the non-residual strain phenomenon during the UEACLUE experiments.

3.2 Uniaxial variable upper cyclic loading limit experiment

To further investigate the non-residual strain phenomenon in sandstone under UEACLUE, a series of uniaxial variable upper cyclic loading limit experiments were conducted. The experiments consisted of three grades, each consisting of 20 cycles, with the upper limit values of CLU set at 20, 40, and 60 kN, respectively. The experiments followed a lower limit of 0 and a loading rate of 0.5 kN/

FIGURE 5
Uniaxial variable upper cyclic loading limit experiment stress paths.

FIGURE 7
Non-residual strain.

FIGURE 6
Uniaxial equal amplitude cyclic loading experiment.

FIGURE 8
Schematic diagram of strain energy.

s. At the end of each cycle, the sample was compressed until failure. Figure 5 illustrates the stress paths observed during the experiments.

Figures 6, 7 show the curve of stress-strain and non-residual strain in the uniaxial equal amplitude cyclic loading experiment. In the uniaxial equal amplitude cyclic loading experiment of sandstone, the residual strains produced in the first cycle of the first stage, second stage and third stage are 1.34×10^{-3}, 0.55×10^{-3}, and 0.44×10^{-3}, respectively. After the non-residual strain phenomenon of rock appears in the first stage of CLU, residual strain will appear again if the loading-unloading experiment has continued. The second stage and third stage cycles have the same evolution law, indicating that after the occurrence of non-residual strain phenomenon, if the upper limit of CLU stress has increased, residual strain phenomenon will appear again. To sum up, in the UCLUE, after the non-residual strain phenomenon of rock appears, increasing the

upper limit value of UCLUE stress and continue to carrying out CLU, the rock will appear non-residual strain again.

4 Rock strain energy evolution

4.1 Strain energy calculation method

Based on the principles of thermodynamics, it is observed that when the rock is subjected to loading, a certain amount of strain energy is stored within the rock and can be reversed under specific conditions. This stored energy is referred to as elastic strain energy. However, during the loading process, another portion of the strain energy is dissipated and cannot be reversed. This dissipated energy is known as dissipative strain energy.
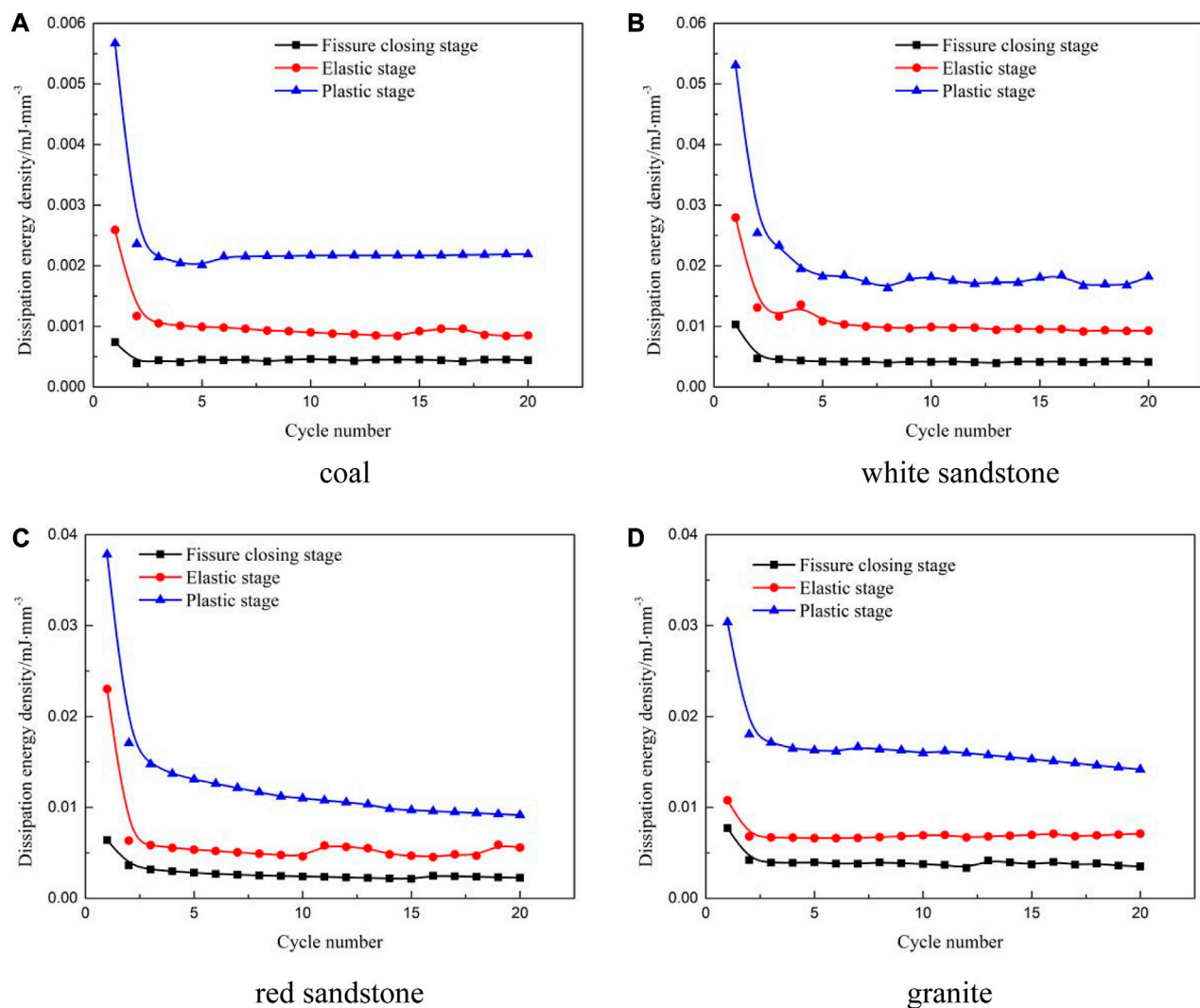
FIGURE 9
Curves of rock strain energy dissipation and cycle numbers under UEACLUE. **(A)** Coal. **(B)** White sandstone. **(C)** Red sandstone. **(D)** Granite.

The relationship is as follows (Meng et al., 2015):

$$u = u^d + u^e$$

Where u is the total strain energy density generated by the work of external load on the rock specimen; u^e is the elastic strain energy density stored in the rock; u^d is the DSED. The distribution has shown in the Figure 8.

As shown in Figure 8, the area under the unloading curve represents the elastic strain energy u^e, and the area enclosed by the loading curve, unloading curve, and horizontal coordinate represents the dissipated strain energy u^d of the rock.

$$u^d = \int_0^\varepsilon \sigma' d\varepsilon' - \int_{\varepsilon''}^\varepsilon \sigma_1'' d\varepsilon_1''$$

$$u^e = \int_{\varepsilon''}^\varepsilon \sigma_1'' d\varepsilon_1''$$

Where ε is axial strain; σ' and ε' represent loading stress and strain. σ'' and ε'' represent unloading stress and strain. Figure 8 shows the stress-strain curve of rock under axial load σ_1. The total ISED of the experimenting machine is u, the DSED is u^d, and the elastic strain energy density is u^e.

4.2 Strain energy dissipation evolution under cyclic load

Using the strain energy analysis method, the stress-strain curve obtained from the UCLUE is integrated.

As depicted in Figure 9. In the UEACLUE, the DSED of rock decreases non-linearly as the number of cycles increases, the strain energy dissipation increasing when the number of cycles is the same with the increase of the upper limit value of UCLUE. The DSED produced by the first loading-unloading of rock is much greater than that produced by the subsequent loading-unloading. Previous
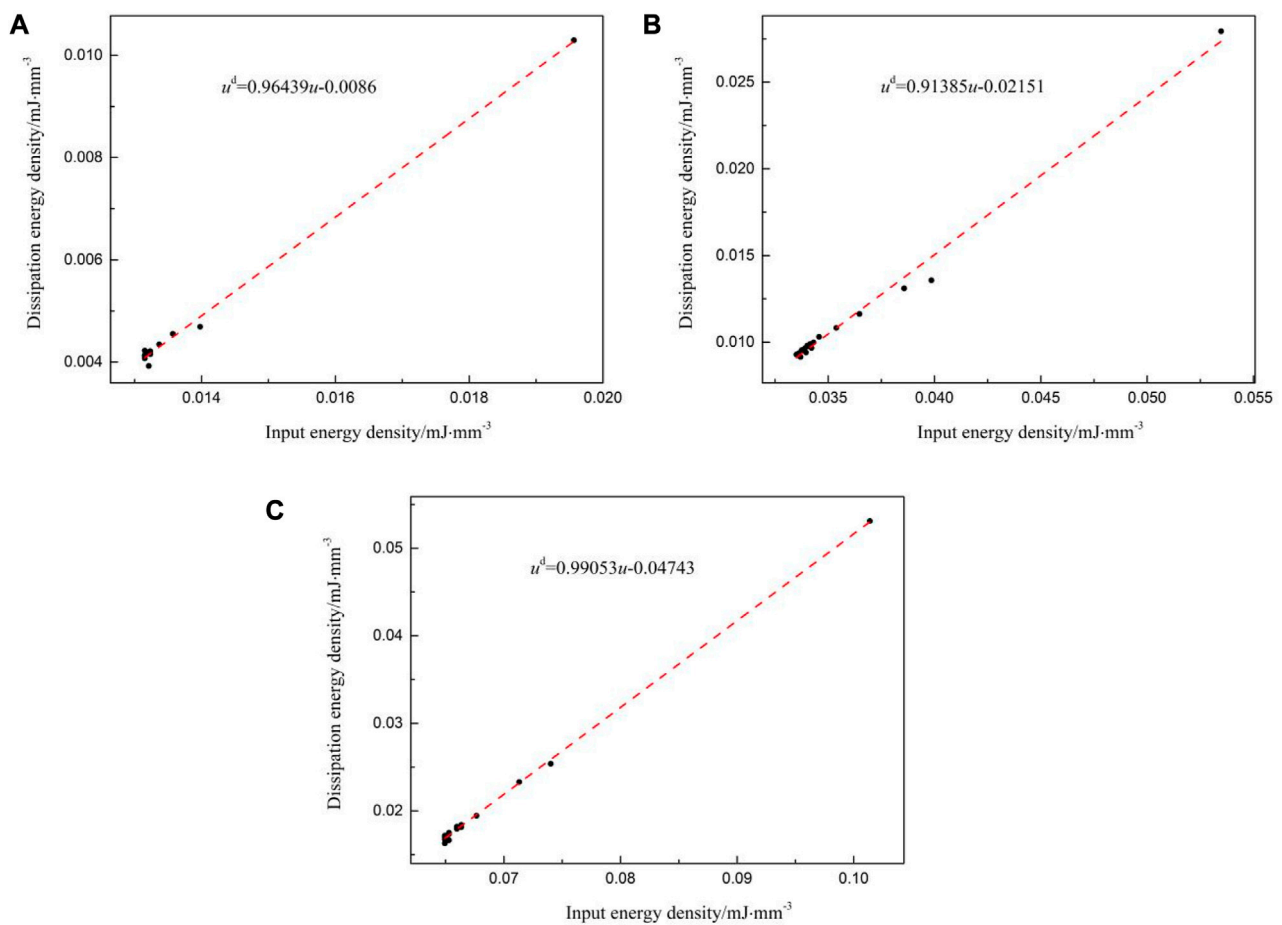
FIGURE 10
(A) is the fitting result of the compaction stage, **(B)** is the fitting result of the elastic stage, and **(C)** is the fitting result of the plastic stage.

studies have suggested that a strong correlation between DSED and the generation of damage in rocks. By understanding the evolution law of DSED, it is possible to establish a theoretical foundation for more precise assessments of rock fatigue damage. By comparing the dissipative energy generated by uniaxial cyclic loading and unloading of four kinds of rocks, it can be seen that in the plastic stage, the dissipative strain energy-cycle curve of coal evolves in an approximate horizontal direction with the increase of cycle times after the 7th cycle, while the dissipative strain energy curve of sandstone fluctuates to a certain extent with the increase of cycle times. The dissipative strain energy of granite and red sandstone in plastic stage decreases linearly with the increase of cycle times. The dissipative strain energy of the four kinds of rocks in the compaction stage, elastic stage and plastic stage is inversely proportional to the peak strength. In the cycle process of the compaction stage, the dissipative strain energy density of coal, red sandstone and white sandstone fluctuates little, while that of granite fluctuates greatly. In the comparison of dissipative strain energy of the four rocks, it can be found that the dissipative strain energy of the white sandstone in the elastic stage has little difference with that of the plastic stage, which indicates that the dissipative strain energy of the sandstone in the elastic stage is relatively large, while the dissipative strain energy of the other three rocks increases

significantly from the elastic stage to the plastic stage. In the uniaxial cyclic loading and unloading test of coal, the maximum difference of dissipated strain energy density generated by each cyclic loading and unloading is 0.00348 mJ·mm^{-3}. In the uniaxial cyclic loading and unloading test of white sandstone, the maximum difference of dissipated strain energy density produced by each cyclic loading and unloading is 0.03488 mJ·mm^{-3}. In the uniaxial cyclic loading and unloading test of red sandstone, the maximum difference of dissipated strain energy density produced by each cyclic loading and unloading is 0.02763 mJ·mm^{-3}. In the uniaxial cyclic loading and unloading test of granite, the maximum difference of dissipated strain energy density produced by each cycle loading and unloading is 0.01619 mJ·mm^{-3}.
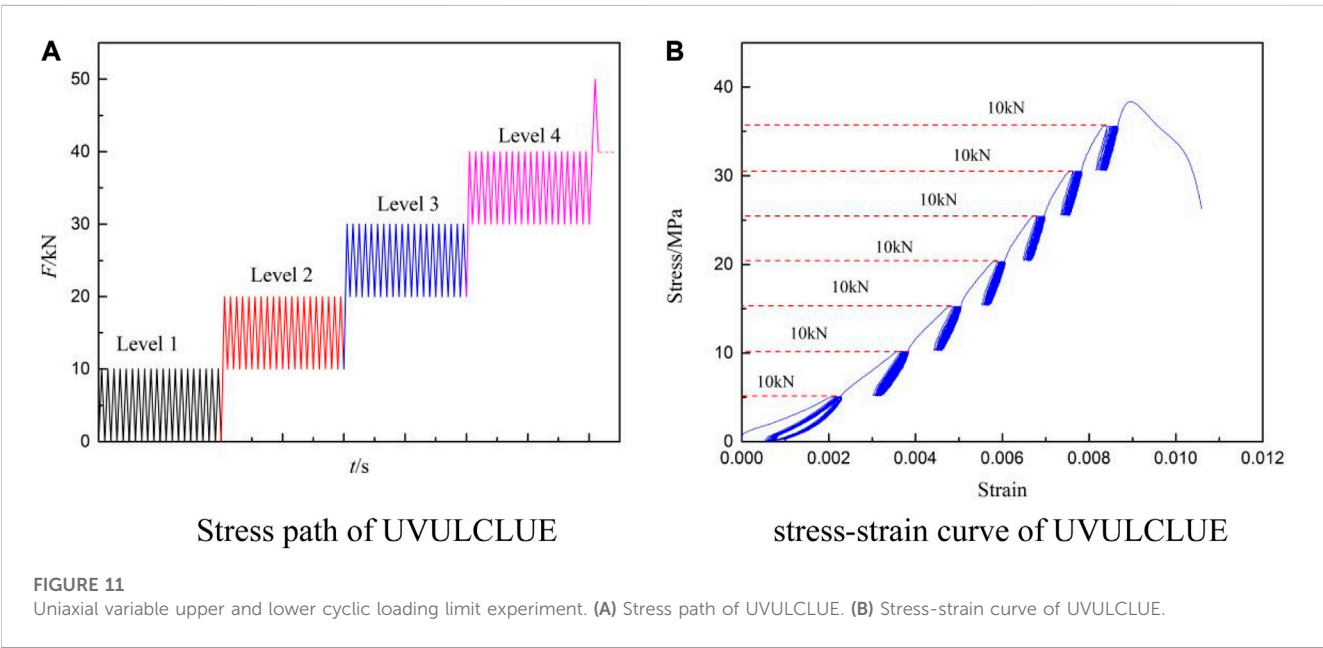
4.3 Cyclic-linear dissipation law (CLDL)

Through a comprehensive investigation of the quantitative relationship between DSED and ISED, a linear functional relationship between the two has been established. This finding confirms the existence of a CLDL in rocks.

$$u^d = au + b$$

TABLE 1 Fitting results of CLDL.

Sample	Cyclic stress upper limit/kN	a	b	Expression	Adj. R-Square
Coal	5	0.87586	−0.00060	$u^d=0.87586u-0.00060$	0.99280
	10	0.79233	−0.00171	$u^d=0.79233u-0.00171$	0.98477
	15	0.94684	−0.00524	$u^d=0.94684u-0.00524$	0.98776
White sandstone	20	0.96439	−0.00860	$u^d=0.96439u-0.00860$	0.99475
	40	0.91385	−0.02151	$u^d=0.91385u-0.02151$	0.99044
	60	0.99053	−0.04743	$u^d=0.99053u-0.04743$	0.99880
Red sandstone	30	0.67349	−0.01801	$u^d=0.67349u-0.00060$	0.99270
	60	0.91905	−0.06641	$u^d=0.91905u-0.06641$	0.99501
	90	0.92363	−0.13430	$u^d=0.92363u-0.13430$	0.99933
Granite	40	0.83383	−0.01269	$u^d=0.83383u-0.01269$	0.98539
	80	0.80422	−0.03634	$u^d=0.80422u-0.03634$	0.94949
	144	0.90324	−0.10077	$u^d=0.90324u-0.10077$	0.99575

Stress path of UVULCLUE

stress-strain curve of UVULCLUE

FIGURE 11
Uniaxial variable upper and lower cyclic loading limit experiment. **(A)** Stress path of UVULCLUE. **(B)** Stress-strain curve of UVULCLUE.

Where a and b represent the fitting parameters in the linear functional relationship between DSED and ISED. The fitting results for white sandstone are exemplified and illustrated in Figure 10.

Figure 10 presents the fitting results for white sandstone as an example. Based on Table 1 and Figure 10, the input strain energy and dissipated strain energy of the four types of rocks were fitted during the experiment. The fitting correction coefficients for all four types of rocks are above 0.98, indicating a good fitting effect. It indicates that there is a linear functional relationship between the input strain energy and dissipated strain energy of rocks under UEACLUE, which is independent of the load level of CLU. Based on the cyclic - linear dissipation law, it is evident that the evolution trend of dissipation strain energy is consistent with that of input strain energy during experiment.
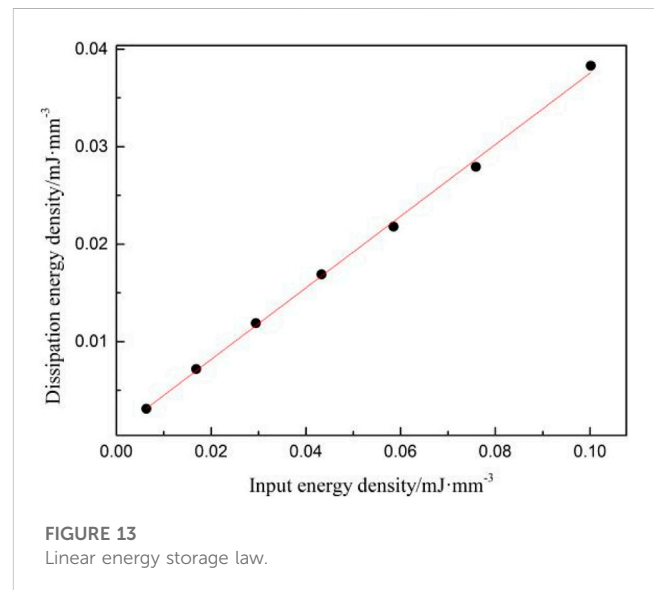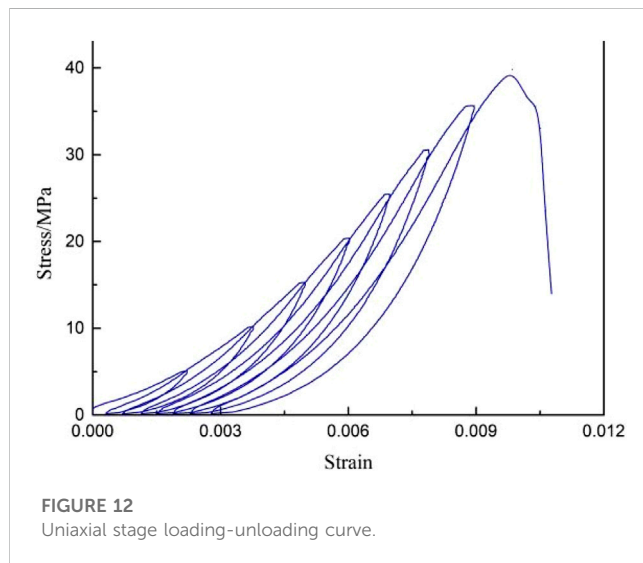
5 Application range of CLDL

5.1 Uniaxial variable upper and lower cyclic loading limit experiment

To validate the aforementioned hypothesis, a uniaxial variable upper and lower with constant amplitude (UVULCLUE) experiment was conducted using the RMT-150B apparatus. The experiment consisted of multiple stages, with each stage characterized by different upper and lower limits of cyclic loading. In the first stage, the upper limit was set at 10 kN, while the lower limit was 0. After completing 20 cycles in the first stage, the experiment progressed to the second stage, where the upper limit was increased to 20 kN, while the lower limit remained the same as

TABLE 2 Fitting results.

Sample	Load limit value/kN	a	b	Expression	Adj. R-Square
White sandstone	10	0.93764	−0.00234	$u^d=0.93764u-0.00234$	0.99501
	20	0.97807	−0.00126	$u^d=0.97807u-0.00126$	0.99842
	30	0.98925	−0.0028	$u^d=0.98925u-0.0028$	0.99911
	40	0.99867	−0.00564	$u^d=0.99867u-0.00564$	0.9926
	50	0.94967	−0.00611	$u^d=0.94967u-0.00611$	0.99298
	60	0.49886	−0.00357	$u^d=0.49886u-0.49886$	0.99772
	70	1.04044	−0.00809	$u^d=1.04044u-0.00809$	0.98535

FIGURE 12
Uniaxial stage loading-unloading curve.

FIGURE 13
Linear energy storage law.

the previous stage's upper limit. The difference between the upper limit values of cyclic loading and unloading stress of adjacent grades is 10 kN. "Stress path of UVULCLUE" as shown in Figure 11A.

As shown in Figure 11B. In the UVULCLUE, the residual strain of 0.55×10^{-3} is generated by the initial loading-unloading in the first stage cycle, which is larger than that generated by other cycles in the first stage cycle, indicating that the initial loading-unloading is caused by the compaction of the internal defects in the sandstone, resulting in a more residual strain than that in other cycles. The residual strain of the rocks from Grade 2 to Grade 7 under initial loading are 2.18×10^{-3}, 0.99×10^{-3}, 0.55×10^{-3}, 0.73×10^{-3}, 0.38×10^{-3}, and 0.35×10^{-3}, respectively.

The strain energy evolution law of UVULCLUE has shown in Table 2. The strain energy calculated at the beginning of the second stage of the UVULCLUE is the strain energy density within the load range of the second level cycle. In other words, the ISED, DSED, and elastic strain energy density of the second level cycle is the strain energy density under 10–20 kN, rather than the strain energy density of the rock under 20 kN.

The quantitative relationship between the DSED and the total ISED was investigated respectively in the UVULCLUE, and it was found that there was also a linear functional relationship between them. It shows that the CLDL not only applies to UEACLUE, but

also applies to other types of CLU experiments, which introduces a novel perspective on the evolution of strain energy in rock during loading-unloading.

5.2 Uniaxial stage loading-unloading experiment

Uniaxial stage loading-unloading adopts the loading-unloading method of increasing load. The loading stage of the experiment is 10 kN, that is, 0→10→0→20→0→30 kN. The uniaxial stage loading-unloading curve as depicted in Figure 12.

The phenomenon of "hardening" in rock specimens under loading-unloading, where the peak load exceeds the uniaxial compressive strength, has been observed consistently in previous studies. For instance, Zuo et al. (2011) investigated the cyclic load behavior of coal and rock mass, while You and Su (2008) studied marble specimens. Building upon the findings of these researchers, it is believed that the "hardening" phenomenon is attributed to the presence of cracks within the rock specimens. Local contact stress between these cracks is significantly higher than the stress induced by axial compression loading. As a result,

the specimens exhibit substantial strain and even localized failure under axial load. Debris formed during the loading-unloading process may detach and fill adjacent cracks, thereby increasing friction and enhancing the bearing capacity of the rock. It is important to note that "hardening" should not be confused with an increase in overall strength, which encompasses tensile, compressive, shear, and torsional resistance. Instead, "hardening" primarily refers to the augmentation of friction and bearing capacity.

As shown in Figure 13. The relationship between the ISED and the DSED with the increase of the unloading level in uniaxial stage loading-unloading is analyzed. And a linear functional relationship between the DSED and the ISED is obtained. When the input strain energy increases, the strain energy dissipating also increases in the same proportion. Meng et al. (2015) believed that the strain and failure of rock is a process of the generation, expansion, connection, penetration, and sliding of micro-cracks within the rock. Strain energy needs to be absorbed to generate new fractured surfaces, while the sliding friction between fractured surfaces dissipates strain energy. In other words, the strain energy density absorbed by rocks is a linear function of the sliding friction strain energy density between fractured surfaces. To sum up, the CLDL applies to various loading-unloading methods in this manuscript and is able to better reflect the strain energy evolution law during the loading-unloading process of rocks.

6 Discussion

Based on the hypothesis proposed regarding the "hardening" phenomenon in rock specimens, several important implications can be derived. Firstly, it is crucial to consider the presence and behavior of cracks in rock specimens when studying their mechanical response under loading-unloading conditions. The high local contact stress between cracks highlights the significance of crack initiation, propagation, and interaction in determining the overall deformation and failure characteristics of the rock.

Secondly, the formation of debris and its subsequent filling between cracks should be taken into account. The accumulation of debris can enhance the frictional contact between cracks, leading to an increase in the bearing capacity of the rock. This phenomenon implies that the mechanical behavior of rocks is not solely governed by the intrinsic properties of the rock material, but also influenced by the interactions and interplay between cracks and debris.

Furthermore, the "hardening" phenomenon challenges the conventional understanding that loading and unloading inherently result in damage to rock mass. Instead, it suggests that under certain conditions, cyclic loading and unloading can actually contribute to the strengthening of rock specimens. This finding underscores the need for a more comprehensive and nuanced understanding of the fatigue and damage processes in rocks, considering the complex interrelationships among stress, deformation, crack evolution, and debris behavior.

Overall, this hypothesis provides a framework for further investigations into the underlying mechanisms of the "hardening" phenomenon and opens up avenues for exploring innovative approaches to enhance the mechanical properties and stability of rock materials.

7 Conclusion

By analyzing the mechanical characteristics and strain energy evolution in UCLUE, we have identified the evolution law of residual strain in rock mass under loading-unloading conditions. Furthermore, through the analysis of strain energy evolution, we have discovered the CLDL. To validate the applicability of the CLDL, we have conducted studies using two additional loading-unloading schemes. The results obtained from these studies are as follows:

(1) In the process of UEACLUE, the residual strain of rock gradually decreases until non-residual strain occurs. If the loading-unloading continues, the residual strain will appear again. In the process of UEACLUE, the occurrence times of non-residual strain phenomenon is proportional to the upper limit value of UEACLUE. Among the four kinds of rocks in this paper, the higher the strength of the rocks, the fewer the occurrence cyclic numbers of non-residual strain phenomenon in the UEACLUE.
(2) In the UCLUE, after the non-residual strain phenomenon of rock occurs, increasing the upper limit value of UCLUE stress and continuing to carry out CLU, the non-residual strain phenomenon of rock will appear again.
(3) The presence of cracks in rock specimens leads to high local contact stress between the cracks, exceeding the stress under axial compression loading. This results in significant strain and even local failure phenomena in the specimens under axial load, with the formation of debris that can fall off and fill nearby cracks. The debris filling between the cracks enhances friction and increases the load-bearing capacity of the rock.
(4) In terms of the different stages of uniaxial cyclic loading and unloading tests, the largest dissipated strain energy difference was observed in the plastic stage of white sandstone, followed by the plastic stage of red sandstone, and the smallest in the plastic stage of coal. By analyzing the dissipated strain energy from four types of uniaxial cyclic loading and unloading tests, it was observed that the dissipated strain energy differences within the same group varied as follows: 0.00348, 0.03488, 0.02763, and 0.01619 mJ·mm^{-3}.
(5) By analyzing the dissipated strain energy and input strain energy in uniaxial cyclic loading and unloading test, there is a linear relationship between ISED and DSED of CLU. The applicability of the CLDL has been verified by other loading-unloading experiment schemes. A new law of rock strain energy evolution in UCLUE is found.

Data availability statement

The original contributions presented in the study are included in the article/Supplementary Material, further inquiries can be directed to the corresponding author.

Author contributions

ZL: Conceptualization, methodology, data curation, and writing-original draft preparation. XL: Data curation,

writing-reviewing and editing, supervision. All authors contributed to the article and approved the submitted version.

Funding

Acknowledgments

Conflict of interest

The authors declare that the research was conducted in the absence of any commercial or financial relationships that could be construed as a potential conflict of interest.

Publisher's note

All claims expressed in this article are solely those of the authors and do not necessarily represent those of their affiliated organizations, or those of the publisher, the editors and the reviewers. Any product that may be evaluated in this article, or claim that may be made by its manufacturer, is not guaranteed or endorsed by the publisher.

References

Ali, F., Moradian, Z., Rivard, P., and Ballivy, G. (2016). Shear mechanism of rock joints under pre-peak cyclic loading condition. *Int. J. Rock Mech. Min. Sci.* 83, 197–210. doi:10.1016/j.ijrmms.2016.01.009

Arora, K., Chakraborty, T., and Rao, K. S. (2019). Experimental study on stiffness degradation of rock under uniaxial cyclic sinusoidal compression loading. *Rock Mech. Rock Eng.* 52, 4785–4797. doi:10.1007/s00603-019-01835-3

Chang, X., Guo, T., Lu, J., and Wang, H. (2019). Experimental study on rock-concrete joints under cyclically diametrical compression. *Geomechanics Eng.* 17 (6), 553–564. doi:10.12989/gae.2019.17.6.553

Ding, Z. W., Jia, J. D., Tang, Q. B., and Li, X. F. (2022). Mechanical properties and energy damage evolution characteristics of coal under cyclic loading and unloading. *Rock Mech. Rock Eng.* 55, 4765–4781. doi:10.1007/s00603-022-02884-x

Gong, F., Yan, J., and Li, X. (2018). A new criterion of rock burst proneness based on the linear energy storage law and the residual elastic energy index. *Chin. J. Rock Mech. Eng.* 37, 1993–2014. (in Chinese). doi:10.13722/j.cnki.jrme.2018.0232

Gong, F., Yan, J., Luo, S., and Li, X. (2019a). Investigation on the linear energy storage and dissipation laws of rock materials under uniaxial compression. *Rock Mech. Rock Eng.* 52, 4237–4255. doi:10.1007/s00603-019-01842-4

Gong, F. Q., Yan, J. Y., Li, X. B., and Luo, S. (2019b). A peak-strength strain energy storage index for rock burst proneness of rock materials. *Int. J. Rock Mech. Min. Sci.* 117, 76–89. doi:10.1016/j.ijrmms.2019.03.020

Guo, T., Liu, K., Ma, S., Yang, J., Xiang, L., Zhou, K., et al. (2022). Dynamic fracture behavior and fracture toughness analysis of rock-concrete bi-material with interface crack at different impact angles. *Constr. Build. Mater.* 356, 129286. doi:10.1016/j.conbuildmat.2022.129286

He, M., Chen, Y., Li, N., and Zhu, C. (2015). Deformation and energy characteristics of sandstone subjected to uniaxial cyclic loading. *J. China Coal Soc.* 40, 1805–1812. (in Chinese). doi:10.13225/j.cnki.jccs.2014.1226

He, M., Li, N., Chen, Y., and Zhu, C. (2017). Damping ratio and damping coefficient of rock under different cyclic loading conditions. *Rock Soil Mech.* 38, 2531–2538. (in Chinese). doi:10.16285/j.rsm.2017.09.009

Justo, J., Castro, J., and Cicero, S. (2018). Energy-based approach for fracture assessment of several rocks containing U-shaped notches through the application of the SED criterion. *Int. J. Rock Mech. Min. Sci.* 110, 306–315. doi:10.1016/j.ijrmms.2018.07.013

Liu, J., Xie, H., Jin, X., Zhou, H., Zhou, J., Fu, C., et al. (2008). Experimental study on damping characteristics of rock under cyclic loading. *Chin. J. Rock Mech. Eng.* 197, 712–717. (in Chinese). doi:10.3321/.issn:1000-6915.2008.04.009

Liu, J., Xu, J., Li, Q., and Li, G. (2010). Experimental research on damping paramerers of rock under cyclic loading. *Chin. J. Rock Mech. Eng.* 29 (5), 1036–1041. (in Chinese).

Liu, Y., Dai, F., Feng, P., and Xu, N. W. (2018). Mechanical behavior of intermittent jointed rocks under random cyclic compression with different loading parameters. *Soil Dyn. Earthq. Eng.* 113, 12–24. doi:10.1016/j.soildyn.2018.05.030

Liu, C., Zhao, G., Xu, W., Meng, X. r., Huang, S. j., Zhou, J., et al. (2020a). Experimental investigation on failure process and spatio-temporal evolution of rockburst in granite with a prefabricated circular hole. *J. Central South Univ.* 27 (10), 2930–2944. doi:10.1007/s11771-020-4519-3

Liu, Z., Wang, W., Luo, J., and Miao, G. (2020b). Method of energy evolution of rock under uniaxial compression test. *J. China Coal Soc.* 45, 3131–3139. (in Chinese). doi:10.13225/j.cnki.jccs.2019.1067

Liu, Z., Zhao, G., Meng, X., Zhang, R., Cheng, X., Dong, C., et al. (2021). Analysis of creep energy evolution of red sandstone based on linear energy storage law. *J. Central South Univ. Technol.* 52, 2748–2760. (in Chinese). doi:10.11817/j.issn.1672-7207.2021.08.021

Liu, H., Pengfei, B., Xin, L., Wei, Y., and Wang, M. (2022). Mechanical properties and energy dissipation characteristics of phyllite under triaxial multi-stage cyclic loading-unloading conditions. *Chin. J. Rock Mech. Eng.* 43, 265–274+281. (in Chinese). doi:10.16285/j.rsm.2021.1352

Liu, C., Zhao, G., Xu, W., Meng, X., Liu, Z., Cheng, X., et al. (2023). Experimental study on failure characteristics of single-sided unloading rock under different intermediate principal stress conditions. *Int. J. Min. Sci. Technol.* 33 (3), 275–287. doi:10.1016/j.ijmst.2022.12.005

Manoj, N., and Petroš, V. (2009). Fatigue and dynamic energy behaviour of rock subjected to cyclical loading. *Int. J. Rock Mech. Min. Sci.* 46 (1), 200–209. doi:10.1016/j.ijrmms.2008.05.002

Meng, Q., Han, L., Pu, H., Wen, S., and Li, H. (2015). Experimental on the effect of strain rate and size on the energy accumulation and dissipation of rock. *J. China Coal Soc.* 40, 2386–2398. (in Chinese). doi:10.13225/j.cnki.jccs.2014.1771

Meng, Q., Liu, J. F., Ren, L., Pu, H., and Chen, Y. l. (2021). Experimental study on rock strength and deformation characteristics under triaxial cyclic loading and unloading conditions. *Rock Mech. Rock Eng.* 54, 777–797. doi:10.1007/s00603-020-02289-8

Momeni, A., Karakus, M., Khanlari, G. R., and Heidari, M. (2015). Effects of cyclic loading on the mechanical properties of a granite. *Int. J. Rock Mech. Min. Sci.* 77, 89–96. doi:10.1016/j.ijrmms.2015.03.029

Rashidi Moghaddam, M., Ayatollahi, M. R., and Berto, F. (2018). Rock fracture toughness under mode II loading: A theoretical model based on local strain energy density. *Rock Mech. Rock Eng.* 51, 243–253. doi:10.1007/s00603-017-1319-7

Stavropoulou, E., Dano, C., and Boulon, M. (2021). Shear response of wet weak carbonate rock/grout interfaces under cyclic loading. *Rock Mech. Rock Eng.* 54, 2791–2813. doi:10.1007/s00603-021-02406-1

Xie, H., Peng, R., Ju, Y., and Zhou, H. (2005). On energy analysis of rock failure. *Chin. J. Rock Mech. Eng.* 24, 2603–2608. (in Chinese). doi:10.3321/j.issn:1000-6915.2005.15.001

Xie, H., Yang, J., Li, L., and Peng, R. (2008). Energy mechanism of deformation and failure of rocks. *Chin. J. Rock Mech. Eng.* 27, 1729–1739. (in Chinese). doi:10.3321/j.issn:1000-6915.2008.09.001

Yang, Y., Duan, H., and Xing, L. (2018). Fatigue deformation and energy evolution of coal under uniaxial cyclic loading. *J. Basic Sci. Eng.* 26, 154–167. (in Chinese). doi:10.16058/j.issn.1005-0930.2018.01.014

Yoshinaka, R., Tran, T. V., and Osada, M. (1997). Mechanical behavior of soft rocks under triaxial cyclic loading conditions. *Int. J. Rock Mech. Min. Sci.* 34, 354.e1–354.e14. doi:10.1016/S1365-1609(97)00243-8

You, M., and Su, C. (2008). Experimental study on strengthening of marble specimen in cyclic loading of uniaxial or pseudo-triaxial compression. *Chin. J. Solid Mech.* 29 (1), 66–72. (in Chinese). doi:10.19636/j.cnki.cjsm42-1250/o3.2008.01.010

Zhang, Z., and Gao, F. (2012a). Research on nolinnear characteristics of rock energy. *Chin. J. Rock Mech. Eng.* 31, 1198–1207. (in Chinese). doi:10.3969/j.issn.1000-6915.2012.06.015

Zhang, Z., and Gao, F. (2012b). Expriment research on energy evolution of red sandstone samples under uniaxial compression. *Chin. J. Rock Mech. Eng.* 31, 953–962. (in Chinese). doi:10.3969/j.issn.1000-6915.2012.05.012

Zhang, Z., and Gao, F. (2015). Experimental investigation on the energy evolution of dry and water-saturated red sand-stones. *Int. J. Min. Sci. Technol.* 25, 383–388. doi:10.1016/j.ijmst.2015.03.009

Zhang, Y., Jiang, X., Yang, H., and Chen, S. (2011). Effect of confining pressure on evolution law of hysteresis loop of sandstone under cyclic loading. *Chin. J. Rock Mech. Eng.* 30, 320–325. (in Chinese).

Zuo, J-P., Xie, H., Meng, B., and Liu, J. (2011). Experimental research on loading-unloading behavior of coal-rock combination bodies at different stress levels. *Rock Soil Mech.* 32, 1287–1296. (in Chinese). doi:10.16285/j.rsm.2011.05.028

Propagation characteristics and control technology of blasting vibration in neighborhood tunnel

Zixiu Qin[1], Yihan Zhao[2], Lu Chen[3], Hongtao Cao[3]*, Ling Zeng[3], Wencan Jiao[1]* and Hong Xu[3]

[1]Guangxi Xinfazhan Communication Group Co., Ltd., Nanning, China, [2]Power China Zhongnan Engineering Corporation Limited, Changsha, China, [3]School of Civil Engineering, Changsha University of Science and Technology, Changsha, China

During the tunnel construction process using the drilling and blasting method, the induced blasting vibration always poses a great threat to the stability and safety of the adjacent tunnel supporting structure. To improve the efficiency and safety of tunnel blasting construction, the vibration propagation and peak particle velocity (PPV) distribution of the lining of an excavated tunnel were investigated during the blasting of an adjacent tunnel located in Guangxi province. The evolution process and distribution characteristics of the PPV of the lining of adjacent tunnels were monitored and analyzed. The results show that the maximum blasting vibration velocity of the lining of the adjacent tunnel can be shown as: PPVx > PPVz > PPVy; hence, the PPVx plays a significant role in the vibration of the adjacent tunnel. According to the tensile stress failure criterion, the PPV threshold was determined to be 12.7 cm/s in this study. To control the damage of surrounding rock induced by the blasting vibration, compound wedge-shaped cutting technology, stress wave dislocation superposition technology, and pre-splitting blasting technology were employed to reduce the impact of blasting vibration on the excavated tunnel.

1 Introduction

When a highway is constructed in a mountain area, the neighborhood tunnel is used frequently, and it is restricted by terrain conditions and environmental factors (Editorial department of China Journal of Highway and Transport, 2022). As the most widely used and efficient method for rock excavation in engineering practice, the drilling and blasting technique is widely used in mountain tunnel excavation (Chen et al., 2023; Liang et al., 2023). However, the dynamic load induced by blasting can easily damage the bearing capacity of the surrounding rock and supporting structure, leading to cracking, spalling, and even collapse of existing tunnel (Li et al., 2014; Xue et al., 2019; Liang et al., 2023). For instance, on 10 September 2020, during the construction at 540 m of the left tunnel of Leye Avenue in Leye County, Guangxi, a sudden rock collapse occurred on top of the tunnel. Nine workers who were working on the tunnel were trapped. The blasting vibration caused by the explosion always poses a great threat to the stability and safety of a tunnel structure (Zhou et al., 2020; Cheng et al., 2021; Yu et al., 2021; Xue et al., 2023). Consequently, the influence of blasting on the stability of adjacent tunnels has attracted wide attention.

At present, the research on the vibration characteristics of tunnel induced by blasting load can be divided into three categories: theoretical analysis, field test, and numerical

analysis (Cao et al., 2016; Yang et al., 2022; Xu et al., 2023). (1) Theoretical analysis: the stress wave theory and tensile stress criterion are the theoretical basis for the analysis of vibration response of tunnels (Jiang and Zhou, 2012; Xie et al., 2016). Li et al. (2013) established the motion equation of an adjacent tunnel structure according to the propagation of the blasting stress wave and theory of energy conservation, calculating the stress distribution of a tunnel. They then proposed a theoretical method for predicting the dynamic response of this tunnel. Chen et al. (2017) employed the separation of variables method to solve the displacement potential function for the propagation of blasting-induced vibration waves. They discussed the peak particle velocity law in surrounding rock under different blast loads and surrounding rock parameters. Luo et al. (2022) derived the frequency domain expression and vibration velocity spectrum expression for the equivalent blasting load in porous media through theoretical analysis, and the propagation and attenuation of the primary frequency of blasting vibration of multiple cutting holes and caving holes in infinite rock mass were explored. (2) Field test: the vibration characteristics of the tunnel structure can be evaluated by the field blasting vibration monitoring test. Zhang et al. (2008) analyzed the blasting vibration characteristics of middle rock and concrete lining of bifurcation tunnel under different modes of cutting blasting. Fu et al. (2011) carried out vibration monitoring on the vault and side wall near a tunnel working face, analyzing the blasting vibration characteristic of the surrounding rock near the blasting source. Dang et al. (2018) arranged three-dimensional velocity sensors in the bottom foot and arch waist of an adjacent tunnel, obtaining the blasting vibration velocity of the lining. Lin (2011) carried out long-term blasting vibration monitoring, investigating the relationship between the PPV and charge, and the stability of the tunnel, which was disturbed by blasting vibration, was then assessed by the dynamic stress ratio method. (3) Numerical analysis: the numerical analysis method is being gradually applied to investigate tunnel engineering with the rapid development of computing technology. Kim et al. (2006) used the PFC 2D software to simulate the blasting of tunnel contour holes, and numerical models with different joint angles and joint spacing were established to analyze the failure mechanism of tunnel blasting, considering the angle and spacing of discontinuous interfaces. Liang et al. (2013) used the three-dimensional numerical analysis method to comprehensively analyze the influence of tunnel static stress and dynamic stress caused by blasting on the existing tunnel lining. Shin et al. (2011) studied the influence of blasting vibration on the performance of existing tunnels from the perspectives of vibration velocity, displacement, and stress of lining. Yu et al. (2014) used ABAQUS software to analyze the blasting vibration characteristics of adjacent tunnels on soft soil foundation, evaluating the safety of tunnels. Liu et al. (2020) established the three-dimensional numerical model using ANSYS/LS-DYNA, analyzing the distribution characteristics of vibration velocity and stress of adjacent tunnels; the relationship between vibration velocity and tensile stress of the tunnel lining was then established. Yang et al. (2015) conducted a three-dimensional numerical simulation study on rock damage evolution during the excavation of deeply buried tunnels using LS-DYNA software. The impact of practical millisecond delay blasting on damage extension was discussed, and the mechanisms of rock damage and evolution were then explored during the excavation process of deeply buried

tunnels. Zhou et al. (2016) established a numerical model for an existing tunnel and an adjacent tunnel under construction at different spacing values, and the vibration response of the existing tunnel to the adjacent blasting construction was analyzed. Yang et al. (2019) employed a three-dimensional dynamic finite element model to validate field monitoring results, and the mechanisms that cause the difference between the surface and inside vibration were discussed in detail.

In general, the vibration criteria of tunnel blasting often simply refers to the degree of safety allowed for the PPV in the tunnel construction process. In the safety regulations for blasting, the allowable range is specified from 10 cm/s to 20 cm/s. However, as research advances, scholars have discovered a critical defect in that the peak vibration velocity is used as the unique criterion for assessing the safety of blasting-induced vibrations in many practical engineering cases (Chen et al., 2023). In fact, the vibration response of the tunnel is determined by objective factors, such as the blasting load and the tunnel's properties (Ling et al., 2021; Song, 2022). It is difficult to control blasting disasters only by referring to the safety regulations for blasting or similar engineering experiences. Therefore, it is important to analyze the propagation characteristics of blasting vibration and the vibration response law of adjacent tunnels, and it is necessary to explore vibration control technology for reducing blasting vibration. Blasting disasters can be effectively controlled, and the safety construction efficiency can be improved.

2 Engineering condition and blasting vibration monitoring

2.1 Engineering condition

A double-line tunnel was excavated using drilling and blasting method in Guangxi. The maximum width of the excavation section is approximately 16.0 m. The minimum horizontal distance between the tunnels is also approximately 16.0 m. That can be considered a small clear distance tunnel. The layout of tunnels is shown in Figure 1. The tunnel passes through the mountain with thin covering soil, and the large area of bed rock is exposed. The surrounding rock is slightly or moderately weathered limestone. However, the rock is hard and complete, and the unconfined compression strength of part rock sample can exceed 100 MPa. Physical and mechanical tests were carried out on the moderately weathered limestone stones collected from the tunnel, and the main physical and mechanical parameters are summarized in Table 1.

The double-line tunnels were excavated step by step. The right line was excavated, followed by the left tunnel. Therefore, the right-line existing tunnel would be disturbed by the vibration caused by the blasting excavation of the left line. The left tunnel was excavated by the bench method, and the upper bench profile was excavated by smooth blasting. The width and height of the excavation section are 16.0 m and 6.6 m, respectively. The design of the excavation footage is 2.0 m, 2.5 m, and 3.0 m, respectively. Under different footage conditions, the charge of each blast holes increased slightly with the increase of footage, and the main parameters, such as the number of blast holes and delay time, were almost kept the same. The blasting parameters are listed in Table 2 and Figure 2, respectively. The type
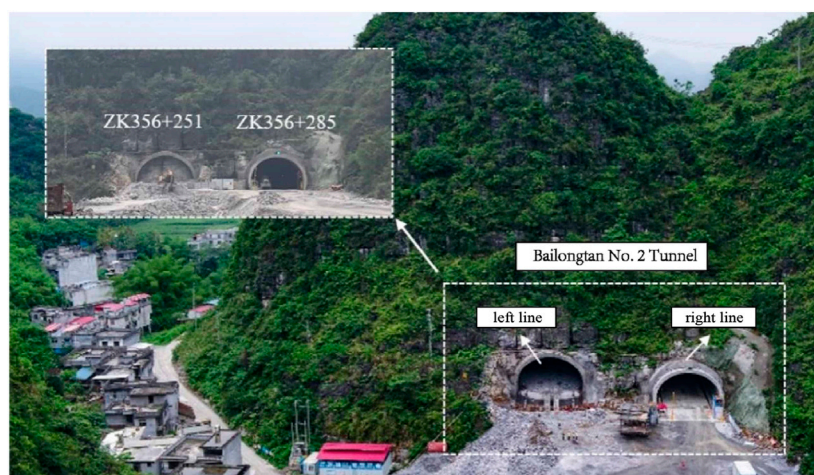
FIGURE 1
Position relationship of double-line tunnel.

TABLE 1 Main physical mechanical parameters of moderately weathered limestone.

Parameters	Minimum	Maximum	Average
Natural density (g/cm3)	2.67	2.67	2.67
Uniaxial compressive strength (MPa)	40.0	98.5	62.9
Elastic modulus (GPa)	2.68	4.02	3.46
Wave velocity (m/s)	4305	5236	4691
Poisson	0.18	0.23	0.21

of hole was defined according to the function of the hole in the tunnel blasting. The symbols of MS1 and x# were used to represent the detonation time. The layout of the blasting holes is shown in Figure 2. Furthermore, to control the blasting vibration, the contour blasting was divided into two parts. The wall was blasted using the MS13, followed by the vault blasting at the MS15.

2.2 Monitoring scheme and technology

Based on the propagation theory of stress wave and the principle of blasting vibration monitoring, the blasting vibration monitoring test was carried out on the adjacent right-line tunnel. The layout of monitoring points is shown in Figure 3. Five monitoring points were arranged on the lining close to the blasting tunnel, which were numbered as 1#, 2#, 3#, 4#, and 5#, respectively. The vertical position of the monitoring points was 1.2 m away from the tunnel floor, and the distance between the monitoring points was 5 m. Monitoring point 3# was parallel to the working face of the excavating tunnel at the tunneling direction. Monitoring points 1# and 2# were located in front of the working face section. The area of the left tunnel parallel to those measuring points is not excavated yet. Monitoring points 4# and 5# were located at the rear of the

working face section, where both the tunnels have been excavated, forming the middle rock. Three-dimensional velocity sensors were installed at each monitoring point to monitor the blasting vibration velocity on the lining of the right excavated tunnel.

In order to comprehensively consider the influence of rock characteristics, mountain structure, geological structure, and other factors on blasting vibration, the intelligent blasting vibration meters are shown in Figure 3, which is composed of the NUBOX-8016 acquisition equipment and TP3V-4.5 three-dimensional speed sensor. The measurement range was from 0.0047 cm/s to 35 cm/s, which can simultaneously measure the vibration signals in the X-horizontal radial, Y-horizontal tangential, and Z-vertical direction. In order to obtain accurate and detailed blasting vibration signals, the frequency, trigger level, acquisition time, and delay time of the instrument were set to 5 kHz, 0.1 cm/s, 1s, and 20 ms, respectively. The blasting vibration meter was installed before detonation, as shown in Figure 3, and this must be activated to await the trigger and store the vibration data when the vibration velocity exceeds 0.1 cm/s.

2.3 Monitoring results

Three kinds of field blasting tests with different maximum charge quantities of a single section were carried out. A total of 15 sets of data were obtained. The vibration velocity data of the monitoring points in the nearby tunnel are listed in Table 3.

Taking the blasting vibration results at the section of the ZK356 + 262 as an example, the curve of vibration velocity and time is shown in Figure 4. It can be seen that eight segments of the blasting vibration wave were monitored during the blasting. As the charge amount of the cutting section (MS1) is the maximum, the PPV is also significantly higher than other segments. Hence, the blasting vibration of the MS1 influence on the adjacent tunnel lining is discussed.

TABLE 2 Main parameters of blasting.

| Blast hole				Time		Explosive		
Type	Number	Length (m)	Angle (°)	Segment	Delay (ms)	Single hole (kg)	Total (kg)	Sum (kg)
Cutting hole	12	3.4	41	MS1	0–50	2.4	28.8	28.8
Auxiliary Cutting hole	8	2.6	51	MS3	50–100	1.8	14.4	14.4
Caving hole #1	8	2.4	58	MS5	100–150	1.8	14.4	14.4
Caving hole #2	8	2.2	66	MS7	150–200	1.5	12.0	19.2
Floor hole #1	4	2.1	90	MS7	150–200	1.8	7.2	
Caving hole #3	4	2.1	74	MS9	200–250	1.5	12.0	21.9
Floor hole #2	4	2.0	90	MS9	200–250	1.8	3.6	
Caving hole #4	7	2.1	90	MS9	200–250	0.9	6.3	
Floor hole #3	2	2.0	90	MS11	250–300	1.8	3.6	9.6
Caving hole #5	4	2.1	83	MS11	300–350	1.5	6.0	
Contour hole #1	20	2.0	90	MS13	350–400	4.5	27.0	27.0
Contour hole #2	22	2.0	90	MS15	400–450	0.6	13.2	16.8
Bottom foot hole	2	2.1	90	MS15	400–450	1.8	3.6	
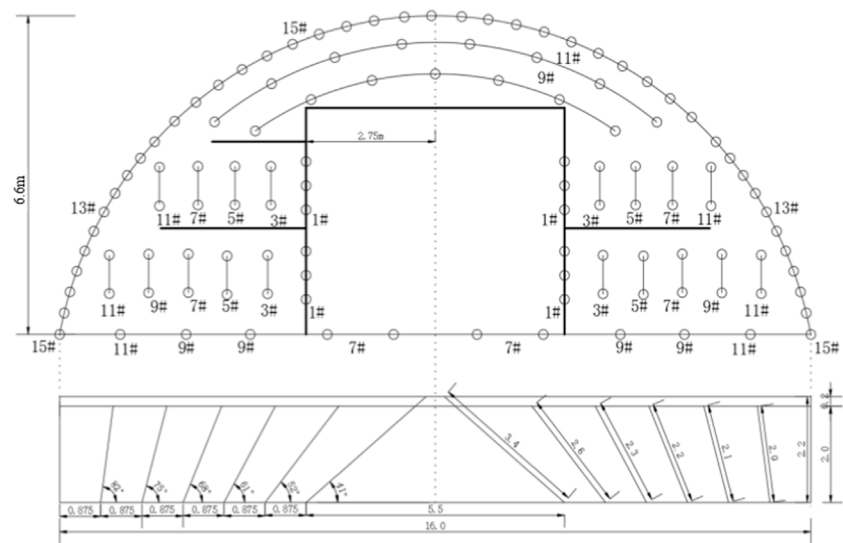
FIGURE 2
Layout of blasting hole.

In order to analyze the vibration characteristics of the adjacent tunnel, the PPV induced by the maximum charge of 28.8 kg, 36.0 kg, and 42.0 kg have been drawn in Figure 5. The position 0 m on the abscissa represents the blasting working position, the positive value represents the unexcavated direction, and the negative value is the excavated direction. The PPV-x of the adjacent tunnel is the largest, followed by the PPV-z, and the PPV-y is the smallest; these results indicate that the horizontal vibration wave plays a significant role in the vibration of the adjacent tunnel. With the increase of explosive dosage, the PPV of the monitoring points gradually increased. In the longitudinal direction of the adjacent tunnel, the PPV at the blasting location is the largest, and then decays in both directions of the tunnel. However, when the distance from the monitoring section is the same, the PPV on the unexcavated side is slightly higher than that on the excavated side; these results indicate that the PPV attenuation rate on the unexcavated side is slower than that on the excavated side. Therefore, more attention should be paid to the blasting vibration on the unexcavated side.
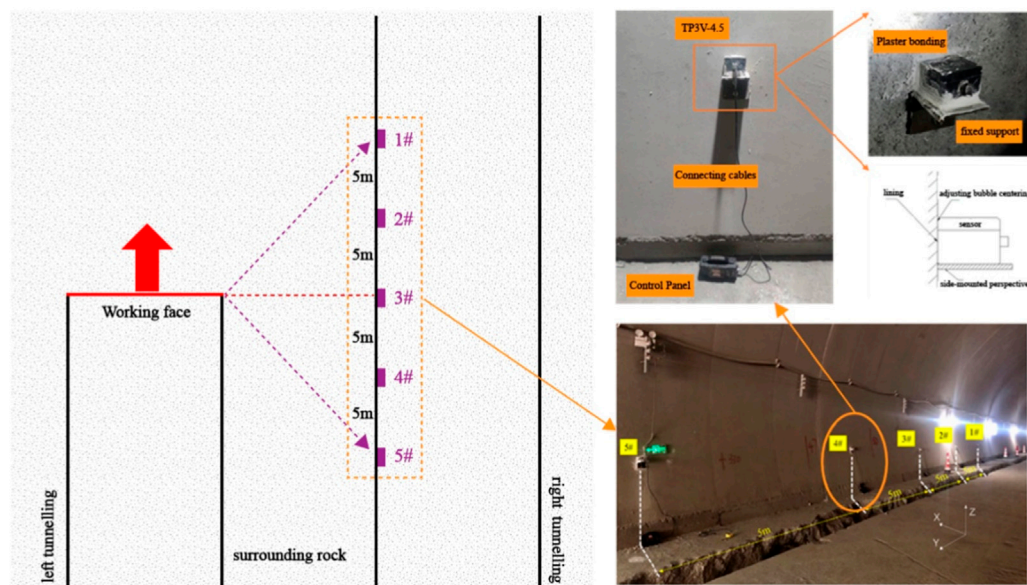
FIGURE 3
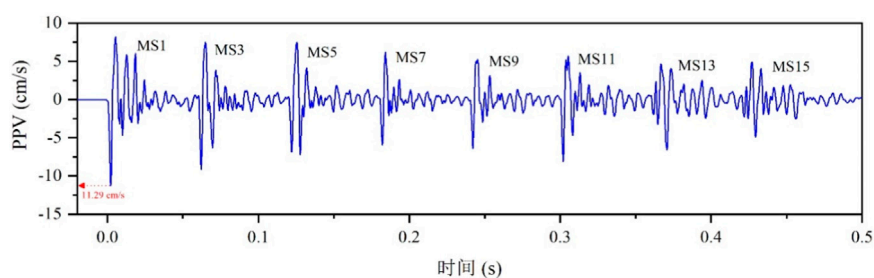Layout of blasting vibration monitoring points.

TABLE 3 Blasting vibration monitoring data of nearby tunnel.

| Monitoring position	Footage (m)	The maximum charge (kg)	Segment	Monitoring point	Blasting center distance (m)	Peak particle velocity (cm/s)			
						PPV_X	PPV_Y	PPV_Z	Resultant velocity
ZK356 + 262	2.0	28.8	MS1	1#	26.0	6.53	2.90	5.80	9.20
				2#	24.5	10.44	3.47	7.29	13.20
				3#	24.0	11.29	4.69	8.70	15.03
				4#	24.5	6.54	3.01	6.09	9.43
				5#	26.0	3.77	2.44	3.97	5.99
ZK356 + 275	2.5	36.0	MS1	1#	26.0	7.50	3.58	3.97	9.21
				2#	24.5	12.12	6.47	7.76	15.78
				3#	24.0	14.19	7.57	10.05	18.96
				4#	24.5	9.31	4.92	6.54	12.40
				5#	26.0	6.02	3.04	5.35	8.51
ZK356 + 303	3.0	42.0	MS1	1#	26.0	9.36	2.13	4.65	10.67
				2#	24.5	12.12	6.47	7.76	15.78
				3#	24.0	17.13	6.54	12.67	22.29
				4#	24.5	10.11	3.01	9.43	14.15
				5#	26.0	7.26	3.58	3.97	9.02

In order to further analyze the difference of the vibration velocity attenuation characteristic between the unexcavated side and the excavated side of the adjacent tunnel, the fitting formula based on the detonation center distance (R) and the single maximum charge quantity (Q) was used to investigate the PPV of the adjacent tunnel. The fitting formula can be described as follows:

$$PPV = K\left(R/Q^{1/3}\right)^{-\alpha} = K\left[SD\right]^{-\alpha} \tag{1}$$

FIGURE 4
Vibration velocity–time curve.
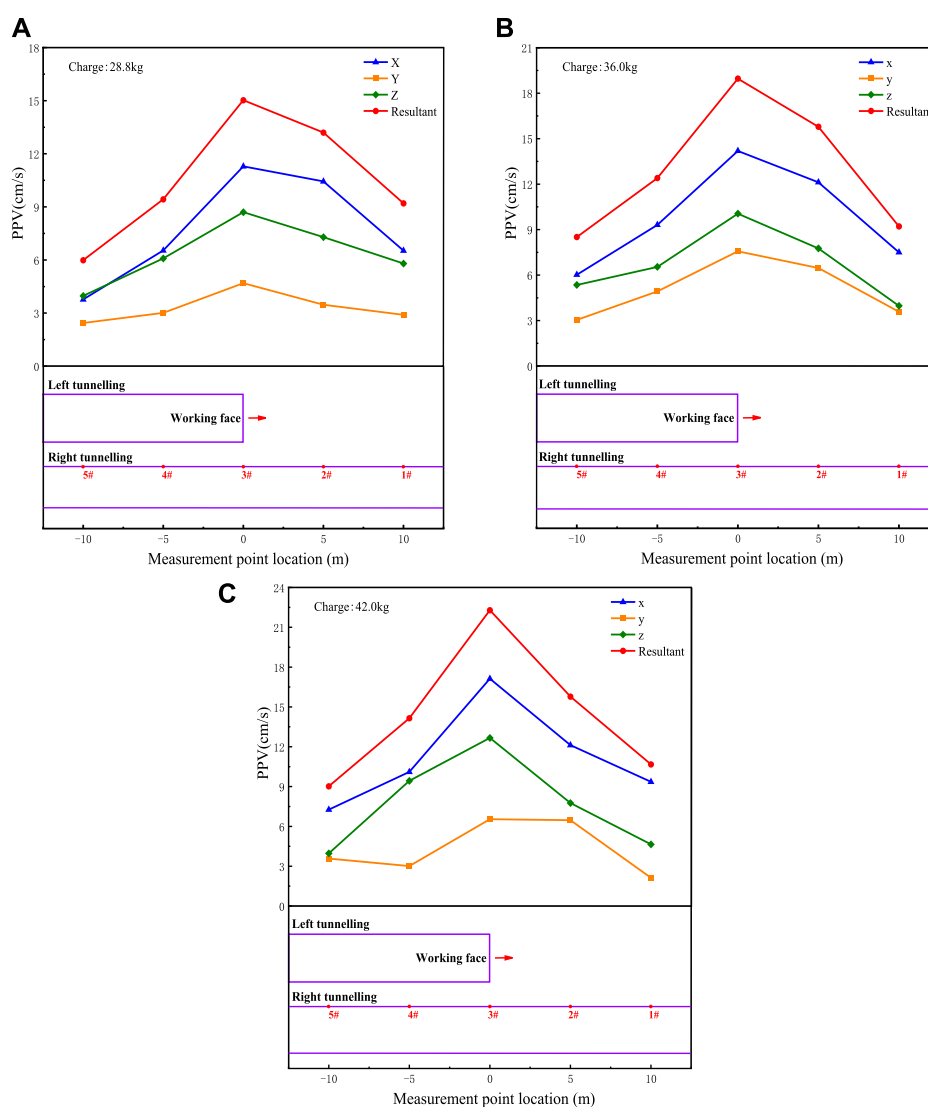
FIGURE 5
The PPV distribution of adjacent tunnel.

where *R* is the linear distance from the explosion source to the monitoring point (m), *Q* is the maximum charge quantity (kg), *K* and *α* are the blasting vibration coefficient, which is dependent on rock characteristics and geological conditions, and *SD* is the scale distance (m/kg$^{1/3}$).

Taking the logarithms of formula (1), formula (2) can be expressed:

$$\ln PPV = \ln K - \ln SD \qquad (2)$$
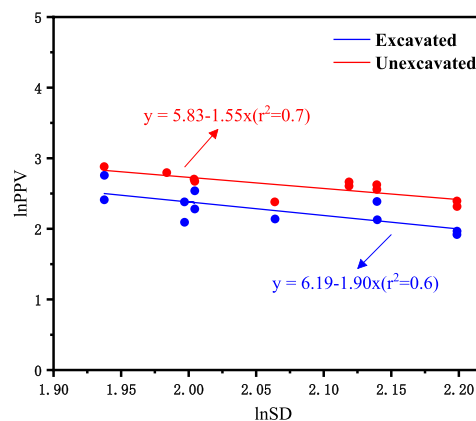
FIGURE 6
Blasting vibration velocity attenuation of the adjacent tunnel.

Let $y = \ln PPV$, $x = \ln SD$, $b = \ln K$, and formula (2) will be:

$$y = b - ax \qquad (3)$$

As shown in Figure 6, according to Eqs 1–3, the PPV is fitted with the proportional distance, and the fitting results of the unexcavated side and excavated side are obtained.

The stress wave propagation attenuation parameters of the K and α are determined. The formula of vibration velocity attenuation (4) is described as follows:

$$\begin{cases} PPV_{unexcavated} = 340.4 \cdot SD^{-1.55} \\ PPV_{excavated} = 487.8 \cdot SD^{-1.90} \end{cases} \qquad (4)$$

The attenuation law of the blasting vibration in the excavating direction and excavating section is different. The values of α are 1.90 and 1.55, respectively. Those are relatively close, indicating that the geological conditions of the rock mass in the tests had tiny differences. The values of K are 487.8 and 340.3, respectively; the difference between the two values is obvious, indicating that the excavation state in the excavating direction and excavated section had a significant impact on the propagation and attenuation of the blasting vibration.

3 Safety criterion of blasting vibration

3.1 The relationship between PPV and tensile stress

During blasting excavation, the blasting disturbance generated by the blasting energy released will eventually propagate outward in the form of elastic waves. On the wave vibration surface, the relationship of the peak vibration velocity of the particle and stress can be expressed as

$$\sigma = v\rho C_P \qquad (5)$$

where σ is the dynamic stress on the wave surface (Pa), v is the peak particle vibration velocity (m/s), ρ is the density of the vibration medium (kg/m3), and C_P is the elastic longitudinal wave velocity of the vibration medium (m/s).

3.2 The PPV threshold

The damage of the adjacent tunnel lining can be judged according to the maximum tensile stress criterion. When the tensile stress on the lining exceeds the tensile strength of the concrete material, it can be judged that the lining structure has been destroyed.

According to the code for the design of concrete structures, the design value of the tensile strength of the C25 concrete is 1.27 Mpa. Considering the strain rate effect, the dynamic tensile strength improvement coefficient of rock is 1.24 (Jiang et al., 2023). The permitted dynamic tensile stress can be obtained using Formula (5), and then, the PPV threshold of the adjacent tunnel is calculated. Hence, the critical value is 12.7 cm/s in this study. In comparison with Table 1, the blasting vibration is smaller than that of the threshold value. Hence, it is necessary to employ useful technology to reduce the vibration.

4 Blasting vibration reduction technology
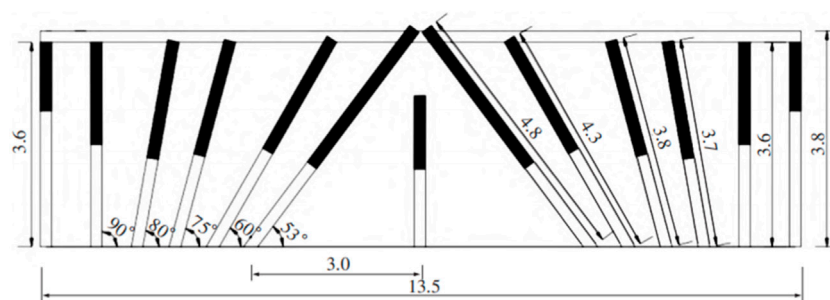
4.1 Compound wedge-shaped cutting technology

During tunnel blasting, the satisfactory cutting blasting effect can be realized using the single-stage large-wedge cutting blasting method (Zhong et al., 2022). However, the vibration intensity is very strong in the cutting blasting process as a great quantity of explosives is necessary. Moreover, the blasting effect is limited by the impact of stress clamping, and most of the energy is converted into vibration rather than being used to break the rock (Tian et al., 2019). Fortunately, as shown in Figure 7, the compound wedge-shaped cutting can reduce the charge as the additional free surface will be provided by the middle hole. When the middle hole is used to break the rock, the stress of the remaining cutting holes will be released, reducing the clamping effect. The explosive energy will be used to break the rock effectively as the energy of vibration is reduced.
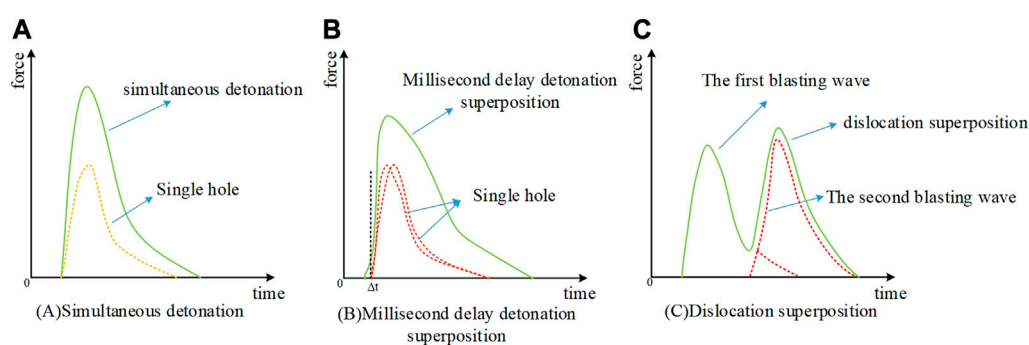
4.2 Stress wave dislocation superposition

From the vibration monitoring analysis of the blasting test area, it could be found that the maximum vibration velocity was caused by the cutting holes. Hence, it is necessary to control the maximum single-segment charge of the cut blasting. As shown in Figure 8, if the stress wave generated by the single blasting hole can be superimposed on the staggered peaks, this can effectively decrease the strength of the seismic waves resulting from the superposition of the total charge of the blasting hole. Fortunately, with the development of electronic detonator technology, the precision of the hole initiation time can be controlled in 1 m (Iwano et al., 2020). The delay time of each cutting blasting hole can be controlled to control the blasting effect.
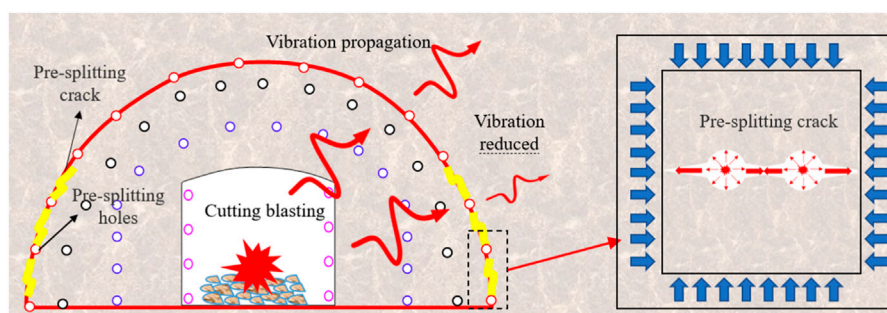
4.3 Pre-splitting blasting

The propagation of blasting seismic waves mainly depended on the wave impedance of the medium. As shown in Figure 9, when the tunneling contour is formed with pre-splitting crack, and the blasting vibration wave reaches the crack, the vibration wave will

FIGURE 7
Compound wedge-shaped cutting.

FIGURE 8
Stress wave dislocation superposition mechanism. **(A)** Simultaneous detonation, **(B)** Millisecond delay detonation superposition and **(C)** Dislocation superposition.

FIGURE 9
The layout of pre-splitting blasting holes.

generate reflection and transmission. The tensile wave will return to the blast zone, and a portion of the damped compression wave will be transmitted. The transmitted wave intensity will be weakened, reducing the vibration behind the pre-splitting crack.

4.4 Analysis of damping effect

The blasting vibration reduction technology is provided and used in the blasting control area. When the compound wedge-shaped cutting technology is used, the blasting vibration can be reduced by about 15%. If the delay time of the cutting blasting hole is set from 3 m to 5 m, the blasting vibration can be reduced by about 20%. When the pre-splitting holes are arranged at the wall of the tunnel, the blasting vibration can be reduced by about 20%–30%. This can reach 60% if the all the contour holes are set as pre-splitting holes. In engineering practice, the blasting vibration must be controlled to reduce the risk. It is necessary to analyze the engineering condition and technical level so that the appropriate technical methods can be employed.

5 Conclusion

In this article, the vibration of blasting excavation of a double-line tunnel project in Guangxi is investigated. The blasting vibration propagation is analyzed by field monitoring. The relationship between the maximum stress and the PPV is analyzed, and a reasonable PPV threshold is proposed. Then, blasting vibration reduction technology is provided. The research results have been successfully applied to guide field construction.

(1) The blasting vibration of the adjacent tunnel can be shown as: $PPV_X > PPV_Z > PPV_Y$, in which the PPV_X plays a significant role in the vibration of the adjacent tunnel.
(2) When the distance from the blasting center to the monitoring points is the same, the PPV located at the unexcavated side is slightly higher than that of the excavated side, which indicates that the attenuation rate of the PPV of the unexcavated side is slower than that of the excavated side. Attention should be paid to the blasting vibration of the unexcavated side.
(3) The relationship between the maximum tensile stress and PPV of the adjacent tunnel lining is analyzed. According to the ultimate tensile stress failure criterion, the PPV threshold of the adjacent tunnel is determined to be 12.7 cm/s in this study.
(4) Compound wedge-shaped cutting technology, stress wave dislocation superposition technology, and pre-splitting blasting technology are employed to reduce the blasting vibration. The blasting vibration can be reduced from 20% to 60%. The blasting vibration must be controlled to reduce the risk. It necessary to analyze the engineering condition and technical level so that the appropriate technical methods can be employed.

Data availability statement

The original contributions presented in the study are included in the article/supplementary material, further inquiries can be directed to the corresponding authors.

Author contributions

Literature search and manuscript writing: ZQ, YZ, and LC. Monitoring design: HC, LC. Field monitoring: WJ. Verification: ZQ, LZ. Writing–first draft preparation: ZQ, YZ, and LC. Writing–review and editing: HX, LC. All authors contributed to the article and approved the submitted version.

Funding

Conflict of interest

Authors ZQ and WJ were employed by the company Guangxi Xinfazhan Communication Group Co., Ltd. Author YZ was employed by the company Power China Zhongnan Engineering Corporation Limited.

The remaining authors declare that the research was conducted in the absence of any commercial or financial relationships that could be construed as a potential conflict of interest.

Publisher's note

All claims expressed in this article are solely those of the authors and do not necessarily represent those of their affiliated organizations, or those of the publisher, the editors and the reviewers. Any product that may be evaluated in this article, or claim that may be made by its manufacturer, is not guaranteed or endorsed by the publisher.

References

Cao, W., Li, X., Tao, M., and Zhou, Z. (2016). Vibrations induced by high initial stress release during underground excavations. *Tunn. Undergr. Space Technol.* 53, 78–95. doi:10.1016/j.tust.2016.01.017

Chen, S.-h., Hu, S.-w., Zhang, Z.-h., and Wu, J. (2017). Propagation characteristics of vibration waves induced in surrounding rock by tunneling blasting. *J. Mt. Sci.* 14 (12), 2620–2630. doi:10.1007/s11629-017-4364-5

Chen, L., Zhou, Z.-L., Gao, S., Cai, X., Wang, S-F., Nie, S-L., et al. (2023). Research status and prospects of blasting excavation of tunnel under high stress condition. *J. Central South Univ. Sci. Technol.* 54 (3), 849–865. doi:10.11817/j.issn.1672-7207.2023.03.006

Cheng, R., Chen, W., Hao, H., and Li, J. (2021). A state-of-the-art review of road tunnel subjected to blast loads. *Tunn. Undergr. Space Technol.* 112, 103911. doi:10.1016/j.tust.2021.103911

Dang, V., Dias, D., Do, N., and Vo, T. (2018). Impact of blasting at tunnel face on an existing adjacent tunnel. *Int. J. Geomate* 15 (47), 22–31. doi:10.21660/2018.47.04640

Editorial department of China Journal of Highway and Transport (2022). Review on China's traffic tunnel engineering research: 2022. *China J. Highw. Transp.* 35 (4), 1–38. doi:10.19721/j.cnki.1001-7372.2022.04.001

Fu, H., Zhao, Y., Xie, J., and Hou, Y. (2011). Study of blasting vibration test of area near tunnel blasting source. *Chin. J. Rock Mech. Eng.* 30 (02), 335–340.

Iwano, K., Hashiba, K., Nagae, J., and Fukui, K. (2020). Reduction of tunnel blasting induced ground vibrations using advanced electronic detonators. *Tunn. Undergr. Space Technol.* 105, 103556. doi:10.1016/j.tust.2020.103556

Jiang, N., and Zhou, C. (2012). Blasting vibration safety criterion for a tunnel liner structure. *Tunn. Undergr. Space Technol.* 32, 52–57. doi:10.1016/j.tust.2012.04.016

Jiang, W., Gao, Q.-D., Wang, Y.-Q., Yang, Y., Fan, Y., and Leng, Z. (2023). Study on blast vibration characteristics and its isolation scheme selection of the existing tunnel in multi-arch tunnel without middle wall. *Chin. J. Geotechnical Eng.* Available at: http://kns.cnki.net/kcms/detail/32.1124.TU.20230115.1144.009.html.

Kim, S., Jeong, W., Jeong, D., and Seok, J. (2006). Numerical simulation of blasting at tunnel contour hole in jointe rock mass. *Tunn. Undergr. Space Technol.* 21 (3), 306–307. doi:10.1016/j.tust.2005.12.162

Li, J. C., Li, H. B., Ma, G. W., and Zhou, Y. (2013). Assessment of underground tunnel stability to adjacent tunnel explosion. *Tunn. Undergr. Space Technol.* 35, 227–234. doi:10.1016/j.tust.2012.07.005

Li, S., Li, K., Lei, G., and Sun, G. (2014). Study of blasting vibration and deformation control for metro construction beneath existing metro tunnel in short distance. *Rock Soil Mech.* 35 (S2), 284–289. doi:10.16285/j.rsm.2014.s2.048

Liang, Q., Li, J., Li, D., and Ou, E. (2013). Effect of blast-Induced vibration from new railway tunnel on existing adjacent railway tunnel in xinjiang, China. *Rock Mech. Rock Eng.* 46 (1), 19–39. doi:10.1007/s00603-012-0259-5

Liang, Y. J., Gao, S., and Chen, L. (2023). Research on deformation analysis and treatment technology of shallow buried tunnels in karst areas. *J. Transp. Sci. Eng.* 39 (2), 49–54. doi:10.16544/j.cnki.cn43-1494/u.20230403001

Lin, D. (2011). The mitigation negative effect of tunnel-blasting-induced vibrations on constructed tunnel and buildings. *J. Coal Sci. Eng. (China)* 17 (1), 28–33. doi:10.1007/s12404-011-0106-4

Ling, T., OuYang, X., Liu, J., and Zhang, S. (2021). Dynamic response analysis of double tunnel lining under blasting vibration. *J. Transp. Sci. Eng.* 37 (02), 20–27. doi:10.16544/j.cnki.cn43-1494/u.2021.02.004

Liu, Z., Jiang, N., Sun, J., Xia, Y., and Lyu, G. (2020). Influence of tunnel blasting construction on adjacent highway tunnel: a case study in wuhan, China. *Int. J. Prot. Struct.* 11 (3), 283–303. doi:10.1177/2041419619888936

Luo, Y., Gong, H., Qu, D., Zhang, X., Tao, Y., and Li, X. (2022). Vibration velocity and frequency characteristics of surrounding rock of adjacent tunnel under blasting excavation. *Sci. Rep.* 12 (1), 8453. doi:10.1038/s41598-022-12203-7

Shin, J. H., Moon, H. G., and Chae, S. E. (2011). Effect of blast-induced vibration on existing tunnels in soft rocks. *Tunn. Undergr. Space Technol.* 26 (1), 51–61. doi:10.1016/j.tust.2010.05.004

Song, H. (2022). Blasting vibration control technology based on blasting velocity attenuation law. *J. China&Foreign Highw.* 42 (02), 188–193. doi:10.14048/j.issn.1671-2579.2022.02.035

Tian, X., Song, Z., and Wang, J. (2019). Study on the propagation law of tunnel blasting vibration in stratum and blasting vibration reduction technology. *Soil Dyn. Earthq. Eng.* 126, 105813. doi:10.1016/j.soildyn.2019.105813

Xie, L. X., Lu, W. B., Zhang, Q. B., Jiang, Q., Wang, G., and Zhao, J. (2016). Damage evolution mechanisms of rock in deep tunnels induced by cut blasting. *Tunn. Undergr. Space Technol.* 58, 257–270. doi:10.1016/j.tust.2016.06.004

Xu, M., Li, X., Xu, K., Liu, T., Zhang, Y., and Yang, T. (2023). Influence of the spatial distribution of underground tunnel group on its blasting vibration response. *Undergr. Space* 10, 248–268. doi:10.1016/j.undsp.2022.10.006

Xue, F., Xia, C., Li, G., Jin, B., He, Y., and Fu, Y. (2019). Safety threshold determination for blasting vibration of the lining in existing tunnels under adjacent tunnel blasting. *Adv. Civ. Eng.* 2019, 1–10. doi:10.1155/2019/8303420

Xue, Y., Ranjith, P., Gao, F., Zhang, Z., and Wang, S. (2023). Experimental investigations on effects of gas pressure on mechanical behaviors and failure characteristic of coals. *J. Rock Mech. Geotechnical Eng.* 15, 412–428. doi:10.1016/j.jrmge.2022.05.013

Yang, J., Lu, W., Hu, Y., Chen, M., and Yan, P. (2015). Numerical simulation of rock mass damage evolution during deep-buried tunnel excavation by drill and blast. *Rock Mech. Rock Eng.* 48 (5), 2045–2059. doi:10.1007/s00603-014-0663-0

Yang, J., Cai, J., Yao, C., Li, P., Jiang, Q., and Zhou, C. (2019). Comparative study of tunnel blast-induced vibration on tunnel surfaces and inside surrounding rock. *Rock Mech. Rock Eng.* 52 (11), 4747–4761. doi:10.1007/s00603-019-01875-9

Yang, J., Wu, Z., Sun, W., Yao, C., and Wang, Q. h. (2022). Numerical simulation on radiation and energy of blast-induced seismic waves in deep rock masses. *J. Central South Univ.* 29 (2), 645–662. doi:10.1007/s11771-022-4908-x

Yu, H., Yuan, Y., Yu, G., and Liu, X. (2014). Evaluation of influence of vibrations generated by blasting construction on an existing tunnel in soft soils. *Tunn. Undergr. Space Technol.* 43, 59–66. doi:10.1016/j.tust.2014.04.005

Yu, W.-j., Li, K., Liu, Z., An, B., Wang, P., and Wu, H. (2021). Mechanical characteristics and deformation control of surrounding rock in weakly cemented siltstone. *Environ. Earth Sci.* 80 (9), 337. doi:10.1007/s12665-021-09626-2

Zhang, Q., Li, L., Li, S., Ding, W., and Hong, W. (2008). Experimental study of blasting dynamic vibration of closely adjacent tunnels. *Rock Soil Mech.* 29 (10), 2655–2660+2666. doi:10.16285/j.rsm.2008.10.012

Zhong, H., Liang, Y., Lan, W., Gao, S., and Liu, X. (2022). Research on compound wedge-shaped cutting in mountain hard rock tunnel. *J. Transp. Sci. Eng.* 38 (03), 72–78+106. doi:10.16544/j.cnki.cn43-1494/u.2022.03.006

Zhou, Y., Wang, S., Wang, J., Wen, J., and Chen, L. (2016). Vascular endothelial growth factor plasma levels before and after treatment of retinopathy of prematurity with ranibizumab. *Chem. Eng. Trans.* 55, 31–36. doi:10.1007/s00417-015-2996-0

Zhou, Z., Cai, X., Li, X., Cao, W., and Du, X. (2020). Dynamic response and energy evolution of sandstone under coupled static–dynamic compression: insights from experimental study into deep rock engineering applications. *Rock Mech. Rock Eng.* 53 (3), 1305–1331. doi:10.1007/s00603-019-01980-9

Mechanical properties and acoustic emission evolution of water-bearing sandstone under triaxial conditions

Lixin Zhang[1]*, Guangchao Liu[1], Xiujie Wei[1] and Yin Zhang[2]

[1]Collage of Mining, Liaoning Technical University, Fuxin, China, [2]School of Mechanics and Engineering, Liaoning Technical University, Fuxin, China

Accidents occur frequently in underground chambers owing to the high-stress environment, poor stability of rocks, and unreasonable mining and construction layout. Significant damage to the deep surrounding rock mass by confined water can result in water inrush and flooding accidents. This study numerically investigated the mechanical properties and acoustic emission (AE) signal evolution mechanism of water-bearing sandstone in deep high-stress mining environments. The results showed that, the lower the confining pressure, the lower is the compressive strength of the specimen, resulting in evident failure. The confining pressure inhibited the radial strain and enhanced the strength of the specimen. Furthermore, under the same confining pressure and different water pressure, the higher the water pressure value, the more evident was the failure phenomenon, and the lower was the peak stress. The water pressure decreased the strength of the specimen and its ability to resist damage. Moreover, for the same water pressure, the smaller the confining pressure, the larger was the maximum AE number and the total cumulative amount of acoustic emissions. When the specimen reached the peak stress and produced macroscopic failure, the AE number reached the maximum value. Finally, the AE activity decreased as the water pressure increased, and the higher the water pressure, the smaller was the cumulative AE number. Owing to the existence of water pressure, the internal structure of the model specimen was affected by the softening effect, which decreased the model strength, thereby suppressing the AE activity of the specimen. Our findings can provide a basis for numerical simulation research on mechanical properties and AE evolution mechanism of water-bearing sandstone under three-way stress state.

KEYWORDS

triaxial stress, water-bearing rock, acoustic emission, mechanical properties, numerical calculation

1 Introduction

As science and technology in China's coal mine development advances, the deep well development in the country also increases, resulting in an increase in the number of underground chambers built in each deep shaft. Major accidents occur frequently in underground chambers owing to high-stress environments, poor stability of surrounding rocks, and unreasonable layout of mining construction sites, which can endanger the life of workers as well as cause property loss. Therefore, it is necessary to conduct in-depth study on the mechanical characteristics of water-bearing rocks affected by multiple factors as well as

the mechanical mechanism reflected by acoustic signals, which have important practical significance and engineering value for monitoring and predicting the occurrence of disasters (Shoufeng et al., 2010; Liu et al., 2012; Shan et al., 2014; Ding et al., 2023a).

As a complex geological structure, there is certain amounts of moisture inside the rock mass. This moisture erodes the internal structure of the rock, which deteriorates the mechanical properties of the rock such as elastic modulus and compressive strength and enhances the plastic deformation. Therefore, studies have been conducted on the mechanical properties of aqueous rocks. Bao et al. (2020) studied the mechanical properties of fine sandstone, mudstone, coal, and medium sandstone in different aqueous states through conventional mechanical experiments. The results showed that the tensile strength of each group of specimens decreased significantly as the moisture content increased. Furthermore, the tensile strength of fine sandstone, mudstone, coal, and medium sandstone decreased in the saturated state of water. Qiao et al. (2017) studied the mechanical effect of water-rock chemistry on the deformation and failure of rock mass. The research status of this mechanism of action is systematically summarized. Zilong et al. (2016) used FLAC3D numerical simulation software to conduct numerical simulation tests under unidirectional stress loading conditions. Furthermore, they compared the numerical analysis results with the test data under uniaxial compression test conditions to investigate the influence of water on rock damage. Chen et al. (2022) focused on the erosion of rocks around chemical elements and conducted a three-axis compression test with ash sandstone. The result showed that the different erosion effects impacted the mechanical properties of ash sandstone. Gui and Lin (2016) analysed the high -pressure underwater bottom plate prominent mechanism and prevention, as well as the control technology, prominent mechanism, and prevention technique of abandoned mines while developing deep coal resources. Evaluated the impact of different moisture contents on the intensity of gypsum ore pillars. The larger the moisture content of the plaster test piece from a single -axis test result, the smaller was the single -axis compressive strength and elastic modulus. Ma et al. (2021), Liu et al. (2018) set up argillaceous siltstone specimens with different moisture content to study the influence of moisture content on the strength of argillaceous siltstone. The results preliminarily analysed the influence of moisture content on the mechanical properties of argillaceous siltstone. Lin et al. (2022) studied the effect of different moisture content on the mechanical properties and creep behaviour of rocks by taking argillaceous siltstone. In recent years, several studies have been conducted on the acoustic signal and induced charge monitoring technology of this technology. Chuanming et al. (2020) elaborated the application prospect of acoustic emission technology in geotechnical engineering and evaluated its application effect in geotechnical research. Several results on the use of acoustic emission techniques in scientific research such as seismic sequences and rupture mechanisms were achieved. Ding et al. (2023b) discussed the effects of stress degree and load loading time on the acoustic emission activity of rock specimens to study the factors that affect the acoustic emission activity of rock specimens. Serdyukov et al. (2022) used the particle flow software PFC2D to study the evolution law of acoustic emission signals on non-uniform granite rock samples. The results showed that the peak intensity of granite sample failure increased as the confining pressure increased.

The form of destruction gradually changed from sudden instability to progressive destruction. Li et al. (2018) studied the evolution mechanism of limestone acoustic emission and the mechanical properties of limestone under three-way stress. Triaxial compression test was conducted on limestone specimens. Based on the experimental results, the mechanical properties and acoustic emission signal evolution of limestone under triaxial compression conditions were summarized. Wang et al. (2022) designed a research experiment on the evolution of rock acoustic emission under periodic loading with fine-grained sandstone. Kong et al. (2017) conducted uniaxial compression experiments to study the influence of temperature changes on the acoustic emission activity and mechanical properties of sandstone. The results showed that different temperatures played a significant role in the increase of the acoustic emission frequency of rocks. (Moradian et al., 2016; Lai et al., 2022; Gu et al., 2023; Li et al., 2023). studied the relationship between the acoustic emission mechanism of rock and the evolution of cracks by conducting acoustic emission experiments using brittle rocks.

The monitoring equipment developed according to the relevant technical and theoretical research institutes has been widely used in coal rock dynamic disaster monitoring and early warning system; however, only a few studies have been conducted on the acoustic emission characteristics of water-bearing rocks under three-way stress-loading conditions, the mechanical properties of water-bearing rocks, and the shortcomings of numerical simulation technology. In this study, RFPA2D-Flow was used to simulate the models with different moisture cuts, observe the distribution of acoustic signals after the model was deformed and damaged, and analyse the influence of rocks with different moisture content on the distribution of acoustic signals under the same loading conditions. Then, the model with the same moisture content was simulated with different confining pressure values, and the acoustic signal distribution was simultaneously measured. Furthermore, the acoustic emission signal distribution law of water-bearing rocks under different confining pressure conditions was analysed.

2 Expected results, numerical modelling and parameters

Considering at the engineering problems of large deformation, the instability of the surrounding rocks of many underground engineering chambers, and the unclear monitoring of the precursor information of the surrounding rock catastrophe, this study investigated the triaxial mechanical properties and failure characteristics of water-bearing rocks, while taking the mechanical response and acoustic signal of rocks with different moisture content under confining compression conditions as the starting point and focusing on the two influencing factors of confining pressure and moisture content. Furthermore, the physical signal response of the instability process was obtained by combining acoustic emission signal monitoring technology to explore the rock failure characteristics affected by moisture content and confining pressure. Finally, the precursor information identification of its destruction process was obtained, and the research proceeded as follows:

(1) study on triaxial mechanical properties of water-bearing sandstone;

(2) study on the evolution of acoustic signals of sandstone samples with different moisture cuts; and

(3) study on the evolution law of acoustic signal of sandstone specimens with moisture content under different confining pressure

This numerical simulation uses RFPA2D-Flow as the platform for stress-seepage coupling numerical simulation and evaluates the influence of different moisture contents and confining pressure values on the mechanical properties and acoustic-charge signal of rocks under three-way stress by discretizing the model into units whose mechanical properties follow the Mohr–Coulomb distribution, which is Mainly based on finite element method for calculation. The RFPA2D-Flow analysis system applies the elastic finite element method to calculate the stress and displacement of the element. If the mechanical properties such as elastic modulus, Poisson's ratio, and tensile strength of the numerical simulation object material meet the specific elastic damage constitutive relationship, and the damage critical value of the constitutive relationship meets the Mohr–Coulomb criterion and the maximum tensile stress criterion, the damage failure of the unit will occur when the stress (strain) of the element reaches the damage critical value. Considering the defects inside the rock mass are randomly distributed and independent of each other, it is assumed in RFPA that the mechanical properties of the discretized mesoprimitives follow the statistical distribution law (as shown in Weibull distribution, Eq. 1), as a result, the relationship between the mechanical properties of macroscopic media and mesoscope is established (Tang, 1997).

$$\phi(\alpha) = \frac{m}{\alpha_0} \cdot \left(\frac{\alpha}{\alpha_0}\right)^{m-1} \cdot e^{\left(\frac{\alpha}{\alpha_0}\right)^m} \tag{1}$$

The mechanical properties and permeability characteristics of the rock mass are affected by the large number of natural pores, cracks, and other defective structures in the rock mass. During instability failure, the degree of crack distribution inside and on the surface of rock mass expands, resulting in the formation, expansion, and penetration of new cracks. The permeability of the rock before the failure is extremely low (almost impermeable), and the coupling effect of seepage stress is not evident. Furthermore, under the influence of water pressure and stress, the degree of damage changes, migration of stress field, seepage field, and damage evolution process affects the instability process of rock mass.

Porosity is an important physical property indicator for measuring the quality of rock engineering. The porosity of a rock reflects the percentage of pores and cracks in the rock; the greater the porosity, the greater is the number of cracks in the rock and the impact on the mechanical properties of the rock mass. The porosity in rock is usually denoted by n. Sandstone was selected as the simulation object in this study, considering the porosity description of sandstone is roughly the same as that of the soil mass, according to the porous medium.

$$n = \frac{V_P}{V} \tag{2}$$

FIGURE 1
Model loading diagram.
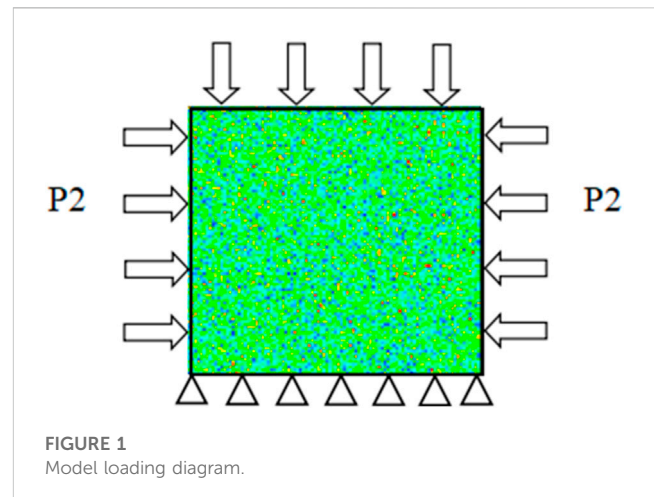
where n is the porosity of the rock, V_p is the volume occupied by pores and fissures in the rock, and V is the total volume of rock. The water in the rock mass can only penetrate along the connecting pores and cracks. Furthermore, the permeability in a rock can be measured by the permeability coefficient, which is mainly determined by the size, direction, and interconnection of the rock pores.

Where k is the seepage rate of porous medium, d is the effective particle size of geotechnical particles, and c is the proportionality constant.

When the stress or strain states of the element meets a given damage threshold, the elastic modulus of the damaged element is expressed as follows:

$$E = (1 - D)E_0 \tag{3}$$

where E and E_0 are the elastic modulus of the damaged and non-destructive units, respectively, and D is the damage variable.

For elements in uniaxial compression-loaded form, the failure criterion for this element adopts the Mohr–Coulomb criterion given as

$$F = \sigma_1 - \sigma_3 \frac{1 + \sin\phi}{1 - \sin\phi} \geq f_c \tag{4}$$

where is internal friction angle and f_c is uniaxial compressive strength. When the shear stress reaches the Moir-Coulomb damage threshold, the loss variable D is expressed as

$$D = \begin{cases} 0 & \varepsilon < \varepsilon_{c0} \\ 1 - \dfrac{f_{cr}}{E_0 \varepsilon} & \varepsilon_{c0} < \varepsilon \end{cases} \tag{5}$$

where f_{cr} is the compressive residual strength of the uniaxial axis. ε_{c0} is the maximum pressure strain. and ε is residual strain.

The numerical model adopts a two-dimensional thin flat plate strain model, divided into 100×100 elements. The model size is 100 mm×100 mm and the axial load P1 is applied to the upper boundary of the model. P1 is loaded in the form of controlled displacement, and the displacement increment is ΔS=0.005 mm. A confining load P2 is applied to the model side boundary. P2 is constantly loaded in the form of stress, and four sets of confining

TABLE 1 Hydraulics parameters.

Parameter name	Numeric value	Parameter name	Numeric value
Homogeneity coefficient m	3	Horizontal permeability	0.01
Poisson's ratio	0.25	Vertical permeability	0.01
Internal friction angle $\varphi/°$	30	Pore pressure coefficient	0.5
Pressure ratio	10	Coupling factor	0.2
Maximum tensile strain coefficient	1.5	Damage penetration multiplies	5
Maximum compressive strain coefficient	200	Pore pressure terminal coefficient	1
Average modulus of elasticity E/MPa	36000	Separation permeation multiplies	100

pressure values, 2 MPa, 4 MPa, 6 MPa, and 8 MPa, are designed. The seepage boundary load P3 is set at the upper boundary of the model, and the water pressure is set to 0.5 MPa, 1 MPa, 2 MPa, and 4 MPa. The numerical model is shown in Figure 1.

2.1 Parameter selection

To study the mechanical properties of rocks with different moisture cuts, this numerical simulation uses the method of applying different water pressures to the model boundary to increase the water content of rock mass to simulate different moisture content conditions. The seepage parameters (such as porosity, coupling coefficient, *etc.*) that conform to the mechanical properties of sandstone are set for the discrete unit to simulate the water content of sandstone in a real environment.

The mechanical parameters required for each numerical model element, such as elastic modulus and Poisson's ratio, are assigned according to the Mohr–Coulomb distribution. Herein, m is the homogeneity coefficient, which is used to indicate the uniformity of the sample, considering the special structure of the sandstone of the simulated object. The homogeneity coefficient is selected as 3 for numerical simulation. Table 1 summarizes the hydraulic parameters of this numerical simulation.

In this study, PFPA2D-Flow was used to numerically simulate the mechanical properties and the evolution of acoustic signals under three-way pressure of rocks with different moisture cuts. The specific embodiments are as follows:

(1) Set the number of elements of the model and the model size. The model is shown in Figure 2. The lower left corner of the model is the positive coordinate axis, and the horizontal and longitudinal axes are the positive X- and Y-axes, respectively.
(2) Set the mechanical parameters of the model and inflow coefficient.
(3) Perform the static load on the model. The application method is the axial compression and peripheral compression, and the formation form is a constant loading. The effect of the load is shown in Figures 3, 4.
(4) The seepage boundary load is applied to the model and the application form is head loading. The initial value is set according to different water pressure sizes.

FIGURE 2
Model design.
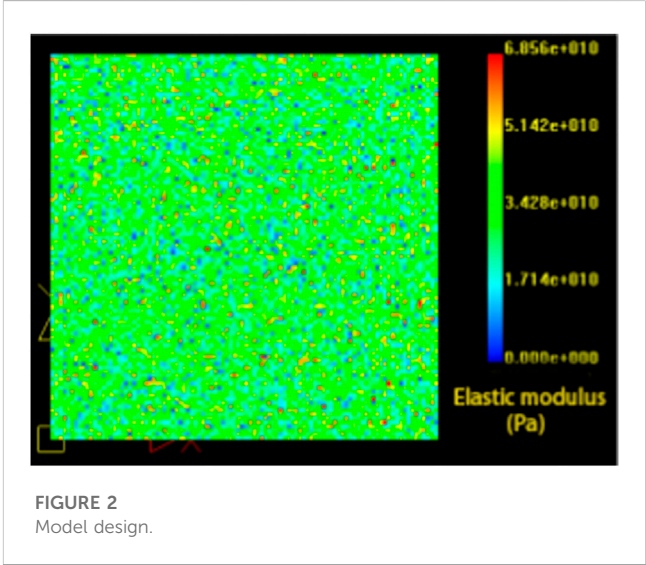
(5) Set the solution control information. The total loading step is 50 steps, the model calculation type is conventional data solving, the plane simplification model is the plane stress model, and the solution problem type is fluid-structure interaction.
(6) Start solving and observe the changes in the stress distribution of the model.
(7) Stop solving after the model shape fails and the stress value no longer changes. The data in the simulation process is output and a curve is formed.

3 Mechanical properties of water-bearing sandstone

3.1 Failure characteristics of water-bearing sandstone under triaxial conditions

Owing to the internal structural defects and the existence of pore fractures, the mechanical properties of rocks are more complicated; as a result, the existence of water further complicates the mechanical properties of rocks. We evaluated the failure process diagram and stress–strain curve of the model specimen under the influence of different confining pressure and water pressure values by
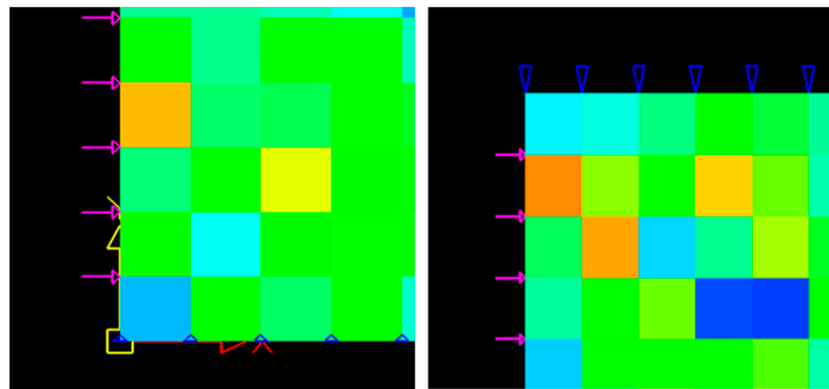
FIGURE 3
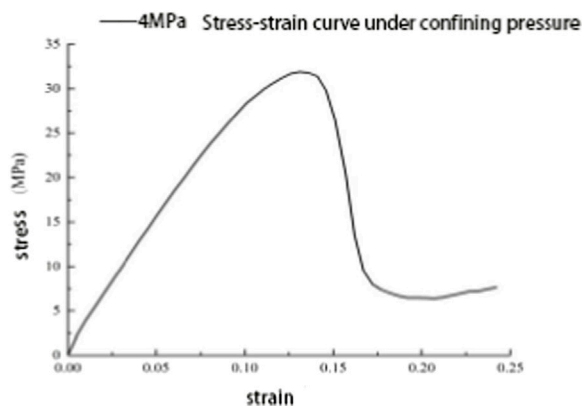Applying loading on the model.

FIGURE 4
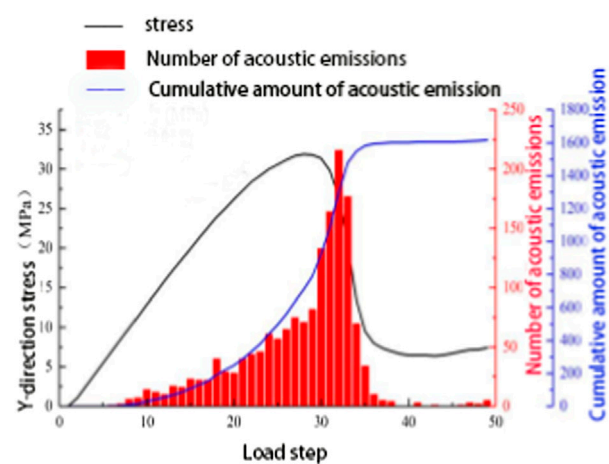Stress−strain curves of model specimens under triaxial stress.

FIGURE 5
Stress−acoustic emission number curve of model specimen under triaxial stress.

performing triaxial compression simulation tests on the water-bearing rock simulation specimens. Then, the failure characteristics and stress–strain characteristics of the water-bearing sandstone in the three-way stress state were analysed.

As shown in Figures 4, 5, the stress–strain curve of the model specimen showed evident phased changes as the loading steps increased, and different stages correspond to the increase in stress. The acoustic emission number (AE number) of the model specimen was small at the beginning of loading, increased significantly after 30 steps, and peaked at 32 steps before decreasing. After 40 steps, almost silent emission activity occurs. As the AE number accumulation increases, the curve shows an upward trend, reaching a maximum at 34 steps and flattening after 34 steps.

As shown in Figure 6, the loading process of the model specimen exhibited an evident crack as the loading step gradually increased. In the early stages of loading, a failure point appeared inside the model specimen between steps 15 to 17. The failure points inside the model specimen from steps 23 to 27 gradually increased, and the stress distribution of the internal elements of the model specimen changed

significantly. Cracks began to appear inside the model specimen at steps 28 to 31, it has been widely expanded inside the model.
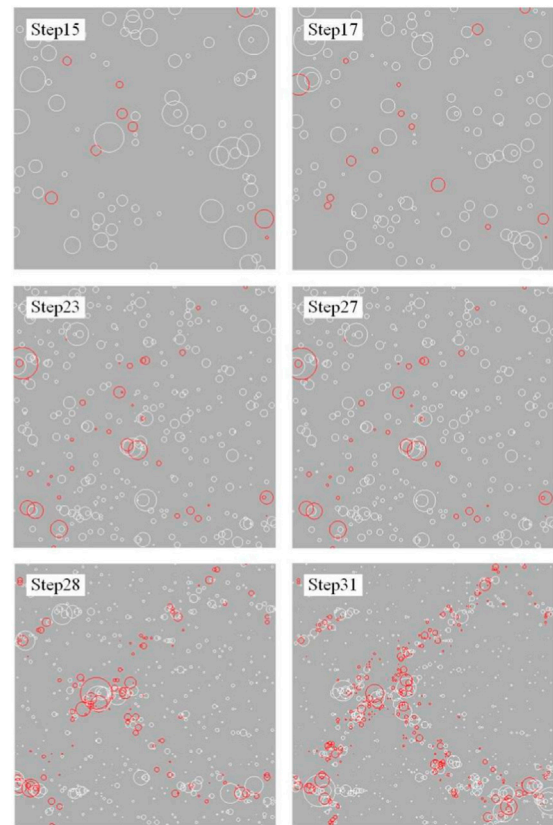
As shown in Figure 7, the acoustic emission degree of the model specimen at different loading stages exhibited a significantly different distribution. At steps 15 to 17, random and irregular acoustic emission signals appeared inside the model specimen. Most of the acoustic emission signals were in the form of compression and shear failure (white circle in the figure), accompanied by a small amount of pull failure signal (red signal in the figure). From steps 23 to 27, the acoustic emission signal inside the model specimen increased significantly compared to steps 15 and 17, and the distribution showed randomness. From steps 28 to 31, the acoustic emission signal of the model specimen concentrated at the crack generation and crack growth surface, whereas the pressure failure signal was concentrated on the crack growth surface.
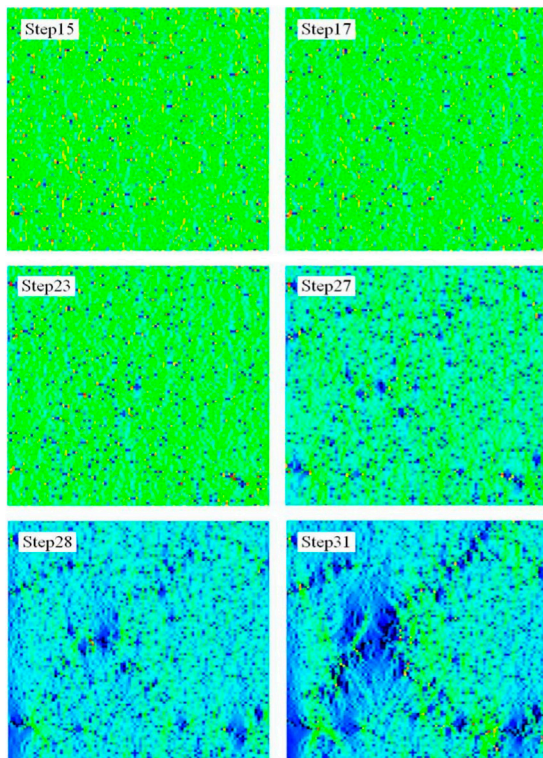
FIGURE 6
Failure process diagram of triaxial loading model specimen.

FIGURE 7
AE process diagram of triaxial loading model specimen.

The entire stress–strain process of the model specimen can be divided into: linear deformation stage, nonlinear deformation stage, and softening stage, as shown in Figures 5–7.

(1) Linear deformation stage (steps 1–22): Affected by mechanical properties such as rock non-uniformity, anisotropy, *etc.*, a small number of failure points appear in the initial loading stage of the model specimen, and the principal stress distribution is random and scattered. The stress–strain behaviour of the model specimen is characterized linearly.

(2) Nonlinear deformation stage (step 23–27): As the load increases, the failure points inside the model gradually increases. Cracks begin to develop at the bottom of the model, near the boundary, and in the middle. A large number of acoustic emission signals in the form of shear damage are generated where the crack is formed. In the nonlinear deformation stage, the stress–strain curve of the model specimen has nonlinear characteristics and the Y stress peaks at 27 steps.

(3) Softening stage (steps 28–50): In the softening stage, the crack further begins to expand, the overall trend is upward, and a large number of shear-damaging acoustic emission signals are generated at the crack. After 35 steps, the crack penetrates the entire model specimen. Some of the cracks have bifurcation and stress concentration on the crack surface. After the peak stress in the Y-direction, the stress gradually decreases as the loading steps increases and the strength of the specimen decreases.

3.2 Mechanical properties of water-bearing sandstone affected by different confining pressures

Figure 8 shows that the maximum principal stress of the model under the condition of 8 MPa confining pressure value is higher than that of the model under the confinement pressure condition of 6 MPa, 4 MPa, and 2 MPa at 35 loading steps, and the lower the confining pressure value, the lower is the corresponding maximum principal stress. At 35 steps, evident cracks appeared in four groups of models with different confining pressure values, among which the 8 MPa model had failure points and micro-cracks at the bottom, and the 6 MPa confinement pressure model had evident cracks and that can penetrate the model. The crack of the 6 MPa model has a greater degree of expansion than the 8 MPa model, and stress concentration occurs in the middle of the crack. The crack development degree of the 4 MPa confining model was expanded further, and the bifurcation phenomenon occurred in the propagation direction of the main crack, and the trend of multiple cracks began to emerge. The model under 2 MPa confining pressure has multiple cracks on the basis of the main crack and runs through the entire model, and the failure phenomenon appears in the lower right corner of the model specimen.

Figures 1–3 indicates that the presence of confining pressure under the same water pressure conditions affects the compressive strength of the model, and the larger the confining pressure value,
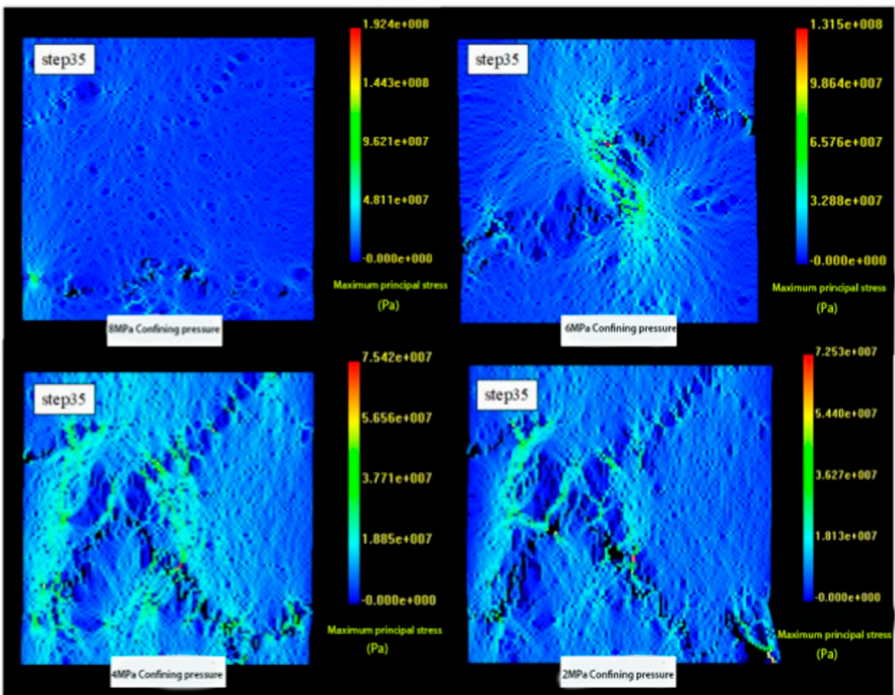
FIGURE 8
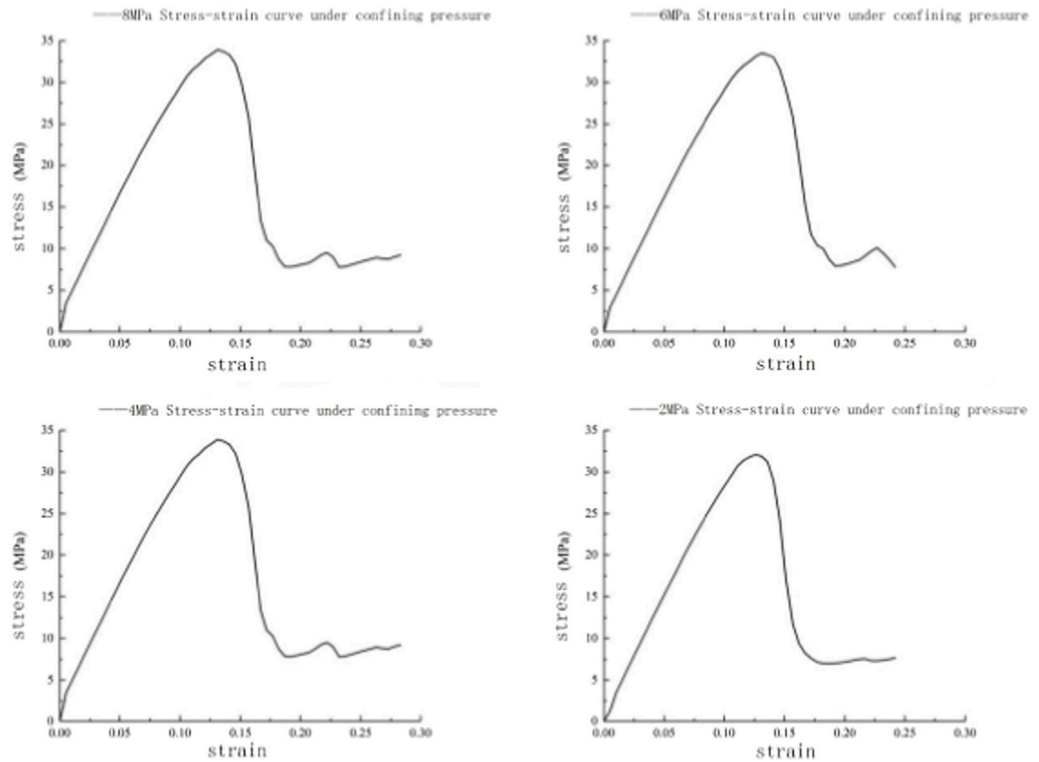Stress distribution at loading step 35 under 4 MPa water pressure.

FIGURE 9
Stress−strain curves under different confining pressures at 4 MPa water pressure.

the greater is the compressive strength of the model, thereby decreasing the chances of failure. When the water pressure is fixed, the increase in confining pressure presses the cracks inside the model, which limits the radial deformation of the model. Therefore, the stiffness of the model increases, which in turn strengthens the compressive strength of the model specimen.

Figure 9 shows that the peak stress under 8 MPa and 6 MPa confining pressure is 33.9 MPa and 33.4 MPa, respectively. The peak stress at 4 MPa and 2 MPa confining pressure is 31.9 MPa and 31.3 MPa, respectively. Four sets of model specimens with different confining pressure values under loading conditions had different peak intensities. The larger the confining pressure value, the greater is the stress peak considering the existence of confining pressure value inhibits the radial strain of the model. The higher the confining pressure value, the more evident is the compression closure phenomenon of the fracture in the model. As a result, the stiffness of the model is improved.

Simultaneously, that the residual stress under 8 MPa confining pressure condition is 9.2 MPa, which reduced to 27% of the peak stress. The residual strength under 6 MPa confining pressure condition is 7.8 MPa, which reduced to 23% of the residual stress. The residual strength is 7.6 MPa and 7.49 MPa when the confining pressure is 4 MPa and 2 MPa, respectively. Evidently, the larger the confining pressure value applied to the model, the higher is its residual strength, considering the model is constantly affected by confining pressure after a large number of cracks. The model elements re-contact at the fracture surface, and the stress concentration and stress redistribution phenomenon occur between the fracture surfaces. The higher the confining pressure value, the greater is the strength of the model after stress redistribution. Therefore, the stress–strain curve has an upward characteristic.

3.3 Mechanical properties of water-bearing sandstone affected by different moisture cuts

As shown in Figure 10, t the maximum principal stress of the model specimen at the 35th loading step under the condition of 0.5 MPa water pressure was higher than that of the other three groups. The larger the water pressure value, the smaller is the maximum principal stress value at 35 loading steps. A small number of cracks appeared at the bottom of the specimen under 0.5 MPa water pressure, which developed upward, and a large number of failure points appear in the middle of the model. The stress distribution around the failure point was more concentrated, resulting in crack germination. The specimen under 1 MPa water pressure exhibited a single crack in the upper left corner of the specimen, which expanded to the lower right corner, resulting in cracks penetrating the model. Furthermore, there is stress concentration around the crack. The model under 2 MPa water pressure exhibited a single crack in the upper right corner of the model developing towards the lower left corner, and the crack fracture surface interval was larger than that of the specimen under 1 MPa water pressure. The specimen under 4 MPa water pressure exhibited cracks penetrating the specimen; there were multiple cracks, and the failure phenomenon occurred in the lower right corner of the specimen.

Under the condition that the confining pressure value is constant, the different water pressure values applied to the model lead to different effects of moisture in the pore structure inside the rock on the rock strength. The larger the water pressure value, the more evident is the penetration softening effect of water on the rock. Therefore, the compressive strength of the rock decreases. The damage phenomenon of specimens with high water pressure value is more severe.

Figure 11 shows that the stress–strain curves of the model specimens are essentially the same in the linear and nonlinear deformation stages when the four groups of different water pressure values are different. The peak stress of the model at 0.5 MPa, 1 MPa, 3 MPa, and 2 MPa water pressures was 33.9 MPa, 33 MPa, 31.7 MPa, and 31.3 MPa, respectively. Therefore, the greater the water pressure value applied to the model specimen, the lower is the peak stress.

The afore described phenomenon can be attributed to the fact that the action of pore water destroys the micropores and cracks in the model specimen, thereby consuming more energy. As the pore water pressure increases further, the cracks in the model specimen were further developed. The greater the water pressure, the more pronounced is the crack propagation (see Figure 10), which significantly reduces the compressive strength of the model specimen.

4 Acoustic signal evolution of water-bearing sandstone specimens under different confining and water pressures

4.1 Acoustic signal distribution of sandstone samples with moisture content affected by different confining pressures

There are many acoustic emission characterization parameters, and this numerical simulation selects the acoustic emission ringing count (CNT) and the acoustic emission cumulative ringing count to study the influence of different confining pressure values and moisture content on the evolution of acoustic emission signals in water-bearing sandstone. To explore the influence of different confining pressure values on the evolution mechanism of acoustic emission in water-bearing sandstone, the results of this numerical simulation on the law of acoustic emission signal and mechanical properties are as follows, and the simulation results are shown in the figure below.

In comparing Figures 12A, B, it was found that the stress in the linear deformation stage was linearly distributed as the loading step increased, and the AE number gradually increased. In the nonlinear deformation stage, the peak stress of the specimen under the 8 MPa confining pressure condition was 33.9 MPa, which was higher than that of 33.4 MPa under the 6 MPa confining pressure condition. The AE number was further accumulated at this stage, and the AE number produced by the specimen under the 6 MPa confining pressure condition was significantly more than that under the 8 MPa confining pressure. In the softening phase, the stress value gradually decreased with the loading step, the AE number reaches the maximum, and the AE number accumulation curve flattened. The cumulative amount of acoustic emission under 6 MPa confining
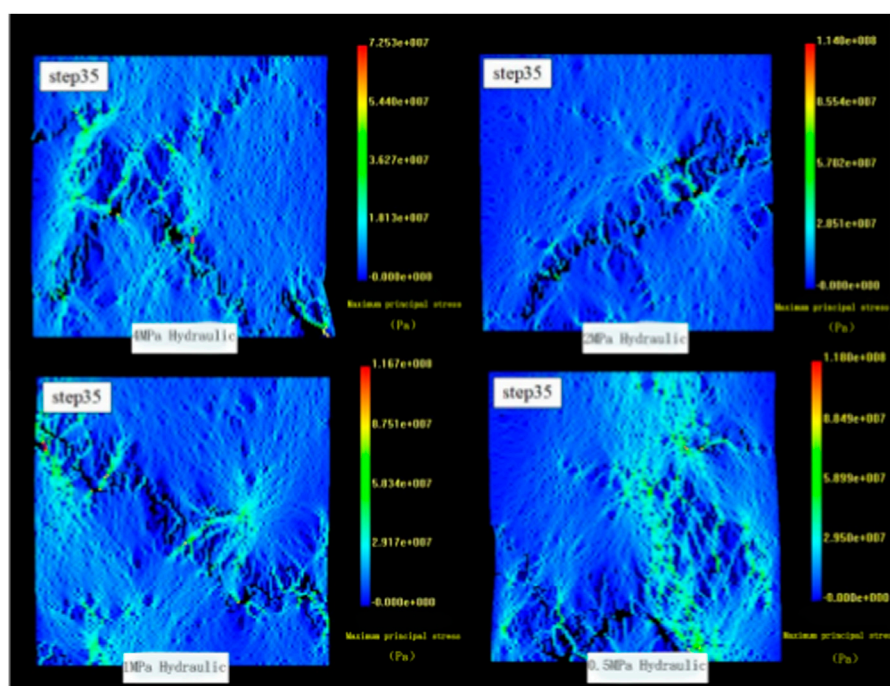
FIGURE 10
Stress distribution at loading step 35 under 2 MPa confining pressure and different water pressure.
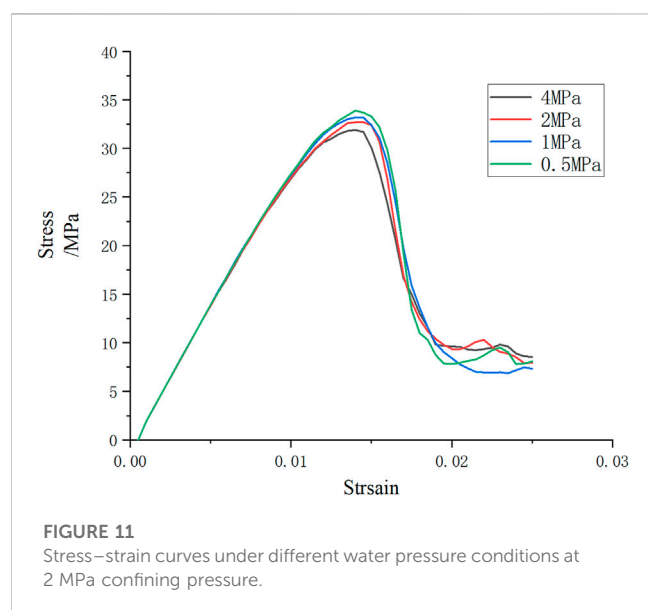

FIGURE 11
Stress−strain curves under different water pressure conditions at 2 MPa confining pressure.

pressure condition was 1338, which was higher than 1112 under 8 MPa confining pressure condition.

When the confining pressure values were 4 MPa and 2 MPa, the peak stress of the model specimen was lower than that under the 8 MPa and 6 MPa confining pressure conditions. The peak stress under 4 MPa and 2 MPa confining pressure was 31.9 MPa

and 31.3 MPa, respectively. In the linear and nonlinear deformation stages, the change trend of stress with loading step was essentially the same as that under 8 MPa and 6 MPa confining pressure conditions. The AE number and the cumulative amount of acoustic emission were significantly higher than those of model specimens with 8 MPa and 6 MPa confining loads applied. The cumulative amount of acoustic emission under the confining pressure conditions of 4 MPa and 2 MPa was 1627 and 1849, respectively. The stress-loading step curves and AE number curves when 4 MPa and 2 MPa confining pressure values were applied to the model specimen under the condition of 4 MPa water pressure value, as shown in Figures 14, 15.

Figure 12 show that the stress-loading step curve corresponding to the four groups of confining pressure values in the linear deformation stage tends to be linear, and the AE number gradually increases. The larger the confining pressure value, the denser is the acoustic emission phenomenon. The application of axial loading and confining pressure loading leads to initial cracks inside the model specimen being gradually compacted and closed, leading to less acoustic emission in the first 10 steps of the model specimen. Furthermore, the AE number increases significantly as the axial load increases owing to the gradual increase of stress on the model elements and the beginning of failure points.

Entering the nonlinear deformation stage, a large number of cracks are generated at the failure point of the model specimen as the loading step increases. The stress-loading step curve shows a linear
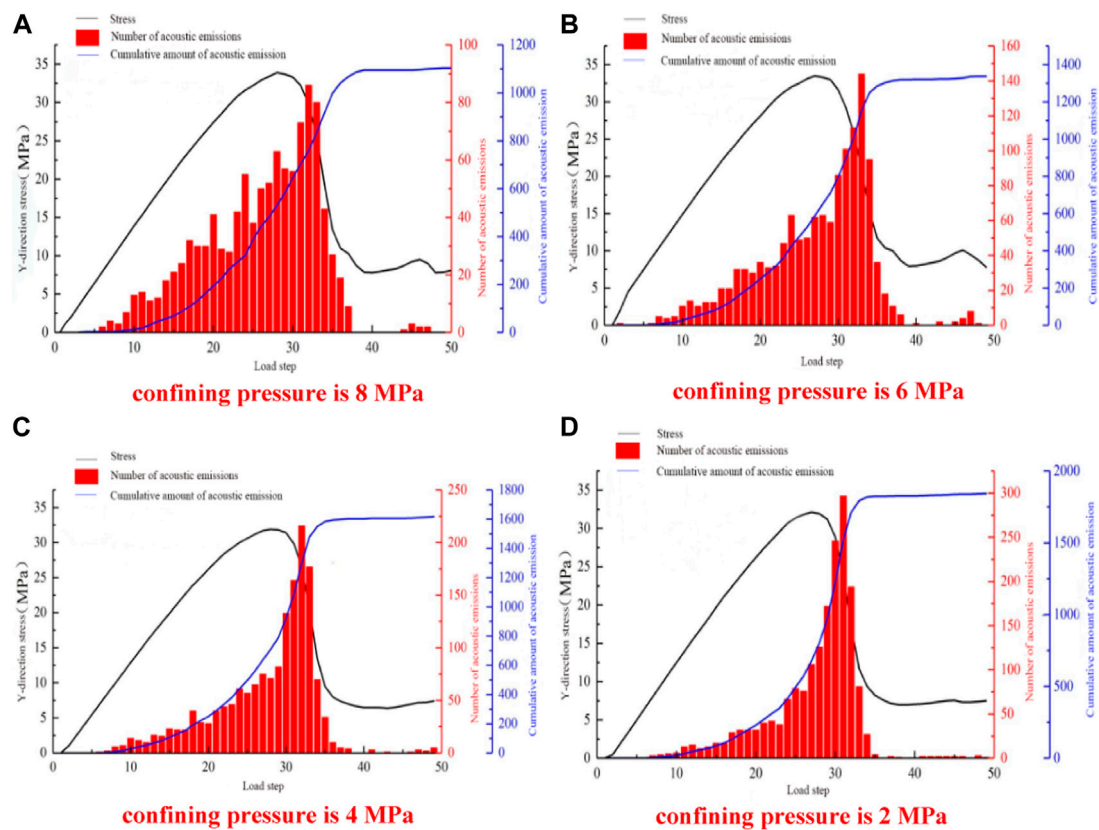
FIGURE 12
Stress-loading step and sound emission number curve of sample at 4 MPa water pressure. **(A)** confining pressure is 8 Mpa, **(B)** confining pressure is 6 Mpa, **(C)** confining pressure is 4 Mpa, and **(D)** confining pressure is 2 Mpa.

phenomenon, and the stress in the Y-direction peaks. The acoustic emission phenomenon of the model under 8 MPa confining pressure condition was more active than that of the other three groups, and the AE number was distributed more at steps 23 to 27, considering the accumulated strain energy inside the model specimen under the influence of 8 MPa confining pressure was more; therefore, the acoustic emission activity at the failure point and the crack generation was more active than that of the other three groups of specimens. All four groups of specimens released strain energy at this stage, and hence, the AE number increased significantly.

The axial load further increased, and the model specimen entered the softening stage. The stress-loading step curve in the Y stress began to decrease. The maximum AE number of the specimens under the action of 2 MPa confining pressure was greater than that of the other three groups of model specimens under the action of confining pressure. The larger the confining pressure value, the smaller was the maximum value of sound emission. The original crack in the specimen developed further, and the new crack converged and penetrated, generating macroscopic fracture surface. As a result, the AE number increases rapidly. After the model specimen reaches peak stress and macroscopic failure, the AE number reaches a maximum.

Figure 13 show that the stress-loading step and AE number curves under 2 MPa water pressure exhibited similar stress curve characteristics as those under 4 MPa water pressure, the peak stress of the model under 8 MPa and 6 MPa confining pressures was 33.5 MPa and 33 MPa, respectively. Furthermore, the peak stress of the model specimen under the action of 4 MPa and 2 MPa confining pressures was 32 MPa and 32.7 MPa, respectively. The four groups of specimens showed that the larger the confining pressure value, the greater was the peak stress, which was the same as the afore described analysis results. It shows that the cumulative amount of acoustic emission corresponding to different confining pressure values under the same water pressure has the following situation: the larger the confining pressure value, the smaller is the cumulative amount of AE number. Compared with the other three groups of confining pressure values, the 2 MPa confining pressure value reduces the suppression of the model failure phenomenon, and the acoustic emission activity of the model is more active in the three stages; therefore, the total cumulative amount of acoustic emission under the 2 MPa confining pressure condition was significantly higher than the cumulative amount of acoustic emission under the other three groups of confining pressure conditions.
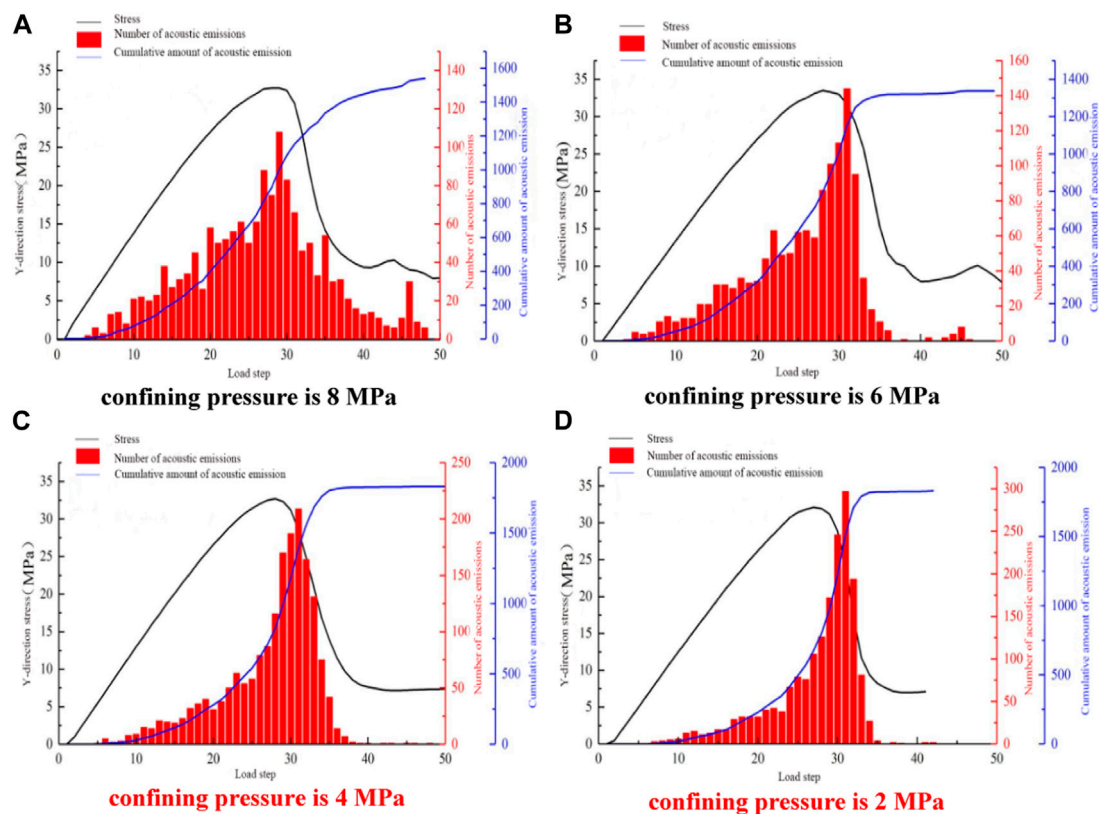
FIGURE 13
Stress-loading step and sound emission number curve of sample at 2 MPa water pressure. **(A)** confining pressure is 8 Mpa, **(B)** confining pressure is 6 Mpa, **(C)** confining pressure is 4 Mpa, and **(D)** confining pressure is 2 Mpa.
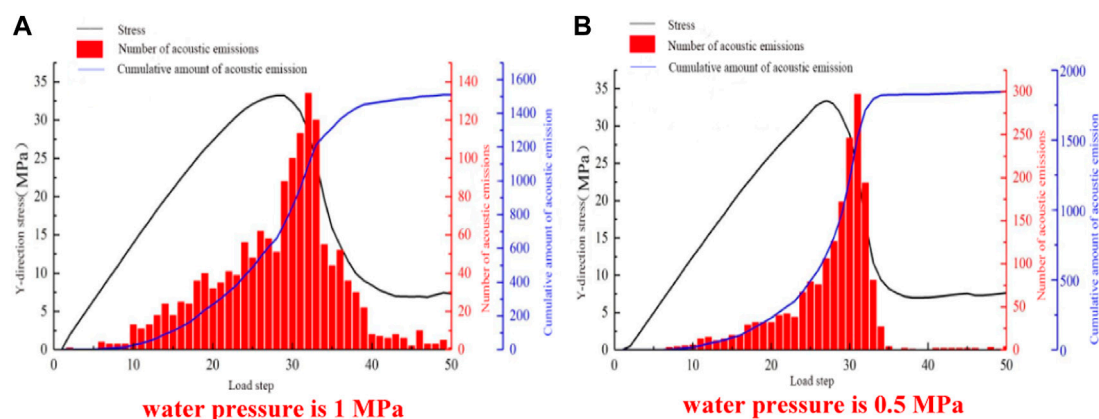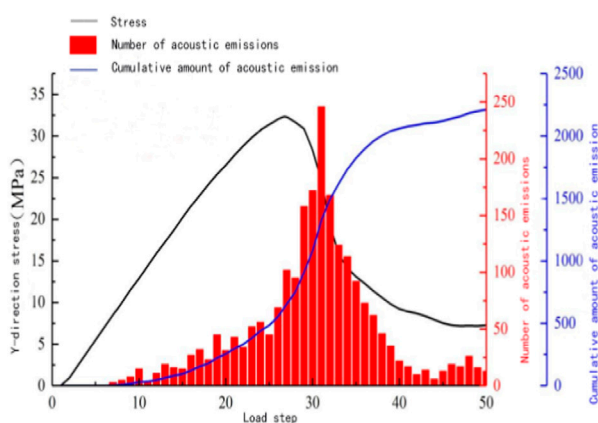

FIGURE 14
Stress-loading step and sound emission number curve of sample at 8 MPa confining pressure. **(A)** water pressure is 1 MPa **(B)** water pressure is 0.5 MPa.

Under the action of four different confining pressure values, the time lag of the maximum AE number of the model specimen lags behind the maximum stress time and macroscopic failure time of the model, considering the existence of confining pressure inhibits the failure of the model specimen, and the slippage phenomenon of the fractures in the model is hindered under the influence of confining pressure. The occurrence of these two phenomena improves the shear strength and post-peak bearing capacity of the model specimen, and the acoustic emission activity of the specimen rupture has an overall backward shift.
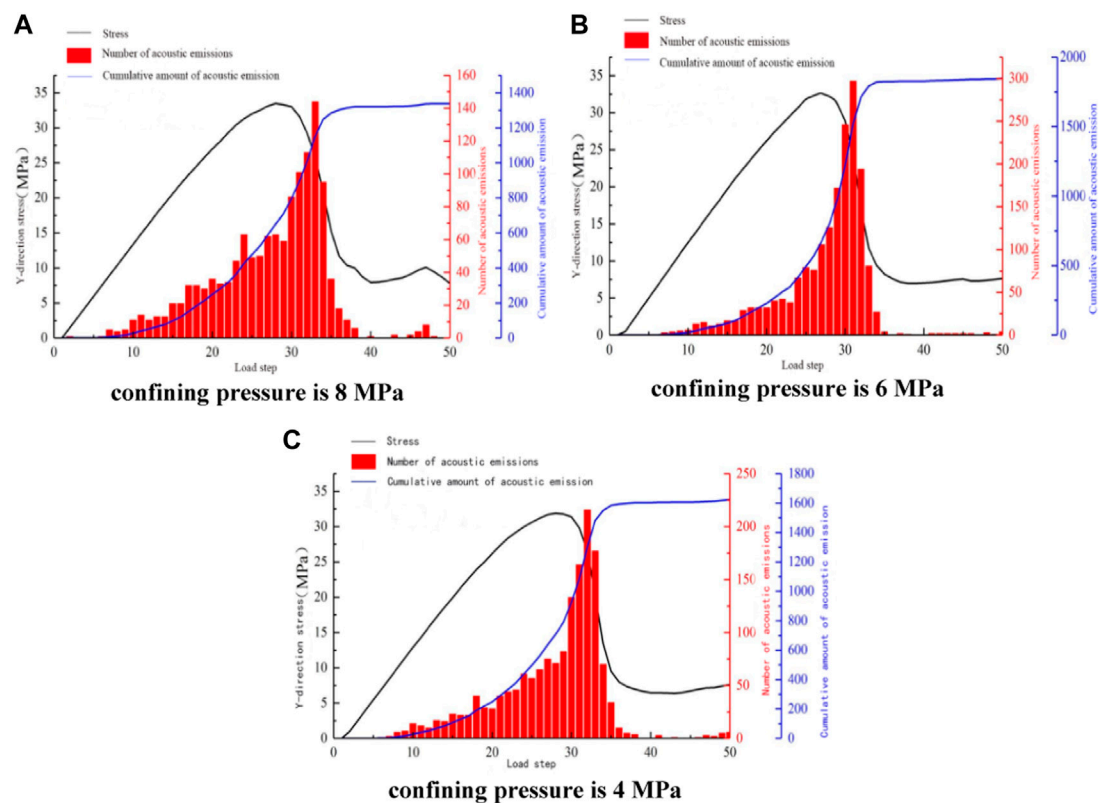
FIGURE 15
Stress-loading step and AE number curve of sample with 1 MPa water pressure. **(A)** confining pressure is 8 Mpa, **(B)** confining pressure is 6 Mpa, **(C)** confining pressure is 4 Mpa.

FIGURE 16
Stress-loading step and AE number curve for 0.5 MPa water pressure at 4 MPa confining pressure.

4.2 Acoustic signal distribution of sandstone specimens with moisture content affected by different water pressure

Comparing Figures 12–14, it can be observed that the smaller the water pressure value of the model specimen

under the confinement pressure condition of 8 MPa, the greater is the maximum value of AE number and the AE number. The maximum cumulative amount of acoustic emission at 0.5 MPa, 1 MPa, 2 MPa, and 4 MPa water pressures is 1802, 1500, 1550, and 1112, respectively. The maximum cumulative amount of visible acoustic emission decreases as the water pressure increases. Water inhibits the acoustic emission activity of the model specimen.

We compared Figures 15–17 in the AE number effected by water pressure and confining pressure conditions. The following analyses can be made:

The action of water reduces the strength of sandstone; therefore, the peak strength of the model specimens with different water pressure of the same confining pressure decreases as the water pressure increases (consistent with the analysis results of 3.3). As the peak intensity of sandstone decreases, the ability of the model specimen to resist deformation and damage weakens, and a large number of failure units appear in the model specimen, resulting in a rapid increase in AE number. In the three destruction stages of the model, the following phenomena occur:

(1) In the linear deformation stage, the axial stress increases as the loading steps increase, showing linear characteristics. The micro-cracks in the model are gradually compact, a small number of failure points appear inside the model specimen,
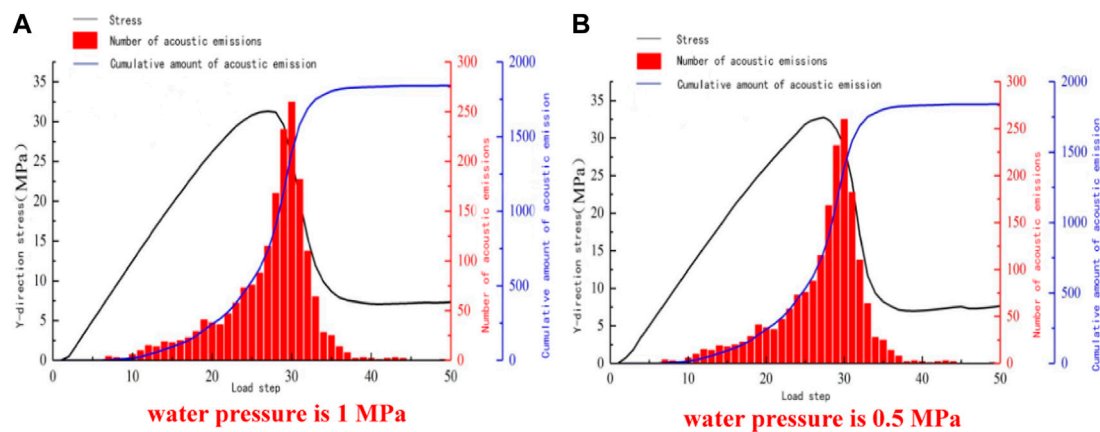
FIGURE 17
Stress-loading step and AE number curve for sample at 2 MPa confining pressure. **(A)** water pressure is 1 MPa **(B)** water pressure is 0.5 MPa.

and the acoustic emission activity gradually becomes active. The test pieces under different water pressure conditions gradually increase in the AE number. On comparing the AE number curves under the condition of 0.5 MPa and 1 MPa water pressure, it was found that the AE number of the specimen under the influence of 0.5 MPa water pressure at 10 to 22 steps was significantly more than that of 1 MPa water pressure. Furthermore, on comparing the AE number curves of 1 MPa and 2 MPa water pressure and the AE number curve of 2 MPa and 4 MPa water pressure conditions, it was found that the larger the water pressure value in the linear deformation stage, the lower was the AE number. It has been explained that water has a certain softening effect on the internal microstructure of the rock, which inhibits the acoustic emission activity of the rock.

(2) In the nonlinear deformation stage, the axial stress of the four groups of model specimens with different water pressure values all appeared nonlinear and reached the maximum value as the loading steps increased. The axial stress reached the maximum value at 27 steps. A large number of failure points in the model specimen begin to occur, and cracks begin to develop from the failure point. The AE numbers of the four groups of specimens increase rapidly; however, the AE numbers of the specimens under the evident condition of 0.5 MPa water pressure was more than that of the other 3 groups, considering that the presence of water pressure value strengthens the softening effect on the model and the acoustic emission activity begins to decrease.

(3) In the softening stage, cracks occur in the model specimen that penetrate the specimen, and new cracks are generated, and there is a phenomenon of intersection between cracks. The AE number increased rapidly and reached the maximum value, among which the AE number under the water pressure value of 0.5 MPa was higher than the maximum AE number under the other three groups of
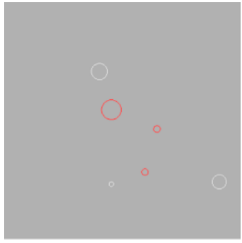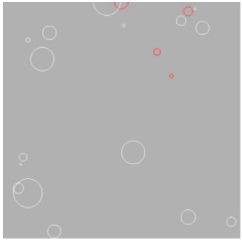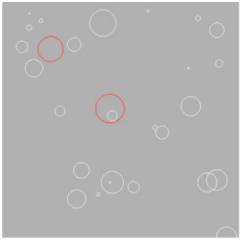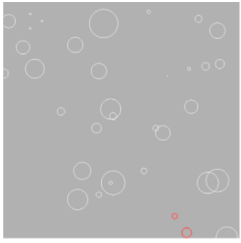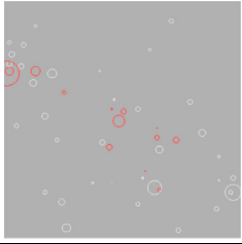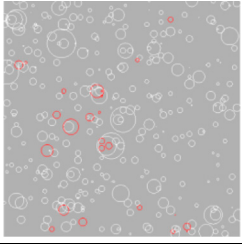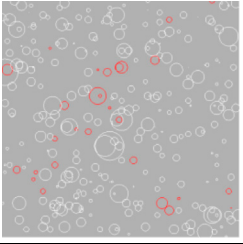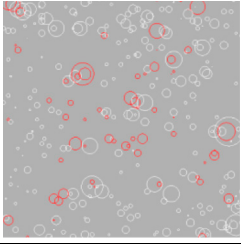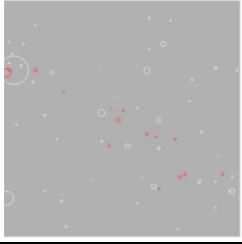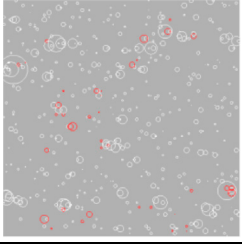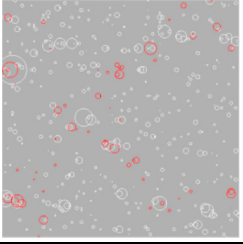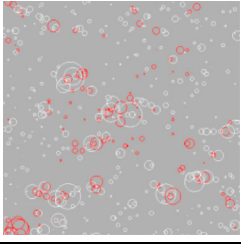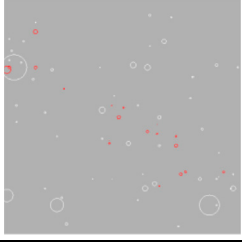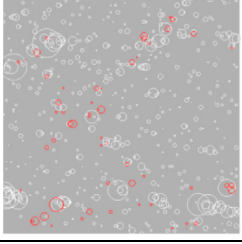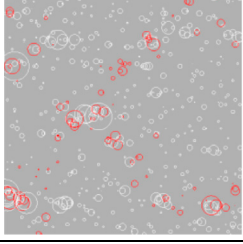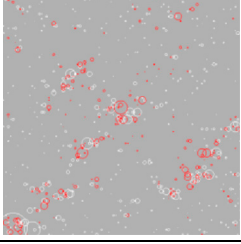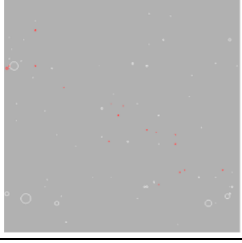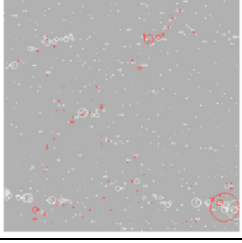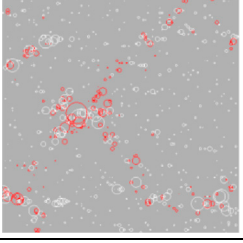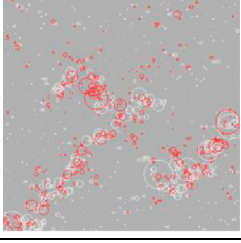
water pressure conditions. On comparing the maximum values of the AE numbers of the four groups separately, it was found that the larger the water pressure value, the smaller was the maximum AE number. With the increase of loading steps. The softening effect of water on the model specimen was further strengthened, resulting in a decrease in the compressive strength of the model and a weakening of acoustic emission activity.

The cumulative AE number at the water pressure value of 4 MPa was significantly lower than that of the model specimen when the other three groups of water pressure values; the lower the water pressure value, the greater was the cumulative amount of AE number owing to the increase in the pore water pressure and decrease in the AE number activity at the moment of rupture of the model specimen. The action of pore water transforms the model from brittle tension to plastic slip during loadin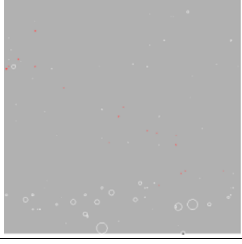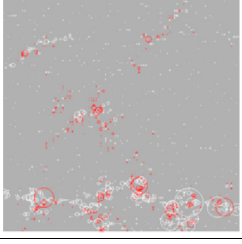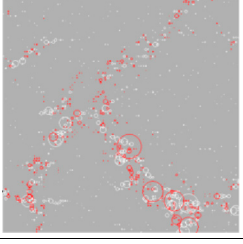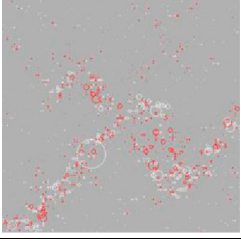g, so that the fracture characteristics of the model change from brittle to ductility. Therefore, in the three stages of destruction, the acoustic emission activity of the model decreased as the water pressure increased, and the acoustic emission accumulation of the model specimen under 4 MPa water pressure was significantly lower than that of the other three groups under water pressure.

4.3 Acoustic signal evolution process of water-bearing sandstone specimens under different confining pressures and different water pressures

A comparative analysis of Tables 2, 3 shows that the AE number in the linear deformation stage gradually increased as the confining pressure under the condition of certain water pressure decreased and is randomly distributed. In the later stage of linear deformation,

TABLE 2 Evolution process of AE signals under different confining pressures at 4 MPa water pressure.

Load step	8 MPa confining pressure	6 MPa confining pressure	4 MPa confining pressure	2 MPa confining pressure
Linear deformation stage Step 10				
Linear deformation stage Step 22				
Nonlinear deformation stage Step 25				
Nonlinear deformation stage Step 27				
Softening phase Step 29				
Softening phase Step 34				

the AE number under the condition of 8 MPa confining pressure was significantly less than that of the other three groups, and the distribution was densely distributed at the boundary of the model. In

the nonlinear deformation stage, the AE number further increased the acoustic emission signal begins to concentrate at the crack in large quantities, the smaller.

TABLE 3 AE signal evolution process of models with different confining pressures under 2 MPa water pressure.

Load step	8 MPa confining pressure	6 MPa confining pressure	4 MPa confining pressure	2 MPa confining pressure
Linear deformation stage Step 10				
Linear deformation stage Step 22				
Nonlinear deformation stage Step 25				
Nonlinear deformation stage Step 27				
Softening phase Step 29				
Softening phase Step 34				

Is the confining pressure value and the greater is the number of acoustic signals generated. In the softening stage, cracks through the model began to appear on the surface of the model specimen, and the acoustic emission activity was mainly concentrated on the crack surface. Therefore, the acoustic signal appeared in steps 29 and 34 at the crack.

TABLE 4 Evolution process of AE signals in different confining pressure models under 1 MPa water pressure.

Load step	8 MPa confining pressure	6 MPa confining pressure	4 MPa confining pressure	2 MPa confining pressure
Linear deformation stage Step 10				
Linear deformation stage Step 22				
Nonlinear deformation stage Step 25				
Nonlinear deformation stage Step 27				
Softening phase Step 29				
Softening phase Step 34				

Tables 2–5 indicate that different water pressure values affect the acoustic emission activity of the model specimen. The lower the water pressure value, the more active is the acoustic emission activity, considering the presence of water reduces the brittle characteristics of the rock, thereby weakening the strength of the rock. Rocks are less resistant

TABLE 5 Evolution process of AE signals under different confining pressures at 0.5 MPa water pressure.

Load step	8 MPa confining pressure	6 MPa confining pressure	4 MPa confining pressure	2 MPa confining pressure
Linear deformation stage Step 10				
Linear deformation stage Step 22				
Nonlinear deformation stage Step 25				
Nonlinear deformation stage Step 27				
Softening phase Step 29				
Softening phase Step 34				

to deformation and damage, becoming more prone to failure. Therefore, under the action of axial load and confining pressure, the acoustic emission activity of the model is less active than that of the other three groups when 4 MPa water pressure is applied. The acoustic emission activity is the most active at 0.5 MPa water pressure, and the model produces a

large number of irregularly distributed acoustic signals in the three deformation and failure stages. Furthermore, the acoustic signals distributed at the cracks are denser than those of the other three groups.

5 Conclusion

(1) In the case of different confining pressures of the same water pressure, the lower the confining pressure, the lower is the compressive strength of the model, and the more evident is the failure phenomenon. This can be attributed to the fact that the cracks inside the model are pressed owing to the increase in the confining pressure value applied, which limits the radial deformation. As a result, the stiffness of the model increases, which strengthens the compressive strength of the model specimen. In the case of different water pressures of the same confining pressure, the higher the water pressure value, the more evident is the failure phenomenon of the model, and the lower is the peak stress in the stress–strain curve. This is because the higher the water pressure value applied to the model, the more evident is the permeation effect of water on the specimen.

(2) The larger the water pressure value, the more evident is the softening effect, which reduces its compressive strength. Furthermore, increased water pressure promoted the development of cracks in the model and reduced the compressive strength of the model. Owing to the different confining pressure, the accumulated strain energy inside the specimen was different, as a result, the resulting acoustic emission activity was different. The smaller the confining pressure value with the same water pressure value, the larger was the maximum AE number o of the model, and the larger was the total cumulative AE number. After the model specimen reaches peak stress and macroscopic failure, the AE number reached a maximum. The larger the confining pressure value, the smaller was the maximum number of sound emissions. The slippage phenomenon of the fractures in the model improved the shear strength and post-peak bearing capacity of the model specimen, and the acoustic emission activity of the rupture of the specimen shifted backward as a whole.

(3) Water has a certain softening effect on the internal microstructure of the rock, which inhibits the acoustic emission activity of the rock. The action of pore water transforms the model from brittle tension to plastic slip

during loading; therefore, the fracture characteristics of the model changed from brittle to ductility. The acoustic emission activity of the model decreased as the water pressure increased, the larger the water pressure value, the smaller was the cumulative AE number.

Data availability statement

The data that support the findings of this study are available from the corresponding author, LZ upon reasonable request.

Author contributions

LZ contributed to the conception of the study, performed the experiment; GL contributed to future analysis and modify the manuscript. XW contributed to future analysis and modify the manuscript. YZ contributed to research ideas. All authors contributed to the article and approved the submitted version.

Conflict of interest

The authors declare that the research was conducted in the absence of any commercial or financial relationships that could be construed as a potential conflict of interest.

Publisher's note

All claims expressed in this article are solely those of the authors and do not necessarily represent those of their affiliated organizations, or those of the publisher, the editors and the reviewers. Any product that may be evaluated in this article, or claim that may be made by its manufacturer, is not guaranteed or endorsed by the publisher.

References

Bao, T., Hashiba, K., and Fukui, K. (2020). Effect of water saturation on the Brazilian tension test of rocks: Mechanics of materials. *Mater. Trans.* 62 (1), 1–9. doi:10.2320/matertrans.M-M2020857

Chen, G., Li, Y., Li, T., and Zhang, G. (2022). Deterioration law of intermittent jointed sandstone mechanical properties under water–rock interaction. *Acta Geophys.* 70 (4), 1923–1935. doi:10.1007/s11600-022-00832-5

Chuanming, L., Nan, L., and Wanrong, L. (2020). Experimental investigation of mechanical behavior of sandstone with different moisture contents using the acoustic emission technique. *Adv. Civ. Eng.* 2020 (3), 1–10. doi:10.1155/2020/8877921

Ding, X., Xiao, X., Cui, J., Di, W., and Pan, Y. (2023b). Damage evolution, fractal dimension and a new crushing energy formula for coal with bursting liability. *Process Saf. Environ. Prot.* 169, 619–628. doi:10.1016/j.psep.2022.11.059

Ding, X., Xiao, X., Lv, X., Wu, D., and Pan, Y. (2023a). Effect of water on mechanical properties of coal, charge induction, and rockburst hazard prevention. *Min. Metallurgy Explor.* 40 (1), 277–290. doi:10.1007/s42461-022-00718-6

Gu, H., Lai, X., Tao, M., Cao, W., and Yang, Z. (2023). The role of porosity in the dynamic disturbance resistance of water-saturated coal. *Int. J. Rock Mech. Min. Sci.* 166, 105388. doi:10.1016/j.ijrmms.2023.105388

Gui, H., and Lin, M. (2016). Types of water hazards in China coalmines and regional characteristics. *Nat. Hazards* 84 (2), 1501–1512. doi:10.1007/s11069-016-2488-5

Kong, B., Wang, E., Li, Z., Wang, X., Niu, Y., and Kong, X. (2017). Acoustic emission signals frequency-amplitude characteristics of sandstone after thermal treated under uniaxial compression. *J. Appl. Geophys.* 136, 190–197. doi:10.1016/j.jappgeo.2016.11.008

Lai, X. P., Zhang, S., Shan, P., Cui, F., Yang, Y. B., and Bai, R. (2022). Experimental study of unconventional modified filling energy absorption and control mechanism in high energy storage rock masses. *Sci. Rep.* 12, 11783. doi:10.1038/s41598-022-15954-5

Li, G., Wang, Y., Wang, D., and Zhang, S. (2023). The creep behavior of rock shear seepage under different seepage-water pressures. *Mech. Time-Depend Mater* 27, 351–365. doi:10.1007/s11043-023-09601-3

Lin, H. X., Zhang, Q. Y., Zhang, L. Y., Duan, K., Xue, T. E., and Fan, Q. H. (2022). The influence of water content on the time-dependent mechanical behavior of argillaceous siltstone. *Rock Mech. Rock Eng.* 55, 3939–3957. doi:10.1007/s00603-022-02826-7

Liu, B., Li, S. C., Wang, J., Sui, Q. M., Nie, L. C., and Wang, Z. F. (2012). Multiplexed FBG monitoring system for forecasting coalmine water inrush disaster. *Adv. Optoelectron.* 2012, 1–10. doi:10.1155/2012/895723

Liu, X. S., Tan, Y. L., Ning, J. G., Lu, Y. W., and Gu, Q. H. (2018). Mechanical properties and damage constitutive model of coal in coal-rock combined body. *Int. J. Rock Mech. Min. Sci.* 110, 140–150. doi:10.1016/j.ijrmms.2018.07.020

Li, Z., Wang, L., Lu, Y., Li, W., and Kai, W. (2018). Experimental investigation on the deformation, strength, and acoustic emission characteristics of sandstone under true triaxial compression. *Adv. Mater. ence Eng.* 2018, 1–16. doi:10.1155/2018/5241386

Ma, H., Song, Y., Chen, S., Yin, D., Zheng, J., Shen, F., et al. (2021). Experimental investigation on the mechanical behavior and damage evolution mechanism of water-immersed gypsum rock. *Rock Mech. Rock Eng.* 54 (9), 4929–4948. doi:10.1007/s00603-021-02548-2

Moradian, Z., Einstein, H., and Ballivy, H. G. (2016). Detection of cracking levels in brittle rocks by parametric analysis of the acoustic emission signals. *Rock Mech. Rock Eng.* 49 (3), 785–800. doi:10.1007/s00603-015-0775-1

Qiao, L., Wan, Z., and Huang, A. (2017). Alteration of mesoscopic properties and mechanical behavior of sandstone due to hydro-physical and hydro-chemical effects. *J. Eng.* 50, 255–267. doi:10.1007/s00603-016-1111-0

Serdyukov, S., Rybalkin, V., Drobchik, A., Vostrikov, N. I., Rybalkin, L. A., Drobchik, A. N., et al. (2022). Acoustic and seismic emission in hydraulic fracturing of cement block under loading. *J. Min. Sci.* 58 (6), 920–929. doi:10.1134/s1062739122060060

Shan, R. L., Kong, X. S., Liu, J., Li, J. F., Bai, Y., and Song, Y. W. (2014). Research status and development trends of roadway surrounding rock stability classification. *Appl. Mech. Mater.* 3307, 1352–1357. doi:10.4028/www.scientific.net/amm.580-583.1352

Shoufeng, T., Minming, T., Junli, H., and Xinmin, H. (2010). Characteristics of acoustic emission signals in damp cracking coal rocks. *Min. Sci. Technol.* 20 (1), 143–147. doi:10.1016/s1674-5264(09)60176-9

Tang, C. (1997). Numerical simulation of progressive rock failure and associated seismicity. *Int. J. Rock Mech. Min. Sci.* 34 (2), 249–261. doi:10.1016/s0148-9062(96)00039-3

Wang, Y., Deng, C., Zeng, D., He, F., Feng, X., Wang, D., et al. (2022). Research on sandstone damage characteristics and acoustic emission precursor features under cyclic loading and unloading paths. *Sustainability* 14 (19), 12024. doi:10.3390/su141912024

Zilong, Z., Xin, C., Wenzhuo, C., Xiong, X., and Xiong, C. (2016). Influence of water content on mechanical properties of rock in both saturation and drying processes. *Rock Mech. Rock Eng.* 49, 3009–3025. doi:10.1007/s00603-016-0987-z

Check for updates

Experimental study on dynamic characteristics of saturated remolded soft clay with sand particles

Sui Wang[1,2,3]*, Yuanqiang Cai[1], Liyong Zhang[2], Yongjian Pan[2], Bin Chen[3] and Peng Zhao[3]

[1]College of Civil Engineering, Zhejiang University of Technology, Hangzhou, China, [2]Zhejiang Engineering Survey and Design Institute Group Co., Ltd., Ningbo, China, [3]School of Civil and Transportation Engineering, Ningbo University of Technology, Ningbo, China

Long-term cyclic tests for different frequencies were carried out on remolded soft clay with different sand contents, investigating how the frequency impacted the stress−strain, the dynamic shear modulus, and the damping ratio of the remolded samples. Accordingly, when the sand content of the remolded specimen was 1.7%, the slope of the hysteresis curve of the remolded specimen tended to increase gradually with the increasing frequency, the hysteresis circle was slender, and the area of the hysteresis circle tended to decrease gradually; when the sand content of the remolded specimen was 20%, the cumulative deformation of the specimen presented a gradual increase with the loading frequency, and the slope of the hysteresis curve decreased gradually. The hysteresis curve shows a gradually decreasing slope, and the enclosed hysteresis circle area also tends to decrease. In addition, the higher the loading frequency, the stronger the deformation-resistant ability held by the specimen, particularly because the pore water pressure between soils' internal particles is not discharged in time, which makes the contact between the internal particles of the soil close, and the closer the structure of the soil, the smaller the compressive deformation of the soil, and the more stable the soil.

KEYWORDS

soft clay, sand interlayer, hysteresis curve, dynamic shear modulus, damping ratio

Introduction

Soft clay is a special soil mass formed by marine and lacustrine sediments in coastal, lake, swamp, and river bay areas in modern times. It features high water content, strong compressibility, weak strength, low permeability, strong sensitivity, and rheology (Andersen, 1977; Talesnick and Frydman, 1992; France and Sangrey, 1997; Guo et al., 2013; Sangrey et al., 1997; Guo et al., 2016; Qian et al., 2016; Patel et al., 2017; Qian et al., 2017; Ecemis, 2021). Among them, according to the survey results of Ningbo Metro, there is a large number of loose sand interlayers, with a thickness of approximately 10 cm in the soft clay of metro tunnel engineering. According to the design code, this kind of interlayer has almost no influence on the evaluation of foundation liquefaction; however, its seismic liquefaction can cause dramatic changes in stratum deformation, which will cause the subway tunnel to bear huge additional horizontal thrust and cause damage to the subway tunnel. Therefore, there is a contradiction between the evaluation results of foundation

liquefaction and the potential damage to subway tunnels. It is of great significance for engineering investigation and subway tunnel design to fully consider the seismic liquefaction of such sand interlayers, deeply study the dynamic characteristics of soft clay with different sand contents, and propose relevant engineering reinforcement measures for its failure form.

Tasiopoulou et al. (2018), Zhao et al. (2018), and Jain et al. (2023) have performed corresponding experimental studies on the dynamic characteristics exhibited by the mixed soil with sand particles in the clay. Yamada, S, et al. (2008) mixed quartz sand with medium-plastic clay in different proportions, measured the dynamic characteristics exhibited by the clay–sand mixture through a cyclic torsion single shear test, and proposed the empirical formula of the dynamic shear modulus (DSM), damping ratio (DR), and shear strain (SS) relationship curve of the remolded clay–sand mixture. Li et al. (2013) paid attention to how confining pressure affected the dynamic characteristics exhibited by remolded red clay through a resonant column test and pointed out that when SS is the same, DSM presents an uptrend and DR presents a downtrend with the confining pressure. Zhao et al. (2015) comparatively examined the DR of undisturbed and remolded sandy mudstone weathered soil through a dynamic triaxial test, finding that when the shear strain value is the same, undisturbed soil shows a larger DR value than plastic soil. Huang et al. (2015) focused on how the fines content affected the dynamic characteristics exhibited by remolded loess using a resonance column test. Research shows that the increase in the fines content is accompanied by decreased DSM and DR of remolded loess. Guo (1998) studied and analyzed a large number of engineering research results and pointed out that in the case of the coarse particle content being less than 30%, a larger coarse particle content reports a smaller permeability coefficient of the mixed soil, and its permeability characteristics are determined by the soil mass and conform to Darcy's law. In the case of a coarse particle content over 75%, the permeability coefficient increases with the coarse particle content, and its permeability characteristics are determined by the coarse particles but not in accordance with Darcy's law. The rock content has a significant impact on its hydraulic damage. Xu (2008) further studied the permeability of the mixture and found that its permeability coefficient was between KME (calculated value of the Maxwell–Eucken model) and KEME (calculated value of the effective medium theoretical model). Miller and Sowers (1958) took the maximum dry density as the control factor, carried out consolidated undrained triaxial shear tests on clay–sand mixtures with different sand contents, and pointed out that the impact of sand content on mixed soils' shear strength has a limit value. Vallejo and Zhou (1994) studied the strength law of soil–sand mixed soil through a direct shear test and reached the conclusion that the limit sand content range is 50%–80%. Vallejo and Mawby (2000) further calculated the porosity of soil–sand mixed soil through theory and finally corrected its limit sand content to 40%–75%. Yamamuro and Covert (2001) and Prakasha and Chandrasekaram (2005) studied the effect of the effective void ratio of the clay–sand mixture on its mechanical properties. Bolton (2000) studied the clay–sand mixed soil and believed that its permeability was closely related to the effective stress and consolidation state. Shi et al. (2011) conducted some indoor tests on laterite with different sand contents and pointed out that the laterite mixed with sand reduced the cohesion, increased the internal friction angle, increased the shear strength, and had an optimal range of the sand content. Zhang et al. (2010) prepared the mixed soil by adding 0%–50% quartz sand to bentonite, found that its cohesion and internal friction angle decreased as the sand mixing rate increased, and statistically estimated that its limit sand mixing amount was 54%–79%. Deng et al. (2012, 2014) designed the indoor direct shear test for the clay–sand mixture, analyzed how the sand content and water content impacted its shear strength, and reached the conclusion that the limit sand content is 50%–70%.

Above all, scholars have conducted little research on the physical and mechanical properties exhibited by soil–sand mixed soil, and even less on muddy soil–sand mixed soil. However, with the continuous progress of rail transit, the treatment of muddy soil–sand mixed soil in tunnel excavation and soft foundation becomes more common; therefore, further research shall be conducted on the soft soil geology.
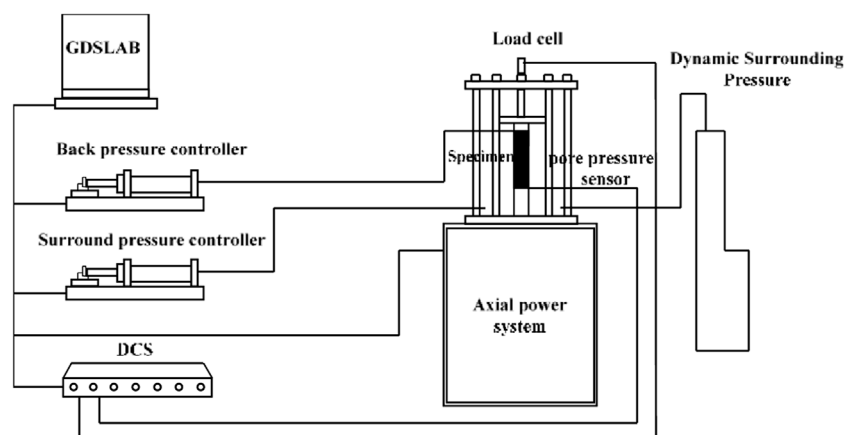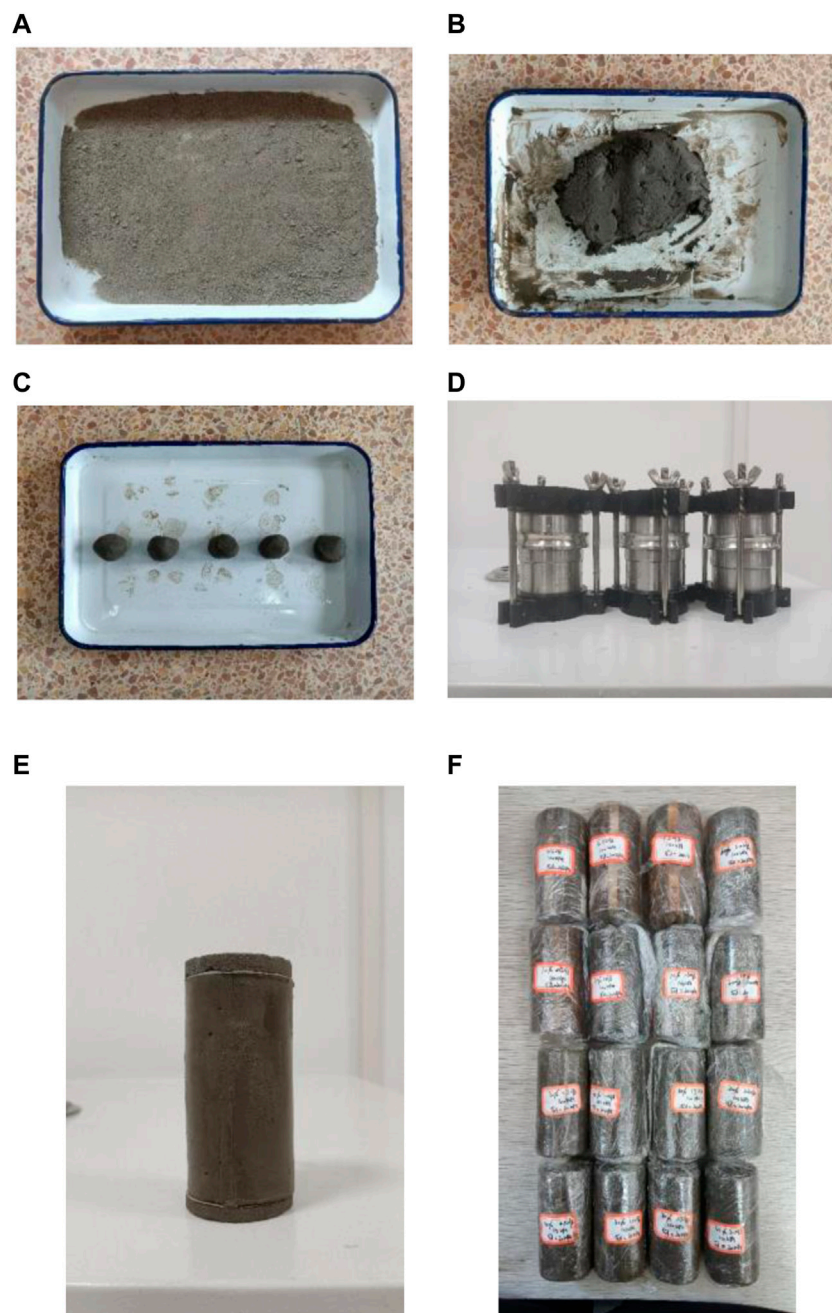

FIGURE 1
GDS bidirectional dynamic triaxial test system.

FIGURE 2
Preparation of soft clay specimens with different sand content remodeling samples.

Research contents and methods

Sample equipment and materials

The British Global Digital Systems (GDS) bidirectional dynamic triaxial test system was adopted (Figure 1). The experimental system has the following six parts: the axial power system, triaxial pressure chamber, dynamic confining pressure loading system, confining pressure controller, backpressure controller, and signal control system (DCS). The GDS test system collects the axial stress, strain, pore pressure, and other data during the vibration process of the sample through the computer (GDS-LAB) and converts DEM, DR, and other indicators through data analysis. The system bears dynamic load, deformation, and stress of up to 10 Hz. The axial load is driven by the base screw driven by a motor, and the axial force and axial deformation are applied from the base of the pressure chamber.

Preparation of remolded samples

1) First, a wooden hammer is used to break up the dried soil sample; then, the soil sample is allowed to pass through a 1-mm
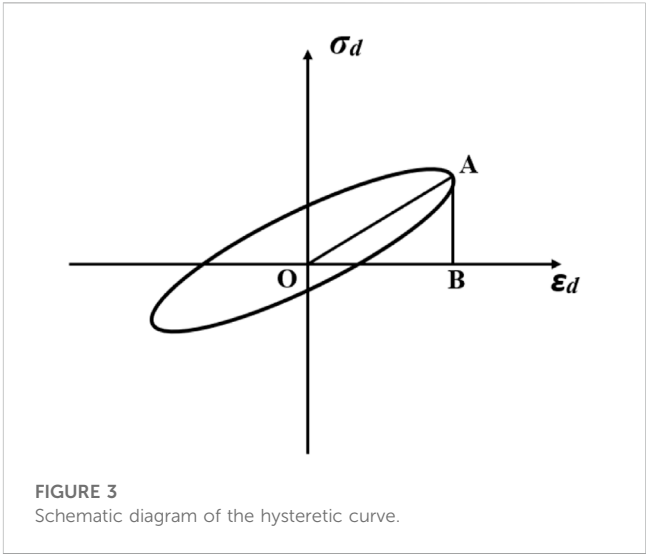
TABLE 1 Soil samples' basic physical parameters.

Property	Value
Density $\rho/$ ($g \cdot cm^{-3}$)	1.82
Plastic limit Ip	15.6
Liquid limit $w_L/\%$	40.1
Dry density $\rho_d/$ ($g \cdot cm^{-3}$)	1.36
Moisture content ω (%)	34.22
Cohesion c (kPa)	18.2
Internal friction angle φ (°)	26.64

FIGURE 3
Schematic diagram of the hysteretic curve.

sieve. The screened soil sample is reserved for standby. 2) The screened air-dried soil is then sieved using a 0.075-mm sieve, and the soil sample obtained after sieving is muddy silt. 3) Preparation of sand is performed as follows: the air-dried soil is sieved using a 0.075-mm sieve and washed with water, and the muddy silt is fully dissolved in water by continuous shaking during the washing process. The washing time should be no less than 20 min, then the washed sand is air-dried for standby. 4) Preparation of remolded samples that have the same moisture content and dry density as the undisturbed soil samples, according to the samples with different sand contents required for the test. 5) Following the Code for Geotechnical Testing (GB/T50123-1999), the dry broken soil with different sand contents should be prepared with distilled water in a soil sample with the same moisture content as the undisturbed sand soft clay and then sealed with a fresh film. In order to make the soil sample fully absorb water and evenly distribute water in the drawing, the prepared remolded soil sample shall be placed in a cool and humid environment for more than 24 h. 6) Vaseline is applied on the inner wall of the three valves to make them fully smooth and reduce the friction between the soil sample and the ring knife inner wall during the test. 7) The mass M of the soil sample is filled into the three valves in five layers into the ring knife, and it is compacted layer by layer. 8) The prepared sample is put into the vacuum cylinder for vacuum saturation, and the sample is prepared. 9) The prepared remolded soil samples with different sand contents are tested on the dynamic triaxial apparatus. Figure 2 demonstrates the process of preparing the remolded soil sample.

The soil sample is taken from the remolded sample of Ningbo Metro Line 6 in Zhejiang province, with a depth of 5 m–10 m. Table 1 lists soil samples' basic physical parameters.
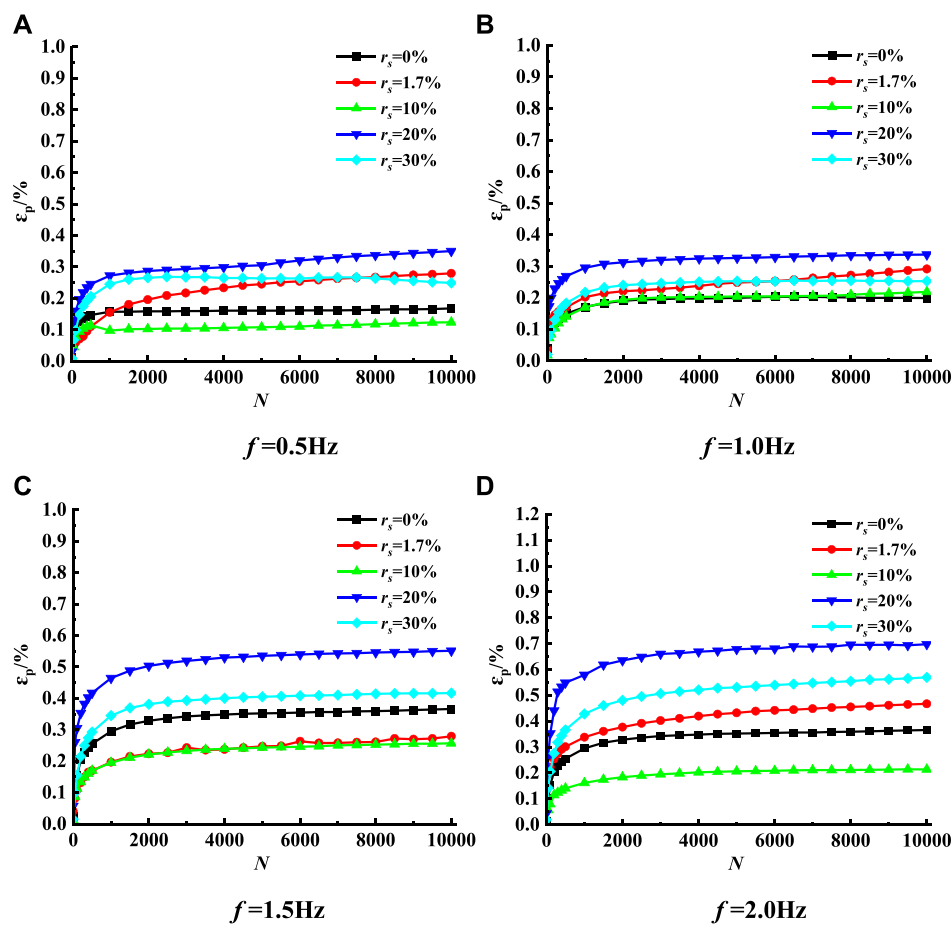
Test procedure

The prepared remolded soil sample is placed into the vacuum saturator for vacuum pumping. When the vacuum pressure is expressed to negative pressure, the vacuum pressure is kept in the cylinder for no less than 1 h and it is allowed to stand for more than 10 h. In order to ensure that the saturation reaches more than 95%, if it fails to meet the requirements, the sample is saturated by backpressure before the test until the sample saturation meets the requirements.

After saturation, the sample is under effective confining pressure σ. The isotropic consolidation is carried out at $\sigma_3'=100$ kPa, and the consolidation is considered to be completed when the B-t curve tends to be flat and the pore pressure drops to equal to the back pressure. The cyclic loading mode is stress-controlled loading, and the dynamic stress waveform is the sine wave. The frequency range of the dynamic wave loaded on a soft soil foundation is 0.1–10 Hz, but mainly 1~2 Hz. For investigating how vibration frequency impacted saturated soft clay with the sand interlayer, the vibration frequency of this experiment is 0.5 Hz, 1.0 Hz, 1.5 Hz, and 2.0 Hz. In order to measure the cyclic axial bias stress, the axial cyclic stress ratio r_c is introduced, as shown in Table 2.

During the test, axial deformation, axial stress, pore pressure, and other data are collected and processed by a computer. When the double-amplitude axial strain of the sample reaches 5% or the loading times reach the set loading times, the test is terminated.

TABLE 2 Pilot scenarios.

ID	Sand content ($r_s/\%$)	Cyclic stress ratio/r_c	Confining pressure (σ_3'/kPa)	Frequency (f/Hz)
1	0	0.1	100	0.5, 1.0, 1.5, and 2.0
2	1.7	0.1	100	0.5, 1.0, 1.5, and 2.0
3	10	0.1	100	0.5, 1.0, 1.5, and 2.0
4	20	0.1	100	0.5, 1.0, 1.5, and 2.0
5	30	0.1	100	0.5, 1.0, 1.5, and 2.0

FIGURE 4
Axial cumulative strain of soft clay with cycles for different frequencies.

In addition, DSM serves as a significant parameter of soil mechanics, referring to soils' non-deformability under dynamic load, i.e., the size of stiffness. In the data file automatically collected by the computer, the data are selected, the stress–strain hysteresis curve at different stages is drawn, and the slope of a vibration cycle is calculated, which is the dynamic elastic modulus (G_d) of the soil given as follows:

$$G_d = \frac{\sigma \mathrm{d}}{\varepsilon d} = \frac{\sigma \max - \sigma \min}{\varepsilon \max - \varepsilon \min}. \tag{1}$$

The damping ratio denotes the nature of dissipation of soil energy due to internal resistance under dynamic stress, which is usually calculated by the following equation:

$$\lambda = \frac{1}{4\pi} \frac{\Delta W}{W} = \frac{1}{4\pi} \times \frac{\text{Area of hysteresis loop}}{\text{Area of triangle OAB}}, \tag{2}$$

where ΔW represents the energy lost by the soil under a cyclic vibration, equal to the area surrounded by the hysteretic curve (Figure 3); and W is the total energy stored under one cycle of vibration, i.e., the triangle OAB area shown in Figure 3.

Test result analysis

Cumulative plastic deformation of samples with different sand contents

Figure 4 shows the cumulative axial deformation regarding remolded soft clay under different sand contents at the same frequency as the change curve of vibration times. The dynamic characteristics and deformation exhibited by remolded soft clay with different sand contents under a long-term cyclic load are analyzed by drawing.

Under the same frequency, when r_s<20%, when the samples' cumulative strain increases with the sand content, the influence of the sand particles inside the sample on the samples' skeleton is not notable, and the deformation of the soil is mainly borne by fine-grained soft clay; when r_s>20%, the content of sand particles in the sample will make the mechanical properties of the sample unstable, resulting in large cumulative axial deformation. At the same time, the influence of the sand content of the sample in the critical state (i.e., r_s =20%) on the cumulative axial deformation will increase with the increase in frequency.
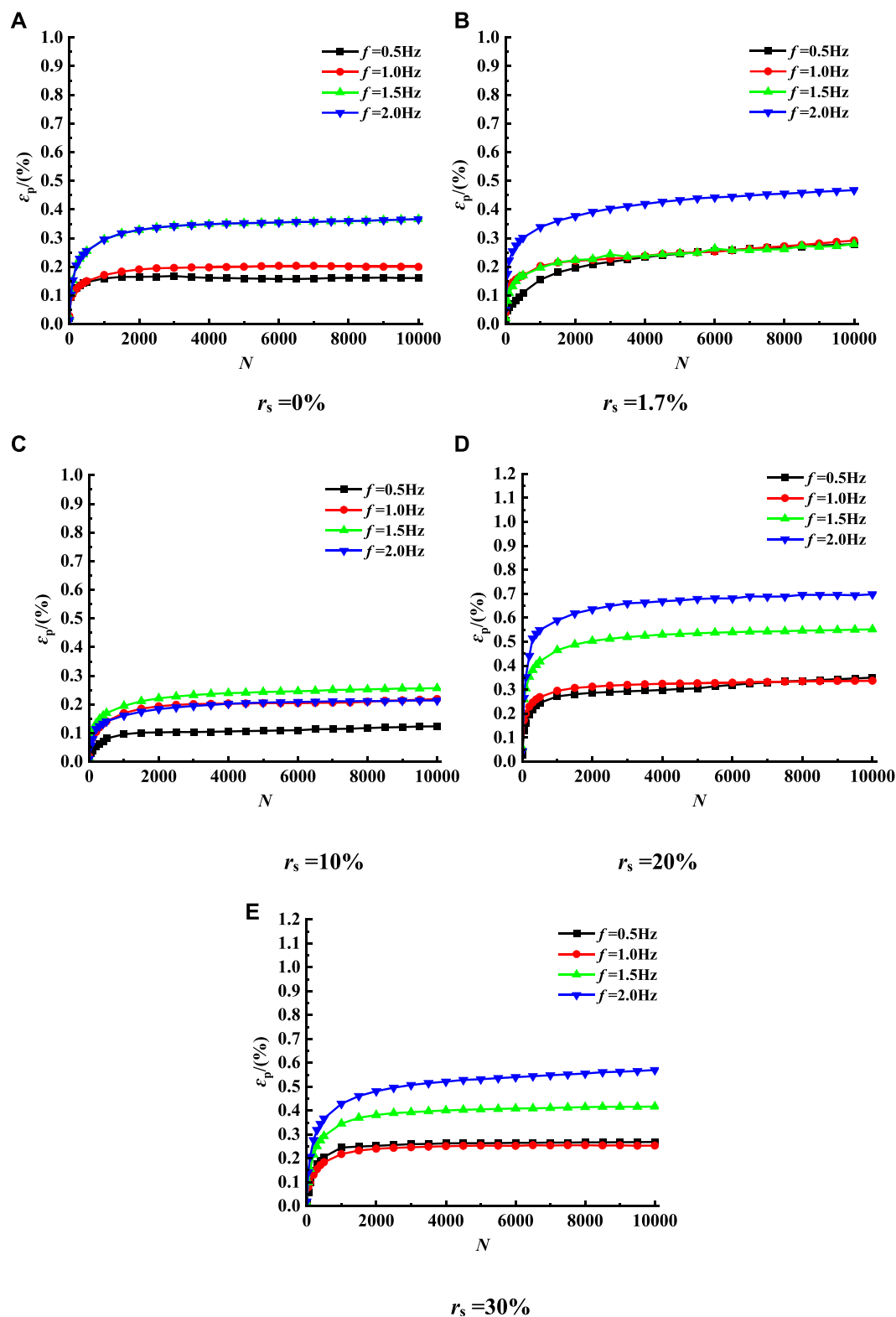
FIGURE 5
Axial cumulative strain with cycles of soft clay for different sand contents.
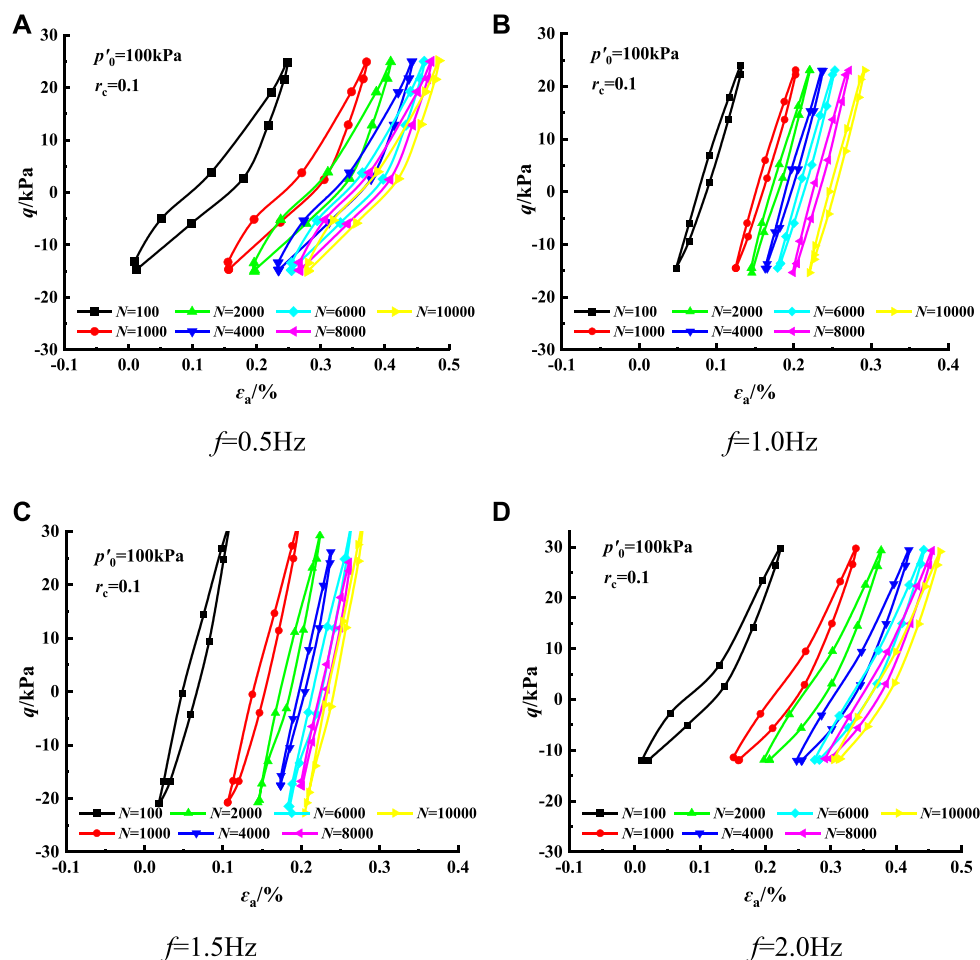
FIGURE 6
r_s=1.7% dynamic stress−strain relationship graph.

Cumulative plastic deformation of samples at different frequencies

Figure 5 shows the cumulative axial deformation of remolded soft clay under the same sand content at different frequencies *versus* the number of vibrations. The dynamic characteristics and deformation of remolded soft clay under a long-term cyclic load at different frequencies are analyzed by drawing.

According to Figure 5, for remolded soil samples with different frequencies, when the sand content is 0%, the influence of frequency on the vertical strain is not significant. Figure 5A shows that there is little difference in strain development when the frequency is 0.5 Hz and 1 Hz. When the frequency is 1.5 Hz and 2 Hz, the strain development is basically the same, but the strain is relatively large; when the sand content is 1.7%, it can be seen from Figure 5B that the strain at f =2 Hz is the highest, while the strain development at the other three frequencies is basically the same; when the sand content is 10%, it can be seen from Figure 5C that the strain is the highest at f =1.5Hz, the strain development is basically the same at f=2 Hz and f =1Hz, and the strain is the lowest at f =0.5Hz; when the sand content is 20%, it can be seen from Figure 5D that the higher the frequency, the greater the strain; when

the sand content is 30%, it can be seen from Figure 5E that the difference in strain development is very small and basically the same when the frequency is 0.5Hz and 1 Hz, implying that the greater the frequency, the greater the strain. Therefore, the frequency is not significant for the strain development pattern under different sand content rates. However, it also shows that the sand content has a great influence on the cumulative axial deformation of the sample.

Effect of vibration frequency on the stress−strain curve of soft clay with different sand contents

Figure 6 and Figure 7 demonstrate the hysteretic curves of remolded soft clay with different sand contents at different frequencies, in which the sand contents of 1.7% and 20% are taken as representative for comparative analysis.

According to Figure 6 and Figure 7, the hysteresis curve of saturated remolded soft clay shows a series of closed hysteresis loops when the sample sand is 1.7%. When the cyclic loading begins, the hysteresis loop is relatively narrow and steep, indicating that the slope is relatively large and dense. As the number of cycles increases,
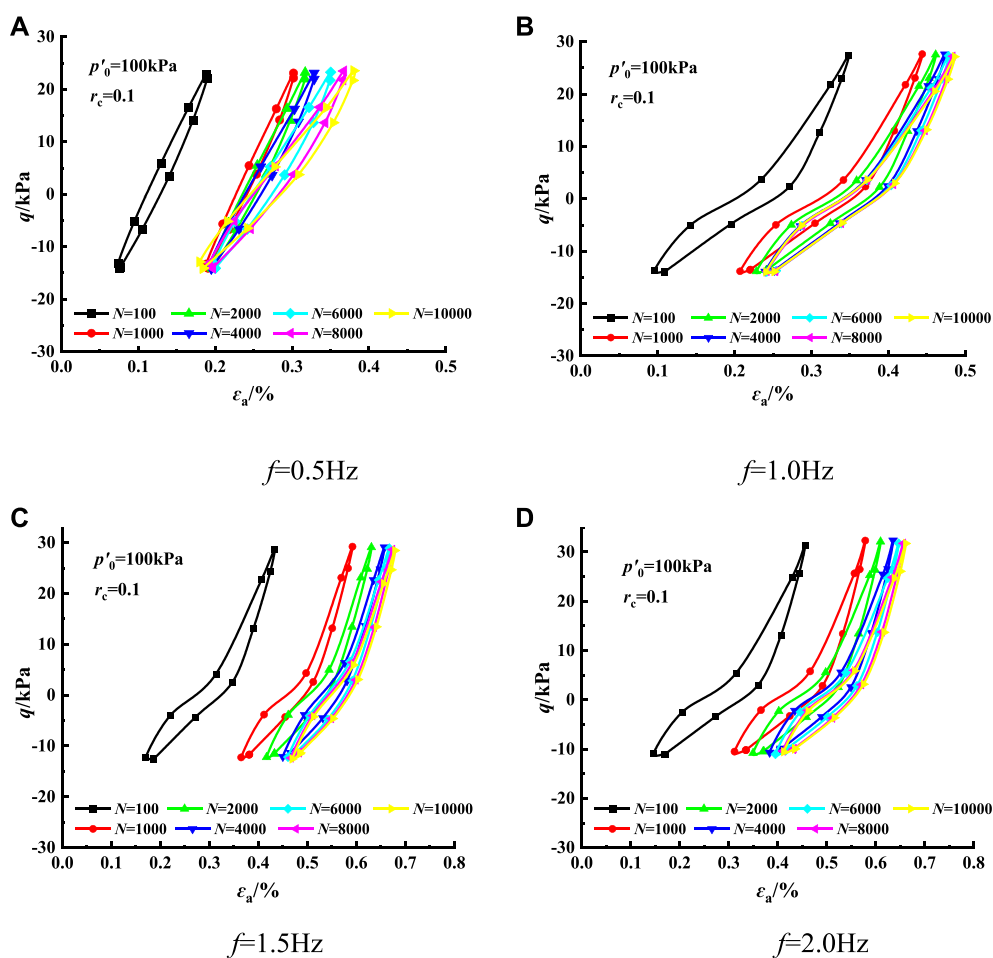
FIGURE 7
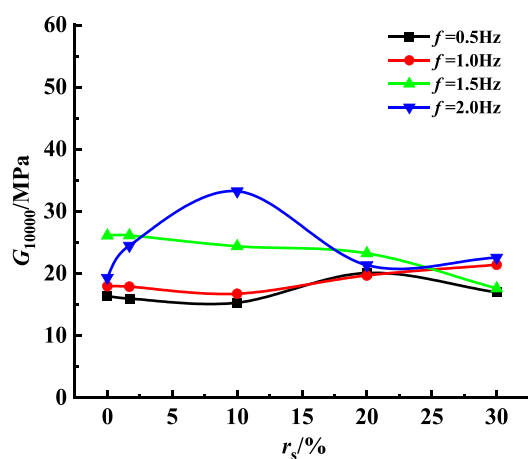r_s=20% dynamic stress−strain relationship graph.

FIGURE 8
Final DSM of soft clay for different sand contents.
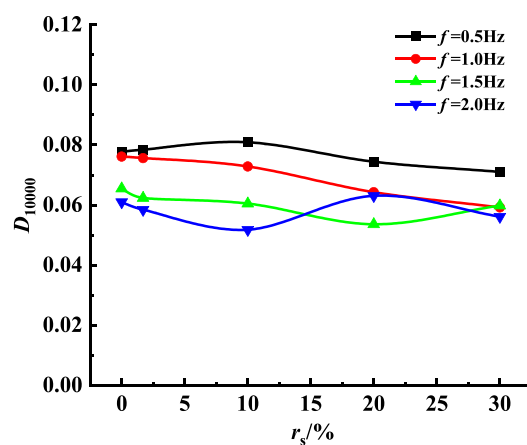

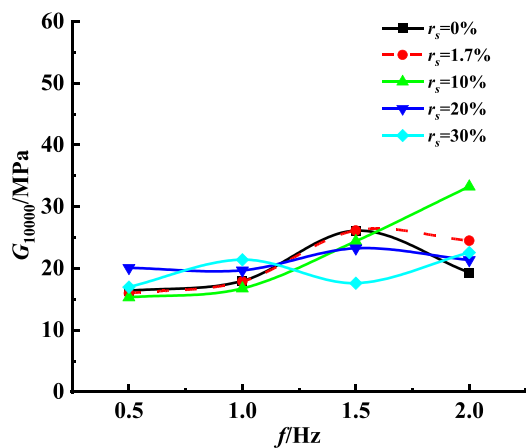**FIGURE 9**
Final damping ratio of soft clay for different frequencies.

FIGURE 10
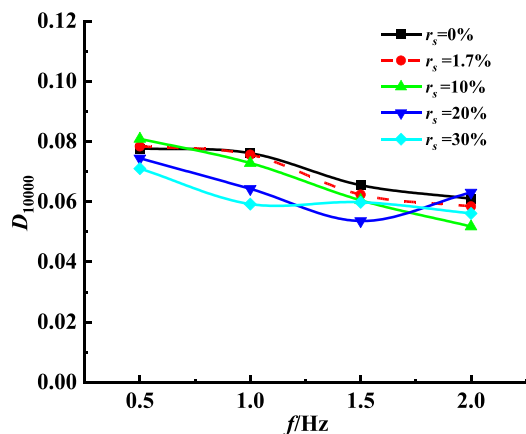Final DSM of soft clay for different frequencies.

FIGURE 11
Final DR of soft clay for different frequencies.

content and DSM and DR is examined by drawing the change curve of the two parameters under different conditions.

Curve of DSM and DR of soft clay with the sand content at different frequencies

According to Figure 8, the DSM of remolded samples at different frequencies presents different change rules. When f=0.5Hz, the DSM of samples presents a non-linear increase with the sand content and reaches the maximum value when r_s=20%. As the frequency increases, DSM at initial vibration approaches the DSM at the final cycle; when the load frequency f=2.0 Hz and r_s<10%, the DSM of the remolded sample increases with the sand content. When r_s>10%, the DSM of the sample is reduced gradually and tends to be stable.

According to Figure 9, the change in DR at different frequencies is similar to the change in DSM, with different change trends. The change trend of the DR of the remolded sample is just opposite to that of the DSM. When f=0.5Hz, the DR of the sample changes non-linearly with the increased sand content and reaches the lowest critical value when r_s=30%. At the same time, as the frequency increases, the DR of the initial vibration of the sample is closer to that of the final cycle; when the load frequency f=2.0 Hz and r_s<10%, the DR of the remolded sample increases with the sand content. When r_s>10%, DR decreases gradually and tends to be stable.

The influence mechanism of frequency on remolded mixed clay–sand can be concluded as follows: when the confining pressure and cyclic dynamic stress are the same, the higher the loading frequency and the stronger the sample's ability to resist deformation. This is mainly because the higher the loading frequency, the shorter the time taken to discharge the pore water pressure between soil particles, rendering the particles in the soil in close contact, the closer the soil structure, the smaller the compression deformation of the soil, and the more stable the soil. When the load is the same, a higher frequency reports a smaller final DR, primarily because with the increase in frequency, the particle contact in the sample becomes closer, there are fewer pores, the propagation path of the wave is also increased, and the propagation speed is faster; so, the energy consumed during wave propagation is reduced so that the DR of the energy loss parameters of the remolded sample with different sand contents will also be reduced after the vibration.

Variation curve of DSM and DR of soft clay

Figure 10 shows the change curve of the final DSM of remolded soft clay with frequency under different sand contents. In samples with a stable sand content, DSM increases with the frequency because the higher the load frequency, the shorter of time for which the dynamic stress of the same size acts on the soil, the shorter of time for which axial deformation occurs. According to the formula of DSM, the smaller the strain value per unit time, the greater the DSM. In the case of the sand content r_s < 20%, the DSM of the sample presents a significant increase trend; when r_s=20%, the final DSM decreases as the frequency increases. However, when r_s =30%, the final DSM tends to increase first, then decrease, and then increase again.

the hysteresis loop slowly shifts to the positive direction of the x-axis, that is, to the direction of strain increase, which indicates a gradual increase in remolded samples' cumulative plastic strain. At the same time, as the number of cycles increases, the hysteresis loop is gradually lengthened, the slope is gradually reduced, and the area enclosed by the hysteresis loop is also gradually reduced. This shows the attenuation of DSM and the increase in the DR of remolded soil samples under cyclic action.

In addition, when the sand content of the remolded sample is 1.7% of that of the undisturbed sample, the hysteresis curve slope of the remolded sample presents a slow increase with the frequency, the enclosed hysteresis loop is thin and long, and the hysteresis loop area has a trend of gradually decreasing; when the sand content of the remolded sample is 20%, the cumulative deformation of the sample gradually increases with the loading frequency, the hysteresis curve slope gradually decreases, and the enclosed hysteresis loop area also decreases. The test shows that the remolded soft clay's DSM and DR are related to the sand content. The relationship between sand

Figure 11 shows the change curve of the final DR of remolded soft clay with frequency under different sand contents. The changes in the DR and DSM of samples that have various sand contents also have similar changes, reaching the critical value when the sand content r_s=20%, that is, when r_s<20%, the resistance ratio of the sample has a significant downward trend; when r_s>20%, the DR of remolded samples has a significant upward trend.

According to Figure 10 and Figure 11, when the sand content in the soil is high, soft soil particles are mainly filled in the pores of sand particles and slightly affect the soil skeleton composition; when the content in the soil is small, the soft soil particles are wrapped with sand particles to form the skeleton of the soil, and the way sand particles affect the skeleton of the soil can be ignored. During the gradual increase in the sand content, there is a critical state of r_s=20%. At this time, the soft soil particles in the soil body not only do not participate in the formation of the soil skeleton but also reduce the content of sand particles that constitute the soil skeleton, exacerbating the instability of the macroscopic mechanical characteristics exhibited by the soil body, resulting in a small dynamic stress corresponding to the same dynamic strain, a decrease in DSM, and an increase in DR.

Conclusions

A large number of soft clay samples with different sand contents were conducted; the effects of frequency, sand content on shear modulus, and damping ratio were studied. The following conclusions can be drawn:

1) When the sand content of the remolded sample is 1.7% of that of the undisturbed sample, the hysteretic curve slope of the remolded sample increases slowly with the frequency, the enclosed hysteretic loop becomes thin and long, and the area of the hysteretic loop has a trend of gradual decrease; when the sand content of the remolded sample is 30%, the cumulative deformation of the sample will gradually increase with the loading frequency, the hysteresis curve slope will decrease slowly, and the enclosed hysteresis loop area will also decrease.

2) When the confining pressure and cyclic dynamic stress are the same, the higher the loading frequency, the stronger the sample's ability to resist deformation. This is mainly because the higher the loading frequency, the less time taken to discharge the pore water pressure between the soil particles, rendering the particles inside the soil in close contact, the tighter the soil structure, the smaller the compression deformation of the soil, and the more stable the soil.

3) When the sand content in the soil is small, the soft soil particles are wrapped with sand particles to form the skeleton of the soil, and the way sand particles affect the soil skeleton can be ignored. When the sand content is gradually elevated, there is a critical state of r_s=20%. At this time, the soft soil particles in the soil body not only do not participate in the formation of the soil skeleton but also reduce the content of sand particles that constitute the soil skeleton, exacerbating the instability of the macroscopic mechanical properties of the soil body, resulting in a small dynamic stress corresponding to the same dynamic strain, a decrease in DSM, and an increase in DR.

Data availability statement

The raw data supporting the conclusion of this article will be made available by the authors, without undue reservation.

Author contributions

SW: data curation, investigation, writing–original manuscript, and writing–review and editing. YC: investigation, methodology, and writing–review and editing. LZ: investigation, methodology, writing–original manuscript, and writing–review and editing. YP: investigation, methodology, formal analysis, and writing–review and editing. BC: investigation, methodology, and writing–review and editing. PZ: investigation, methodology, and writing–review and editing.

Conflict of interest

Authors SW, LZ, and YP were employed by Zhejiang Engineering Survey and Design Institute Group Co., Ltd.

The remaining authors declare that the research was conducted in the absence of any commercial or financial relationships that could be construed as a potential conflict of interest.

Publisher's note

All claims expressed in this article are solely those of the authors and do not necessarily represent those of their affiliated organizations, or those of the publisher, the editors, and the reviewers. Any product that may be evaluated in this article, or claim that may be made by its manufacturer, is not guaranteed or endorsed by the publisher.

References

Andersen, K. H. (1977). "Effect of cyclic loading on clay behaviour," in *Proc. BOSS ICE* London, 75–79.

Bolton, A. J. (2000). Some measurements of permeability and effective stress on a heterogeneous soil mixture: implications for recovery of inelastic strains. *Eng. Geo-logy* 57, 95–104. doi:10.1016/s0013-7952(00)00019-3

Cai, Y., Gu, C., Wang, J., Juang, C. H., Xu, C., and Hu, X. (2013). One-way cyclic triaxial behavior of saturated clay: comparison between constant and variable confining pressure. *J. Geotechnical Geo-environmental Eng.* 139 (5), 797–809. doi:10.1061/(asce)gt.1943-5606.0000760

Deng, T. F., Ai, Z. W., Luo, S. H., and Gui, Y. (2014). Experimental study on shear characters of clay-sand mixture. *People's Yangtze River* 45 (9), 95–101. (In Chinese). doi:10.3969/j.issn.1001-4179.2014.09.026

Deng, T. F., Gui, Y., Luo, S. H., and Zhou, J. P. (2012). Study on slope stability of granite residual soil cutting excavation with rainfall. *J. Earth Sci. Environ.* 34 (4), 88–94. (In Chinese). doi:10.3969/j.issn.1672-6561.2012.04.012

Ecemis, N. (2021). Experimental and numerical modeling on the liquefaction potential and ground settlement of silt-interlayered stratified sands. *Soil Dyn. Earthq. Eng.* 144 (10), 106691. doi:10.1016/j.soildyn.2021.106691

France, J. W., and Sangrey, D. A. (1997). Effects of drainage in repeated loading of clays. *J. Geotechnical Eng.* 103GT (7), 769–785. doi:10.1061/ajgeb6.0000454

GB/T 500123-1999 (1999). *Standard for soil test methods. GB/T 500123-1999 [S]*. Beijing: Ministry of Water Resources of the People's Republic of China. (In Chinese).

Guo, L, Chen, J., Wang, J., Cai, Y., and Deng, P. (2016). Influences of stress magnitude and loading frequency on cyclic behavior of K0-consolidated marine clay involving principal stress rotation. *Soil Dyn. Earthq. Eng.* 84, 94–107. doi:10.1016/j.soildyn.2016.01.024

Guo, L., Wang, J., Cai, Y. Q., Liu, H. L., Gao, Y. F., and Sun, H. L. (2013). Undrained deformation behavior of saturated soft clay under long-term cyclic loading. *Soil Dyn. Earthq. Eng. Soil Dyn. Earthq. Eng.* 50, 28–37. doi:10.1016/j.soildyn.2013.01.029

Guo, Q. G. (1998). *Engineering characteristics and application of coarse-grained soil [M]*. Zhengzhou: Yellow River Water Conservancy Press. (In Chinese).

Huang, Z. Q., Li, L., Jia, J. C., Yue, K. X., and Sun, Y. (2015). Study of resonant column experiment of dynamic shear module and damping ratio of unsaturated loess. *People's Yangtze River* 46 (5), 69–72. (In Chinese). doi:10.16232/j.cnki.1001-4179.2015.05.016

Hyde, A. F. L., and Ward, S. J. (1986). The effect of cyclic loading on the undrained shear strength of a silty clay. *Mar. Geotechnol.* 6 (3), 299–314. doi:10.1080/10641198609388192

Idriss, I. M., Dobry, R., and Singh, R. D. (1978). Nonlinear behavior of soft clays during cyclic loading. *J. Soil Mech. Found.* 104 (12), 1427–1447. doi:10.1061/ajgeb6.0000727

Jain, A., Mittal, S., and Shukla, S. K. (2023). Liquefaction proneness of stratified sand-silt layers based on cyclic triaxial tests. *J. Rock Mech. andGeotechnical Eng.* 15 (7), 1826–1845. doi:10.1016/j.jrmge.2022.09.015

Kammerer, A. M., Seed, B., and Wu, J. (2004). Pore water development in liquefiable soils under bi-directional loading conditions. *Proc. 11th Int. Conf. Soil Dyn. Earthq. Eng.* 2, 697.

Li, J., Chen, S. X., Jiang, L. F., and Xiong, S. D. (2013). Resonant column teston dynamic shear modulus and damping ratio of the remolded red clay. *J. Sichuan Univ. Eng. Sci. Ed.* 45 (4), 62–68. (In Chinese). doi:10.15961/j.jsuese.2013.04.003

Liang, R. Y., and Ma, F. J. (1992). Anisotropic plasticity model for undrained cyclic behavior of clays. I: theory. *J. Geotechnical Eng.* 118 (2), 229–245. doi:10.1061/(asce)0733-9410(1992)118:2(229)

Matsui, T., Bahr, M., and Abe, N. (1992). Estimation of shear characteristics degradation and stress-strain relationship of saturated clays after cyclic loading. *Soil Found.* 32 (1), 161–172. doi:10.3208/sandf1972.32.161

Miller, E. A., and Sowers, G. F. (1958). The strength characteristics of soil-aggregate mixtures. *Highw. Res. Board Bull.* (183), 16–32.

Narasimha, R. S. (2003). Behaviour of marine clay under wave type of cyclic loading. *Proceedings of the international conference on off-shore mechanics and arctic engineering-OMAE* 3, 495–503.

Patel, A., Ingale, R., and Bhanarkar, K. B. (2017). Effect of compaction states and the confining pressure on Poisson's ratio of stratified and non-stratified soils. *Arab. J. Sci. Eng.* 1-17, 1983–1999. doi:10.1007/s13369-017-2846-y

Prakasha, K. S., and Chandrasekaram, V. S. (2005). Behavior of marine sand-clay mixtures under static and cyclic triaxial shear. *J. geotechnical geoenvironmental engineering* 131 (2), 213–222. doi:10.1061/(asce)1090-0241(2005)131:2(213)

Qian, J. G., Du, Z. B., and Yin, Z. Y. (2017). Cyclic degradation and non-coaxiality of soft clay subjected to pure rotation of principal stress directions. *Acta Geotech.* 14 (3), 943–959. doi:10.1007/s11440-017-0567-8

Qian, J. G., Wang, Y. G., Yin, Z. Y., and Huang, M. S. (2016). Experimental identification of plastic shakedown behavior of saturated clay subjected to traffic loading with principal stress rotation. *Eng. Geol.* 214 (1), 29–42. doi:10.1016/j.enggeo.2016.09.012

Seed, H. B., and Lee, K. L. (1966). Liquefaction of saturated sands during cyclic loading. *J. Soil Mech. Found. Div.* 92 (6), 105–134. doi:10.1061/jsfeaq.0000913

Shi, C. X., Huang, Y., Yang, Y. T., Feng, H., and Bo, T. Z. (2011). Research on mechanical properties and sand-doped mechanism of the laterite improved with sand. *Eng. Surv.* 39 (4), 1–8. (In Chinese).

Silvestri, V., and Bouteldja, M. (1993). "On the consolidation response of a sensitive clay under cyclic loading," in *In can-adian geotechnical conference*, 455–464.

Talesnick, M., and Frydman, S. (1992). Irrecoverable and overall strains in cyclic shear of soft clay. *Soils Found.* 32 (3), 47–60. doi:10.3208/sandf1972.32.3_47

TasiopoulouGiannakouChacko, P. A. J., and De Wit, S. (2018). Liquefaction triggering and post-liquefaction deformation of laminated deposits. *Soil Dyn. Earthq. Eng.* 124, 330–344. doi:10.1016/j.soildyn.2018.04.044

Vallejo, L. E., and Mawby, R. (2000). Porosity influence on the shear strength of granular material-clay mixtures. *Eng. Geol.* 58 (2), 125–136. doi:10.1016/s0013-7952(00)00051-x

Vallejo, L. E., and Zhou, Y. (1994). "The mechanical properties of simulated soil-rock mixtures[C]," in *Proceedings of the 13th international conference on soil mechanics and foundation engineering* New Delhi, India, 365–368.

Whichtmann, T., Niemunis, A., and Triantafyllidis, Th (2007). On the influence of the polarization and the shape of the strain loop on strain accumulation in sand under high-cyclic loading. *Soil Dyn. Earthq. Engine* 27 (1), 14–28. doi:10.1016/j.soildyn.2006.05.002

Xu, W. J. (2008). *Research on meso structural mechanics and slope stability of soil rock mixture [D]*. Beijing: Institute of Geology and Geophysics, Chinese Academy of Sciences.

Yamada, S., Hyodo, M., Orense, R. P., Dinesh, S. V., and Hyodo, T. (2008). Strain-dependent dynamic properties of remolded sand-clay mixtures. *J. Geotechnical Geoenvironmental Eng.* 134 (7), 972–981. doi:10.1061/(asce)1090-0241(2008)134:7(972)

Yamamuro, J. A., and Covert, K. M. (2001). Monotonic and cyclic liquefaction of very looses and swith high silt content. *J. geotechnical geoenvironmental engineer-ing* 127 (4), 314–324. doi:10.1061/(asce)1090-0241(2001)127:4(314)

Yasuhara, K., Murakami, S., Song, B. W., Yokokawa, S., and Hyde, A. F. L. (2003). Postcyclic degradation of strength and stiffness for low plasticity silt. *J. Geotechnical Geoenvironmental Eng.* 129 (8), 756–769. doi:10.1061/(asce)1090-0241(2003)129:8(756)

Zhang, H. Y., Liu, J. S., Cui, S. L., and Liang, J. (2010). Controlling mechanism of quartz sand content on shear strength of bentonite-sand mixtures as buffer/backfill material. *J. Rock Mech. Eng.* 29 (12), 2533–2542. (In Chinese). doi:10.13885/j.issn.0455-2059.2018.03.004

Zhao, Y., Li, Y. H., Zhao, K., and Zahng, P. (2015). Comparative study on damping ratio test of remodeled and undisturbed saprolite. *People's Yangtze River* 46 (9), 80–83+105. (In Chinese).

ZhaoKosekiSasaki, C. J. T. (2018). Image based local deformation measurement of saturated sand specimen in undrained cyclic triaxial tests. *Soils Found.* 58 (6), 1313–1325. doi:10.1016/j.sandf.2018.07.008

Frontiers in
Earth Science

Investigates the processes operating within the major spheres of our planet

Advances our understanding across the earth sciences, providing a theoretical background for better use of our planet's resources and equipping us to face major environmental challenges.

Discover the latest Research Topics

See more →

Frontiers

Avenue du Tribunal-Fédéral 34
1005 Lausanne, Switzerland
frontiersin.org

Contact us

+41 (0)21 510 17 00
frontiersin.org/about/contact

frontiers | Research Topics